Amorphous Weathering Products:

Evidence for Basalt-Water Interactions and the Relevance to Paleo-environments on Mars

by

Rebecca Smith

A Dissertation Presented in Partial Fulfillment
of the Requirements for the Degree
Doctor of Philosophy

Approved July 2016 by the
Graduate Supervisory Committee:

Philip Christensen, Chair
Sang-Heon Shim
Hilairy Hartnett
Thomas Sharp
Everett Shock

ARIZONA STATE UNIVERSITY

August 2016

ABSTRACT

Amorphous phases are detected over large regions of the Martian surface from orbit and in more localized deposits by rovers on the surface. Amorphous silicates can be primary or secondary in origin, both having formed through very different processes, so the unambiguous identification of these phases is important for understanding the geologic history of Mars. Secondary amorphous silicates are poorly understood and underrepresented in spectral libraries because they lack the long-range structural order that makes their crystalline counterparts identifiable in most analytical techniques. Fortunately, even amorphous materials have some degree of short-range order so that distinctions can be made with careful characterization.

Two sets of laboratory experiments were used to produce and characterize amorphous weathering products under probable conditions for the Martian surface, and one global spectral analysis using thermal-infrared (TIR) data from the Thermal Emission Spectrometer (TES) instrument was used to constrain variations in amorphous silicates across the Martian surface. The first set of experiments altered crystalline and glassy basalt samples in an open system under strong (pH 1) and moderate (pH 3) acidic conditions. The second set of experiments simulated a current-day Martian weathering scenario involving transient liquid water where basalt glass weathering solutions, formed in circumneutral (pH ~5.5 and 7) conditions, were rapidly evaporated, precipitating amorphous silicates. The samples were characterized using visible and near-infrared (VNIR) spectroscopy, TIR spectroscopy, scanning electron microscopy (SEM), energy dispersive X-ray spectroscopy (EDS), and X-ray diffraction (XRD).

All experiments formed amorphous silicate phases that are new to spectral libraries. Moderately acidic alteration experiments produced no visible or spectral evidence of alteration products, whereas exposure of basalt glass to strongly acidic fluids produced silica-rich alteration layers that are spectrally consistent with VNIR and TIR spectra from the circum-polar region of Mars, indicating this region has undergone acidic weathering. Circum-netural pH basalt weathering solution precipitates are consistent with amorphous materials measured by rovers in soil and rock surface samples in Gale and Gusev Craters, suggesting transient water interactions over the last 3 billion years. Global spectral analyses determine that alteration conditions have varied across the Martian surface, and that alteration has been long lasting.

DEDICATION

To my sister Carrie, who has always encouraged me to push boundaries.

ACKNOWLEDGMENTS

I could not have completed this work without the help of many people. First I thank my advisor Phil Christensen for allowing me this opportunity and for all of his support throughout these years. I must also thank my committee members Everett Shock, Hilairy Hartnett, Tom Sharp, and Dan Shim, who have stuck through this journey with me, guiding me to become the scientist that I am today. Mike Kraft deserves special recognition for his mentorship, enthusiasm, friendship, and humor; our long science conversations were what I had imagined graduate school would be like.

Thank you to the friends, colleagues, and collaborators I've had the pleasure to work with throughout my graduate career, including, but not limited to: Alicia Rutledge, Kristen Bennett, Andy Ryan, Michael Veto, Christopher Edwards, Christopher Haberle, Steve Ruff, Briony Horgan, Mark Salvatore, Deanne Rogers, Matthew Jungers, Jun Huang, Sean Peters, Dale Noss, Ken Rios, and many others at the Mars Space Flight Facility and SESE. Don Doerres, Kris Fecteau, Brian St. Clair, Emmanuel Soignard, and Meg Smith deserve special thanks for all of their assistance with my research. Thank you to my family; mom, dad, Carrie, and Nick for their unwavering love, support, and encouragement, and to my dear Arizona friends Nathan Leach, Jamie Shaffer, Kate Paxton, Ana Marie, and Vanessa Cianci for being the best adventure partners one could hope for.

This work was supported through grants associated with NASA's THEMIS instrument, aboard the spacecraft Mars Odyssey.

TABLE OF CONTENTS

Page

CHAPTER Page

CHAPTER Page

CHAPTER Page

CHAPTER Page

LIST OF TABLES

LIST OF FIGURES

CHAPTER 1

INTRODUCTION

A number of remote sensing techniques have detected chemical and mineralogical evidence for the aqueous alteration of the predominantly basaltic Martian surface. These observations have important implications for the past, present, and future habitability of the planet. Chemical weathering of igneous surfaces involves the dissolution of primary minerals into their chemical constituents that are then precipitated as more stable, secondary phases [*Putnis and Putnis*, 2007]. The phases that precipitate depend on the physical and chemical conditions of their formation environment, and so the nature and habitability of aqueous environments can be determined through unambiguous identification of secondary phases.

Much of our knowledge about the mineralogical variations across the Martian surface comes from spectroscopic observations made from orbiting spacecraft. Thermal infrared (TIR) spectrometry instruments such as the Thermal Emission Spectrometer (TES) [*Christensen et al.*, 1992] allow the derivation of bulk mineral abundances so that lithologies can be studied. Visible and near-infrared (VNIR) spectrometers such as the Observatoire pour la Minéralogie, l'Eau, les Glaces et l'Activité [OMEGA; *Bibring et al.*, 2004] and the Compact Reconnaissance Imaging Spectrometer for Mars [CRISM; *Murchie et al.*, 2007] instruments allow the detection of hydrated minerals at high spatial resolution. A number of factors complicate our interpretation of the data from these instruments including: 1) the physical state of a surface, such as particle size, which can affect the spectral contrast and/or induce transparency features [e.g., *Salisbury and Wald*, 1992; *Ruff*, 2002], 2) Current spectral analysis methods depend on matching measured

spectra features with those in a mineral spectral library; the absence of a specific mineral or phase in the spectral library can lead to inaccurate spectral models, 3) Poorly crystalline phases, which are common components of primary and secondary surfaces, lack the long-range order that make their crystalline counterparts so distinctive in spectral data. Despite these limitations, investigations with these instruments have greatly increased our understanding of the composition and geologic history of Mars.

The relatively dust-free, low-albedo regions of Mars are known to be composed of some combination of the primary minerals olivine, pyroxene, and feldspar, with some regions also containing one or more high-silica phases of indeterminate origin [e.g., *Mccord et al.*, 1982; *Singer*, 1982; *Bell et al.*, 1997; *Christensen*, 1998; *Bandfield et al.*, 2000a; *Bandfield*, 2002; *Rogers and Christensen*, 2007]. The high-silica phase component modeled in TES spectra was initially interpreted as volcanic glass [*Bandfield et al.*, 2000a], suggesting that some surfaces on Mars were andesitic. The high-silica signature has since been re-interpreted to represent a weathered basaltic surface based on the TIR spectral similarities between volcanic glass and a number of secondary phases including clay minerals [*Wyatt and McSween*, 2002], zeolites [*Ruff*, 2004], and poorly crystalline/amorphous silicates such as palagonite [*Morris et al.*, 2003], allophane, Al-Si gels [*Rampe et al.*, 2012] and secondary silica [*Kraft et al.*, 2003]. Most of these phases have VNIR spectral features associated with hydration (~1.4 and 1.9 μm). However, these features are absent in the OMEGA and CRISM datasets from the regions associated with high-silica phases [*Bibring et al.*, 2005; *Mustard et al.*, 2005; *Salvatore et al.*, 2010], which may argue against aqueous alteration. A number of studies have shown that the VNIR spectral hydration bands are sometimes absent or weak in aqueously altered rocks

when the alteration products are found as fracture fill or as coatings [*Michalski et al.*, 2006], and in some secondary silica phases such as silica-rich coatings/alteration layers [*Kraft et al.*, 2007; *Minitti et al.*, 2007]. Of the above-mentioned, high-silica phases, clays, zeolites, allophane, and Si-Al gels have been used to provide good fits to Martian surface spectra. However, none of these phases can individually provide exact or unique matches. Thus the high-silica phases in the Martian surface remain poorly constrained.

Amorphous (noncrystalline) to poorly crystalline phases have become favorable prospects for the high-silica phases due to the TIR spectral detection of amorphous silica-rich volcanic glass. Amorphous silicates can be primary or secondary in nature, and secondary amorphous phases are common products of terrestrial pedogenic and alteration processes [e.g., *Ashley*, 1909; *Allen et al.*, 1981; *Colman*, 1982; *Curtiss et al.*, 1985; *Wada*, 1987; *Stefánsson and Gíslason*, 2001; *Tosca et al.*, 2004; *Chemtob et al.*, 2010; *Seelos et al.*, 2010; *Levard et al.*, 2012]. Yet, because their structures lack long-range order, the variety of secondary amorphous silicate materials and their formation environments, as well as their spectral properties remain poorly studied and understood. Therefore, it is important to study the structural, chemical and spectral properties of amorphous to poorly crystalline phases so that they might be better identified on the Martian surface.

1.1 Purpose and goals

The overarching goal of this dissertation is to help constrain amorphous and poorly crystalline high-silica phase components on the Martian surface, in order to determine the chemical weathering environments that have persisted over large regions of the planet's surface. Phases are constrained by characterizing the spectral, chemical,

structural, and morphological properties of aqueous basalt weathering products formed in acidic to neutral pH environments. This is achieved through laboratory experiments and analyses as well as through fundamental thermal-infrared spectral techniques using global TES data from Mars.

Chapters 2 and 3 are a set of companion papers detailing the methods and results of spectral and microscopic analyses of basaltic materials altered in an acidic environment. Chapter 4 uses the fundamentals of vibrational spectroscopy to identify variations in the structures of the high-silica phases from different regions on the Martian surface. Chapter 5 describes laboratory experiments that form secondary amorphous silicates through the rapid evaporation of basalt weathering solutions produced under acidic to neutral pH environments. The precipitates are compared to orbital and rover datasets from the Martian surface.

1.2 Background

1.2.1 Chemical weathering on Earth

Chemical weathering is a complex process that involves the coupling and feedback of dissolution, precipitation, and mineral replacement reactions [*Gislason and Oelkers*, 2003]. On Earth, dissolution is facilitated by aqueous fluids that penetrate rocks via fractures, veins, sheer zones, and crystal grain boundaries [*Austrheim*, 1986; *Holness*, 1997; *Bach and Früh-Green*, 2010; *Jonas et al.*, 2014]. Fluids interact with and dissolve primary minerals and glasses within a rock in sequences that depend on a number of factors including the environmental pH, temperature, and pressure. Because the Martian surface is primarily basaltic in composition, I focus on the chemical weathering of basaltic materials.

Chemical weathering on Earth takes place in a wide range of environments that vary in pH, temperature, water/rock ratios, and alteration time. Basaltic minerals and glasses persist at timescales that are highly dependent on pH [*Hausrath et al.*, 2008]. In general, at typical Earth surface temperatures and at very low pH (<= 2) the minerals dissolve in this sequence: basalt glass > olivine > plagioclase > pyroxene. At more moderate to neutral pH (2 < pH < 8), olivine dissolves first, followed by basalt glass, then plagioclase and pyroxene [*Hausrath et al.*, 2008]. Dissolution rates can be affected by other factors such as pressure and crystal grain size, but in general, these rates help determine the composition of a weathering solution for a given starting material.

Chemical weathering products form through the alteration of parent minerals or through the precipitation of soluble species [*Essington*, 2004]. Weathering products are most commonly found as coatings, rinds, fracture fill, or as colloid to clay size particles in soils [*Colman*, 1982; *Eggleton et al.*, 1987], and they generally make up a small fraction of the inorganic materials in weathered rocks and soils [*Essington*, 2004]. The products that form through chemical weathering reactions are highly dependent on the starting material, the composition of the weathering fluids, and the formation environment (i.e., temperature, pressure, atmospheric composition, etc.). Weathering products can be crystalline (having repetitive, long-range order) or noncrystalline/poorly-crystalline (generally some short-range order). Amorphous is used synonymously with noncrystalline, because phases typically considered amorphous, such as glasses, are shown to have some degree of short-range order [*Handke and Mozgawa*, 1993].

Noncrystalline phases can form from most solutions with bulk compositions that contain a sufficient concentration of network forming components (e.g., Si, Al, Fe), and it

is generally thought that formation time is an important factor determining whether a composition will form as crystalline or noncrystalline phases [*Yamane and Asahara*, 2000]. Volcanic glasses generally form when magmas are quenched quickly, giving little time for the atoms to arrange themselves [*Yamane and Asahara*, 2000]. Likewise, noncrystalline weathering products, such as allophane and Si-Al gels, are commonly thought to be intermediate alteration products representing the incomplete development of clay minerals from primary minerals [*Colman*, 1982].

1.2.2 Infrared spectroscopy

Spectroscopy has been used to map the distribution of minerals across the Martian surface using two main wavelength ranges: the visible and near-infrared (VNIR), from ~0.4 – 5 μm, and the thermal-infrared (TIR), from ~5 – 50 μm (2000 – 200 cm^{-1}). For most geologic materials, crystal lattice vibrational energy levels fall within these spectral ranges. Minerals absorb photons at specific wavelengths, depending on their chemistry and crystal structure, making them identifiable based on the absorption features in their spectrum.

The VNIR range measures the upper few micrometers of a surface, and is especially important for detecting hydrated minerals because H_2O and OH stretching and bending vibrations occur within this spectral range [*Clark*, 1999]. Additionally, the visible section of the VNIR range measures electronic transitions within a material as electrons are excited to a higher energy level in transition metals (i.e., Fe, Mn, Cu). Thus, VNIR is used to detect both Fe-bearing minerals and hydrous minerals.

Thermal-infrared spectroscopy is able to detect molecular vibrations within silicates, carbonates, sulfates, and oxides, and the sampling depth is generally the upper

few 10s of micrometers of a surface, but can vary depending on the absorption coefficient of the material being measured. The TIR spectrum of a surface is a linear combination of the components within the surface, scaled to the aerial abundance of each mineral, because minerals have high absorption coefficients in the TIR wavenumber range and photons are expected to interact with only one particle before being emitted from the surface [*Lyon*, 1965; *Thomson and Salisbury*, 1993; *Ramsey and Christensen*, 1998]. Thus, mineral abundances can be derived from a surface spectrum through spectral deconvolution methods that use a linear least squares fitting algorithm and a mineral spectral library to model the measured spectrum [*Ramsey and Christensen*, 1998]. Fine-grained (< ~10s of micrometers) particle surfaces do not combine linearly in the TIR because the small grains are optically thin so that photons are transmitted through particles, interacting with multiple particles before exiting the surface. Therefore, dusty surfaces are generally avoided in TIR spectral analyses.

1.2.3 Chemical weathering on Mars

Despite significant differences between the planets, observations of chemical weathering on Earth can help to constrain past conditions on Mars. Currently, Mars is much colder than Earth with daily average surface temperatures in the equatorial regions of ~226 K (-47°C) [*Hamilton et al.*, 2014] though this varies significantly between regions and seasonally [*Kieffer et al.*, 1977]. Mar's average atmospheric pressure is around 6 mbar (0.006 atm) for equatorial regions [*Haberle et al.*, 2001], and Mars has a different atmospheric composition (96% CO_2, 1.9% Ar, 1.9% N_2, and 0.15% O_2) [*Mahaffy et al.*, 2013] than Earth. Thus, liquid water is not currently stable on the Martian surface. However, it is thought that Mars might have had a thicker atmosphere early in its

history that could have lead to warmer temperatures and increased stability of liquid water [*Bibring et al.*, 2006].

Mineral assemblages on Mars vary on a number of spatial scales from "regions" with areas that are ~10^4 to 10^6 km^2, to "locales" with areas ~10^1 to 10^3 km^2 [*Rogers and Christensen*, 2007; *Rogers and Hamilton*, 2015], to "outcrops" with areas ~10^{-1} – 10 m^2 [*Squyres*, 2004]. For example, the Spirit rover mapped evidence for aqueous alteration (e.g., enhanced Cl, Br, S, and Fe^{3+}/Fe_{total}) in the Watchtower class rock outcrops in Gusev Crater and found that the distribution varied over distances less than 1 m in a stratigraphic section and over ~10 m laterally [*Squyres*, 2004]. *Ehlmann et al.* [2009] mapped hydrated phyllosilicate and sulfate mineral variations across the Nili Fossae location, a highly weathered area that lies within the larger, primarily unaltered basaltic Syrtis Major region. Thus, alteration has varied across the Martian surface at the outcrop and locale scales, and is also thought to vary from region to region.

CHAPTER 2

ACID WEATHERING OF BASALT AND BASALTIC GLASS: I. NEAR-INFRARED SPECTRA, THERMAL-INFRARED SPECTRA, AND IMPLICATIONS FOR MARS

2.1 Introduction

Acidic weathering creates a unique suite of alteration products that are not observed under the neutral to alkaline weathering conditions that are more common in aqueous environments on Earth. On Mars, the products of acidic alteration appear to be widespread, and have been used to support the hypothesis that the Martian environment became much more acidic and oxidizing through time [*e.g., Bibring et al.*, 2006]. In addition to the acid sulfates observed at sites like Meridiani Planum and Mawrth Vallis [*Squyres et al.*, 2004; *Farrand et al.*, 2009], recent studies have shown that the low albedo regions of the north polar sand sea and much of the northern plains of Mars are spectrally consistent with acid leached glass [*Horgan and Bell*, 2012]. This inference of leached glass is based on studies of the near-infrared spectra of volcanic glasses altered naturally *in situ* by acidic fluids at low water:rock ratios, which produce very thin leached and silica-enriched rinds on the surface of glass, often overlain by silica-rich coatings [*Minitti et al.*, 2007; *Seelos et al.*, 2010; *Chemtob et al.*, 2010]. However, the origin of the unique near-infrared spectral signature of the rinds and their spectral development over time are poorly understood.

One method that could confirm the presence of acid leached glass at these locations on Mars would be thermal-infrared spectra from instruments like the Thermal Emission Spectrometer (TES) [*Christensen et al.*, 1998]. Intriguingly, the regions on Mars where near-infrared spectra are consistent with leached glass coincide with regions

that are also spectrally distinct in TES thermal infrared spectra. Unlike the more common olivine basalt composition (TES Surface Type 1), models of spectra from the northern plains and several other locations on Mars require an additional high-silica component (TES Surface Type 2) [*Bandfield et al.*, 2000a]. The nature of this high-silica component is not well constrained, and could be consistent with either primary volcanic glasses (e.g., obsidian in an andesitic basalt; *Bandfield et al.*, 2000a] or with secondary alteration products (e.g., opal, zeolites, allophane, silica coatings) [*Kraft et al.*, 2003; *Wyatt and McSween et al.*, 2005; *Michalski et al.*, 2002; *Ruff and Christensen*, 2007; *Rampe et al.*, 2012). The close association between the near-infrared signatures of leached glass and TES high-silica phases in the northern plains suggests that silica rinds could be the dominant high-silica phase in TES Surface Type 2. However, the effect of leached rinds on the thermal infrared spectra of glasses and whether or not this could be spectrally consistent with TES Surface Type 2 is not well understood. Previous studies of natural leached glasses indicated a possible consistency with TES Surface Type 2 [*Minitti et al.*, 2007], but their thermal-infrared spectra have not been investigated in detail.

Thus, in this study we seek to understand the near-infrared and thermal-infrared spectral effects of acid weathering on basaltic glasses, how those spectral effects differ from those caused by acid weathering of crystalline basalts, as well as how varying pH affects basaltic weathering. This basic understanding may help us to constrain the composition and weathering history of large regions of the Martian surface.

2.2 Background

2.2.1 Previous acid weathering experiments

Previous experiments have simulated acid weathering of basalts on Mars, with a focus on the secondary minerals produced by these processes. In general, these studies have found that highly acidic alteration (starting pH 0 – 1) leads to precipitation of sulfates and silica, while more moderately acidic alteration (starting pH 3 – 4) mainly leads to precipitation of iron oxides. However, an important additional outcome of many of these experiments is that glasses behave differently and are often less reactive under acidic alteration than their crystalline counterparts.

Banin et al. [1997] submerged palagonitized basaltic tephra in acidic fluids for 7 days at 25 °C (a closed system) and showed that gypsum and alunogen were the primary alteration products using x-ray diffraction (XRD). In a similar closed system experiment, Tosca *et al.* [2004] submerged sand-size basaltic andesite (~57 wt% SiO_2), basalt (~48 wt% SiO_2), and their glass counterparts in acidic fluids of varying concentrations (starting pH 0 – 4). The results after 14 days at 25 °C varied with both crystallinity and composition. For the crystalline samples, highly acidic weathering favored deposition of sulfates and amorphous silica while the solution maintained a persistently acidic pH, and moderately acidic weathering released enough solutes to buffer the solution to higher pH and then precipitated iron oxides. At low pH, precipitation of amorphous silica and Fe/Mg-sulfates was enhanced by the dissolution of olivine in the basalt, while Ca-sulfate precipitation was related to dissolution of Ca-bearing pyroxene and plagioclase feldspar in both the basalt and basaltic andesite. Follow up experiments by *Yant et al*. [2016] recreated the *Tosca et al*. [2004] experiments over a period of 14 days with an expanded suite of glasses and showed that more mafic glasses showed more intense alteration spectral signatures than the more silicic glasses over the duration of the experiment,

including strong silica and sulfate signatures and blue spectral slopes in the visible/near-infrared and silica absorptions in the thermal-infrared.

The glass samples in *Tosca et al.* [2004] behaved quite differently from their crystalline counterparts. The high-Si (basaltic andesite) glass dissolved non-stoichiometrically, indicating that the glassy SiO_4 network was more resilient to dissolution than network modifying cations (Fe^{2+}, Mg^{2+}, Ca^{2+}, Na^{+}, etc.). This effect was more pronounced at higher pH (starting pH 4, buffered up to 11), which caused significant removal of Na^{+} and deposition of halite (NaCl). At lower pH (starting pH 1 – 2, buffered up to 6), the high-Si glass was actually more resistant to dissolution than either of the crystalline samples, producing only poorly crystalline Na/Ca-sulfates and minor gypsum from removal of Ca. At low pH starting pH 0, (buffered to 1), the high-Si glass initially dissolved stoichiometrically to form amorphous silica coatings, but rapidly ceased dissolution altogether once the coatings became thick enough to prevent further infiltration. In contrast, the low-Si (basaltic) glass completely dissolved to form amorphous silica at very low pH, and formed coatings of iron oxides at higher pH. These results are consistent with the observation that the dissolution rate of glasses in both natural and laboratory environments is inversely proportional to silica content [*Glass*, 1984; *Wolff-Boenisch et al.*, 2004].

In order to test the effects of different alteration conditions on alteration precipitates, *Golden et al.* [2005] performed similar closed system experiments alongside open system (three stage) and vapor alteration experiments, all 6 days in total length, at high temperature (145°C), and a very low starting pH (0 – 1). The materials in these experiments included an olivine-rich basaltic sand and a plagioclase and glass-rich

basaltic tephra, as loose 500 – 1000 μm grains, ground and sieved to <53 μm loose grains, and as compressed thick sections. In the closed system experiments, they found that amorphous silica was the primary precipitate for all samples, similar to the very low pH *Tosca et al.* [2004] results. The open system and acid fog (vapor alteration) experiments gave similar results, with additional precipitation of Mg/Fe/Al-sulfates in all olivine-bearing samples, and additional Ca-sulfates in all samples in the acid fog experiments. Although the effects on primary phases were not a focus of this study, the authors did note that basaltic glass appeared to be the least reactive phase under acidic leaching in all experiments, followed by plagioclase, and then olivine as the most reactive. Subsequent modeling has suggested that pyroxene falls between olivine and plagioclase on this scale [*McAdam et al.*, 2008].

In a further permutation of possible weathering regimes, *Hurowitz et al.* [2005] conducted flow-through acid weathering experiments on basalts, using both entirely fresh fluids and multiple batches of recycled fluids, for up to 17 days. Evaporite minerals from these experiments were dominated by sulfates and amorphous silica, similar to previous experiments, with significantly more sulfates produced under batch experiments. SEM and Raman analysis of reacted basalt indicated significant amorphous silica as well as limited occurrences of poorly crystalline iron oxide phases, potentially consistent with ferrihydrite.

Marcucci et al. [2014] exposed plagioclase, olivine, and pyroxene mineral separates and basaltic cinders to acidic alteration (starting pH 0 – 3.5) under closed system, hydrothermal conditions (65, 150, and 200°C) with variable water:rock ratios for up to 60 days. The main alteration products in their experiments included diverse sulfates

with compositions corresponding to cations that were available from the primary phase undergoing weathering. They found that varying the experimental conditions within the parameter ranges of their experiments did not significantly affect the mineralogy of precipitated alteration products, but did alter their relative abundance. Plagioclase and olivine weathering both produced significant amorphous silica coatings, with aluminum-bearing silica coatings forming on plagioclase. While all of these experiments were conducted at moderate to high temperatures, other dissolution experiments suggest that similar weathering trends persist at low temperature, although the rate of dissolution (especially of silica) is much lower [*Hausrath et al.*, 2010].

Together, these results confirm that amorphous silica, sulfates, and sometimes iron oxides are all common secondary minerals produced during acidic weathering of both basalts and basaltic glasses. However, the differences observed in the secondary precipitates and in the relative stability of the crystalline basalts vs. the glasses suggest that different mechanisms facilitate acidic weathering in these two phases.

2.2.2 Acid leaching of mineral and glass surfaces

In our experiments, we are interested in the effects of acid leaching on primary minerals and glasses, and, in particular, on the formation of leached rinds and precipitated coatings. Previous studies have suggested that these two types of weathering products are formed via different processes [*e.g., Minitti et al.*, 2007]. During exposure to acidic fluids, most silicate minerals undergo stoichiometric dissolution, wherein all elements in the silicate structure are extracted at similar rates [*e.g., Ruiz-Agudo et al.*, 2012]. Once the elements are in solution, their relative solubilities determine their fate. Oxidized iron and silica both have low solubilities at low to neutral pH, and so are often rapidly re-

deposited on the surface of the mineral as a poorly crystalline or amorphous coating [*Petit et al.*, 2009; *King et al.*, 2011]. Similar silica-rich and sometimes iron-bearing coatings can form without any alteration of the substrate, such as those due to dissolution of windblown dust in a desert environment, or precipitation of transported silica sourced from alteration elsewhere in the system, as in silica sinters or diagenesis of quartz-rich sandstones [*Dorn*, 1998]. Because they have an external source for the silica, these coatings can become very thick, often exceeding millimeters in thickness [*Oguchi*, 2004].

Leached rinds, however, are thought to be unique to glasses and a few other minerals, including some varieties of feldspar. When these phases are exposed to acidic fluids, their dissolution is non-stoichiometric. In the case of glasses, the canonical model is that the polymerized silicate structure and constituent cations (Si^{4+} and Al^{3+}) in glass are more difficult to remove than the more weakly bound univalent and divalent network-modifying cations (Fe^{2+}, Mg^{2+}, Ca^{2+}, Na^{+}, etc.), so the network-modifying cations are preferentially removed [*White*, 1983; *Oelkers and Gislason*, 2001]. This produces a residual leached outer rind on the glass surface that is composed exclusively of the silicate network. Thus, this rind appears to be enriched in silica relative to the interior, but is actually just depleted in all other major oxides [*Chemtob et al.*, 2010]. Alternatively, more recent studies of this process in crystalline minerals have suggested that these apparently leached layers may instead be formed through a highly localized process of total dissolution followed by non-stoichiometric precipitation [*Ruiz-Agodo* et al, 2012; *Hellmann et al.*, 2012). This process may also be responsible for producing leached layers in glasses [*Crovisier et al.*, 1987; *Geisler et al.*, 2010; *Geisler et al.*, 2015]. See our companion paper for a more in depth discussion of this topic [*Smith et al.*, submitted].

For continuity with previous Mars-relevant work [e.g., *Minitti et al.*, 2007; *Chemtob et al.*, 2010; *Horgan and Bell*, 2012], here we will continue to refer to these leaching and/or dissolution fronts on glass as leached rinds.

In either case, due to their limiting effect on the diffusion rate of additional cations from their substrate, these leached rinds are often self-limiting in their depth, and rarely exceed 10 μm [*White*, 1983; *Minitti et al.*, 2007; *Chemtob et al.*, 2010]. This steady state condition (full rind development) can occur quickly with continuous exposure to low pH. For example, in silicic glass (64 – 79 wt% SiO_2) dissolution experiments, *White* [1983] found that rinds, as indicated by steady-state concentrations of cations in solution, were fully developed after 3 weeks at 25°C and pH 1.0, but were not developed after 6 months at pH 6.2. After their initial exposure and rapid dissolution, leached glasses are highly resistant to further leaching, as dissolution of the rind itself occurs at a much slower rate than the initial cation leaching. Dissolution of the rind occurs as H^+ from the solution exchanges with Al substituted for Si in the silicate structure, which partially liberates adjoining silica tetrahedral, that eventually become detached and dissolve [*Oelkers and Gislason*, 2001]. Deposition of silica coatings on the exterior of the glass can also lead to even slower dissolution of the rind [*Berger et al.*, 1994], especially at low pH or at low temperatures, when silica solubility is low [*Gislason and Oelkers*, 2003]. Because of this stability under long term leaching, glass is the most common material used to construct vessels for the underground storage of radioactive materials [*Techer et al.*, 2001; *Grambow*, 2006].

2.2.3 Spectral signatures of leached rinds and coatings

Leached rinds and silica coatings exhibit different spectral signatures in the near-infrared. Silica exhibits diagnostic absorption bands near 1.4 and 1.9 μm due to overtones of OH stretching vibrational modes in adsorbed H_2O, as well as a broad doublet absorption band near 2.21 and 2.26 μm due to Si-OH rotation and stretching vibrational modes [*e.g.,* Langer and Florke, 1974; *Rice et al.*, 2013]. Thick silica coatings on basalt exhibit these absorption bands, but also often exhibit a strong blue spectral slope (less reflectance at longer wavelengths) from the visible into the near-infrared [*Milliken et al.*, 2008]. Similar blue spectral slopes have been observed in studies of other bright coatings, like ferric oxides [*Fischer and Pieters*, 1990]. The skin depth of reflected light is usually estimated to be on the order of the wavelength of the light, so in that study, the cause of the blue slope was hypothesized to be greater skin depths of the reflecting light at longer wavelengths, leading to more absorption by the underlying dark materials, and thus decreasing reflectance with increasing wavelengths. In contrast, very thin silica coatings (a few μm thick) do not exhibit either the blue spectral slope or detectable absorption bands [*Kraft et al.*, 2007].

Minitti et al. [2007] examined the near-infrared spectra of natural silica-coated glassy basalts from the surface of a forty-year old flow on Mauna Kea, Hawaii. Both the silica absorption bands and the blue spectral slope are present in spectra of some of the samples. However, other samples exhibit not just blue, but also concave up spectral slopes, the strongest of which occur without corresponding silica absorption bands. In a detailed investigation of the samples, *Minitti et al.* [2007] showed that concave up spectral slopes were exhibited both by some of the white or orange silica coatings as well

as by thin (<3 μm), dull, and dark rinds that appeared to underlie these coatings. *Minitti et al.* [2007] hypothesized that these rinds formed due to acidic leaching, and scanning electron microscope (SEM) and back-scattered electron (BSE) images of these samples confirm that they exhibit residual and silica-enriched glassy rinds consistent with a leaching origin [*Chemtob et al.*, 2010]. Based on lab and field observations, the leaching most likely occurred due to both syn-depositional and post-depositional alteration by acidic volcanic vapors [*Chemtob et al.*, 2010]; *Seelos et al.* [2010] confirmed that the leached rind signature is apparent in aerial near-infrared spectra of the Mauna Kea flow, suggesting that similar signatures could contribute to regional spectral signatures on Mars. Laboratory leaching experiments by *Yant et al*. [2016] showed that, after 14 days of leaching, the occurrence and strength of the concave up and blue spectral slopes varies with both glass composition (*e.g.,* mafic vs. silcic) and pH.

Thus, the primary difference between near-infrared reflection spectra of well-developed residual leached rinds and silica coatings deposited without leaching is both a lack of silica or hydration absorption bands and the concave up shape in the leached rind spectra. The lack of silica and hydration bands in the leached rind spectra is consistent with the leaching process being dominated by removal as opposed to deposition or exchange, as proposed by studies discussed above. However, the origin of the concave up slope is unclear. The slope is typically fit well by an inverse power law function in wavelength, with an exponent between -2 to -4 [*Horgan and Bell*, 2012]. This function is similar to power law effects that occur due to Tyndall scattering in colloids [*He et al.*, 2009], and similar spectral effects in the VNIR are observed due to scattering by sub-micron grains [*Brown*, 2014]. Thus, we hypothesize in this study that the concave up

spectral shape is due to wavelength-dependent scattering by structures at the sub-micron scale, perhaps related to surface textures or micron-scale porosity in the rinds.

In the mid- or thermal-infrared (5 – 50 μm), emission dominates over reflection on planetary surfaces, and leached rinds and thin coatings are thin enough that thermal photons emitted from the unaltered substrate could potentially penetrate the rind or coating. However, laboratory studies of depositional silica coatings have shown that even very thin coatings (<10 μm) dominate the resulting thermal-IR spectra, and entirely obscure the substrate [*Kraft et al.* 2003]. Spectra of silica coatings strongly resemble high-silica glasses like obsidian [*Kraft et al.*, 2003; *Michalski et al.*, 2006], although their absorption features are shifted relative to these phases. However, the thermal-infrared spectral character of leached rinds is unclear. Thermal-IR spectra of the natural Hawaiian leached samples in *Minitti et al.* [2007] also appear similar to high-silica glass, but as the thermal-IR spectra reported are that of the bulk rock surface and not individual spots like in the near-infrared, it is unclear what the contribution of leached rinds is to these spectra.

2.3 Methods

2.3.1 Acid leaching experiments

Four samples were used in this study, with varying degrees of crystallinity: a Columbia River Plateau basalt from the Rosa dike (BAS205), a partially glassy or hypocrystalline (crystals embedded in a glassy matrix) Icelandic olivine basalt from a subaqueous pillow lava (ICE170), a Hawaiian glassy basalt from a subaerial flow (BAS101), and Hawaiian basaltic glass sand, produced during explosive quenching of a lava flow entering the ocean and concentrated on a black sand beach (BSB101; see Table 2.1 for sample information). Grain size is an important factor in weathering, so each

basalt hand sample was both cut into cm-scale fragments using a diamond rock saw and ground into sand (500 – 1000 μm) using a mortar and pestle. The cm-scale fragments exhibit both porous natural weathered surfaces as well as smooth fresh-cut surfaces. The basaltic glass was collected in the field as sand, so no cm-scale fragments are available.

For our experiment, we have chosen to recreate an open hydrologic system, which we simulated by placing our samples in oxidizing and acidic solution baths and then frequently replacing the fluids with a fresh acid solution. Two stock acid solutions were made up using concentrated H_2SO_4 and distilled H_2O, with a pH of 1.0 (Acid A) and 3.0 (Acid B). Approximately 7 g of the four granular samples and the three cut samples were placed in separate Teflon vessels with 30 ml of the stock sulphuric acid solution and 10 ml of 30% H_2O_2. Hydrogen peroxide was chosen as the oxidizing agent because superoxides and peroxides have been suggested as candidates for the purported oxidant in Martian surface materials [*Zent and McKay*, 1994; *Golde*n *et al.*, 2005]. The samples were fully immersed in the solutions initially for one day at a time, and gradually for longer durations as the alteration progress slowed. In total, all samples were exposed to acid for 220 days at 25°C. Figure 2.1 shows an example of the sand-size glassy basalt (BAS101), before immersion and after 69 days of leaching in Acid A (starting pH ~1). The grains exhibit white-colored coatings or rinds and possible pitting, both indications of surface weathering.

Table 2.1. Sample information.

Sample	***Description***	***Surface Type***		
		Grains	*Cut*	*Natural*
BSB101	Basaltic Glass, black sand beach, Hawaii (collected by R.B. Singer)	A, B[1]		
ICE170	Basalt, pillow lava, Dagmalafell, Iceland (collected by E. Cloutis)	A, B	A, B	A, B
BAS101	Basaltic Glass, Kilauea Caldera, 1956 flow, Hawaii (collected by E. Cloutis)	A, B	A	A
BAS205	Basalt, Roza Dike, Columbia River Plateau (collected by S. Atkinson[2])	A, B	A, B	A, B

[1] A and B indicate which acid solutions were used to weather samples, as described in text.
[2] *Atkinson et al.* [1990], sample #SA-78

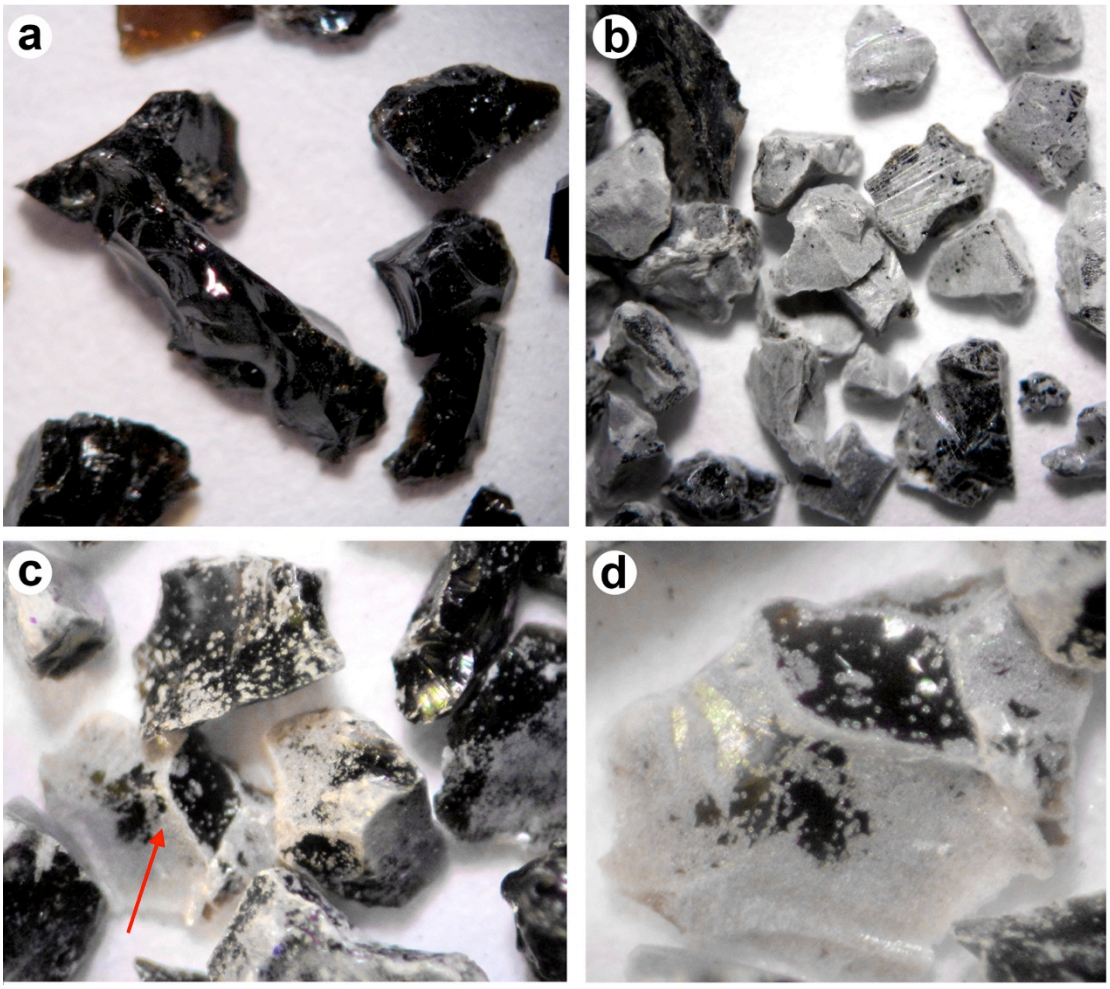

Figure 2.1. Visible microscope images of Hawaiian glassy basalt BAS101 ground sand samples; all grains are 500 – 1000 mm in diameter. (a) Before immersion in acidic solutions. (b) After 69 days of leaching in Acid A, under diffuse lighting. (c) After 69 days of leaching in Acid A, under directed lighting. Arrow indicates location of grain shown in close-up in (d), with possible pitted textures.

2.3.2 Near-infrared spectroscopy

Initial diffuse reflectance spectral data were collected as a baseline from all the samples using an ASD FieldSpec Pro HR spectrometer over the wavelength range of 0.35 to 2.5 μm. A 150 W QTH light source was used to illuminate the samples and reflectance spectra were measured at i=30°, e=0°; 200 spectra were collected and averaged to improve SNR. To reduce the effects of specular reflections, all 500 – 1000 μm samples were spun on a turntable at 33.5 rpm during data collection. Some spectral signatures may still be attributable to diffraction effects related to specular reflection off of the ground glass sand samples, as shown by wavy spectra at visible wavelengths in Figure 2.5 (BAS101 Acid A).

On the days scheduled for spectra collection, the pH of each solution was recorded and the acid was decanted into an evaporation dish for future analysis. In order to remove all loose alteration products (*i.e.,*, all alteration products other than coatings or rinds), the decanted samples were rinsed with distilled H_2O and dried at 80°C for two hours prior to spectral analysis. To ensure consistency, the same procedures used to collect the baseline spectra were implemented during each spectral measurement. Following data collection, a few grains of each sample were also set aside for future analysis. A fresh solution of acid and H_2O_2 was then prepared, the pH was recorded, and the samples were again placed in the solution.

2.3.3 Thermal infrared spectroscopy

Thermal-infrared emission spectra (TIR) were measured at the Arizona State University Mars Space Flight Facility using a Nicolet Nexus 670 spectrometer that is configured to measure emissivity [*Ruff et al.*, 1999]. Spectra were collected at a spectral

resolution of 2 cm^{-1} over the range of 200 – 2000 cm^{-1}. Samples were placed in copper cups coated with black paint to achieve near unit emissivity. The cups and samples were heated to 80 °C for multiple hours prior to being measured, and this temperature was maintained during spectral acquisition by actively heating the sample with a hotplate. All TIR spectral measurements were taken after the acid leaching experiments were complete. TIR spectra were acquired for un-altered starting materials, end-stage materials (220 days of alteration), and select intermediate samples removed at various stages during the experiment.

Mineral abundances were estimated for sand-size samples by modeling the TIR spectra using a spectral library of potential phases (Table 2.2), including common basalt minerals and weathering products, and a blackbody spectrum to obtain a non-negative linear least squares fit to each measured spectrum [*Ramsey and Christensen*, 1998; *Rogers and Christensen*, 2007]. End-members were chosen based on multiple parameters including spectrum quality, sample quality, and sample size - selecting coarse particulate or hand samples when possible. The detection limit for the linear deconvolution method ranges between 5 – 10% [*Feely and Christensen*, 1999], and the quality of the model is quantified by the root-mean-square (RMS) error, a parameter that compares the modeled emissivity spectrum to the measured spectrum [*Ramsey and Christensen*, 1998]. In general, a lower RMS value indicates a better fit, though the model should also be visually inspected for quality. Additionally, it is possible for the algorithm to select phases not present in the sample to substitute for end-members that are not available in the spectral library [e.g*., Ruff et al.*, 2006].

Table 2.2. Thermal-infrared spectral endmember library

Mineral Group	*Endmember*
Alkali feldspar	Microcline CUR-3460A
Plagioclase	Albite WAR-0235 Andesine WAR-0024 Anorthite BUR-340 Bytownite WAR-1384 Labradorite BUR-3080A Oligoclase BUR-060
Orthopyroxene	Bronzite NMNH-93527 Enstatite HS-9.4B Hypersthene NMNH-B18247
High-Ca clinopyroxene	Augite NMHN-93527 Augite NMHN-9780 Diopside WAR-6474 Hedenbergite manganoan DSM-HED01
Low-Ca clinopyroxene	Avg. Lindsley pigeonite
Olivine	Fayalite WAR-FAY01 Forsterite AZ-01 KI3008Fo10 KI3373Fo35 KI3362 Fo60 KI3115 Fo68
Phyllosilicates	Montmorillonite (Ca) STx-1 Montmorillonite (Na) Swy-2 Saponite < 0.2 mic Serpentine HS-8.4B Smectite Swa-1
Sulfate	Anhydrite S16 Coquimbite/Para-coquimbite S46 Gypsum S6 Kieserite
Zeolite	Crystalline heulandite Crystalline stilbite
Carbonate	Calcite C40 Dolomite C20
Oxide	Hematite BUR-2600 Ilmenite WAR-4119 Magnetite WAR-0384 Titanomagnetite
Amorphous alumino-silicate	Allophane Si:Al 0.58 ALL0058 Aluminous opal
Amorphous silica	Opal-A Opal-CT
Felsic volcanic glass	Dacite glass MEM-4 K-rich glass (obsidian) SiO2 glass
Mafic volcanic glass	TES basalt proxy glass MEM-1

[1] *Rampe et al*. [2012]

Some physical properties of natural and laboratory samples are known to influence a spectrum such that the materials combine in ways that are not necessarily linear, and so they should be considered when analyzing modeled mineral abundances. Relatively thin (~10 μm) silicate weathering rinds and coatings can significantly contribute to, and sometimes completely obscure the TIR signature of a surface [*Kahle et al.*, 1988; *Crisp et al.*, 1990; *Kraft et al.*, 2003; *Minitti et al.*, 2007], and thus the abundance of such phases can be overestimated. Additionally, spectral contrast decreases with particle size, and so mineral mixtures of various particle sizes can cause certain phases to be over- or underestimated [*Rogers and Christensen*, 2007].

2.4 Results

2.4.1 Near-infrared spectra

We observe four key types of near-infrared spectral changes during acid alteration of our basalt, glassy basalt, and basaltic glass samples, as summarized in Figure 2.2. These changes are almost all observed exclusively at pH ~1, as we find very little near-infrared spectral evidence for alteration of the residual primary grains by pH ~3 fluids. First, we observe changes to the relative strength of broad absorptions near 1 and 2 μm due to primary, iron-bearing minerals and glasses. This includes both the weakening of these iron bands overall as well as the strengthening of some iron bands relative to others (usually pyroxene absorptions at the expense of olivine absorptions). Second, we observe the appearance and sometimes the disappearance of narrow absorption bands near 1.4,

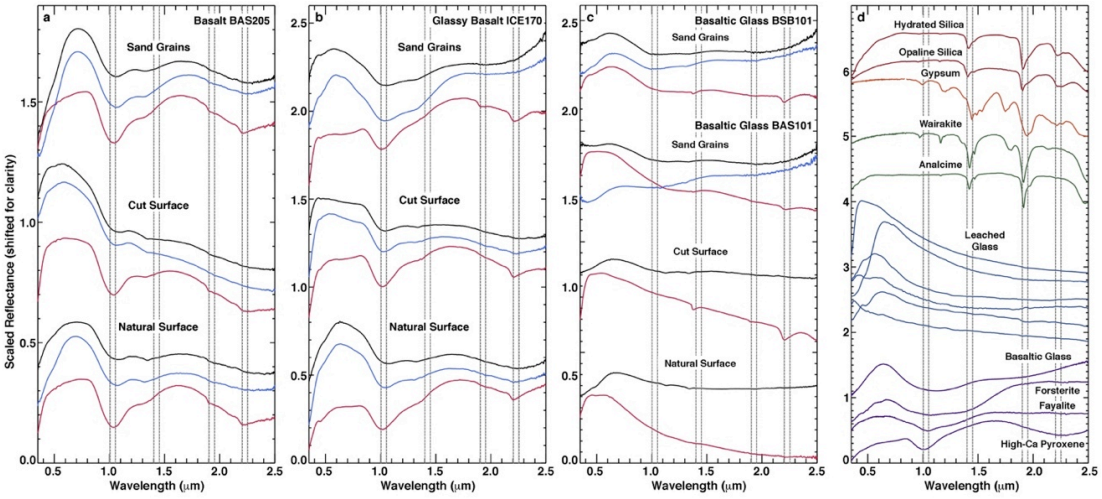

Figure 2.2. Summary of visible/near-infrared spectral results, showing spectra of glass and basalt samples before and after 213 days of alteration. Black spectra are from before alteration, blue are after alteration in Acid B (starting pH ~3), and red are after alteration in Acid A (starting pH ~1). (a) BAS205 crystalline basalt, (b) ICE170 partially glassy basalt, and (c) BAS101/BSB101 basaltic glasses, compared to (d) laboratory spectra [e.g., *Clark et al.*, 2006] of primary minerals (purple), zeolites (green), sulfates (orange), and silica (red) and naturally altered glasses (blue) [*Minitti et al.*, 2007]. Dashed lines indicate key absorption features in some spectra at 1.00, 1.05, 1.40, 1.45, 1.90, 1.95, 2.20, and 2.25 μm.

1.9, 2.2, and 2.4 μm, consistent with the deposition (and sometimes the removal) of various alteration minerals (*e.g.,* silica, hydrated glass, gypsum, and other sulfates). Third, we observe a flattening of spectra at short visible wavelengths (typically between 0.4-0.7 μm), perhaps related to dissolution of fine-grained oxides. Lastly, we observe the development of strong spectral slopes in glassy samples, most likely related to the development of rinds and coatings on the samples. We find that increasing spectral change correlates with both increasing acid strength and decreasing crystallinity. These results are detailed in the following section.

2.4.1.1 Basalt samples

Spectra of crystalline Columbia River basalt (BAS205) are shown in Figure 2.3. Prior to alteration, the BAS205 samples all exhibit broad absorptions bands with minima near 1.05 – 1.07 μm, consistent with olivine, high-Ca pyroxene, or a mixture of the two [*e.g., Adams*, 1968; *Cloutis and Gaffey*, 1991]. Some samples also exhibit a second broad absorption near 2.2 μm, consistent with a high-Ca pyroxene component, which is strongest in the sand-size samples. A strong shoulder on the 1 μm band near 1.3 μm suggests a contribution from olivine, which exhibits a shoulder at this location that is often apparent in mixtures [*e.g., Horga*n *et al.*, 2014]. The depth of the 1.3 μm shoulder without a corresponding ~0.85 μm olivine shoulder may be enhanced by Fe-bearing plagioclase feldspar, which exhibits a band near 1.3 μm that is usually only visible for high ratios of plagioclase to pyroxene and olivine [*e.g., Cheek et al.*, 2014]. This primary mineral assemblage of significant plagioclase with lesser amounts of olivine and pyroxene is supported by thermal-infrared spectral analysis (Section 2.4.2).

As exposure time progresses, the acids appear to have limited or no effect on the spectra of the rinsed basalt samples, with Acid B (starting pH ~3) causing no apparent spectral changes. All BAS205 samples exposed to Acid A (starting pH ~1) do exhibit a strengthening of the 1 and 2 μm bands, without a concomitant increase in the strength of the 1.3 μm olivine/plagioclase shoulder. We hypothesize that the overall strengthening of the bands is due to either exposure of larger grains and/or the preferential dissolution of opaque components, such as those that may be present as a fine-grained matrix. The fact that the 1.3 μm shoulder band depth remains relatively unchanged could be consistent with a preferential dissolution of olivine, but not plagioclase, relative to pyroxene, resulting in spectra dominated by pyroxene signatures. In addition, acid A causes a significant flattening of the spectra of all samples between 0.45 – 0.70 μm, perhaps also consistent with the removal of fine grained, Fe/Ti oxide-bearing matrix materials. Lastly, acid A also causes the appearance of very weak narrow absorption bands near 1.9 and 2.2 μm, likely due to small amounts of hydrated silica. It is key to note that surface texture and grain size appear to have no influence on observed spectral changes in this crystalline basalt, unlike many of the samples discussed below.

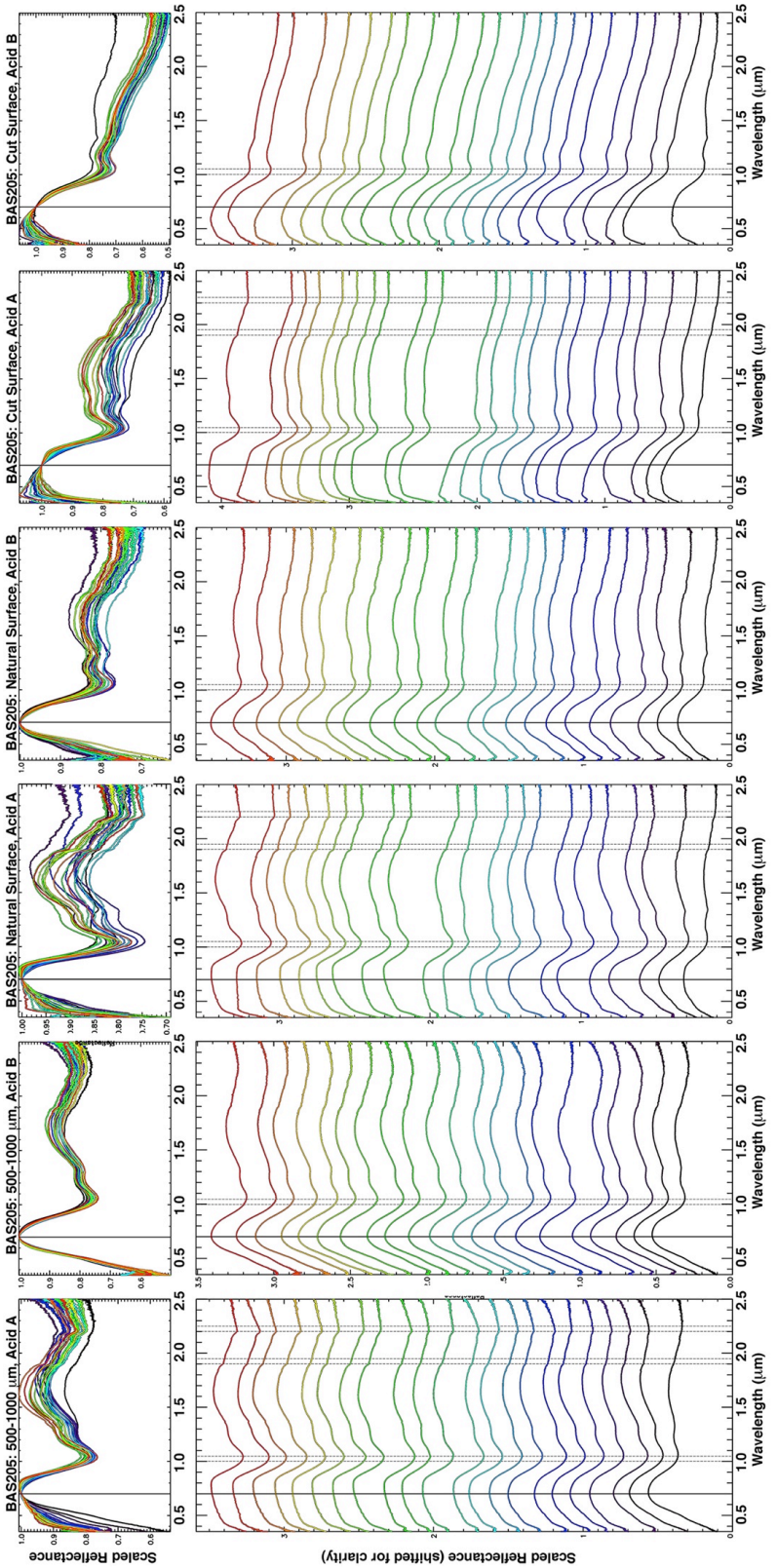
BAS205: 500-1000 µm, Acid A
BAS205: 500-1000 µm, Acid B
BAS205: Natural Surface, Acid A
BAS205: Natural Surface, Acid B
BAS205: Cut Surface, Acid A
BAS205: Cut Surface, Acid B
Scaled Reflectance
Scaled Reflectance (shifted for clarity)
Wavelength (µm)

Figure 2.3. Near-infrared spectra of Columbia River flood basalt sample BAS205 before, during, and after 213 days of leaching (days 0, 1, 2, 3, 4, 6, 8, 10, 13, 16, 20, 23, 29, 36, 43, 50, 59, 69, 83, 101, 122, 213). All spectra have been normalized near 0.6 mm, as shown in the top row. The bottom row shows these same spectra stacked for clarity, with dashed lines for reference shown where needed at 1.00, 1.05, 1.40, 1.45, 1.90, 1.95, 2.20, and 2.25 mm. Anomalous spectra not shown: 500-1000 mm Acid B day 59 and natural surface Acid A day 13.

2.4.1.2 Glassy basalt samples

Spectra of the glass-bearing Icelandic pillow basalt (ICE170) are shown in Figure 2.4. Prior to alteration, most of the ICE170 samples exhibit broad absorption bands with minima near 1.05 and 2.2 μm that are consistent with a high-calcium pyroxene, with a contribution from olivine, as indicated by a strong shoulder near 1.25 μm and a corresponding weaker shoulder near 0.85 μm. These absorptions are demonstrated most clearly in the sand size samples. However, there is variability within the starting samples. The cut surfaces of the larger samples both exhibit more subdued olivine absorptions and a flattening in the visible compared to the sand size sample, which we hypothesize is due to lower spectral contrast in the slab. The natural surface of the sample exposed to Acid A exhibits absorptions centered near 1.05 and 2.25 μm consistent with pyroxene; however, the 1 μm band has an asymmetrical shape due to additional absorption at longer wavelengths. While this could be consistent with an olivine component, the lack of the corresponding ~0.85 μm feature observed in the other, likely olivine-bearing samples suggests that this asymmetry is instead due to iron-bearing glass, which exhibits an iron absorption band centered at longer wavelengths (1.1 – 1.2 μm). The spectrum of the natural surface of the sample exposed to Acid B clearly exhibits a broad, glass-like 1 μm absorption band centered closer to 1.12 μm. The presence of glass on the natural surface is consistent with a glassy quench rind on this pillow lava.

Acid B (starting pH ~3) has very little effect on the spectra of the sand grains and the cut surface of the Icelandic basaltic pillow lava, with virtually no clear difference between the spectra of the cut surface from day 0 and day 213 (Figure 2.4). Notably, the

sand grains still exhibit a strong olivine signature at the end of the experiment, which may be somewhat stronger than the starting sample, perhaps due to some preferential loss of pyroxene. The natural glassy quench rind surface does exhibit significant variability throughout exposure to Acid B – at various stages exhibiting absorption bands consistent with olivine, pyroxene, or glass. We interpret this variability to represent heterogeneity in the sample, either due to concentrations and/or phenocrysts of these phases being exposed by the acid over time, or to the rough surface texture and variation in the precise viewing geometry emphasizing some phases over others in subsequent spectra. However, the spectra of the natural surface eventually stabilize, exhibiting absorption bands and an overall shape that are very similar to the spectra of the cut surface.

In contrast, all Icelandic pillow basalt samples (ICE170) exposed to Acid A (starting pH ~1) exhibit clear spectral signatures of alteration. As soon as days 2 – 4, all samples exhibit weak absorption bands near 1.9 and 2.2 μm. The 2.2 μm absorption deepens over the course of the experiment, and develops an asymmetric shape with more absorption toward longer wavelengths. These spectral features are consistent with hydrated silica or hydrated glass, as shown in Figure 2.2, most likely present as a coating on the samples. The natural surface of the larger sample also exhibits transient spectral features near 1.45, 1.75, 1.95, 2.27, and 2.42 μm on day 59 that are consistent with the hydrated Ca-sulfate gypsum, as shown in Figure 2.2. Additionally, on days 43 and 50, this same sample exhibits spectral features near 1.42, 1.92, 1.78, 2.1, and 2.46 μm that are most consistent with a combination of Al and Mg-bearing sulfates (*e.g.,* alunite and kieserite [*Cloutis et al.*, 2006]), as shown in Figure 2.2. All of these sulfates are known products of acid alteration [*e.g., Tosca et al.*, 2004; *Golden et al.*, 2005; *Marcucci et al.*,

2010]. The fact that they are only observed transiently on the natural surface of the larger sample suggests that we observed them because the rough surface texture temporarily prevented them from being removed during the rinsing step.

The final spectra of all three Icelandic pillow basalt samples (sand grains, natural surface, and cut surface) exposed to Acid A look remarkably similar. In addition to the narrow silica absorption bands near 1.9 and 2.2 μm, all three samples exhibit broad high-Ca pyroxene absorptions near 1.05 and 2.25 μm and a similar spectral shape. The 1 μm pyroxene absorptions have become clearer due to the loss of longer-wavelength olivine and glass absorptions, suggesting that preferential dissolution of olivine and glass occurred on the grain and sample surfaces. Finally, similar to the crystalline basalt samples, alteration by Acid A tends to flatten the spectra in the short wavelengths, in this case between 0.4 – 0.8 μm.

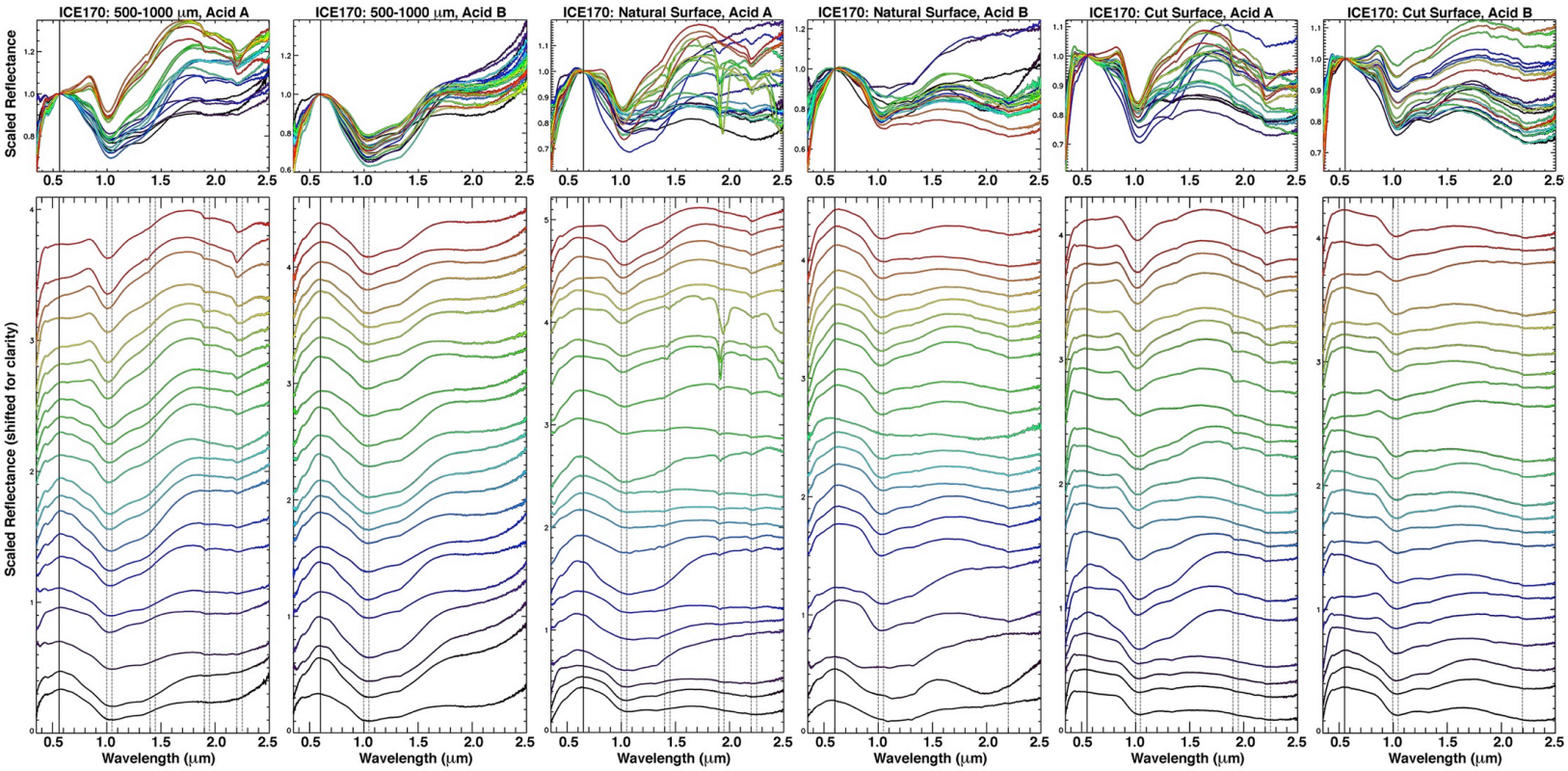
ICE170; 500-1000 μm, Acid A
ICE170; 500-1000 μm, Acid B
ICE170: Natural Surface, Acid A
ICE170: Natural Surface, Acid B
ICE170: Cut Surface, Acid A
ICE170: Cut Surface, Acid B
Scaled Reflectance
Scaled Reflectance (shifted for clarity)
Wavelength (μm)

Figure 2.4. Near-infrared spectra of Icelandic glass-bearing basalt ICE170 before, during, and after 213 days of leaching (days 0, 1, 2, 3, 4, 6, 8, 10, 13, 16, 20, 23, 29, 36, 43, 50, 59, 69, 83, 101, 122, 213). All spectra have been normalized near 0.6 mm, as shown in the top row. The bottom row shows these same spectra stacked for clarity, with dashed lines for reference shown where needed at 1.00, 1.05, 1.40, 1.45, 1.90, 1.95, 2.20, and 2.25 mm. Missing spectrum not shown: 500 – 1000 mm Acid A day 69.

2.4.1.3 Glass samples

Spectra of the glass-rich Hawaiian basaltic lava (BAS101) and glass-rich pyroclastic beads (BSB101) are shown in Figure 2.5. Prior to alteration, the granular lava sample (BAS101) exhibits broad but shallow absorption bands near 1.15 and 1.95 μm that are classic examples of iron absorptions in glass [*e.g., Adams*, 1974; *Minitti et al.*, 2002]. The pyroclastic bead sample (BSB101) exhibits similar bands, but with additional absorption within the 1 μm band near 1.05 and 1.3 μm consistent with some degree of recrystallization to olivine within the glass.

On alteration in Acid B (starting pH ~3), these absorption bands in all samples remain unchanged throughout the experiment, and no silica or hydration bands are observed. However, both granular samples develop a strong red slope (reflectance increasing to longer wavelengths) as well as additional absorptions near 0.5 μm, which together are most consistent with an oxide coating [*e.g., Fischer and Pieters*, 1993].

On exposure to Acid A (starting pH ~1), the granular glassy samples exhibit nearly opposite behavior from Acid B. In both samples, the glass absorptions initially appear to strengthen significantly. In both samples, diffraction effects die out as the 1 and 2 μm bands become subdued. In the final spectra, while the 1 μm band is still clearly visible, the 2 μm band has largely disappeared in both samples. The olivine absorptions in the beads (BSB101) also have disappeared, leaving a symmetric shape centered near 1.1 μm that is much more consistent with glass. Over the course of the experiment, both granular samples develop a strong concave-up slope (greater blue slope at shorter wavelengths). This shape is characteristic of leached rinds that have been shown to form on natural glass samples due to acid leaching, as discussed above (Sections 2.2.2 – 2.2.3).

The lava grains (BAS101) also develop a strong blue slope (decreasing reflectance at longer wavelengths) that is most apparent at longer wavelengths (1.5 – 2.5 μm). Both granular samples develop narrow absorptions near 1.38 and 2.20 μm consistent with hydrated silica or hydrated glass.

Prior to alteration, the natural surface of the glass-rich lava (BAS101) already exhibits a weak concave up slope characteristic of leached glassy rinds, without any absorptions due to glass, olivine, hydration, or any alteration phases. Over the course of the experiment, the strength of the concave up slope gradually increases, and the short visible wavelengths also flatten out, as observed in the granular sample. Like in the BAS101 Acid A grains, the slope is blue as well as concave. No absorption bands are observed to form in the natural surface spectra throughout the experiment.

The cut surface exhibits very different spectral characteristics from any other sample, both initially and throughout the experiment. The cut surface initially only exhibits a weak glass band near 1.15 μm with no corresponding 2 μm band, superposed on a weak linear (non-concave) blue slope. With exposure, the glass band appears to strengthen, and while some of this may be due to diffraction, some of the increase may be real, as the Day 59 spectrum exhibits no apparent diffraction but does exhibit very strong glass bands. Eventually, the glass bands are completely subdued. This is most likely due to the development of a hydrated silica coating, as suggested by both the strong blue slope of the altered spectra as well as the strong absorptions near 1.38, 1.9, and 2.2 μm.

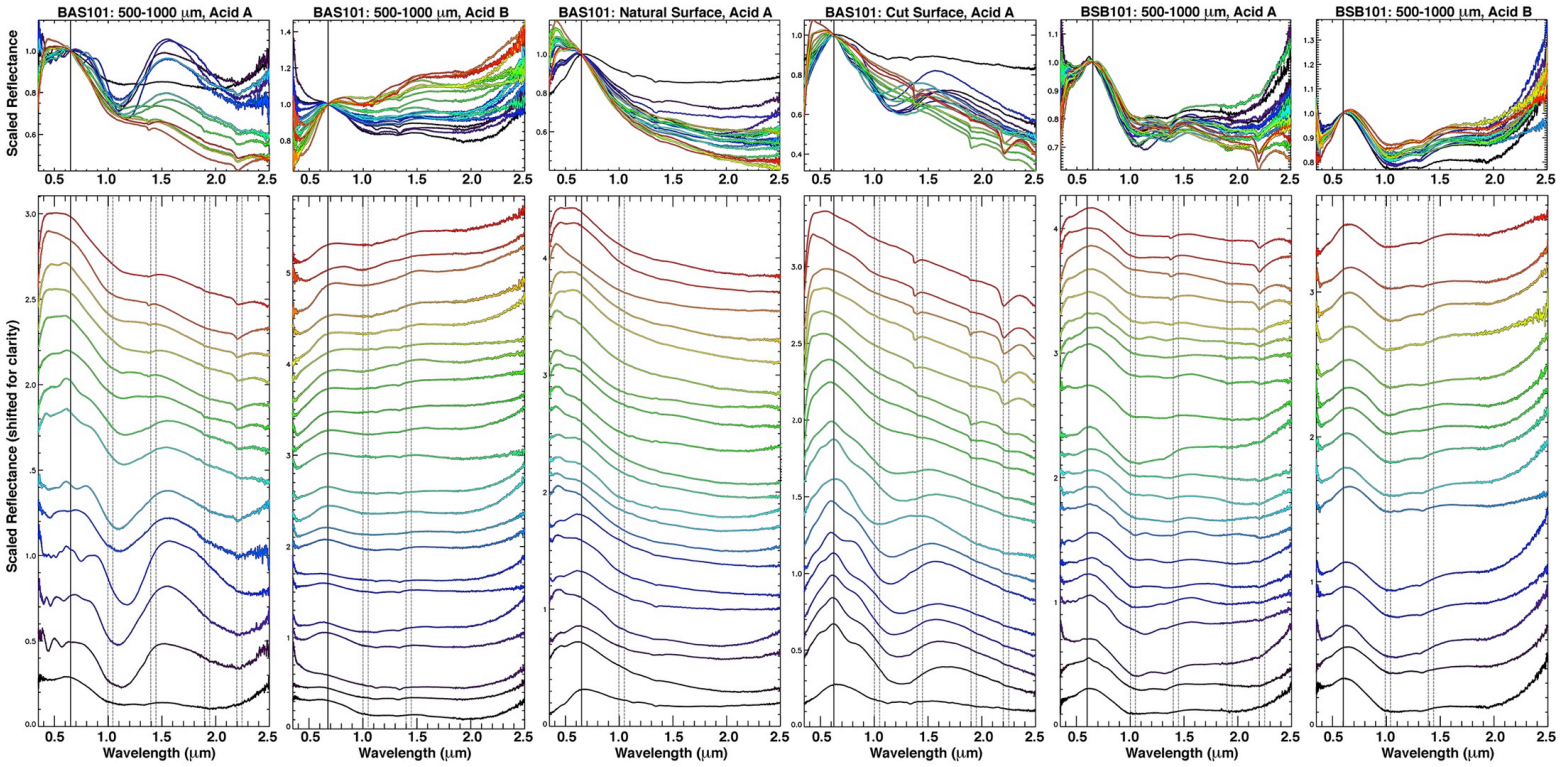
BAS101: 500-1000 μm, Acid A
BAS101: 500-1000 μm, Acid B
BAS101: Natural Surface, Acid A
BAS101: Cut Surface, Acid A
BSB101: 500-1000 μm, Acid A
BSB101: 500-1000 μm, Acid B
Scaled Reflectance
Scaled Reflectance (shifted for clarity)
Wavelength (μm)

Figure 2.5. Near-infrared spectra of Hawaiian glass-rich samples – glassy basalt sample BAS101 and glass sand sample BSB101 – before, during, and after 213 days of leaching (days 0, 1, 2, 3, 4, 6, 8, 10, 13, 16, 20, 23, 29, 36, 43, 50, 59, 69, 83, 101, 122, 213). All spectra have been normalized near 0.6 mm, as shown in the top row. The bottom row shows these same spectra stacked for clarity, with dashed lines for reference shown where needed at 1.00, 1.05, 1.40, 1.45, 1.90, 1.95, 2.20, and 2.25 mm. Possible diffraction effects are apparent in BAS 101 Acid A grains before Day 36, although the strongest diffraction-obscured or otherwise anomalous spectra are not shown: BAS101 500-1000 mm Acid A days 1, 2, 4, 6, 8, 16, 20, and 29; BAS101 Natural Surface day 23; and BAS101 Cut Surface days 1, 2, 8, and 10.

2.4.2 Thermal-infrared spectra

In general, we see changes in the thermal-infrared spectral shape in two main wavenumber regions for the acid leached basalt, glassy basalt, and basaltic glass samples, as summarized in Figure 2.6. As with the near-infrared, the spectral changes are observed almost exclusively at pH ~1, and there is little spectral evidence for alteration of the primary grains by pH ~3 fluids. The first spectral change is a shift of the emissivity minimum in the wavenumber range of the fundamental Si-O asymmetric stretching vibration between ~900 – 1300 cm^{-1}, suggesting that the weathering process is affecting the silicate structure of the samples. When exposed to acid A, most samples show emissivity minima shifted to a higher wavenumber (~1100 cm^{-1}), indicating increased polymerization of the material [*White and Minser*, 1984; *Crisp et al.*, 1990; *Michalsk*i *et al.*, 2005]. However, this emissivity minimum is lower than that of pure opal (1115 cm^{-1}) indicating that the material probably contains network modifying cations (e.g., K^{+}, Na^{+}, Mg^{2+}) and/or water molecules that cause the structure to depolymerize. Samples exposed to acid B generally show emissivity minima shifted toward lower wavenumbers, which suggests a preferential loss of more polymerized phases, such as plagioclase (Figure 2.6).

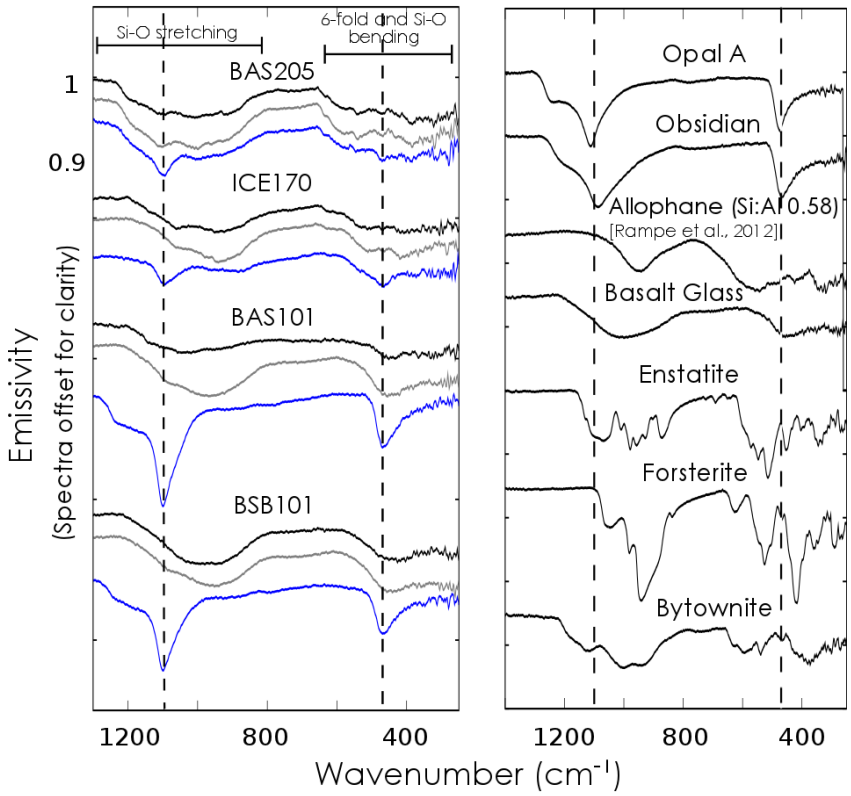

Figure 2.6. (left) Thermal-infrared spectra of all sand-size samples. Black spectra indicate starting material, grey spectra indicate grains weathered in acid B (starting pH 3) for 213 days, and blue spectra indicate grains weathered in acid A (starting pH 1) for 213 days. Vertical dashed lines indicate emissivity minima at 1100 cm^{-1} and 465 cm^{-1} for the materials weathered in pH 1 acid. (right) Laboratory spectra from the Arizona State University Online Spectral Library Tool, showing examples of some of the endmember phases in Table 2.2. Vertical dashed lines indicate emissivity minima positions at 1100 cm^{-1} and 465 cm^{-1} for the materials weathered in pH 1 acid.

The second spectral change is a shift of the emissivity minimum between ~300 – 600 cm^{-1}. The absorptions in this region are more complicated for crystalline samples, because of overlap in the energy levels of tetrahedral Si-O bending vibrations as well as vibrations of cations in 6-fold coordination sites [*Michalski et al.*, 2005], and so each case is examined separately. However, in general, we see the development of a local emissivity minimum around 465 cm^{-1} in all samples exposed to acid A, which can most likely be attributed to tetrahedral Si-O bending vibrations [*Lippincott et al.*, 1958]. These observations are detailed in the following sections. The spectral differences between samples as they relate to micro-scale weathering features and starting material physical properties are discussed in our companion paper [*Smith et al.*, submitted].

2.4.2.1 Basalt samples

The two broad absorption features of the crystalline basalt (BAS205) starting material are centered near 1010 cm^{-1} and 360 cm^{-1}, which are consistent with a mafic composition [*Feely and Christensen*, 1999; *Bandfield et al.*, 2000a]. The abundance of superposed high frequency absorption features suggests the presence of crystalline phases (Figure 2.6). Linear unmixing suggests that BAS205 is predominantly composed of plagioclase feldspar, mafic glass, oxides (titanomagnetite), olivine, and high-Ca clinopyroxene (Figure 2.7).

The spectral changes to BAS205 grains after exposure to acid B are very subtle. We observe an overall increase in spectral contrast with increasing alteration time at all wavenumber, and especially between 880 cm^{-1} and 1190 cm^{-1} (Figure 2.8). We also observe a decrease in the absorption feature centered at 918 cm^{-1} (Figure 2.8). These changes in the spectral shape are interpreted in the unmixing models as a relative increase

in plagioclase and amorphous silicate/silica phases at the expense of mafic glass and oxides (Figure 2.7). In both Acid A and Acid B samples, the relative increase in primary phases (including plagioclase and pyroxenes) after alteration suggests that some material was totally lost to solution, rather than re-precipitated as an alteration product.

After exposure to acid A for 4 days, the main Si-O stretching emissivity minimum of the granular samples shifts to 1100 cm^{-1}, while still retaining the local emissivity minimum at ~1010 cm^{-1} (Figure 2.8). After 29 days in acid A, the overall spectral absorption shape becomes slightly broader at lower wavenumbers, the spectral contrast decreases between ~ 320 – 420 cm^{-1} and 500 – 650 cm^{-1}, and a 465 cm^{-1} feature deepens. Around day 69, the 1100 cm^{-1} feature begins to deepen further so that at the end of the experiment at 220 days, the 1100 cm^{-1} feature is dominant. However, there still remains an absorption feature centered near 980 cm^{-1}, apparent as a shoulder on the main Si-O stretching absorption. The linear deconvolution model attributes these changes to a relative decrease in mafic glass and oxides, and an increase in amorphous silicate/silica phases (including a felsic glass) and sulfate minerals (Figure 2.7). The sulfate minerals are most likely not actually present in the altered sample because their inclusion creates a sharp feature ~1020 cm^{-1} in the model that is not apparent in the measured spectrum.

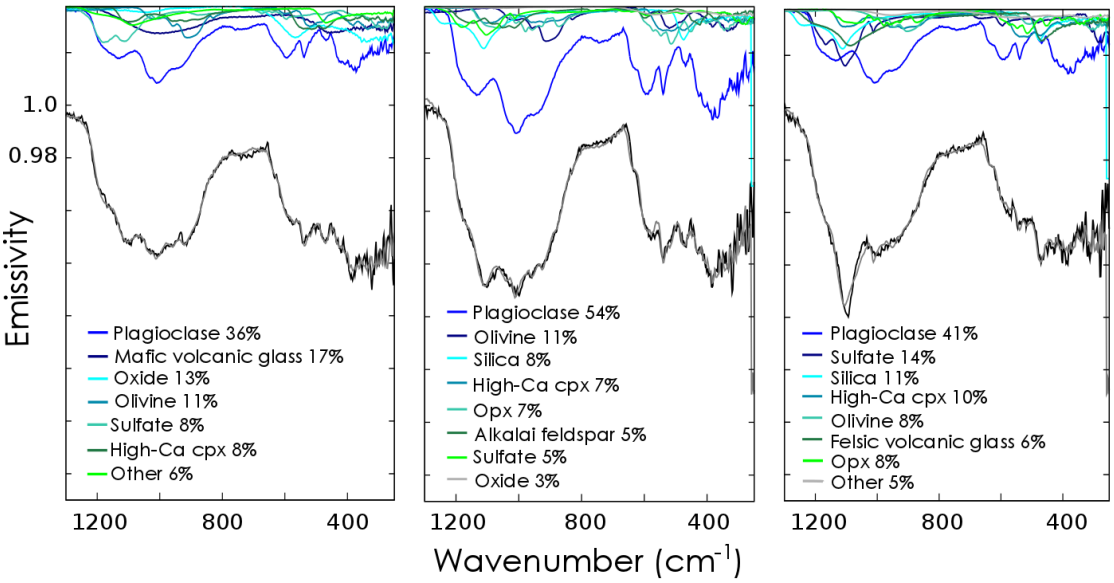

Figure 2.7. Linear deconvolution of thermal-IR spectra of BAS205 starting material (left), grains exposed to acid B (middle), and grains exposed to acid A (right) using mineral endmember library in Table 2.2. The "Other" category is a bin for phases modeled in abundances < 5%. RMS error = 0.17%, 0.23% and 0.22%, respectively. Black and grey indicate the measured and modeled spectra, respectively.

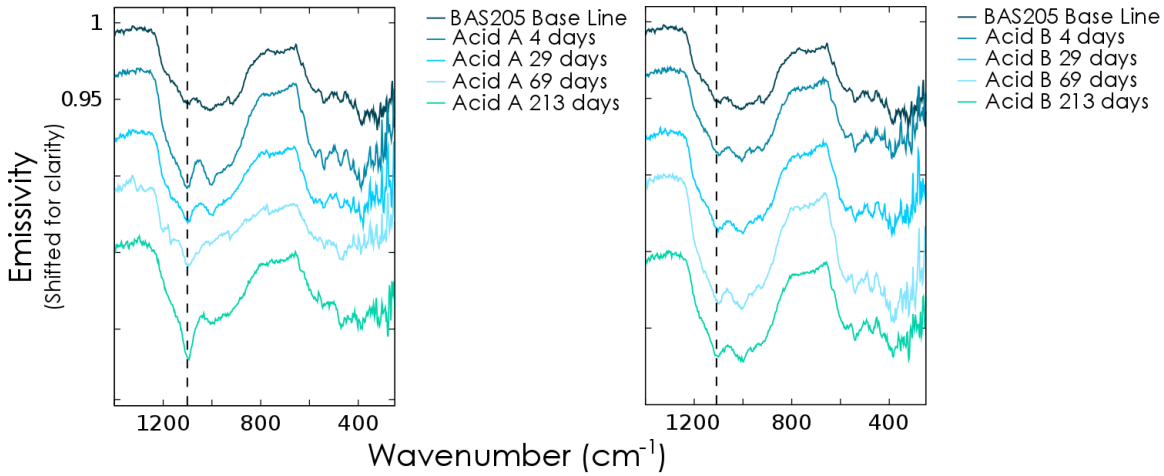

Figure 2.8 Thermal-infrared spectral evolution of BAS205 grains exposed to acid A (left) and acid B (right) over the duration of the experiment. The dashed line in the left plot indicates 1100 cm^{-1}, the final location of the shifting Si-O stretching emissivity minimum. In the right plot, the dashed line is centered at 918 cm^{-1}, indicating a relative decrease in mafic glass and oxide abundances.

2.4.2.2 Glassy basalt samples

ICE170 grains initially look similar to BAS205 starting material, but with slightly broader absorption features centered on 1000 cm^{-1} and 400 cm^{-1} that can be attributed to a greater abundance of basaltic glass (Figure 2.6). This is evident in the linear deconvolution result that uses mostly basaltic glass, olivine and pyroxene to model the measured spectrum (Figure 2.9).

The Si-O stretching emissivity minimum of ICE170 shifts to higher wavenumber after exposure to acid A for only 6 days (Figure 2.10). The spectral shape stays nearly the same until the end of the experiment at 220 days, when the sample develops sharp emissivity minima at 1095 cm^{-1} and 465 cm^{-1} while retaining local minima centered around 925 cm^{-1} and 380 cm^{-1} (Figure 2.10). These changes are modeled as an overall decrease in basaltic glass and a relative increase in high-silica phases such as phyllosilicates, amorphous silica, and zeolites, as well as sulfates (Figure 2.9). The dominant high-silica phase used to model the spectrum of the material after 220 days is montmorillonite, which has a Si-O stretching emissivity minimum at ~1070 cm^{-1}, yet there is no indication of clays in the near-IR spectra. Additionally, sulfates do not appear to be real components in the samples because their inclusion in the spectral modeling induces features at 1010 cm^{-1} and 290 cm^{-1} that are not present in the data. Due to this sulfate misfit and the lack of near-IR clay or sulfate absorptions bands in this sample, we hypothesize that the model is using these high-silica and sulfate phases to replicate the spectrum of another high-silica endmember not present in our library. This phase appears to have a minimum near 1095 cm^{-1}, suggesting that it may be somewhat less polymerized

than opaline silica. There is also a modeled increase in clinopyroxene, mainly at the expense of glass, but also due to some loss of olivine and plagioclase.

After exposure of ICE170 to acid B for 4 days, the spectral feature at 940 cm^{-1} deepens significantly, becoming the dominant emission feature (Figure 2.10). There is little change to the spectrum until the end of the experiment at 220 days when a feature at 1060 cm^{-1} essentially disappears (Figure 2.10). At lower wavenumber, the sample retains the major absorption features of the starting material at 415 cm^{-1} and 510 cm^{-1}, but the 415 cm^{-1} feature deepens greatly. These spectral changes are modeled as a relative increase in more mafic phases such as basaltic glass and olivine, at the expense or pyroxene and plagioclase (Figure 2.9). Notably, no significant alteration phases are detected; however, the Si-O stretching emissivity minimum shift to lower wavenumber indicates that the sample has become more structurally disordered.

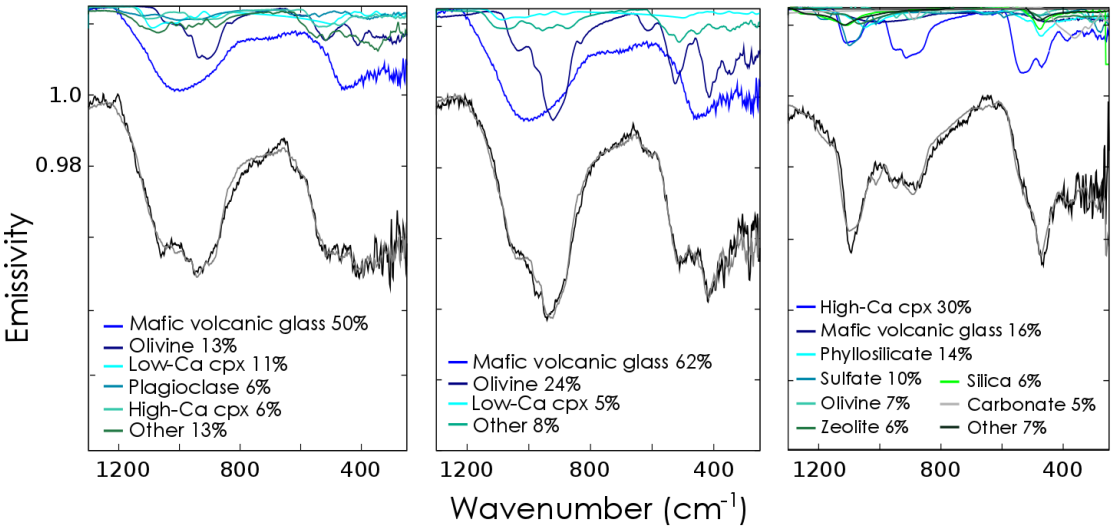

Figure 2.9. Linear deconvolution of thermal-IR spectra of ICE170 starting material (left), grains exposed to acid B (middle), and grains exposed to acid A (right) thermal-infrared spectrum using mineral endmember library in Table 2.2. RMS error = 0.22%, 0.24% and 0.21%, respectively. Black and grey indicate the measured and modeled spectra, respectively.

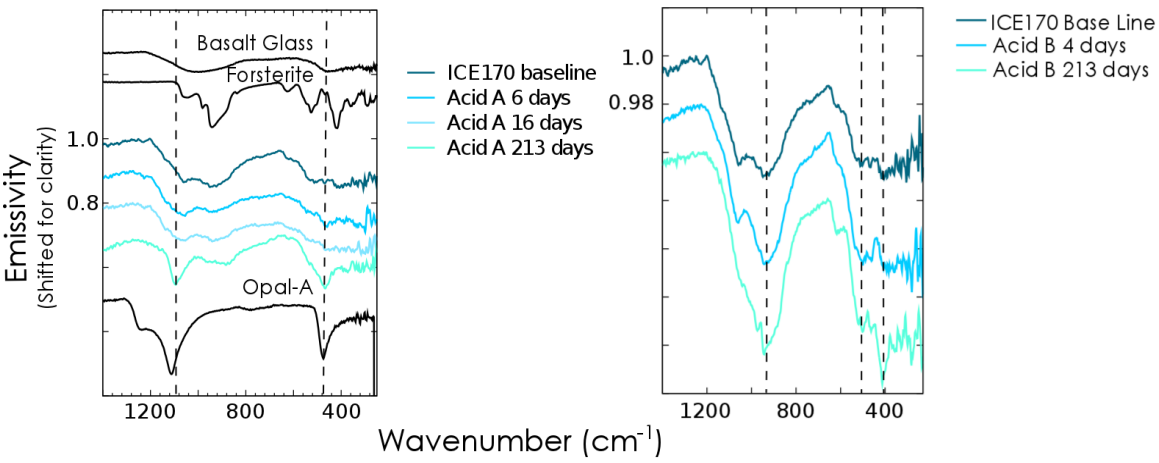

Figure 2.10. Spectral evolution of ICE170 grains weathered in acid A (left) and acid B (right) for the duration of the experiments. Black spectra are taken from the spectral library and are shown for comparison. Dashed lines indicate emissivity minima of final products from experiments at 1095 cm^{-1} and 465 cm^{-1} (left), and at 940 cm^{-1}, 510 cm^{-1}, and 415 cm^{-1} (right).

2.4.2.3 Glass samples

The thermal-IR spectra of the unaltered glass-rich Hawaiian basaltic lava (BAS101) and glass-rich pyroclastic beads (BSB101) are shown in Figure 2.6. Both spectra look very similar to a typical basaltic glass, with broad Si-O stretching and bending spectral features centered around 1010 cm^{-1} and 445 cm^{-1} for the lava grains and ~980 cm^{-1} and 430 cm^{-1} for the pyroclastic beads (Figure 2.6). The spectra also have very few superposed narrow absorption features, which suggests a high abundance of basaltic glass, and this interpretation is supported by the linear unmixing analysis (Figure 2.11). The glass-rich BSB101 sand samples have a wider Si-O stretching absorption feature shifted to lower wavenumber than that of a typical basaltic glass (Figure 2.6), which suggests the presence of olivine and is supported by the linear unmixing model (Figure 2.13).

Both of the basaltic glass samples exposed to acid B show Si-O stretching features shifted toward lower wavenumber. BAS101 exposed to acid B alters very slowly, remaining spectrally unchanged until near the end of the experiment at 220 days when a shallow absorption feature around 1060 cm^{-1} is lost, which shifts the center of the Si-O stretching absorption feature to lower wavenumber (~970 cm^{-1}; Figure 2.12). Similarly, the Si-O stretching feature of BSB101 is shifted to ~960 cm^{-1} (Figure 2.6). At lower wavenumbers, the absorption feature ~450 cm^{-1} deepens for both samples, and a feature at ~340 cm^{-1} is almost completely removed from the BAS101 spectrum.

The spectral changes for BAS101 are represented in the unmixing model as a loss of clinopyroxene and relative increase in basaltic glass (Figure 2.11). The loss of the absorption feature at ~340 cm^{-1} possibly indicates a decrease in iron oxides. This could

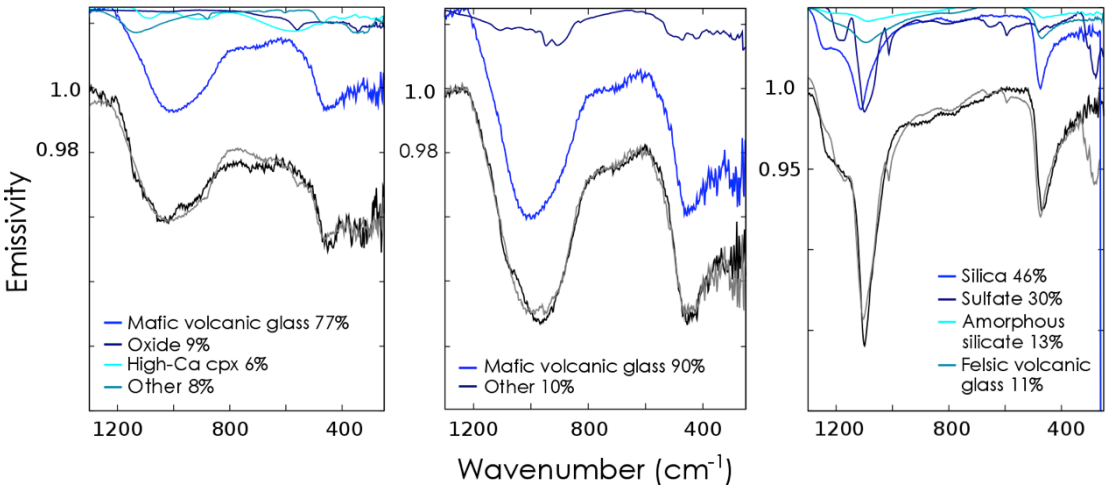

Figure 2.11. Linear deconvolution of thermal-IR spectra of BAS101 starting material (left), grains exposed to acid B (middle), and grains exposed to acid A (right) using mineral endmember library shown in Table 2.2. The "Other" category is an additive bin for phases modeled in abundances < 5%. RMS error = 0.28 %, 0.81% and 0.26%, respectively. Black and grey indicate the measured and modeled spectra, respectively.

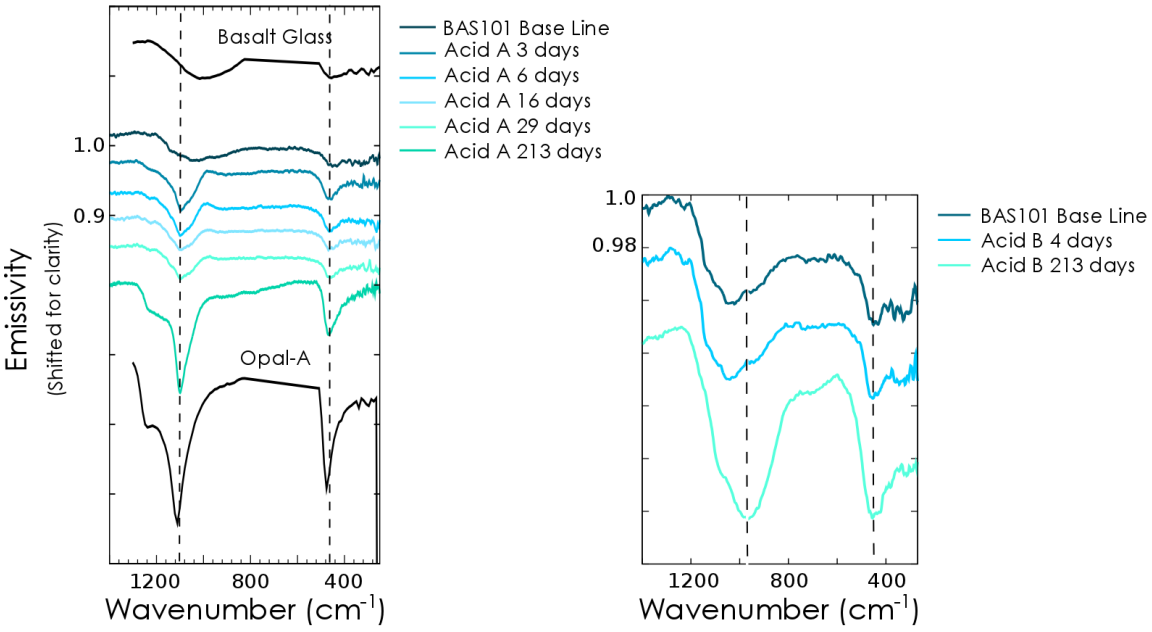

Figure 2.12. Thermal-infrared spectral evolution of BAS101 grains exposed to acid A (left) and acid B (right) over the duration of the experiment. Black spectra are taken from the spectral library and are shown for comparison. Dashed lines indicate emissivity minima positions for final products from both experiments at 1100 cm^{-1} and 465 cm^{-1} (left), and at 970 cm^{-1} and 450 cm^{-1} (right).

be consistent with the visible spectral character of BAS101 unaltered surfaces, which exhibit shallow but broad absorptions near 500 and 750 nm, the former of which could be consistent with magnetite. These absorptions vary in intensity during the experiment, but are not apparent at the end of the experiment. In general, the shift of the emissivity minimum toward lower wavenumber suggests that the sample has become more structurally disordered.

The spectral change for BSB101 grains exposed to acid B for 220 days is not reflected in the abundances derived by the linear unmixing model, which remain unchanged from the unaltered materials; however the misfit between the measured and the modeled spectrum is increased (Figure 2.13). The inclusion of olivine in the model induces features in the model at ~900 cm^{-1} and 450 cm^{-1} that are not present in the measured spectrum of the altered glass. The BSB101 starting material is modeled with the same abundance of olivine without inducing spectral features, and so we can assume that olivine was actually present in the starting material, but was preferentially lost when altered in acid B (Figure 2.13).

Exposure of the basaltic glass samples to acid A creates a much more drastic spectral change than for either of the more crystalline samples (Figure 2.6). After just 3 days in the acid, the Si-O stretching and bending absorption features of the lava grains become much more narrow and the minima shift to 1100 cm^{-1} and 465 cm^{-1}. Additionally, a very shallow shoulder centered at 1220 cm^{-1} starts to develop (Figure 2.12). These features deepen over the time of the experiment, and the resulting spectral shape for both basalt glass samples is very similar to that of opal-A, but with emissivity

minima at 1100 cm^{-1} and 465 cm^{-1}, instead of 1115 cm^{-1} and 470 cm^{-1} as would be expected for pure opal-A (Figure 2.6).

The resulting spectral shapes of the basaltic glass samples altered in pH 1 acid look very similar to basaltic glasses naturally weathered in acidic environments [*Minitti et al.*, 2007]. For example, naturally weathered Hawaiian basaltic glasses from the Mauna Iki flow (MIO) and from near the outgassing Halemaumau vent at Kilauea (KWY and KW) also have Si-O stretching emissivity minima between 1087 cm^{-1} and 1100 cm^{-1}, Si-O bending emissivity minima between 450 cm^{-1} and 170 cm^{-1}, and spectral shoulders ~1220 cm^{-1} [*Kahle et al.*, 1988; *Crisp et al.*, 1990; *Minitt*i *et al.*, 2007]. *Minitti et al.* [2007] performed SEM and electron microprobe analyses on the samples and found that the distinct spectral signature was coming from leached rinds coated with layers of silica-rich material. *Crisp et al.* [1990] studied samples from Hawaiian lava flows of varying age, and found that lava flows exhibit similar spectral features when they are greater than a few years old. They attributed the spectral features to the accumulation of silica-rich depositional coatings over time. Our companion paper found silica-rich layers on the basalt glass sand samples in this study, and so we also assign the combination of ~1100 cm^{-1}, 465 cm^{-1} and 1220 cm^{-1} features to silica-rich alteration layers [*Smith et al.*, submitted].

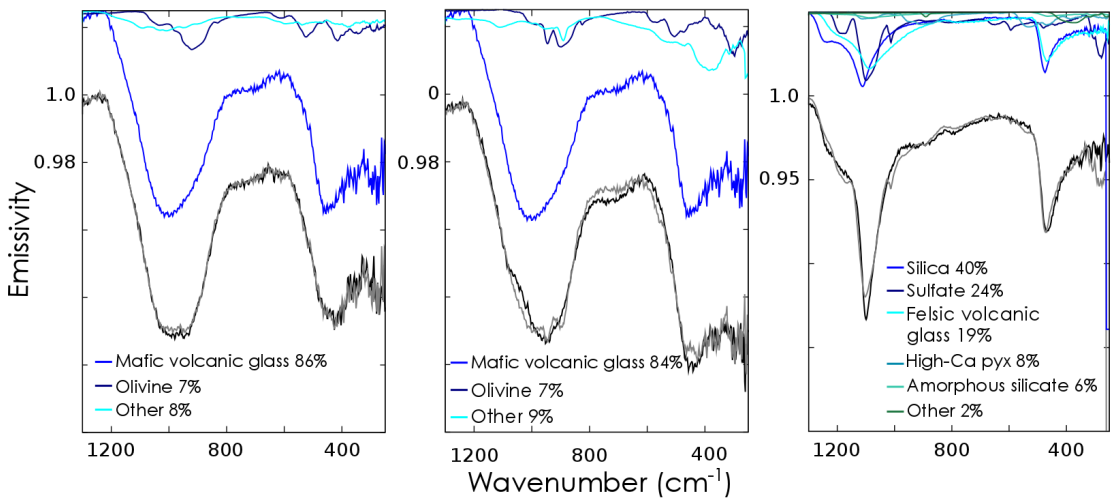

Figure 2.13. Linear deconvolution of TIR spectrum of BSB101 starting material (left), grains exposed to acid B (middle), and grains exposed to acid A (right) using mineral endmember library shown in Table 2.2. The "Other" category is an additive bin for phases modeled in abundances below the detection limit (< 5%). RMS error = 0.15%, 0.42% and 0.27%, respectively.

The 1220 cm^{-1} shoulder on the deeper 1100 cm^{-1} absorption band is found in many silica-rich glasses and silica-rich amorphous alteration phases, and represents one of two states of the SiO_2 asymmetric stretching mode [*Minitti et al.*, 2007]. The feature has been noted to change in depth with viewing angle for natural and synthetic amorphous silica [*Almeida*, 1992; *Ruff et al.*, 2011]. The feature can also be completely absent from spectra of surfaces that otherwise look like silica-rich coatings/leached rinds – for example, it is not present in the spectrum of ICE170 altered in acid A but it is present in the spectrum of BAS101 altered in acid A (Figure 2.6). It is unknown what would cause the feature to be absent, but suggestions include the effects of coating thickness [*Crisp et al.*, 1990; *Kraft et al.*, 2003] and/or material porosity [*Ruff,* personal communication].

Crisp et al. [1990] found that all three spectral features associated with silica-rich coatings/layers (~1090 – 1100 cm^{-1}, 465 cm^{-1}, and 1220 cm^{-1} shoulder features) are very common in spectra from lava flows over 50 years old, which presumably have well developed silica-rich coatings. Flows that are weeks old also have spectral features associated with silica-rich coatings/layers, but the 1220 cm^{-1} shoulder feature is usually absent. Likewise, *Kraft et al.* [2003] measured TIR spectra of Columbia River Basalt coated with varying thicknesses of amorphous silica and found that the 1220 cm^{-1} spectral feature did not appear until the coatings were ~3 μm thick. These studies suggest that the feature only becomes present when the silica-rich coating/layer is of sufficient thickness. However, *Minitti et al.* [2007] found that one sample with silica-rich coatings/layers ~2 – 3 μm thick (MUO) had the 1220 cm^{-1} spectral shoulder, while another sample with generally thicker coatings/layers (~5 – 7 μm; MIY) did not. Thus,

there must be other factors controlling the presence or absence of the 1220 cm^{-1} shoulder feature.

We hypothesize that the presence or absence of the 1220 cm^{-1} spectral feature is due to the overall percentage of silica making up the outer surface of the sample. The 1220 cm^{-1} feature is present in the spectra of basalt glass altered in acid A, but not in the spectra of the more crystalline basalt altered in acid A. Based on SEM analyses, our companion study found that the basalt glass samples have silica-rich alteration layers that are ~10 – 100 μm thick, and so the surface measured in the thermal-infrared is almost 100% silica-rich material. On the other hand, alteration penetrated the interior of the glassy basalt sand grain samples (ICE170), leaving parts of the surface of the grains relatively unaltered, so that the fraction of silica-rich material measured in the thermal-infrared was much less. The silica-rich phases in both the basalt glass and the glassy basalt were fractured and porous, so we do not think porosity is causing the spectral difference in this case [*Smith et al.*, submitted].

2.4.3 Effects of surface texture on thermal-IR spectra

The detailed thermal-infrared analysis presented above is limited to the sand-size samples, as thermal infrared spectra were acquired after the completion of the experiment, and we were only able to save grains from each stage of the experiment. This level of analysis was not possible for the large cm-scale fragment samples. However, we can draw some conclusions about the effects of weathering on the surfaces of the cm-scale fragments based on the spectra of the final altered samples, as shown in Figure 2.14. Fragment samples of BSB101 are not shown, as this sample was collected in the field as sand.

After 220 days of alteration, naturally rough surfaces of the fragments (black lines in Figure 2.14) are spectrally similar to the equivalent sand grain spectra (blue lines in Figure 2.14), suggesting that our interpretations of weathering processes hold for granular sediments as well as most rocks. However, the artificially smooth cut surfaces (gray lines in Figure 2.14) consistently exhibit silica absorption bands near 1100 cm^{-1} and 465 cm^{-1} in all experiments except BAS101. In the Acid A (PH ~1) experiments, these bands are deeper than those in the equivalent sand or natural surface spectra. On the glass sample (BAS101), the somewhat stronger silica bands appear to correlate with strong linear blue slopes in the near-infrared, consistent with a depositional silica coating. In the Acid B experiments (pH ~3), silica bands are present in the thermal infrared spectra of the cut surfaces of the basalts, even though no silica bands are detected in any of the near-infrared spectra of these samples. For the glass (BAS101), silica bands are present in spectra of the natural surface, and are correlated with a strong concave up blue slope in the near infrared on the unaltered samples, suggesting that the natural surface of this sample has a pre-existing leached rind that was not affected by the pH 3 solution. While the strong silica bands in the basalts would also seem to imply an additive effect like in a coating, this is not consistent with near-infrared results for those samples. Thus, the form of the silica indicated by thermal-infrared spectra on the cut surfaces of the basalts is unclear.

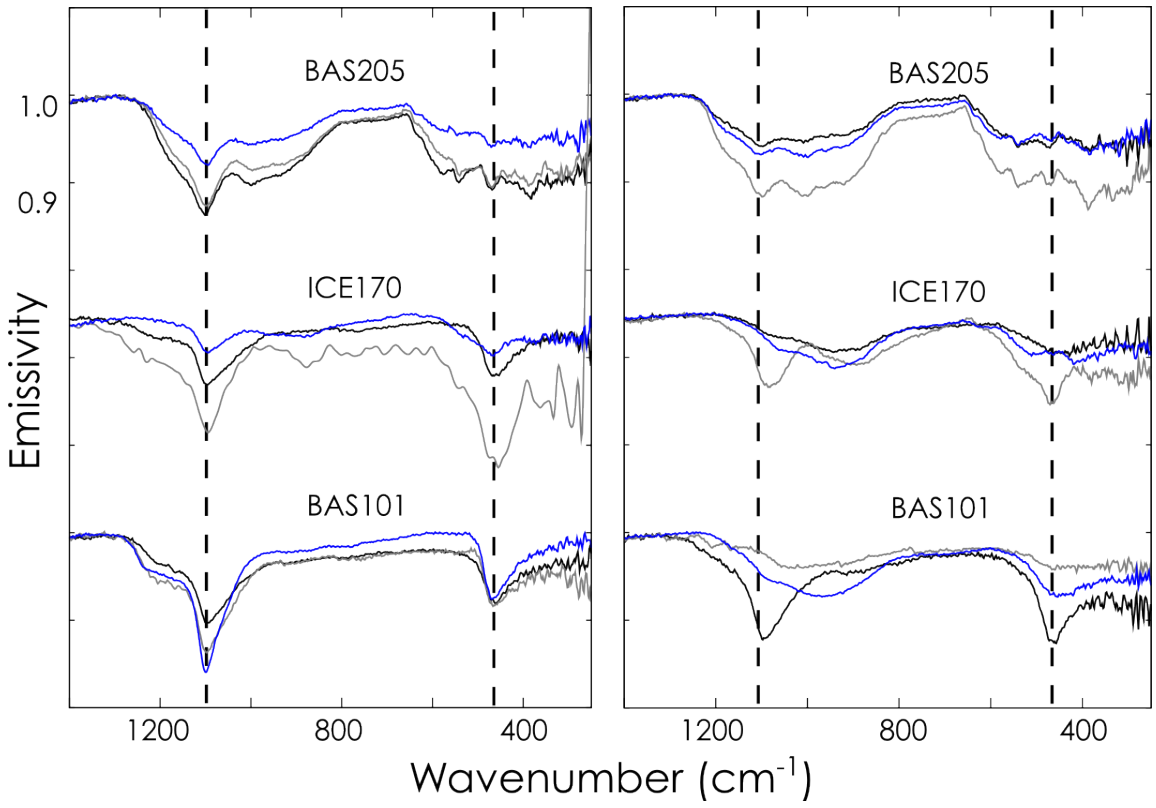

Figure 2.14. TIR spectra of altered oriented fragment surfaces for samples weathered in acid A (left) and acid B (right). Naturally textured surfaces (black lines) of these fragments are spectrally similar to the equivalent sand grain spectra (blue). However, the artificially smooth cut surfaces (grey) exhibit much deeper silica absorption bands. This is especially true in moderate pH experiments, even though silica coatings were not observed on either the sand grains or natural surfaces. Dashed lines in both plots indicate the position of the shifted emissivity minima to ~1100 cm^{-1} and 465 cm^{-1}.

2.5 Discussion

2.5.1 Weathering under moderately acidic conditions

Our spectral observations and interpretations are summarized in Table 2.3. Both visible/near-infrared and thermal-infrared observations indicate that weathering at moderate pH (acid B, starting pH ~3) for 220 days on naturally textured surfaces results in no clear spectral signatures of surface alteration for crystalline basalt, and only very subtle signatures of alteration for most of the glassy samples, and did not modify pre-existing silica-rich coatings on one glassy sample (BAS101 natural surface). Even for the glassy samples, these subtle signatures are only detectable in the thermal-infrared spectra, which show a clear enrichment in mafic phases (mainly glass and olivine if present). In all cases in the near-infrared, the spectra after 200 days of alteration are almost indistinguishable from their unaltered counterparts, with only minor changes in the strengths of some mafic bands and subtle changes in spectral slopes occurring in some samples. Thermal-infrared spectra also generally show no added alteration phases. The lack of alteration rinds suggests that some dissolved phases like silica remained in solution and thus were removed from the system when the fluids were refreshed. Other dissolved phases may have also been deposited as easily soluble and surficial secondary phases that were removed upon rinsing of the sample. In support of this observation, SEM results show no alteration phases or coatings adhered to the samples in the Acid B (starting pH~3) experiments [*Smith et al.*, submitted]. The only exception was our observation of minor silica in thermal-IR spectra (but not near-IR spectra) of BAS205, which with time, could possibly develop into a more prominent alteration coating or other alteration phase. The precipitation of silica in BAS205 and not the other samples may be

due to greater abundance of olivine in this sample, as observed in previous acid alteration studies [*e.g., Tosca et al.*, 2004; *Golden et al.*, 2005; *Hurowitz et al.*, 2005].

However, thermal-infrared spectra of natural surfaces do consistently show two subtle spectral changes that we attribute to alteration, which may also help to explain the even more subtle changes in near-infrared spectra: (1) Some loss of mafic minerals, presumably due to preferential dissolution, and (2) A shift of Si-O glass absorption to wavelengths lower than expected for basaltic glass, perhaps due to depolymerization.

Table 2.3: Summary of spectral interpretations

Starting mineralogy in order of decreasing abundance (inferred or modeled)			
	Near-Infrared	***Thermal-Infrared***	***Modeled Glass Wt.%***
BAS205	Olivine, HCP, Plagioclase	Plagioclase, Glass, Oxides, Olivine, HCP	17
ICE170	HCP, Olivine, Glass	Glass, HCP, Olivine, minor Plagioclase	50
BAS101	Glass	Glass, minor CPX, minor Oxide	77
BSB101	Glass, Olivine	Glass, Olivine	86

Acid A: Effects of alteration (starting pH ~1)			
	Near-Infrared	***Thermal-Infrared***	***Alteration Mechanism***
BAS205	Addition of minor hydrated silica Relative increase in pyroxene Loss of oxides	Increased silica and sulfates Increased polymerization Relative increase in plag/pyroxene due to loss of glass/oxides	Acid infiltrates sample interior, where crystals are dissolved and replaced with poorly crystalline silica phases.
ICE170	Hydrated silica coating Relative increase in pyroxene due to loss of glass/olivine Loss of oxides	Increased silica Increased polymerization Relative increase in pyroxene due to loss of glass/olivine/plagioclase	
BAS101	Leached rind on glass Hydrated silica coating Loss of oxides	Complete replacement by high-silica phases	Acid infiltrates near-surface of glass, causes local dissolution and reprecipitation to form a silica-rich leached rind
BSB101	Leached rind on glass Hydrated silica coating Loss of olivine Loss of oxides	Complete replacement by high-silica phases	

Acid B: Effects of alteration (starting pH ~3)			
	Near-Infrared	***Thermal-Infrared***	***Alteration Mechanism***
BAS205	No effect	Addition of minor silica Loss of glass and oxides	Minimal alteration via stoichiometric dissolution of all phases.
ICE170	Relative increase in olivine due to loss of pyroxene	Relative increase in glass/olivine due to loss of pyroxene and plagioclase Decreased polymerization	Preferential dissolution of fine grained mafics relative to coarser grains and glass, as well as surficial depolymerization of glass.
BAS101	Addition of iron oxides	Loss of all phases other than mafic glass Decreased polymerization	
BSB101	Addition of iron oxides	Relative loss of olivine Decreased polymerization	

2.5.1.1 Preferential dissolution of primary minerals

In a simple model of basalt dissolution, minerals with higher solubilities should dissolve first. Both plagioclase and glass exhibit solubilities that are dependent on pH, but at the starting pH of acid B (~3), pyroxene and plagioclase should have comparable solubilities, and glass exhibits a solubility higher than these phases but lower than olivine [*Hausrath et al.*, 2008]. Thus, olivine should dissolve the fastest, followed by glass, then pyroxene and plagioclase at similar rates. This simple model generally works when applied to our crystalline basalt (BAS205), which experiences some loss of mafic phases (mainly glass) relative to plagioclase when altered by either moderately or highly acidic solutions. However, this simple solubility model is not consistent with our observation of a loss of pyroxenes relative to glass in the glassy sample BAS101 after alteration at pH ~3.

We hypothesize that preferential dissolution of pyroxene in BAS101 at pH ~3 is most likely driven by crystal grain size. Finer crystals have higher surface area to volume ratios than large crystals, and thus dissolve more quickly. In SEM images of BAS205 presented in the companion paper to this study [*Smith et al.*, submitted], plagioclase, olivine, and pyroxene are all easily identified as large crystals of similar sizes. In contrast, BAS101 and BSB101 tend to exhibit only large plagioclase crystals, surrounded by a glassy matrix. Thus, the pyroxene identified in both near-IR and TIR spectra must be present in the glassy matrix, perhaps as devitrified glass. These small crystals would be much more susceptible to dissolution than if they were present as larger grains. In support of this hypothesis, we also observe the loss of pyroxene relative to olivine in ICE170, and only the olivine is present as larger grains in SEM images of this sample. However, under

highly acidic alteration (pH ~1), ICE170 does exhibit loss of glass/olivine relative to pyroxene (Table 2.3), perhaps suggesting that solubility dominates over grain size effects at lower pH.

2.5.1.2 Depolymerization of basaltic glass

The other spectral change that we observe in thermal-infrared spectra of glassy samples weathered under moderately acidic conditions is a shift of Si-O glass absorption to wavelengths lower than expected for basaltic glass. This effect is most notable in BAS101, which shifts from ~1010 cm^{-1}, typical for basaltic glass, to ~970 cm^{-1}. In BSB101, the shift is similar but less strong, from ~980 to ~960 cm^{-1}. This change is modeled as a significant increase in the proportion of basaltic glass; however, the modeled fit is unable to replicate the low band minimum of the spectrum, suggesting that basaltic glass alone is insufficient to explain the spectral changes. Instead, this shift could also be caused by decreased polymerization in the sample surface.

Silicate glass is composed of SiO_4 tetrahedra linked by shared (bridging) oxygens. The degree of polymerization of a glass or mineral refers to how well interlinked the tetrahedra are, as measured by the number of bridging oxygens. A silicate becomes less polymerized or depolymerized when those oxygens are bonded to cations other than Si^{4+}. This can occur due to the presence of network-modifying cations like Na^{+}, Ca^{2+}, Mg^{2+}, $Fe^{2+/3+}$, or Al^{3+}, none of which are capable of bonding with as many oxygens as Si^{4+}, or due to the presence of water, which reacts with bridging oxygen to form hydroxyl molecules. Thus, the more mafic a glass or mineral is, the less polymerized it is. The endmembers of this trend are quartz, which can be totally polymerized, and olivine, which is totally depolymerized. The apparent depolymerization of the mafic glasses

during moderately acidic leaching may thus be due either to a relative increase in mafic network modifying cations, a decrease in their oxidation state (e.g., Fe^{3+} either reduced to or preferentially removed over Fe^{2+}), or the addition of water.

The more crystalline ICE170 glassy basalt also exhibits increased absorption near ~940 cm^{-1} after weathering at moderately acidic pH. Given the partially glassy nature of this sample, we hypothesize that this shift is due to a combination of increased exposure of olivine and mafic glass at the expense of other phases, and to decreasing polymerization in the glass.

Depolymerization may be affecting the near-infrared spectra of the glasses as well. All three partially to fully glassy samples altered at moderately acidic pH also exhibit red slopes in the near-infrared. Previously, red slopes in glasses has been associated with greater reduced or metallic iron content [*Moroz* et al 2009], which suggests that the red slopes that we observe could be consistent with depolymerization due to a relative increase in reduced iron. While we can neither confirm nor refute this hypothesis based on our results, the red slopes do appear to be correlated with spectral evidence for depolymerization in the mid-infrared.

2.5.2 Weathering under highly acidic conditions

In contrast to the moderate pH experiments, both visible/near-infrared and thermal-infrared observations indicate that weathering at low pH (acid A, starting pH ~1) for 220 days results in clear spectral signatures of alteration. In the visible/near-infrared, most samples develop clear absorption bands near 2.21 and sometimes 1.9 μm, and in glassy samples, these bands are superposed on strong concave up blue spectral slopes. Thermal-infrared spectra of all samples show the development of absorption bands near

1090 cm^{-1} and 465 cm^{-1}. These spectral changes could all be attributed to silica in some form. A key constraint on the nature of the silica is that the silica spectral signatures persist after repeated rinsing of the samples, suggesting that they are due to a depositional coating, a leached rind, or pervasive alteration of the sample. However, the mode and extent of alteration appears to vary between the samples, as indicated by variations in the strength of VNIR spectral slopes, VNIR absorption bands, and TIR absorption bands. Indeed, all of these spectral features generally appear to increase in strength along with the fraction of glass in the samples.

2.5.2.1 Effects of crystallinity on mode of alteration

Based on visible/near-infrared and thermal-infrared spectral analysis along with SEM observations, degree of crystallinity appears to determine the type of surface alteration that basalts experience. The crystalline sample (BAS205) showed only weak spectral signatures of hydrated silica in both the visible/near-infrared and thermal-infrared, while the partly glass basalt (ICE170) showed clear addition of hydrated silica, and the fully glassy basalt and basaltic sand (BAS101 and BSB101) both became spectrally dominated by silica (with variable hydration). Furthermore, visible/near-infrared spectral slopes consistent with leached rinds or coatings were only observed on the fully glassy samples.

SEM observations of altered samples in our companion paper confirm that there are significant physical differences between partially glassy and fully glassy samples [*Smith et al.*, submitted]. Of the samples examined using SEM, only the fully glassy sample (BAS101) showed clear evidence for the development of silica-enriched rinds or coatings on the exterior of the sample. While our SEM compositional profiles do not

have sufficient resolution to uniquely differentiate a silica-rich replacement layer from a true leaching rind with a very sharp compositional boundary, the layers are 10-100 μm thick – often much thicker than expected for a leached layer (1-10 μm) [e.g., *Chemtob et al.*, 2010]. Thus, we hypothesize that the external alteration took place via localized dissolution and reprecipitation to form a leached rind.

In contrast, the partially glassy sample (ICE170) does not show evidence for an exterior rind or coating, and instead shows evidence for pervasive alteration penetrating into the interior of the sample. The interior of the sample is characterized by a relatively unaltered glassy matrix surrounding silica-rich zones that appear to have replaced plagioclase quench crystals. Indeed, the presence of crystals appears to control the movement of alteration fluids within the sample, as alteration zones tend to propagate along crystal boundaries.

These SEM observations suggest that alteration is restricted to the surface for glass, but rapidly penetrates into the interior of even partially crystalline samples, due to the fluid pathways enabled by fractures and crystal boundaries. Because spectral investigations are only sensitive to the upper few microns of the surface, the glass exhibits stronger signatures of alteration than the less glassy sample, even though the latter is much more pervasively altered. We assume that these results extend to highly crystalline samples as well. SEM analysis was only performed on unaltered BAS205, but given that these images showed long fractures penetrating the unaltered sample to depth and that BAS205 showed minimal evidence for surface alteration in either VNIR or TIR spectra, we hypothesize that any alteration that occurred was also dominantly in the interior of BAS205.

2.5.2.2 Comparison to natural silicic coatings and rinds

Figure 2.15 shows spectra of a selection of basalts weathered by hydrothermal vapors/fluids and sulfuric acid precipitation from Iceland and Hawaii. The samples fall into two clear categories – samples with consistent absorption bands near 0.9, 1.9, and 2.2 μm and variable spectral slopes shown in Figure 2.15a, and samples with consistent blue concave up spectral slopes and variably present absorption bands at 0.9, 1.9, and 2.2 μm shown in Figure 2.16b. The samples differ primarily in their crystallinity, as the samples in Figure 2.15a are fairly typical basaltic lavas, and the samples in Figure 2.16b are pahoehoe basalt that all exhibit homogeneous glassy cooling rinds [*Chemtob and Rossman,* 2014]. The physical appearance of the two sample sets is also different, as shown in Figure 2.16, as the samples in Figure 2.15a appear bright, rough and orange, yellow, or white in color, while the samples in Figure 2.15b appear smooth, glossy, and blue, white, yellow, or orange in color. This variability in color often appears on a given sample, and is reflected in the significant spectral variability of these surfaces shown in Figure 2.15.

We interpret the spectra in Figure 2.15a as consistent with a variable mixture of hydrated or opaline silica (indicated by absorption bands at 1.4, 1.9, and 2.2 μm, sometimes with a strong shoulder at 2.25 μm) and ferric sulfates like jarosite (indicated by absorption bands at 0.44, 0.95, 1.48, 1.95, and 2.26 μm). The silica absorption bands in the sulfate-free spectra in this group resemble the silica bands in our more crystalline samples weathered under strongly acidic conditions, although the spectral signature of the underlying basalt is completely masked in the natural samples. Although we see more evidence for volumetric alteration rather than physical coating development in our more

crystalline samples, we suggest these samples either could develop thick coatings after exposure to a more closed system than our simulation provided, or that long enough exposure would cause the surface of the sample to become fully altered to silica at depth, which would resemble a coating physically and spectrally.

We interpret the spectra in Figure 2.15b as consistent with leached rinds on glass (as indicated by the strong concave up blue spectral slope) with additional precipitated silica (as indicated by absorption bands at 1.4, 1.9, and 2.2 μm) and Fe/Ti-oxide coatings (as indicated by absorption bands near 0.5 μm and overall decreased reflectance shortward of 0.6 μm). These spectra are quite similar to spectra of glass samples altered under strongly acidic conditions, confirming previous results that these rinds are formed in open hydrologic systems where limited deposition from solution occurs [*Minitti et al.*, 2007; *Chemtob et al.*, 2010; *Chemtob and Rossman*, 2014]. In addition, although both sets of samples shown in Figures 2.15 and 2.16 exhibit evidence for some type of silica coating, silica coatings on basalt and silica coatings/rinds on glass are quite spectrally distinct, supporting this same result from our laboratory leaching study.

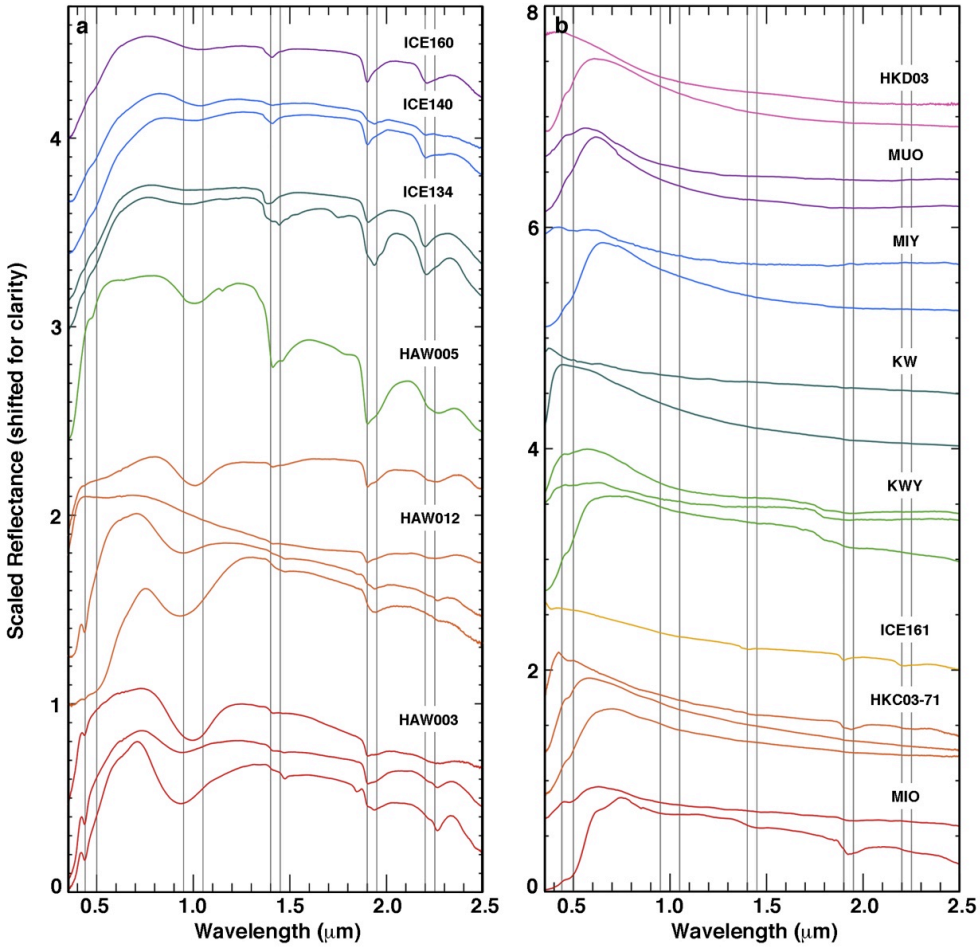

Figure 2.15. Spectra of naturally altered samples. Color groups correspond to spectra from different parts of the surface of one sample, vertical lines are positioned at 0.45, 0.50, 0.95, 1.05, 1.40, 1.45, 1.90, 1.95, 2.20, and 2.25 μm. (a) Siliceous and sulfurous coatings, exhibiting silica bands near 1.90 and 2.20 μm and Fe-sulfate bands near 0.95, 1.95, and 2.26 μm. (b) Leached glasses, exhibiting blue concave up spectral slopes and, sometimes, 1.9 and 2.2 μm silica bands. HAW003, HAW012, and HAW005 are coated basalts from Kilauea Caldera, Hawaii; ICE134, ICE140, ICE160, and ICE161 are weathered basalts from hydrothermal vents in Hveragerdi, Iceland. HKD03, HKC03-71, MIY, MIO, MUO, KW, and KWY are leached pahoehoe basalts with glassy cooling rinds from the Ka-ʻu Desert, Kilauea, Hawaii [*Minitti et al.*, 2007; *Seelos et al.*, 2010].

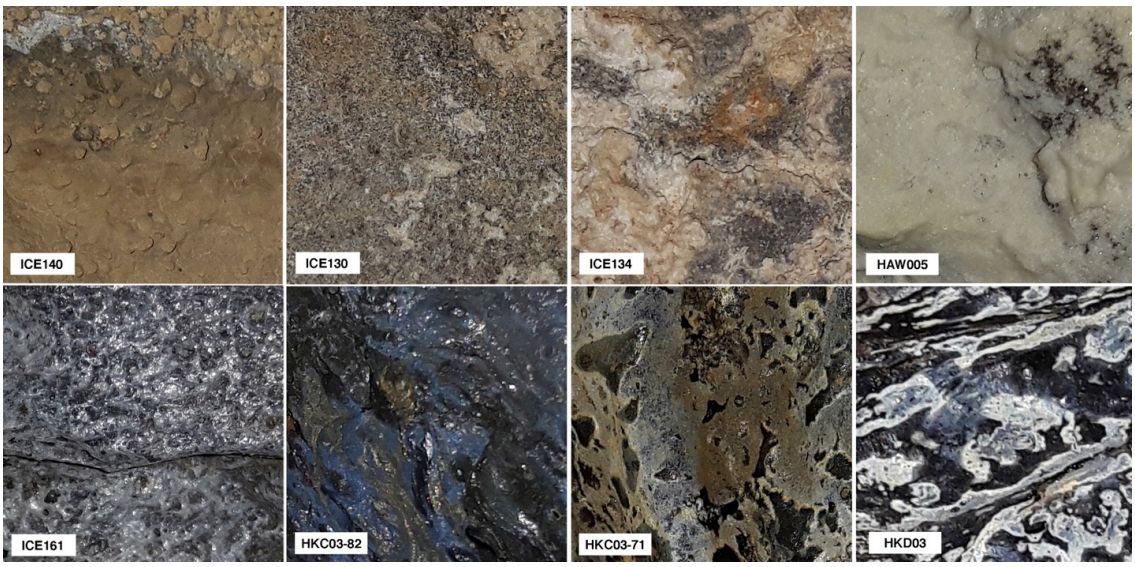

Figure 2.16. Photos of naturally weathered and coated basalt surfaces, corresponding to spectra shown in Figure 2.15. Top row are siliceous and sulfurous coatings on basalt, and bottom row are leached rinds and coatings on glass. All images are approximately 2 cm wide.

2.5.3 Implications for Mars

The results of this study show that the spectral signatures of acid alteration should persist in mafic sediments or surface bedrock units on Mars even when sulfates and other secondary alteration products have been removed by subsequent aqueous activity or physical abrasion. However, the visible/near-infrared and thermal-infrared spectral signatures of acid alteration vary depending on the acidity of the solution, and this has major implications for our interpretation of the alteration history of the Martian surface.

2.5.3.1 Detecting moderately acidic alteration in spectral datasets

One of the most surprising results of this study is that moderately acidic solutions do not cause major compositional changes to basalts or glasses undergoing alteration. Indeed, this type of alteration in an open system produces no obvious evidence of coatings, rinds, or other physical alteration phenomena in the visible/near-infrared, with the exception of a red spectral slope that would be difficult to differentiate from typical Martian dust. However, the thermal-infrared appears to be more sensitive to alteration of basalts and glassy basalts by these moderately acidic solutions (e.g., pH ~3). Together, a combination of anomalously low Si-O band minima (e.g., below 1000 cm^{-1}) and high pyroxene/glass, pyroxene/olivine, or plagioclase/pyroxene ratio in thermal-infrared spectra could indicate this type of moderately acidic weathering. However, detecting these weak spectral effects in a planetary dataset in the absence of secondary weathering products may be challenging. Thus, in an open hydrologic system exposed to multiple aqueous events or to post-diagenesis physical modification that remove friable secondary alteration products, moderately acidic weathering might leave no clear spectral signature on the weathered parent material.

2.5.3.2 Detecting strongly acidic alteration in spectral datasets

Both visible/near-infrared and thermal-infrared spectral datasets should be able to detect residual silica coatings and dissolution/replacement zones caused by alteration in strongly acidic solutions (e.g., pH ~1), even when other secondary products have been removed from the system. Both spectral ranges are sensitive to silica deposited during strong acid leaching, and thus ideally both datasets should detect hydrated silica absorption bands in most locations where significant acid leaching has occurred. Visible/near-infrared spectra can also indicate the presence of coatings/leached rinds that appear to uniquely form on glass during strongly acidic alteration. Natural surfaces of altered glasses exhibit strong concave up blue spectral slopes in the visible/near-infrared, and in the thermal-infrared, these slopes appear to be correlated with a strong 1200 cm^{-1} shoulder on the 1100 cm^{-1} silica absorption band, which we interpret as indicating high abundances of amorphous silica. This is even though visible/near-infrared hydrated silica bands are generally not present in spectra of leached surfaces that exhibit the strongest spectral slopes due to rinds (Figure 2.2) [*Minitti* et al 2007]. Thus, thermal-infrared silica detections correlated with visible/near-infrared concave slopes could also be a good indicator of past strongly acidic alteration.

It is important to note that the experiments in this study were conducted at room temperature, but that mineral solubilities and other important parameters that control the kinetics and mode of alteration are strongly dependent on environmental variables like fluid temperature. Thus, the spectral signatures discussed here are indicative of relatively stronger or weaker acid solutions, and if detected on Mars, should not be interpreted as indicating a specific pH range.

2.5.3.3 Implications for TES Surface Type 2

Globally, TES Surface Type 2 is somewhat variable and displays a range of spectral shapes. This is demonstrated in Figure 2.17 by the large range of Si-O band emissivity minima that Surface Type 2 areas exhibit (1075 – 1110 cm^{-1}) [*Michalski et al.*, 2005]. While this range encompasses the emissivity minima exhibited by basalt and basaltic glass altered at low pH in our experiments (~1090 – 1100 cm^{-1}), it is also consistent with a variety of other high-silica phases. However, the range of acceptable minima shrinks considerably if we consider only the northern plains of Mars (Acidalia Planitia, Utopia Planitia, and the north polar sand sea), where the strongest Surface Type 2 signatures are found. Strong Surface Type 2 signatures in these regions tend to exhibit emissivity minimum between 1090 – 1110 cm^{-1}, and are best fit using an obsidian endmember with a minima at ~1087 cm^{-1}. Thus, TES spectra of this type locality for Surface Type 2 are potentially consistent with an acid-altered basalt or basaltic glass in the thermal-infrared (Figure 2.17).

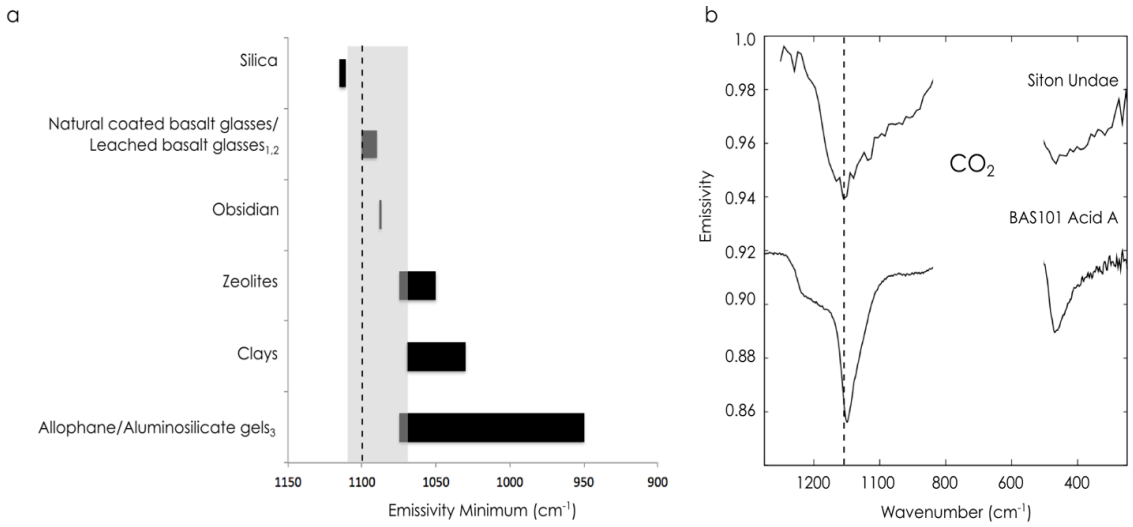

Figure 2.17. (a) Plot comparing the TIR Si-O stretching emissivity minima ranges of some "high-silica" phases. All data were taken from *Michalski et al*. [2005] except (1) *Minitti et al*. [2007], (2) *Horgan et al*. [this study], and (3) *Rampe et al.* [2012]. The grey box indicates the range of emissivity minima for TES Surface Type 2 spectra between 1070 and 1110 cm^{-1} [*Michalski et al*., 2005], and the dashed line marks the emissivity minimum position of TES spectra from Siton Undae shown in (b). (b) Average TIR spectrum from Siton Undae (centered at 293.80°E, 74.80°N) compared to the spectrum of BAS101 grain samples exposed to acid A for 213 days. Dashed line is in same position as in (a).

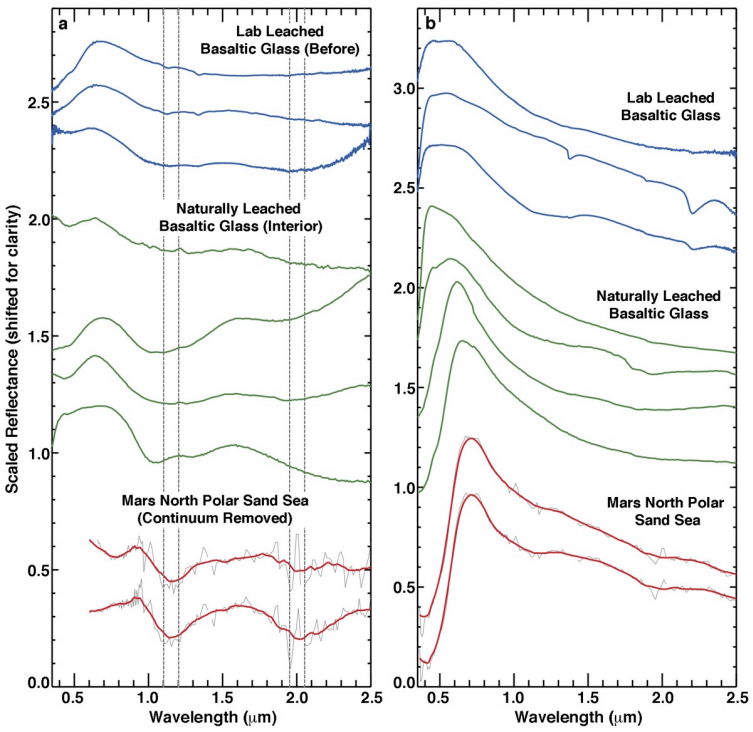

Figure 2.18. Comparison between OMEGA spectra from the North Polar Sand Sea on Mars interpreted as leached glass (red) [Horgan and Bell, 2012], naturally leached glasses (green) [Minitti *et al.*, 2007], and laboratory-leached glasses (blue; BAS101 Acid A). (a) Unaltered glass spectral signatures showing broad iron absorptions near 1.15 and 2 μm. Spectra were acquired from sample surfaces prior to alteration for the lab-leached glasses and from the interior beneath the alteration rinds for the naturally leached glasses. OMEGA spectra shown for the Mars North Polar Sand Sea have been ratioed to a dusty spectrum and continuum removed to reveal glass absorption bands compared to the original albedo spectra as shown in (b). The thick red lines have been smoothed compared to the original spectra, shown as thin grey lines. Dashed vertical lines indicate the ranges over which broad glass absorption bands are typically centered. (b) The altered surfaces of the glass samples in (a), showing the concave up spectral shape that we interpret as due to leached rinds on glass.

This interpretation of an acid leached basalt or basaltic glass for the high-silica component of TES Surface Type 2 in the northern plains is supported by the visible/near-infrared spectral shape of the northern plains. As shown in Figure 2.18b, these areas exhibit a strong concave up or linear blue slope [*Horgan and Bell*, 2012], similar to the basaltic glass weathered by strongly acidic solutions (pH ~1) in our experiments. Indeed, Figure 2.18a shows that some areas of the north polar sand sea also exhibit broad shallow absorption bands superposed on this concave up slope that are consistent with an iron-bearing glass like those used in this study [*Horgan and Bell*, 2012].

The combination of both thermal-infrared spectral models requiring a high-silica phase and visible/near-infrared spectra consistent with silica-enriched rinds on glass in the northern plains strongly suggests that these regions are at least partially covered in glass-rich materials that have undergone acidic alteration at very low pH. We propose that fluids derived from snow or ice melt at low water:rock ratios are capable of obtaining the acidity needed to form alteration layers on basaltic glass [*Horgan and Bell*, 2012].

2.5.3.4 Stability of glass under acidic alteration

Lastly, this study confirms the important but often overlooked fact that glass is actually more stable under long-term acidic alteration than other mafic phases. As discussed above, previous studies have shown that glass has high stability in lower pH solutions, and our results show that this is due to the fact that glass undergoes dissolution and alteration in a fundamentally different manner than more crystalline samples. SEM analysis of glass and partially crystalline samples show that alteration is restricted to the surface of glasses but penetrates in the interior of more crystalline samples [*Smith et al.*, submitted], likely leading to more pervasive dissolution and alteration of crystalline

samples over the long term. This suggests that glass would be more stable than other mafic phases in a dominantly acidic planetary environment. This finding is contrary to the common assumption in studies of Mars that because glass in unstable to weathering at neutral to alklaine pH, the presence of glass at a site indicates that little to no aqueous activity has taken place at that location. Instead, the presence of glass alone indicates only that prolonged aqueous activity at neutral pH has not occurred. Based on our results and previous experiments, if glass is present along with sulfates, halite, or exhibits coatings or leaching rinds, this is a strong indication of potentially prolonged aqueous activity at moderately to strongly acidic pH.

2.6 Conclusions

By submerging basalt and basaltic glasses in highly acidic solutions for 220 days, we have shown that highly acidic alteration (pH ~1 at ~20°C and standard atmospheric pressure) produces abundant residual silica on both basalt and basaltic glasses, but the nature of the silica and the associated alteration mechanism vary with the crystallinity of the sample undergoing alteration. In glassy samples, the alteration is restricted to the surface of the sample, and forms a leached, silica-enriched rind via highly localized dissolution and reprecipitation reactions. In crystalline samples, the alteration penetrates into the interior through fractures and along crystal boundaries, and causes dissolution and replacement of both matrix and phenocrysts by poorly-crystalline high-silica phases in the interior of the samples. One consequence of the difference in alteration styles between glass and crystalline basalt is that glass is actually more stable than crystalline basalt under highly acidic alteration.

While alteration of both glass and basalt at low pH results in silica absorption bands in visible/near-infrared and thermal-infrared spectra, only the leached rind on the glass is associated with strong concave-up slopes in visible/near-infrared spectra. Thus, strong silica rind signatures in both visible/near-infrared and thermal-infrared spectra of Mars could indicate highly acidic alteration in the past. Indeed, concave-up slopes in the visible/near-infrared and strong silica absorptions in the thermal-infrared are observed together across large regions of the Martian surface. These regions were previously classified as the silica-enriched TES Surface Type 2, suggesting that at least portions of this major Martian surface type could be the result of widespread acidic alteration.

In contrast, moderately acidic alteration (pH ~3 at ~20°C and standard atmospheric pressure) for 220 days does not appear to produce resistant rinds or coatings on either basalt or basaltic glass. The only residual spectral effects on the parent materials are subtle visible/near-infrared slopes and thermal-infrared band shifts that we interpret to be due to surficial depolymerization. However, these spectral effects may be difficult to detect in a complex natural setting. Some units and sediments on Mars that have been exposed to acidic solutions may retain no clear sign of alteration, as secondary alteration products that are produced under these moderately acidic conditions (mainly sulfates) may be easily removed by subsequent aqueous activity or abrasion.

CHAPTER 3

ACID WEATHERING OF BASALT AND BASALTIC GLASS: II. MICROSCOPIC ANALYSES AND ALTERATION MECHANISMS

3.1 Introduction

Most of the Martian surface is basaltic in composition [*Singer et al.*, 1979; *Bandfield et al.*, 2000a; *Hamilton et al.*, 2001; *Rogers and Christensen*, 2007; *Rogers et al.*, 2007], and it has been suggested that basaltic glass should be present on the surface based on environmental conditions that would be more conducive to explosive volcanism [*Wilson, L., Head III*, 1994; *Minitti and Hamilton*, 2010]. However, primary volcanic glass was not found to be a significant component in studies examining the thermal-infrared spectra of expansive regions of the Martian surface [*Minitti and Hamilton*, 2010]. Therefore, either basaltic glass was never a dominant rock type on Mars, or it was produced and altered post-emplacement.

Alteration of glass is quite likely given the vast evidence for the presence of sustained liquid water on the surface of Mars throughout the Noachian and Hesperian, and the propensity of glass to devitrify due to the instability of its amorphous structure [*Minitti and Hamilton*, 2010]. The most common secondary phases resulting from water-basalt glass interactions include palagonite [e.g., *Peacock, M.A.; Fuller*, 1928; *Hay and Iijima*, 1968; *Staudigel and Hart*, 1983; *Stroncik and Schmincke*, 2002], amorphous silica coatings and rinds [*Farr and Adams*, 1984; *Curtiss et al.*, 1985; *Fulignati et al.*, 2006; *Minitti et al.*, 2007; *Chemtob et al.*, 2010; *Seelos et al.*, 2010], sulfates, and iron oxides [*Tosca et al.*, 2004; *Golden et al.*, 2005].

Large expanses of the low-albedo regions in the northern lowland plains of Mars have been shown to be spectrally consistent with silica-enriched rinds on acid-leached basaltic glass after comparing near-infrared (NIR) spectral data from natural and laboratory samples to data from the Mars Express OMEGA (Observatoire pour la Minéralogie, l'Eau, les Glaces, et l'Activité) imaging spectrometer [*Horgan and Bell*, 2012]. These same regions on Mars have thermal-infrared (TIR) spectra that are modeled as requiring high abundances of seemingly amorphous high-silica material [*Bandfield*, 2002; *Rogers and Christensen*, 2007]. Subsequent studies found that Hawaiian basaltic glasses naturally altered in acidic fluids have TIR spectra dominated by an amorphous silica signature [*Minitti et al.*, 2007]. In the companion paper to this study, natural basalt, basaltic glass and glass-bearing basalt exposed to strong acid in a laboratory setting were also found to have TIR spectra indicating significant concentrations of amorphous silica [*Horgan et al.,* submitted]. Thus, the thermal-infrared data suggests that acid-leached basaltic glasses may be present in the northern lowlands. Furthermore, very similar but more moderate high-silica TIR spectral signatures are commonly observed in dark terrains across the planet [*Bandfield*, 2002; *Rogers and Christensen*, 2007], suggesting that glass may in fact be present across large regions of the Martian surface.

Our spectral analyses of laboratory acid leached basalt and basaltic glasses show that both the degree of alteration and the resulting alteration products are largely determined by the crystallinity of the sample [*Horgan et al.,* submitted]. Both the TIR and visible and near-infrared (VNIR) spectra of acid altered basaltic materials show that acid leached crystalline basalt and glassy basalt are spectrally distinct from acid leached basalt glass, even when altered under similar conditions (pH and duration of experiment) (see Table

3.1 for sample information). These variations indicate physical and compositional differences between the alteration materials that form on the different glassy vs. crystalline substrates, and suggest different pathways to alteration. Thus, the properties of the parent material must have some control over how the materials are altered, which in turn, affects the resulting spectral properties of the altered material. Therefore, it is important to understand the effects of substrate crystallinity on the resulting alteration morphology, composition, and spectral signature before we can infer the primary lithology of an altered Martian surface from spectral data.

In this study we use scanning electron microscopy (SEM) to analyze the laboratory acid-leached basalt, glassy basalt, and basaltic glass samples from *Horgan et al*. (submitted), and compare these results to their infrared spectra. We investigate the microscopic properties of the parent materials as well as the properties of the samples after exposure to sulfuric acid solutions of starting pH 1 and pH 3 in order to understand what control crystallinity has on weathering modes and alteration morphology, and how the morphology of alteration coatings, rinds, and other textures in turn determines the spectral character of the altered material. This basic understanding will help constrain the composition and weathering history of large regions of the Martian surface, and help understand how the weathering environment and parent material can be determined based on spectral features.

3.2 Background

3.2.1 Silicate dissolution mechanisms and alteration texture terminology

There are two competing dissolution mechanisms that are commonly evoked for multi-oxide mineral dissolution: (1) Leaching, which involves the solid state

interdiffusion of network modifying cations followed by the hydrolysis of Si-O bonds [e.g., *Luce et al.*, 1972; *Paces*, 1973; *Oelkers*, 2001; *Schott et al.*, 2012], and (2) dissolution-reprecipitation [*O'Neil and Taylor*, 1967; *Hellmann et al.*, 2003, 2004; *Daval et al.*, 2011; *King et al.*, 2011].

For decades, leaching has been the favored explanation for the apparent incongruent dissolution of many silicate minerals. Incongruent, or nonstoichiometric dissolution is assumed to be taking place when the elemental molar ratios measured in a fluid are different from those in the solid [*Schott et al.*, 1981]. Many silicates dissolve nonstoichiometrically at first, but eventually reach a steady state stoichiometric dissolution [*Brantley*, 2008]. However, under some circumstances, there are minerals that never reach stoichiometric dissolution.

During the leaching process in acidic conditions, weaker monovalent metal-oxide bonds break more rapidly than di- or trivalent metal-oxide bonds, which break faster than Si-O bonds [*Schott et al.*, 2009]. The Si-O structure is finally broken when Al cations are exchanged for protons, leaving behind partially detached Si atoms that are more readily removed from the structure [*Oelkers*, 2001; *Schott et al.*, 2009]. Thus, leaching is consistent with nonstoichiometric dissolution measurements, and can also explain the amorphous silica-enriched layers that commonly form on the surfaces of silicate minerals, such as plagioclase [*Nesbitt and Muir*, 1988], pyroxenes [*Petit et al.*, 1987], and wollastonite [*Casey et al.*, 1993; *Schott et al.*, 2012] after dissolution. Thus, the preferential removal of lower valence cations is thought to leave behind the silica tetrahedral framework to form a "leached rind."

Currently, there is growing evidence that dissolution-reprecipitation is the

fundamental mechanism behind all mineral dissolution, whether the cation release rate is stoichiometric or not [*Hellmann et al.*, 2012; *Ruiz-Agudo et al.*, 2012, 2014; *Putnis and Ruiz-Agudo*, 2013]. *O'Neil and Taylor* [1967] were among the first to suggest dissolution-reprecipitation as an alternative mechanism to leaching. Dissolution-reprecipitation occurs when the parent silicate material is first stoichiometrically dissolved, and then a secondary phase (most commonly amorphous silica) is precipitated onto the surface of the parent material. These reactions take place in a supersaturated boundary layer of fluid between the parent and product surfaces [*Hellmann et al.*, 2012; *Ruiz-Agudo et al.*, 2012]. So while all crystalline samples undergo stoichiometric dissolution in this model, the reprecipitation of phases removes cations from the solution, which can make the elemental molar ratios between solid and fluid appear incongruent. Reprecipitation explains the amorphous silica-enriched layers commonly associated with apparent incongruent dissolution, and also addresses the problem that "leaching" was noted to occur in basic pH systems where proton-cation exchange would not be relevant [*Hellmann et al.*, 2012].

Amorphous (short-range order) glasses, much like crystalline minerals, have also been thought to undergo leaching as a dissolution mechanism [*Doremus*, 1975; *Oelkers and Gislason*, 2001]. However, [*Crovisier et al.*, 1987] were among the first to suggest that basalt glass actually undergoes dissolution-reprecipitation, and recent isotope tracer corrosion experiments on borosilicate glass [*Geisler et al.*, 2010, 2015] have supported the hypothesis that glasses dissolve via this alternate mechanism. One of the arguments against dissolution-reprecipitation as the mechanism for forming silica-rich layers in glasses are observations of a silica-rich layer substituting, as opposed to coating, the

original glass structure – for example, *Chemtob et al.*, [2010] used the observation of a silica-rich layer creating a thin wall over a vesicle as an argument that the layer had to be substituting a previously existing structure instead of coating a void space. However, a highly localized dissolution-reprecipitation process could also be used to explain this and similar observations.

As noted above, amorphous silica is a common product accompanying apparent incongruent mineral and glass dissolution. The literature describes many different forms of amorphous silica enrichment in naturally and synthetically weathered samples. Here we classify these into four different texture categories based primarily on formation mechanism and silica source. These categories are: (1) coatings, (2) leached rinds/layers, (3) precipitated layers/zone, and (4) replacement. When we want to describe silica enrichment without evoking a specific mechanism or silica source, we will refer to such features as "surface altered layers".

Silica coatings are accreted layers on a rock or grain surface that have been formed via precipitation out of a bulk solution. The main distinguishing property of silica coatings is that the silica is derived from an external source, whether it comes from dissolved silicate dust particles, or from a source that is millimeters to meters away [*Dorn*, 1998]. The key point is that the silica is not derived from the substrate itself [*Dixon et al.*, 2002].

Leached layers (sometimes called leached rinds or hydrated residual glass are derived from the substrate, and so the silica source is internally derived. When a silica-rich layer is designated as a leached rind, it is necessarily implied that the substrate underwent incongruent leaching in order to create the observed amorphous silica feature [*Casey et*

al., 1989a, 1989b, 1993; *Petit et al.*, 1989, 1990]. The leached rind is found on the outside of the sample, and is commonly thought to undergo further alteration by at least one of the following processes: repolymerization [e.g., *Casey and Bunker*, 1990; *Casey et al.*, 1993; *Schweda et al.*, 1997], recrystallization [*Banfield et al.*, 1995], restructuring [*Casey et al.*, 1993; *Tsomaia et al.*, 2003] and structural collapse [*Paces*, 1973].

Precipitated layers/zones are a term we use to describe silica-enriched layers occurring on or within a substrate that formed via dissolution-reprecipitation. Like leached layers, precipitated layers/zones are created using silica from the substrate, and so they are also internally derived. The main difference is that leached layers are residual material left behind after incomplete dissolution of the parent material, while precipitated layers/zones are formed when the parent material is first completely dissolved, releasing the oxides that are re-precipitated onto the surface of the parent material. Thus, only the formation mechanism differentiates precipitated layers from leached layers, and only silica source differentiates precipitated layers from coatings.

Mineral replacement is a term used to describe when a more stable mineral replaces a less stable mineral, while the preserving the original crystal morphology (pseudomorphism). Replacement is thought to occur through dissolution-reprecipitation [*Velbel*, 1982; *Putnis and Putnis*, 2007; *Hellmann et al.*, 2012; *Ruiz-Agudo et al.*, 2014]. *Hellmann et al.*, [2012] argued that dissolution-reprecipitation is the underlying mechanism behind all chemical weathering, and that the nature of the secondary phase defines the two end-members of the continuum of weathering reactions. On one end of the spectrum are reactions that produce amorphous secondary phases, and on the other end are replacement reactions that create crystalline minerals. Therefore, in this paper, we

will only use replacement to describe a crystalline secondary phase that has pseudomorphically replaced an original crystalline phase.

3.2.2 Morphology and chemistry of silica-rich alteration textures

Many researchers have attempted to use micro-scale morphology and chemistry to differentiate between the four alteration textures and compositions of silica-enrichment noted above [e.g., *Doremus*, 1975; *Farr and Adams*, 1984; *Nesbitt and Muir*, 1988; *Casey et al.*, 1989b; *Petit et al.*, 1989, 1990; *Dorn*, 1998; *Dixon et al.*, 2002; *Hellmann et al.*, 2004, 2012; *Minitti et al.*, 2007; *Chemtob et al.*, 2010; *Chemtob and Rossman*, 2014]. Confusingly, some of the more recent studies have used technological advances in micro-scale analytical chemistry techniques to challenge the validity of previously accepted distinguishing characteristics. Here we summarize the findings and conclusions from these studies.

Silica coatings are generally characterized by having sharp compositional and morphological boundaries between the coating and the substrate [*Farr and Adams*, 1984; *Dorn*, 1998]. Compositionally, silica coatings are mostly made of X-ray amorphous silica, but can contain varying abundances of Fe and Al [*Dorn*, 1998]. Thicknesses range from microns to almost a millimeter [*Dorn*, 1998, and the coatings generally appear as accreted layers in cross-section [*Farr and Adams*, 1984; *Dorn*, 1998]. Additionally, silica coatings frequently incorporate other material such as dust and/or crystalline particles [*Dorn*, 1998].

Purported leached rinds on minerals are generally quite thin with thicknesses ranging from 50 nm – 10 μm [e.g., *Casey et al.*, 1993; *Minitti et al.*, 2007]. According to *Minitti et al.* [2007], experimentally produced leached layers are rarely pure SiO_2. For example,

Berger et al. [1987] reported a leached layer with ~15 wt. % Al_2O_3. Additionally, leached layers are commonly described as being fractured and brittle, and may detach from the underlying surface [*Gislason and Oelkers*, 2003; *Tosca et al.*, 2005; *Schott et al.*, 2009, 2012; *Chemtob et al.*, 2010; *Seelos et al.*, 2010].

For many decades, the strongest argument for a leached rind/layer has been the presence of a sigmoidal elemental profile between the rind/layer and the substrate [*Doremus*, 1975; *Nesbitt and Muir*, 1988; *Casey et al.*, 1989b; *Petit et al.*, 1989, 1990], which has been used to argue for a diffusive reaction surface. However, with recent technological advances, it has been shown that the technique used to measure the profile is very important. Ion beam measurements such as SIMS and EDS, produce scattered radiation – called an "electron skirt" – from some depth, which effectively broadens the electron probe diameter [e.g., *Ganguly et al.*, 1988; *Belkorissat et al.*, 2004]. The broadened probe diameter creates a spatial averaging effect that produces a chemical profile resembling a diffusion profile, but the chemical boundary might actually be much sharper [e.g., *Ganguly et al.*, 1988; *Hellmann et al.*, 2004; *Gin et al.*, 2013].

Precipitated layers, like silica coatings, occur on the perimeter of the sample, and are indicated by very abrupt (nm scale) chemical and morphologic boundaries between the layer and the substrate [*Hellmann et al.*, 2004, 2012], though, as discussed above, the chemical profile depends strongly on the measurement technique. Precipitated layers are made of mostly hydrous SiO_2, but frequently contain traces of other ions such as Al, Ca and Mg [*Hellmann et al.*, 2012]. Purported precipitated silica layers vary in thickness between ~5 to 870 nm on various silicate minerals [*Hellmann et al.*, 2012], and 10 – 300 μm on borosilicate glasses altered for 96 hours [*Geisler et al.*, 2010]. Precipitated layers

are essentially replacing the parent material with a more stable amorphous phase, and replacement reactions commonly involve volume changes, both positive (expansion) and negative (shrinkage), which can generate stresses sufficient to cause fracturing in and between the parent and product phases [*Ruiz-Agudo et al.*, 2014]. Therefore, precipitated silica layers, have similar morphology and chemistry to leached layers, such as fractures and other trace elements, making the distinction nearly impossible without proper elemental profiles.

In summary, silica coatings are distinguished from all other forms of silica enrichment noted here by their accreted appearance and the inclusion of mineral or other detritus into the coating. Silica enrichment via leaching or dissolution-reprecipitation can generally only be distinguished by a diffuse or sharp elemental profile between the layer and the substrate. "Replaced zone" is a term used only to describe crystalline secondary phases, not the product amorphous silica phases we find in this study.

3.2.3 Previous acidic alteration experiments involving basalt and basaltic glass

The way a rock chemically weathers in a given environment is dependent on multiple properties including the composition, crystallinity, and porosity of the parent material. In general, basaltic glass initially weathers more rapidly than its crystalline counterpart [*Colman*, 1982; *Eggleton et al.*, 1987; *Gislason and Oelkers*, 2003][*Colman*, 1982; *Eggleton et al.*, 1987] . Furthermore, initial bulk SiO_2 concentration of a material can have a significant effect on the degree of alteration. For example, a basalt glass (~ 48 wt% SiO_2) releases cations at a rate that is orders of magnitude greater than that of a basaltic andesite glass (~ 57 wt% SiO_2) due to the increased number of non-bridging oxygen (NBO) atoms in basalt glass [*Tosca et al.*, 2004]. NBOs tend to have weaker

bonds than the more covalent Si-O bonds, and so the general structure of basalt glass is less thermodynamically stable than basaltic andesite [*Jantzen and Plodinec*, 1984].

Tosca et al. [2004] performed closed system dissolution experiments on crystalline basalt, basaltic andesite, and their glass counterparts in acidic fluids of varying composition (starting pH 0 – 4). They found that the secondary phases formed depended on both crystallinity and composition of the starting material. Amorphous silica was precipitated in all experiments except for the ones involving the basaltic andesite glass, and residual amorphous silica was observed on the basaltic glass altered at low starting pH (1 and 2). These residual layers were described as having resulted from nonstoichiometric dissolution, or leaching. Gypsum and other various sulfates were formed in almost all of the experiments except for those with the highest starting pH. Fe oxides were also found to precipitate in all experiments where the pH of the solution was buffered to > 4 by solute concentrations increasing as the reactions proceeded.

Golden et al. [2005] subjected two distinct glassy basalt samples (one olivine-rich, one plagioclase-rich) to three different acid weathering environment simulations all at elevated temperatures (145°C): (1) sulfuric acid vapor, (2) sulfuric acid open system, and (3) sulfuric acid closed system. The results from each of these experiments were similar to the findings of *Tosca et al.* [2004]. The major secondary phases formed for both samples during the acid fog simulations were amorphous silica and various sulfates. Jarosite, Mg- and Ca-sulfates as well as amorphous silica formed from the olivine-rich basalt in the open system acidic environment, whereas only amorphous silica formed from the plagioclase-rich tephra in the same environment. Only amorphous silica formed in the closed system experiments for both samples.

Thus, *Tosca et al.* [2004], *Golden et al.* [2005], along with numerous other studies [e.g., *Banin et al.*, 1997; *Morris et al.*, 2000; *Hurowitz et al.*, 2006; *Hamilton et al.*, 2008; *Marcucci and Hynek*, 2014], have determined that acid weathering of basaltic substances will commonly form amorphous silica, sulfates, and sometimes iron oxides. Our companion paper supports these previous results as the acid-altered samples used this study were found to exhibit spectral features consistent with amorphous silica and potentially iron oxides and sulfates [*Horgan et al.,* submitted]. Here we focus mostly on amorphous silica coating and rind formation because it is so pervasive, it is easily measured in the infrared spectra of altered basaltic substances, and the spectral effects of this type of surface alteration are poorly understood.

3.2.4 Spectral effects of silica-enriched alteration textures

Many workers have studied the spectral effects of natural [e.g., *Kahle et al.*, 1988; *Crisp et al.*, 1990; *Christensen and Harrison Thliveris*, 1993; *Michalski*, 2004; *Michalski et al.*, 2006; *Minitti et al.*, 2007; *Seelos et al.*, 2010] and synthetic [*Kraft et al.*, 2003; *Horgan et al.*, submitted] rock coatings. The penetration depth of the spectral measurement is highly dependent on the wavelength (longer wavelengths penetrate deeper). Visible and near-infrared (VNIR, 0.35 to 2.5 μm) wavelengths measure only the very outer surface of a sample, whereas the mid-infrared (MIR, 5 to 50 μm) wavelengths are able to penetrate a depth of up to ~ 100 μm. Additionally, visible wavelength measurements inform about the electron transitions, and therefore, what transition metals are in the material, while near- and mid-infrared give information about the structural vibrations happening within, and therefore the mineralogy of, the material.

Silica coatings and surface altered layers can alter and obscure the visible and

infrared spectrum of a substrate [*Kahle et al.*, 1988; *Crisp et al.*, 1990; *Abrams et al.*, 1991; *Kraft et al.*, 2003; *Minitti et al.*, 2007; *Seelos et al.*, 2010; *Horgan et al.*, submitted]. *Kraft et al.* [2003] created colloidal silica coatings of varying thickness on natural basalt samples, and found that coatings only ~7 - 10 μm thick can completely mask the TIR spectral signature of the underlying rock. This finding was remarkable give the penetration depth of TIR wavelength measurements. *Kraft et al.* [2003] also found that when silica coatings were less than ~ 7 μm thick, the coating and substrate TIR spectra would not combine linearly to accurately model the measured sample spectrum, adding complication to the general assumption that surface spectra are linear mixtures of the components.

Additionally, TIR spectra of natural silica coatings and surface altered layers on basalt and basaltic glass are generally spectrally consistent with increased amorphous silica [*Kahle et al.*, 1988; *Crisp et al.*, 1990; *Minitti et al.*, 2007; *Ruff et al.*, 2011; *Horgan et al.*, submitted]. Samples with silica-rich alteration layers show strong tetrahedral Si-O stretching spectral features with minima between ~1087 - 1100 cm^{-1}, Si-O bending features between ~450 - 470 cm^{-1}, and sometimes a shoulder on the tetrahedral Si-O stretching feature ~ 1220 cm^{-1} [e.g., *Kraft et al.*, 2003; *Minitti et al.*, 2007; *Ruff et al.*, 2011; *Horgan et al.*, submitted]. The Si-O stretching features occur at lower wavenumber than that of opal-A at ~1115 cm^{-1}, yet the shoulder at 1220 cm^{-1} is the same in opal-A. Additionally, the Si-O stretching feature of silica-rich alteration layers are sometimes comparable with, but often higher wavenumber that of obsidian at ~1087 cm^{-1}. The position of the Si-O stretching feature is positively correlated to the degree of polymerization of the silica tetrahedral network, so that a decrease in the degree of

polymerization would cause the emissivity minimum to shift to lower wavenumber [*White and Minser*, 1984; *Crisp et al.*, 1990; *Michalski et al.*, 2005]. Thus, we have some constraints on the structure and composition of natural silica-rich coatings and/or surface altered layers. The structures are less polymerized than opal-A, but more polymerized than obsidian glass.

The 1220 cm^{-1} absorption feature is found in many silica-rich glasses and silica-rich amorphous alteration phases, and represents one of two states of the SiO_2 asymmetric stretching mode [*Minitti et al.*, 2007]. The feature has been noted to change in depth with viewing angle for natural and synthetic amorphous silica [*Almeida*, 1992; *Ruff et al.*, 2011]. The feature can also be completely absent from spectra of surfaces that otherwise look like silica-rich coatings/leached rinds (e.g., compare ICE170 acid A and BAS101 acid A in figure 3.1). It is unknown what would cause the feature to be absent, but suggestions include the effects of coating thickness [*Crisp et al.*, 1990; *Kraft et al.*, 2003] and/or material porosity [*Ruff*, personal communication].

[*Crisp et al.*, 1990] found that all three spectral features associated with silica-rich coatings/layers (~1087-1100 cm^{-1}, ~450 - 470 cm^{-1}, and 1220 cm^{-1} shoulder features) are very common in spectra from lava flows over 50 years old, which presumably have well developed silica-rich coatings. Flows that are weeks old also have spectral features associated with silica-rich coatings/layers, but the 1220 cm^{-1} shoulder feature is usually absent. Likewise, *Kraft et al.* [2003] measured TIR spectra of Columbia River Basalt coated with varying thicknesses of amorphous silica and found that the 1220 cm^{-1} spectral feature did not appear until the coatings were ~3 μm thick. These studies suggest that the spectral feature only becomes present when the silica-rich coating/layer is of

sufficient thickness. However, *Minitti et al*. [2007] found that one sample with silica-rich coatings/layers ~2 - 3 μm thick (MUO) had the 1220 cm^{-1} spectral shoulder, while another sample with generally thicker coatings/layers (~5 – 7 μm; MIY) did not. Thus, there are most likely other factors controlling the presence or absence of the 1220 cm^{-1} shoulder feature.

In the visible and near-infrared, silica exhibits diagnostic absorption bands near 1.4 and 1.9 μm due to overtones of OH stretching vibrational modes in adsorbed H_2O, as well as a broad doublet absorption band near 2.21 and 2.26 μm due to SiOH rotation and stretching vibrational modes [*Langer and Flörke*, 1974; *Rice et al.*, 2013]. Purported leached rinds are generally distinguished from silica coatings by the lack of silica hydration bands at 2.21 and 2.26 um and a concave up spectral slope [*Minitti et al.*, 2007; *Seelos et al.*, 2010; *Horgan and Bell*, 2012; *Horgan et al*., submitted]. To date, the non-linear concave up spectral shape has only been observed in glass-rich samples thought to have leached layers, and is hypothesized to be due to wavelength-dependent scattering by structures at the sub-micron scale, perhaps related to surface textures in the rinds *Horgan et al*. [submitted]. Coatings, on the other hand, exhibit a linear blue spectral slope (less reflectance at longer wavelengths) from the visible into the near-infrared, regardless of their substrate [*Kraft et al.*, 2007; *Milliken et al.*, 2008].

It is apparent that coatings and surface altered layers complicate the remote sensing data we receive from a planetary surface, and can lead to erroneous geologic interpretations. Thus, it is important to better understand their spectral properties and the morphological reasons behind them.

3.3 Methods

3.3.1 Acid Leaching Experiments

Four samples were used in this study, with varying degrees of crystallinity [*Horgan et al*., submitted; see Table 3.1 for sample information]: a Columbia River Plateau basalt from the Rosa dike (BAS205; ~15% glass), a partially glassy Icelandic olivine basalt from a subaqueous pillow lava (ICE170; ~50% glass), a Hawaiian glassy basalt from a subaerial flow (BAS101; ~75% glass), and Hawaiian basaltic glass sand, produced during explosive quenching of a lava flow entering the ocean and concentrated on a black sand beach (BSB101; ~85% glass). Each basalt hand sample was both cut into cm-scale fragments using a diamond rock saw and ground into sand (500-1000 μm) using a mortar and pestle. The cm-scale fragments exhibit both porous natural weathered surfaces as well as smooth fresh-cut surfaces. The basaltic glass was collected in the field as sand, so no cm-scale fragments are available. To simplify this study, we only analyze the sand-sized particles.

For our experiment, we chose to recreate an open hydrologic system such as channel or groundwater flow, which we simulated by placing our samples in acid solution baths and then frequently replacing the fluids with a fresh acid solution. Two stock acid solutions were made up using concentrated H_2SO_4 and distilled H_2O, with a pH of 1.0 (Acid A) and 3.0 (Acid B). Approximately 7 g of the four granular samples and the three cut samples were placed in separate Teflon vessels with 30 ml of the stock sulphuric acid solution and 10 ml of 30% H_2O_2. Hydrogen peroxide was chosen as the oxidizing agent because superoxides and peroxides have been suggested as candidates for the purported oxidant in Martian surface materials [*Zent, A. P; McKay*, 1994; *Golden et al.*, 2005]. The

Table 3.1. Sample information.

Sample	***Description***	***Surface Type***		
		Grains	*Cut*	*Natural*
BSB101	Basaltic Glass, black sand beach, Hawaii (collected by R.B. Singer)	A, B[1]		
ICE170	Basalt, pillow lava, Dagmalafell, Iceland (collected by E. Cloutis)	A, B	A, B	A, B
BAS101	Basaltic Glass, Kilauea Caldera, 1956 flow, Hawaii (collected by E. Cloutis)	A, B	A	A
BAS205	Basalt, Roza Dike, Columbia River Plateau (collected by S. Atkinson[2])	A, B	A, B	A, B

[1] A and B indicate which acid solutions were used to weather samples, as described in text.
[2] *Atkinson et al.* [1990], sample #SA-78

samples were fully immersed in the solutions initially for one day at a time, and gradually for longer durations as the alteration progress slowed. In total, all samples were exposed to acid for 220 days at 25°C. All samples were washed with deionized water prior to analysis to remove loose secondary minerals, because our study was focused on analyzing physically adhered alteration rinds and coatings on the samples.

3.3.2 Spectroscopy

Here we summarize the methodology for spectral measurements, and the details can be found in *Horgan et al*. (submitted). Thermal-infrared emission spectra (TIR) were measured at the Arizona State University Infrared Spectroscopy Laboratory using a Nicolet Nexus 670 spectrometer that is configured to measure emissivity [*Ruff et al.*, 1997]. Spectra were collected at a spectral resolution of 2 cm^{-1} over the range of 200 – 2000 cm^{-1}. The samples were heated to 80 °C for multiple hours prior to being measured, and this temperature was maintained during spectral acquisition by actively heating the sample with a hotplate. All TIR spectral measurements were taken after the acid leaching experiments were complete.

Visible and near-infrared (VNIR) reflectance spectra were collected from all the samples using an ASD FieldSpec Pro HR spectrometer over the wavelength range of 0.35 to 2.5 μm. A 150 W QTH light source was used to illuminate the samples and reflectance spectra were measured at i=30°, e=0°; 200 spectra of each sample were collected periodically when the sample was removed from the acid bath and averaged to improve SNR. To reduce the effects of specular reflections, all 500 – 1000 μm samples were spun on a turntable at 33 rpm during data collection.

3.3.3 Scanning Electron Microscopy

In order to perform detailed microscopic analyses of the weathered particles, we randomly selected three grains of each starting material and ten grains of each ending material from the experiments listed in Table 3.1 for Scanning Electron Microscope (SEM) analysis. Grains were aligned on double-sided tape and then encapsulated in a two-part epoxy cured at room temperature. The sample stub was polished to 0.25 μm using progressively smaller sized particle diamond suspension and diamond paste in order to get a cross-sectional view through the grains.

The sample stub was carbon coated and then examined at the Arizona State University Center for High Resolution Electron Microscopy using an XL-30 SEM. The coating/rind thickness and morphology was examined using secondary electron (SE) and back-scattered electron (BSE) imaging. Qualitative chemistry was measured using spot and line analyses as well as elemental maps obtained from the energy-dispersive x-ray spectroscopy (EDS) system on the SEM. All SEM measurements were made at a working distance of 11 mm, an accelerating voltage of 20 kV, and a spot size of 3 or 4.

3.4 Results

3.4.1 TIR Spectra of Grains

A detailed analysis of the TIR spectra can be found in our companion paper (*Horgan et al*., submitted), but the results from that study are summarized here. In general, we see changes in the thermal-infrared spectral shape in two main wavenumber regions for the acid leached basalt, glassy basalt, and basaltic glass samples. The most extreme spectral changes are found in samples exposed to starting pH ~1 acid (acid A) solutions. When exposed to acid A, most samples exhibit a narrowing of the Si-O

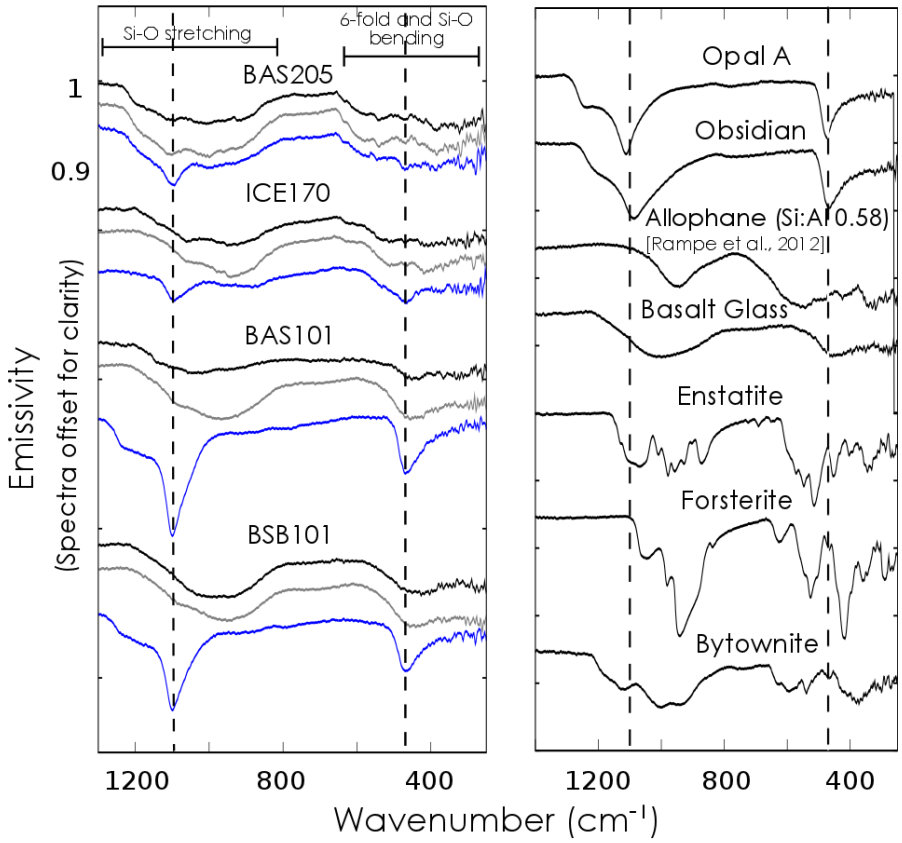

Figure 3.1. TIR spectra of basalt grains from these experiments. (Left) plot shows unaltered basalt grains (black), grains weathered in pH 3 acid (grey), and grains weathered in pH 1 acid (blue) for each experiment. Dashed lines mark the 1100 cm^{-1} and 465 cm^{-1} positions of the final emissivity minima for all samples weathered in acid A. (Right) plot showing TIR spectra of common minerals and phases from the ASU online spectral library for reference.

stretching band combined with a shift to a higher wavenumber, indicating increased polymerization of the material (Figure 3.1) [*White and Minser*, 1984; *Crisp et al.*, 1990; *Michalski et al.*, 2005]. In contrast, when exposed to starting pH ~3 acid solutions, all samples except the most crystalline (BAS205) show emissivity minima shifts toward lower wavenumbers in this region, which suggests increased disorder (Figure 3.1).

The second wavenumber region that experiences spectral change is between ~ 300 cm^{-1} – 600 cm^{-1}. The attribution of spectral features in this wavenumber region to specific vibrational modes is not so straightforward because of overlap in the energy levels of tetrahedral Si-O bending vibrations as well as vibrations of cations in 6-fold coordination sites [*Michalski et al.*, 2005]. However, in general, the samples exposed to acid A develop a local emissivity minimum near 465 cm^{-1}, which can most likely be attributed to tetrahedral Si-O bending vibrations (Figure 3.1) [*Ruff and Christensen*, 2007; *Rampe et al.*, 2012]. This wavenumber region remains unchanged for samples exposed to acid B (Figure 3.1).

More specifically, basaltic glass samples (BAS101 and BSB101) exposed to acid A for 220 days develop very strong amorphous silica spectral signatures that mask any signal from the underlying basaltic glass (Figure 3.1). The spectral shape of these samples is very similar to that of opal-A, but with a Si-O stretching emissivity minimum shifted toward slightly lower wavenumber (~ 1100 cm^{-1} instead of 1115 cm^{-1} as it is for opal-A). This difference indicates that the new phase is not pure silica, and that there is most likely either some tetrahedral substitution (Al^{3+}, Fe^{3+}) or possibly H_2O or OH^- causing the decrease in polymerization [*Farnan et al.*, 1987; *Michalski et al.*, 2005]. Additionally, the basaltic glass samples develop a spectral shoulder at 1220 cm^{-1}, which

also occurs in spectra of most opaline silica and high-Si glasses like obsidian as discussed in Section 3.2.4.

The more crystalline basalt samples (BAS205 and ICE170) exposed to acid A for 220 days also develop amorphous silica spectral signatures with emissivity minima near 1100 cm^{-1}. However, less polymerized phases are still detected based on the absorption features near 950 cm^{-1}, suggesting that the altered samples are a mixture of silica-rich alteration phases with other alteration phases and/or unaltered material.

In summary, TIR spectra of basaltic materials exposed to acid A indicate the deposition of an amorphous silica-rich phase. The TIR spectrum of basaltic glass altered in acid A is completely dominated by a strong amorphous silica-rich spectral signature, leaving no indication of the starting material. The TIR spectra of the more crystalline phases retain some of the mafic signature of the starting material, indicating that some of the mafic material remained unaltered in the optically active part of the sample. The TIR spectra of all samples exposed to acid B, except the most crystalline (BAS205) indicate increased disorder.

3.4.2 VNIR Spectra of Grains

We observe four key types of visible/near-infrared (VNIR) spectral changes during alteration of our samples in acid A (Figure 3.2). First, we observe changes to the relative strength of broad absorptions near 1 and 2 μm that are present in all starting materials, and are due to ferrous-bearing minerals such as olivine, pyroxene, and glass. Changes to these bands during alteration include both the weakening of the iron bands overall, most likely due to obscuration by an overlying coating or rind, as well as the strengthening of one iron band relative to the other, due to preferential dissolution of

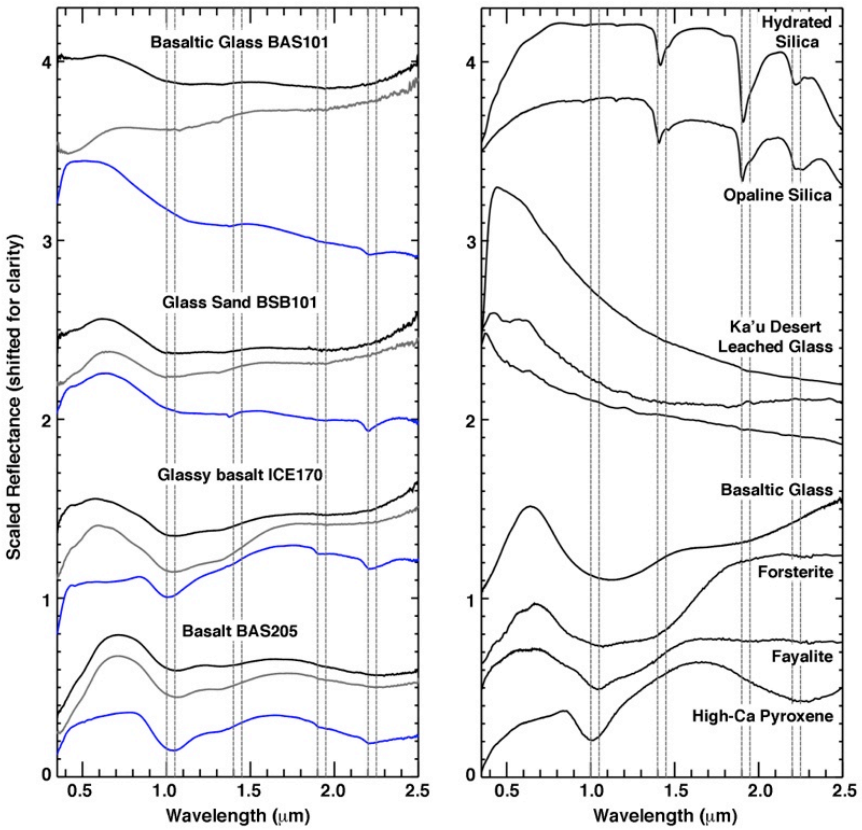

Figure 3.2. VNIR spectra of basaltic grains from these experiments. (Left) plot shows unaltered basaltic material (black), grains weathered in pH 3 acid (grey), and grains weathered in pH 1 acid (blue) for each experiment. Lines mark the positions of the most spectral change (1.0, 1.4, 1.9, and 2.2 μm). (Right) plot showing VNIR spectra of common minerals and for reference. Lines are in the same positions as in the figure on the left.

some phases relative to others (usually strengthened pyroxene absorptions at the expense of olivine absorptions). The minerals inferred to be lost vary with starting composition, but are consistent with those modeled as lost based on thermal-IR spectra. In general, both wavelength ranges detect losses of mafic glass, olivine, and pyroxene. Second, we observe the appearance of narrow absorption bands near 1.4, 1.9, and 2.2 μm, consistent with the deposition of alteration minerals that include silica and hydrated glass. The appearance of these bands correlates well with models of increased high-silica phases in thermal-IR spectra. Third, we observe a flattening of spectra between 0.4-0.7 μm, which we hypothesize, is due to dissolution of fine-grained oxides. A potential decrease in oxides is also observed in the thermal-IR. Lastly, and most importantly, we observe the development of strong blue spectral slopes (decreasing reflectance with increasing wavelength) with concave up and/or linear shapes. These spectral slopes only occur in the glass-rich samples, and thus we hypothesize that the concave up and linear blue slopes are related to the development of leached rinds and coatings on the glass, respectively [*Horgan and Bell*, 2012]. The appearance of these spectral slopes is correlated with the appearance of a shoulder at 1220 cm^{-1} in the thermal-IR spectra of these samples.

In contrast, samples altered under pH ~3 (Acid B) show very little VNIR spectral evidence for alteration. VNIR spectra of the crystalline samples are virtually unchanged after 220 days exposure to Acid B, while some glass-rich samples develop weak absorption edges in the visible and red spectral slopes (increasing reflectance with increasing wavelength), both potentially consistent with the addition of ferric iron in some form, most likely amorphous. In general, we find that increasing spectral change correlates with both increasing acid strength and decreasing crystallinity.

In summary, VNIR spectra of basaltic material exposed to starting pH ~1 acid indicate a relative loss of olivine from the parent material and the deposition of alteration minerals (silica, hydrated glass, gypsum, and other sulfates), and have concave up and linear blue slopes that are hypothesized to be a result of the development of leached rinds and coatings on the glass. In contrast, the VNIR spectra of basaltic material exposed to starting pH ~3 acid show little change except for the potential addition of amorphous ferric iron oxides.

3.4.3 SEM

3.4.3.1 Starting material

Overall, the crystalline basalt and glassy basalt samples (BAS205 and ICE170) have more crystal boundaries, pores, and fractures than the basalt glass samples (BAS101 and BSB101) (Figure 3.3), making them more permeable to alteration fluids. BAS205 samples contain visible phenocrysts that are comprised mostly of plagioclase, pyroxene, and olivine. These phases were detected in the VNIR and TIR spectra of the sample [*Horgan et al*., submitted]. Deconvolution of the TIR emission spectrum of BAS205 starting material modeled mafic glass in abundance of 50%, yet there is no clear indication of basalt glass when the sample is viewed in SEM [*Horgan et al*., submitted]. However, the difference between a partially glassy matrix and a microcrystalline matrix of the same composition would be difficult to distinguish using only imagery and EDS chemical data. BAS205 exhibits abundant fractures hundreds of microns long that reach from the rim of the grain in toward the center. ICE170 is less crystalline than BAS205, yet the sample does have some plagioclase crystals with pyroxene crystallite intergrowth within the overall homogeneous (glassy) matrix, indicating rapid quenching during

formation (Figures 3.3b and c). ICE170 grains also exhibit numerous fractures that reach up to ~500 microns long, and sometimes almost cut completely across the grain. BAS101 is a much more homogeneous glass, containing only a few ~30 - 60 μm plagioclase crystals in each grain. The fractures in BAS101 grains are relatively small (tens of microns in length), and run parallel to the grain boundary, barely reaching into the interior (Figures 3.3d and e). BSB101 starting material looks very similar to BAS101, with few small plagioclase and olivine crystals and small fractures (Figures 3.3f and g). It should be noted that no secondary phases were found on any of the grains observed, which is consistent with the lack of significant secondary phases modeled in the TIR spectra of the starting material [*Horgan et al*., submitted].

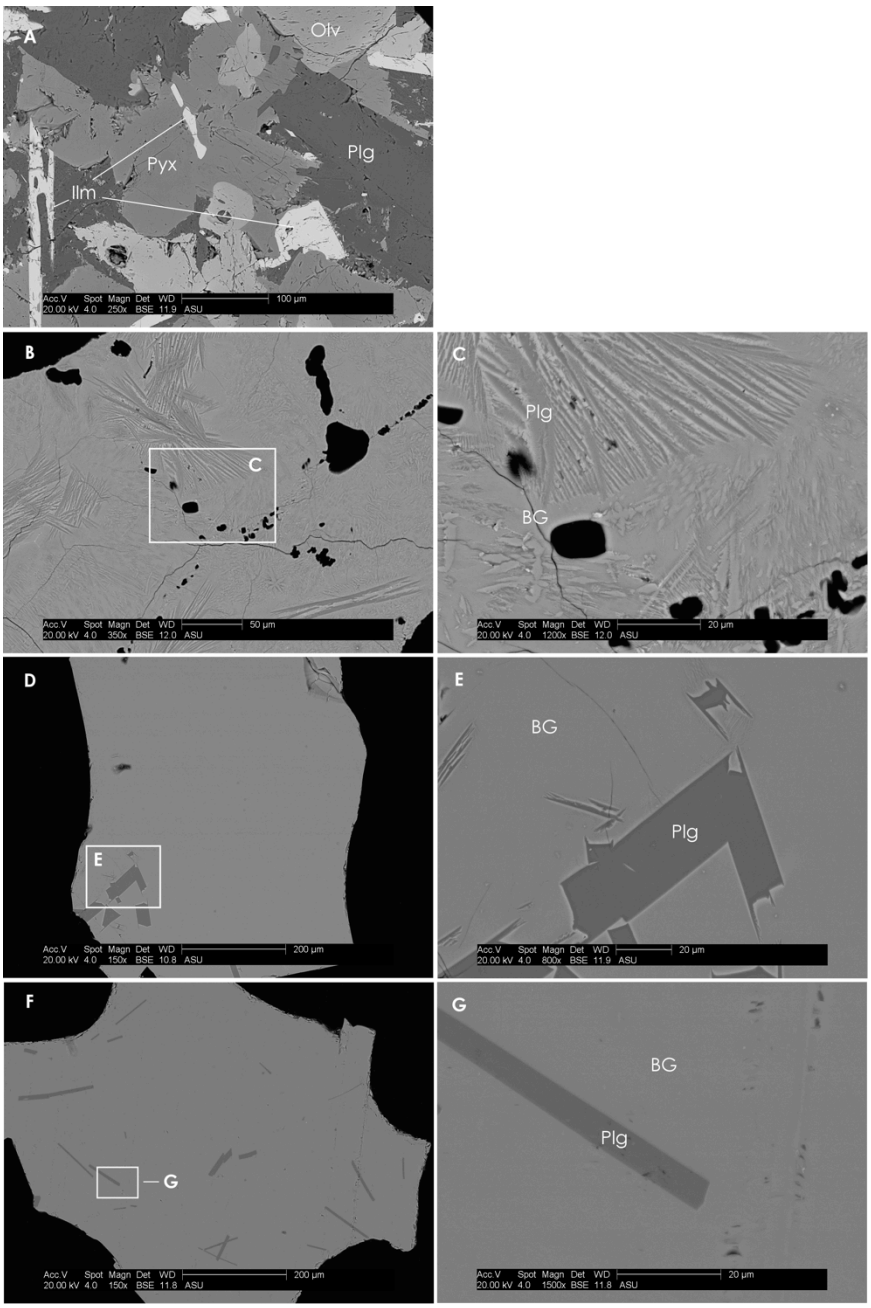

Figure 3.3. BSE images of starting material BAS205 (a), ICE170 (b and c), BAS101 (d and e), and BSB101 (f and g). White rectangles indicate region enlarged in picture on the right.

3.4.3.2 Glassy basalt in low pH acid

BSE imaging reveals that glassy basalt ICE170 grains exposed to starting pH ~1 acid (acid A) do not have continuous surface altered layers. Rather, the relative contrast changes in the BSE images (Figure 3.4) and EDS point scans (Figure 3.5) show that there are multiple alteration phases throughout the sample. We separate the altered areas into two different phases based on composition and morphology, "altered glass" and "Si-enriched regions". The altered glass areas are smooth and intermediate grey in the BSE image, and exhibit decreased Na, Mg, Al, and Ca content and increased Si and Fe content relative to the starting material. The Si-enriched areas are dark and fractured in the BSE images, and exhibit complete loss of Na, Mg, and Fe, while some Al and Ca remain in less abundance than in the starting material. The wt% Si is nearly doubled from that of the original material and nearly 1/3 greater than in the altered glass areas. Thus, acid alteration appears to be patchy, having permeated the entire grain, and produces silica-rich phases.

As far as we observed, alteration exclusively affects the plagioclase quench crystals, while the pyroxene and spinel crystals remained unaltered during the experiments. Si-enriched regions occur within the boundaries of the plagioclase quench crystals, taking on their original shape, though the new silica-rich phase is highly fractured indicating a volumetric change. SE imaging also displays the highly fractured nature of the Si-enriched areas, and shows nanometer-scale particulate in the fractures (Figures 3.6a and b). This particulate material could either represent newly precipitated material or residue left behind as the original structure was destroyed during the leaching process.

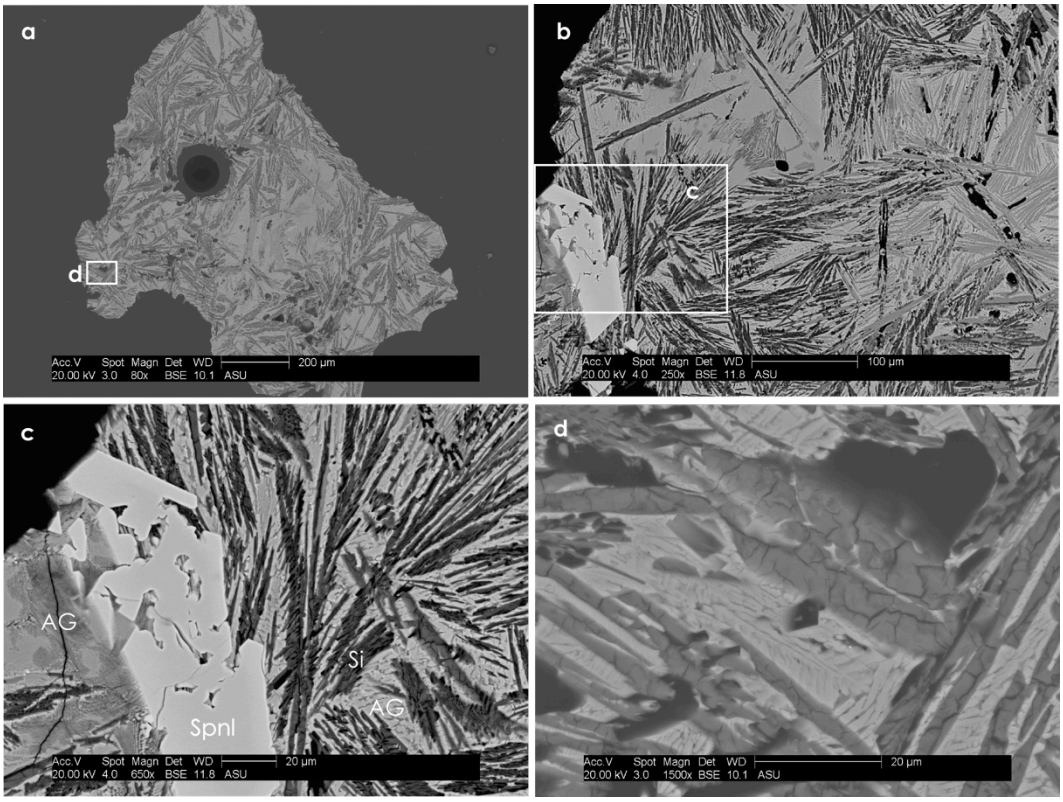

Figure 3.4. BSE images of ICE170 weathered in pH 1 acid for 220 days. (a) Overview of a grain showing heterogeneous interior alteration morphology with white box showing region enlarged in d. (b) Context image of another grain with white box showing region enlarged in (c). (c) AG is altered glass, Spnl is spinel, Si are areas comprised of nearly pure silica. (d) Close-up of Si and AG regions showing the fractured nature of the Si.

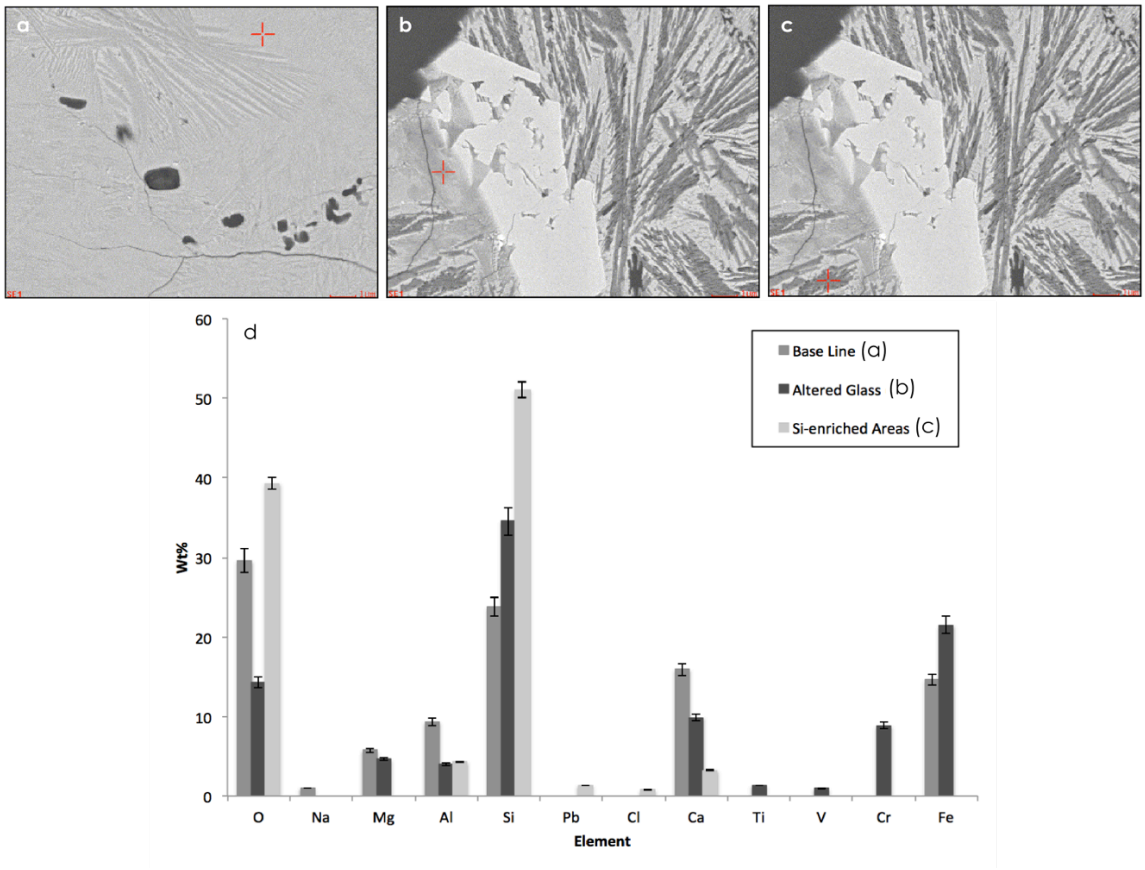

Figure 3.5. Locations of EDS point scans from basalt glass in ICE170 baseline (a; point location shown by red cross); (b) altered glass in ICE170 altered in acid A for 220 days (point location shown by red cross), and (c) Si-enriched regions in ICE170 after alteration in acid A for 220 days (point location shown by red cross). (d) Results from EDS measurements for each location in a, b and c in wt% of major elements.

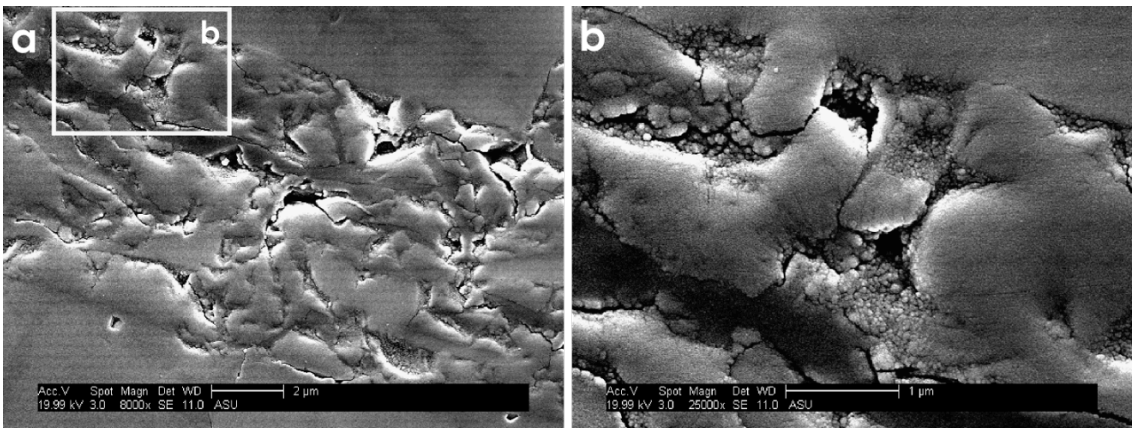

Figure 3.6. SE cross-sectional view of ICE170 grains mounted in epoxy after exposure to pH 1 acid for 220 days. (a) Shows the fractured topography of the altered regions within the grains, and upon closer inspection (b) spherical deposits/debris is visible within in the altered regions.

3.4.3.3 Basaltic glass in low pH acid

The outer surfaces of the basaltic glass BAS101 grains weathered in starting pH ~1 acid (acid A) display two main textures, a honeycomb-like texture and a highly fractured texture (Figure 3.7a). The honeycomb texture looks pockmarked and relatively interconnected (Figure 3.7b), and is similar to the honeycomb texture found on feldspar crystals described by [*Berner and Holdren*, 1977]. They concluded that this texture forms when etch pits grow and eventually coalesce. The grain surfaces beneath the honeycomb texture appear to be relatively smooth and rounded suggesting that this texture forms on natural surfaces (Figure 3.7a). The fractured texture consists of ubiquitous sharp and angular cracks, making the region appear very brittle (Figure 3.7c). Large conchoidal fractures and angular features can be see beneath the fractured texture indicating that this texture forms on surfaces that were broken during sample processing (Figure 3.7a).

When viewed in cross-section, the grains appear to have nearly continuous alteration layers around the perimeter that vary in thickness from several to tens of microns (Figure 3.8a). Similar to the Si-enriched areas in ICE170, the alteration layers of BAS101 are highly fractured with nanometer-scale particulate in the fractures (Figures 3.8b, c and d).

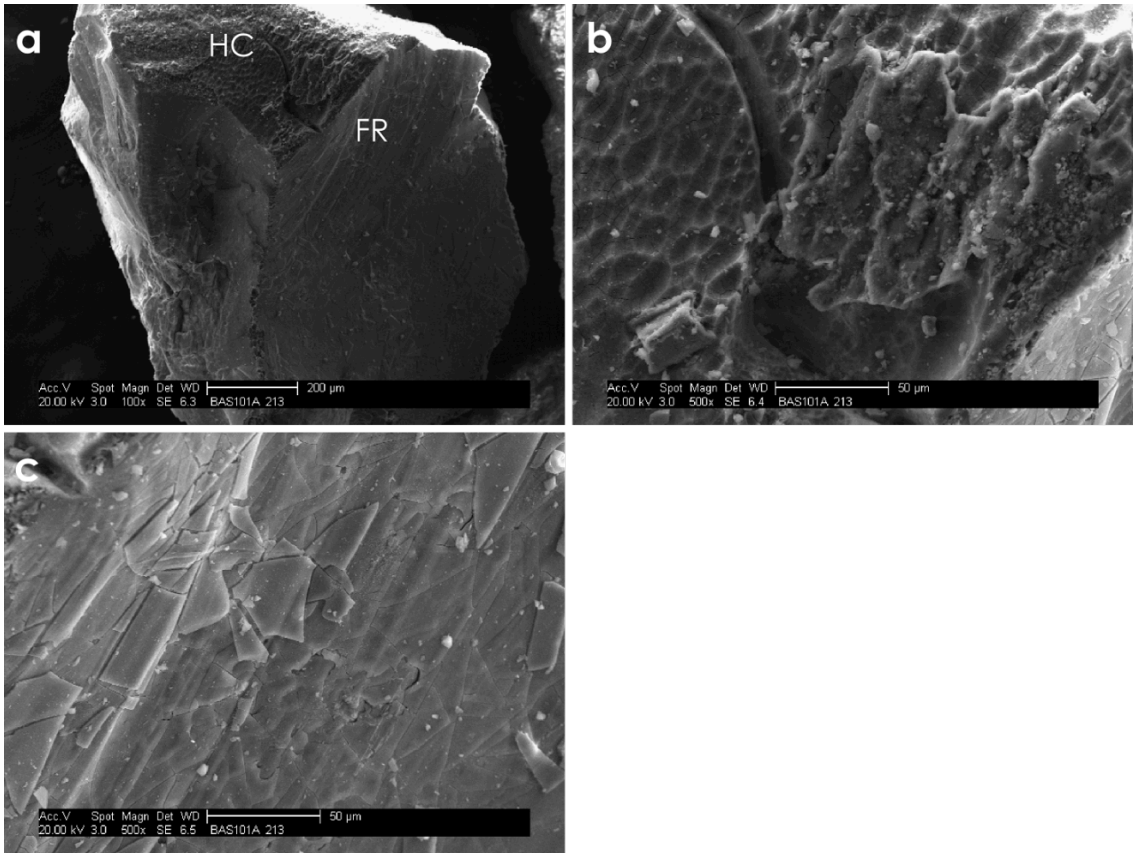

Figure 3.7. SE images of entire grains of BAS101 after exposure to acid A for 220 days. (a) Context image of an altered BAS101 grain showing relationship between HC (honeycomb texture) and FR (fractured texture). (b) Close-up of HC texture. (c) Close-up of FT.

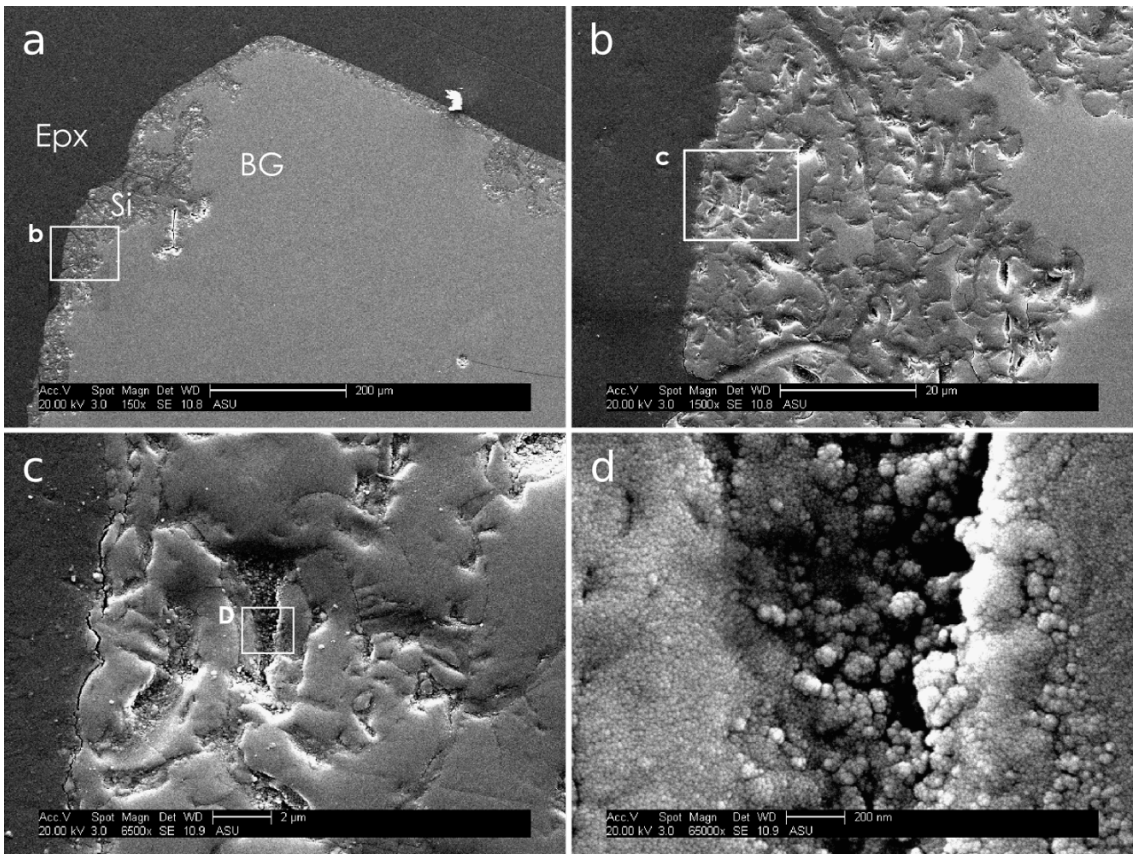

Figure 3.8. SE images of cross-section views of BAS101 grains exposed to acid A for 220 days. (a) context image where Epx indicates epoxy, Si indicates alteration rind that is highly enriched in silica, and BG indicates basalt glass. (b) Magnified to show fractured texture of Si. (c) and (d) Magnified Si to show deposited particulate in fractures.

Most of the alteration occurs along the perimeter of the grains, and in BSE imagery, the alteration layers appear dark and have conchoidal fractures (Figures 3.9 a and b). The alteration can proceed inward along thin fractures and crystal grain boundaries and starts to affect the plagioclase crystals, though the plagioclase crystals are not as thoroughly altered as the surrounding glass (Figure 3.9a). EDS point scans show that the surface alteration rind is enriched in SiO_2 with minor traces of Al, while the interior is chemically consistent with basalt (Figure 3.9c). In summary, we see basalt glass and plagioclase altering to form fractured Si-enriched layers/areas, and the glass is preferentially altered over the plagioclase.

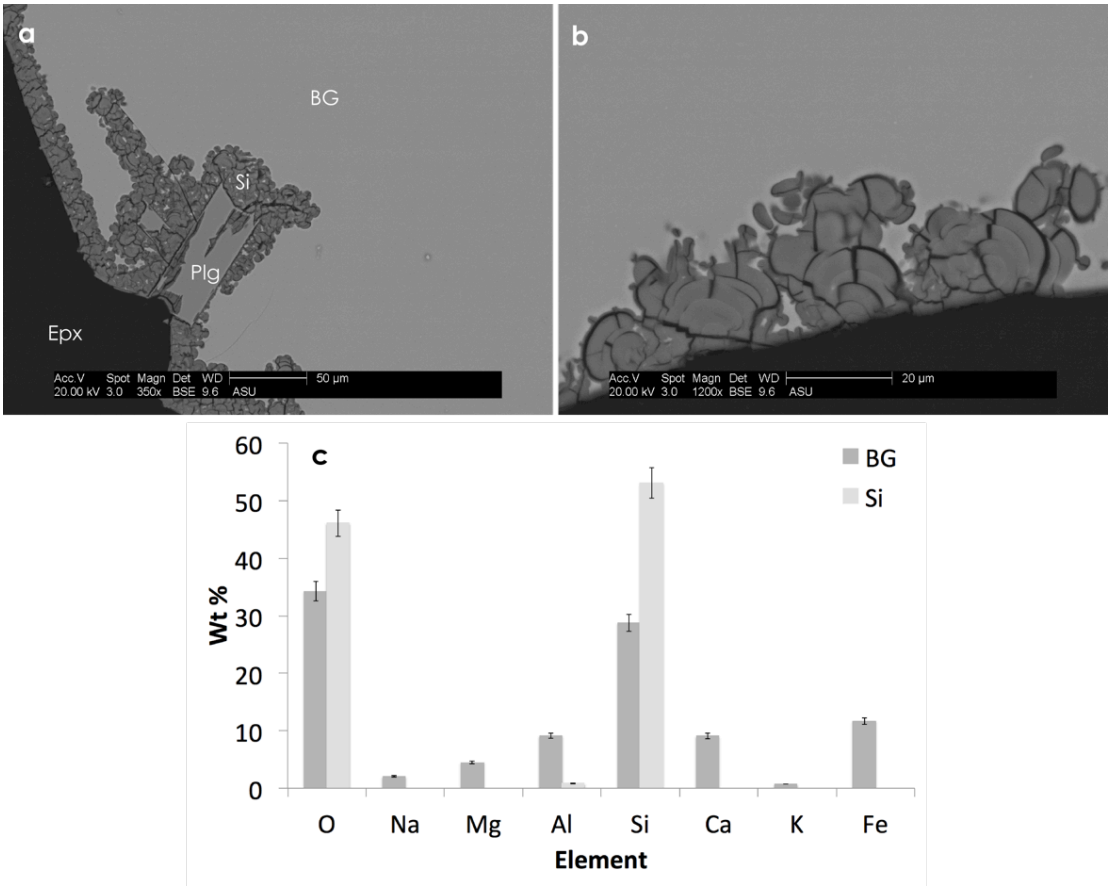

Figure 3.9. BSE images of BAS101 samples after exposure to acid A for 220 days. (a)

Epx is epoxy, Plg is plagioclase, Si is regions highly enriched in silica, and BG is basalt glass. Si rind is nearly continuous around the perimeter of the grains and is a different phase than the BG. It is also highly fractured (b) and intrudes into grain along crystal boundaries (a). EDS data (c) shows that the interior (BG) is consistent with basalt glass, and the Si-enriched areas are almost completely SiO_2, with minor traces of Al.

3.4.3.4 Glassy basalt in moderate pH acid

Dissolution etch pits and pit chains appear on the surfaces of ICE170 grains weathered in starting pH ~3 acid (acid B) for 220 days (Figure 3.10 a. b. c). The pits range from ~ 1 – 10 μm in diameter, and the chains can reach ~ 60 μm in length. Larger circular depressions (> ~100 μm) are interpreted as primary vesicles. The etch pits resemble collapse features, which suggests that they formed as a result of a dissolution process. When viewed in cross section in BSE imagery, the grains show some concave features along the edges of the grains that could be the etch pits (Figure 3.11a). Some of the concave features contain small amounts of a dark toned material that look similar to the Si-enriched regions in the samples exposed to acid A, but were too small for EDS analysis (Figure 3.11a). Otherwise, point and line EDS scans showed no elemental evidence for any phases other than basalt glass, plagioclase and pyroxene. The crystal grain boundaries look smooth and relatively unaltered when compared to those in the samples exposed to acid A, and the overall morphology of the grains is very similar to that of the starting material (Figures 3.11 b and c). Light toned regions and rims that occur in and around ICE170 grains exposed to acid B are due to charging on the sample (Figures 3.11 a and b).

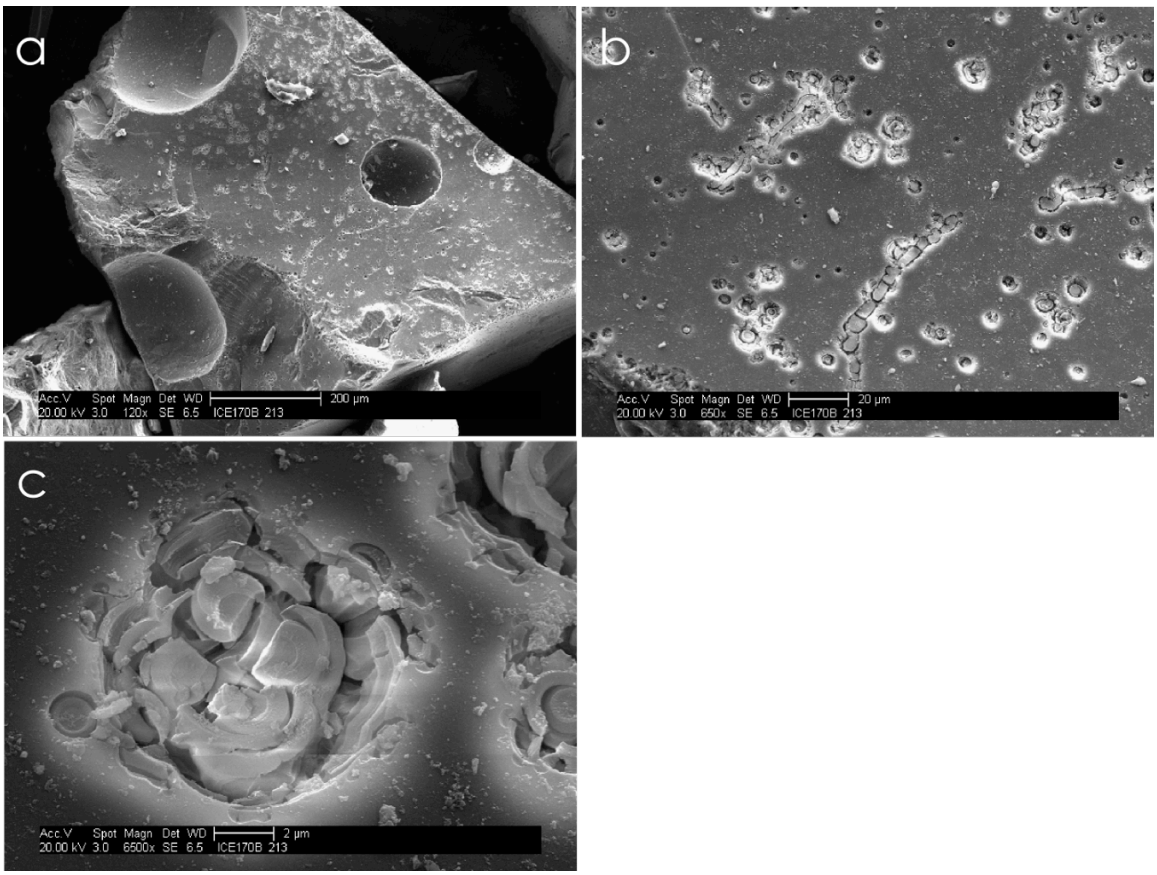

Figure 3.10. SE images of ICE170 grains weathered in acid B for 220 days. (a) Context image showing distribution of etch pits on surface of grain. We interpret the very large pits ~100-200 µm to be vesicles. (b) The same grain at greater magnification showing the pits and pit chains in greater detail. (c) Close up of a pit.

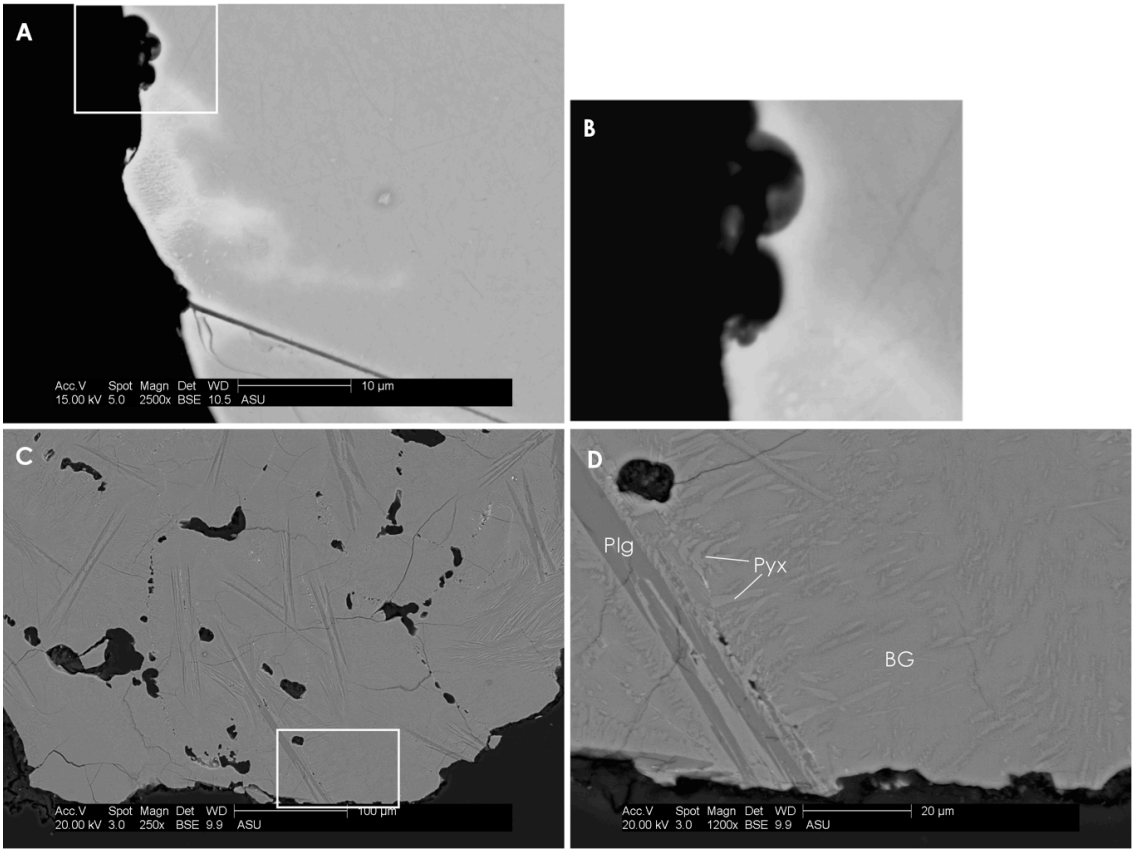

Figure 3.11. Cross-sectional BSE images of ICE170 grains weathered in acid B for 220 days. (a) One ICE170 grain that shows cross-section through potential etch pits in the basalt glass (in white box). (b) Enlarged region from (a) with white arrows pointing to darker material in potential etch pits. (c) Context image with white box showing region enlarged in (d). (d) Enlarged region showing inside of grain with relatively unaltered plagioclase and basalt glass. Note that there is a very thin light-toned rind around much of the perimeter of the grain when viewed at higher magnification (a, b, d), which is due to charge buildup on the sample.

3.4.3.5 Basaltic glass in moderate pH acid

The outer surfaces of basaltic glass BAS101 grains altered in starting pH ~3 acid (acid B) for 220 days show no obvious alteration textures when viewed in SE images (Figure 3.12), unlike their counterparts altered in acid A. Additionally, there is no noticeable pitting on the grain surfaces as there was with ICE170 samples exposed to acid B.

When viewed in cross-section, the plagioclase phenocrysts crystal grain boundaries are sharp and unaltered, and the EDS point scans show no evidence for elemental change from the starting material. The lack of alteration rinds suggests that some dissolved phases like silica remained in solution and were removed from the system when the fluids were refreshed. Other dissolved phases may have also been deposited as easily soluble and surficial secondary phases that were removed upon rinsing of the sample. The light-toned region around the sample grains is a resulting of charging on the sample (Figures 3.13 a and b).

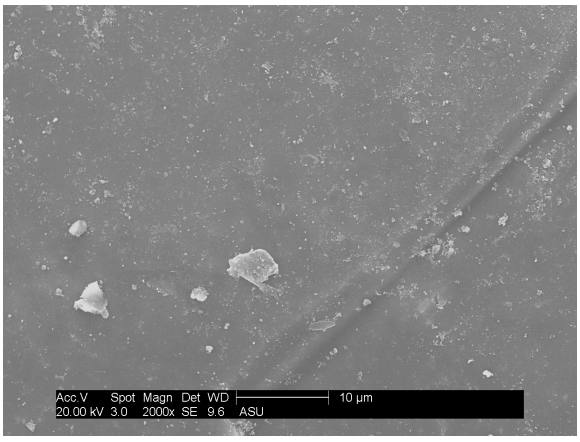

Figure 3.12. SE image of BAS101 grains weathered in acid B for 220 days. There are no noticeable etch pits, alteration phases, leached rinds, or deposited layers.

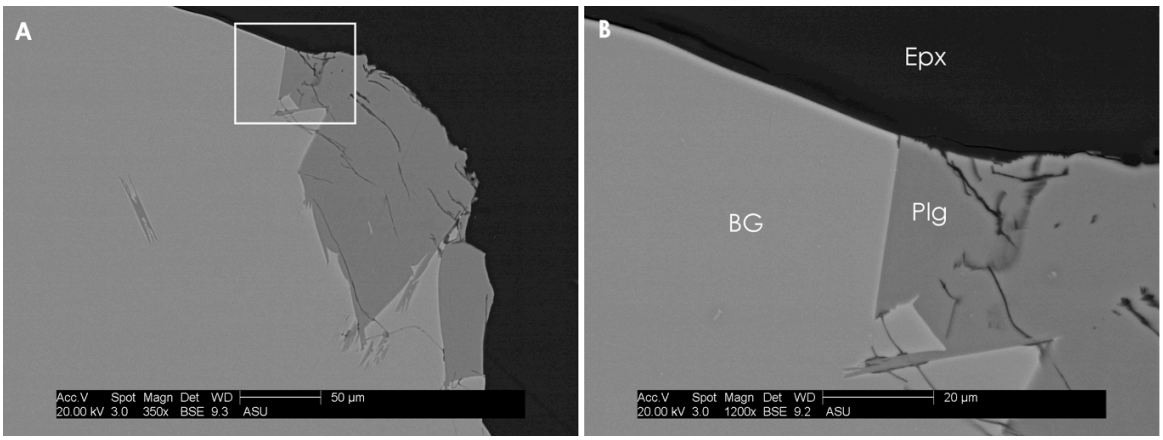

Figure 3.13. BSE images of BAS101 grains weathered in acid B for 220 days. Epx indicates epoxy, Plg indicates plagioclase, and BG indicates basalt glass. (a) is a context image of a cross-section of a grain, and the white box shows the region enlarged in (b). The interior is relatively unaltered, and there is a very thin light-toned rind around much of the perimeter of the grain when viewed at higher magnification (b).

3.5 Discussion

3.5.1 Effects of crystallinity on alteration texture and morphology

Crystal grain boundaries are effective pathways that enable fluid to infiltrate a sample [*Jonas et al.*, 2014]. Thus, low pH alteration fluids are able penetrate the interiors of the more crystalline samples (ICE170), developing patches of altered material throughout the sand-sized grains. The glass samples (BAS101 and BSB101), on the other hand, have fewer phenocrysts, and so there are fewer zones of weakness for the solution to penetrate. In the absence of crystal grain boundaries, the acid is forced to attack the perimeter of the grain, propagating inward through the conchoidal fracturing of the altered material as a result of volume change with phase change (Figure 3.9b). The volume change appears to be negative because the dark, silica-rich areas are slightly recessed from the unaltered

interior in Figure 3.9b. Thus, crystal grain boundaries allow for a more heterogeneous interior alteration, and fewer crystal grain boundaries promote the development of a continuous alteration layer.

The materials altered in the weaker (pH 3 acid) also show differences based on crystallinity. The partially glassy basalt (ICE170) samples develop etch pits on the surface of the grains, which indicate that some dissolution is taking place. The basalt glass grains, on the other hand, do not have any etch pits, and are relatively smooth. Etch pits easily form on crystallographically controlled surface features, such as defects [*Berner and Holdren*, 1977; *Berner*, 1978], which an amorphous, glassy surface might have fewer of. This topic is discussed in detail in the following section.

3.5.2 Effects of pH on alteration morphology

The differences between materials altered in low vs. moderate pH acid solutions are extreme. Materials exposed to moderate pH (~3) acid solutions show little sign of alteration to both the interior and exterior of the sample grains, and there is no indication of precipitated secondary phases, except in the TIR spectrum of the most crystalline sample (BAS205). These observations suggest that either the dissolved material remains in solution long enough to get flushed away as the acid baths are refreshed, or that precipitated phases are loosely bound to the grains so that they are easily removed as the samples are washed. On the other hand, materials exposed to low pH (~1) acid solutions exhibit alteration at the surface and throughout the grains, and have layers/regions of amorphous silica-rich phases indicating that the environment must be conducive for the retention or precipitation of amorphous silica.

While dissolution is surely taking place, none of the samples exposed to acid B

show evidence for major phase changes or alteration of large crystals in the BSE images or in the VNIR spectra. The only evidence for alteration is in the TIR spectra and in the etch pits visible on the surface of the ICE170 sample grains. The lack of residual material resembling a silica-rich "leached layer" suggests that the glass and minerals are mostly dissolving congruently and that the dissolved silica is transported away rather than being reprecipitated onto the grains. It should be noted that there is potentially some precipitated or residual material found in some of the etch pits on the surface of the ICE170 samples. The etch pits form in the basalt glass, and contain a very small amount of some phase that looks silica-rich, but is too small for EDS analysis. *Hu et al.* [2005] demonstrated that etch pits only form on a surface when ions are being dissolved stoichiometrically, supporting our hypothesis that these materials are undergoing congruent dissolution.

The TIR spectra of all materials exposed to acid B indicate some form of preferential dissolution. In a simple model of basalt dissolution, minerals with higher solubilities should dissolve first, and many silicates exhibit solubilities that are dependent on pH. At the starting pH of acid B (~3), the solubility is usually olivine > basalt glass > pyroxene ≈ plagioclase [*Hausrath et al.*, 2008]. Thus, olivine should dissolve the fastest, followed by glass, then pyroxene and plagioclase at similar rates. The TIR spectrum of BAS205 suggests that the sample preferentially lost basalt glass and oxides, which can be consistent with the simple dissolution model presented above. However, the TIR spectra of the other three samples model a preferential loss of pyroxene and plagioclase over olivine and basalt glass. Our companion paper hypothesizes that the preferential dissolution of pyroxene in the more glassy samples is driven by the generally smaller

grain size of pyroxene crystals (e.g., Pyx crystallites compared to Plg quench crystals in ICE170, Figure 3.11d), and so we do not see the same order of dissolution in the most crystalline sample (BAS205) because it contains large crystals of comparable size. Other properties that influence the dissolution rates of minerals include increased surface defect density, surface curvature, and the number of edges and corners per unit volume of the crystals [*Berner*, 1978]. It seems likely that these properties would be more prevalent in the plagioclase and pyroxene quench crystals in the more glassy samples than in the slowly formed equigranular crystals in the more crystalline basalt. Thus the preferential dissolution of minerals can also be related to grain size and geometry.

The basaltic materials exposed to acid A develop significant spectral and microscopic signs of alteration. VNIR and TIR spectra of all altered samples suggest an increase in hydrated amorphous silica-rich phases, but the glass samples are spectrally distinct from the more crystalline samples because the VNIR spectra have a concave upward slope (greater blue slope at shorter wavelengths) and the TIR spectra show no signs of the basalt precursor. SEM and EDS investigations of the glassy basalt and basalt glass samples confirm the presence of silica-rich secondary phases, and show that the basaltic glass samples have thick silica-rich layers while the more crystalline samples exhibit silica-rich zones throughout the grains. Thus, a highly acidic environment is more conducive for forming silica-enriched weathering products than a moderate pH environment.

When exposed to low pH (~1) acid solutions, the glassy basalt and basalt glass samples develop fractured terrain, honeycomb texture, altered glass, and silica-enriched regions and layers (Table 3.2). As mentioned in Section 3.4.3.3, the honeycomb texture

on the basaltic glass sample resembles similar textures found on feldspar crystals, which were hypothesized to form as coalescing etch pits [*Berner and Holdren*, 1977]. The presence of etch pits indicates congruent dissolution [*Hu et al.*, 2005], and so we assume that the honeycomb texture is suggesting the basalt glass is also undergoing congruent dissolution.

At very low pH, the order of solubility is usually basalt glass > olivine > plagioclase > pyroxene [*Hausrath et al.*, 2008]. At starting pH ~1, this simple model generally works when applied to our basalt glass sample (BAS101) in which we see the preferential alteration of glass over plagioclase phenocrysts in the BSE images as well as in the TIR spectral data. When applied to the more crystalline sample (ICE170), the model works in that plagioclase is preferentially lost relative to pyroxene as indicated by BSE imaging, and VNIR and TIR spectroscopy. Yet, BSE images clearly show that plagioclase is being preferentially lost relative to basalt glass. In general, ICE170 has more quench crystals than the basalt glass samples, and so we hypothesize that the dissolution order discrepancy is related to crystal grain size and geometry, as with the samples altered in acid B.

It should be noted that *Tosca et al.* [2004] found that highly acidic weathering of crystalline basalt favored deposition of sulfates and amorphous silica at a persistently acidic pH, while moderately acidic weathering released enough solutes to buffer the solution to higher pH and then precipitated iron oxides. However, neither ICE170 nor BAS101 altered in acid A developed evidence of sulfates, and neither of the samples exposed to acid B developed iron oxides. However, it is possible that these phases formed, but were removed when the grains were gently washed.

3.5.3 Effects of silica-rich alteration morphology on thermal-infrared spectra

In the mid-infrared, heterogeneous/discontinuous alteration and continuous alteration layers look very different. The more crystalline samples (ICE170) exposed to low pH (~1) acid solutions have heterogeneous perimeters consisting mostly of altered basalt glass, Si-enriched areas, and other primary minerals such as spinel. Correspondingly, the spectra appear as mixtures of high-silica phases (~1100 cm^{-1} and 465 cm^{-1} emissivity minima) and mafic minerals (~950 cm^{-1} emissivity feature), whereas the glass samples (BAS101) exposed to acid A develop thick (~10 – 100 μm) continuous rinds made of nearly pure silica that effectively mask any spectral signal from the underlying substrate. Additionally, the glass samples have a 1220 cm^{-1} spectral shoulder on the 1100 cm^{-1} Si-O stretching emission feature, whereas the more crystalline samples do not.

The spectral shape of altered ICE170 is very similar to that of crystalline basalt coated with very thin layers of colloidal silica [*Kraft et al.*, 2003]. Pure silica coatings ~1 μm thick on crystalline basalt have emission features associated with the silica coatings at ~1120 cm^{-1} and 470 cm^{-1}, and with the crystalline basalt at ~950 cm^{-1} (Figure 3.2) [*Kraft et al.*, 2003]. The silica emission features are shifted to slightly higher wavenumber than the same features in the altered ICE170 spectra, because the silica-rich areas in our samples are not pure silica and contain some impurities that depolymerize the structure. Neither the ICE170 nor the *Kraft et al.* [2003] samples with coatings < ~3 μm exhibit the 1220 cm^{-1} feature found in the glass samples and in other naturally altered basaltic samples [*Minitti et al.*, 2007].

On the other hand, the basalt glass grains (BAS101) altered in acid A solutions have TIR spectra that look very similar to crystalline basalt with silica coatings > ~ 6 μm

[*Kraft et al*., 2003] and naturally altered Hawaiian basalt glass samples with thick (10 – 70 μm) silica layers [*Minitti et al*., 2007]. All have TIR spectral features only associated with silica-rich phases with a shoulder at ~1220 cm^{-1}, and emissivity minima at ~1090 – 1120 cm^{-1} and 465 – 470 cm^{-1}. The exact positions of the features depend on the composition of the silica-rich phase.

TIR wavelength measurements generally sense the upper ~100 μm of material in a surface, and so the complete spectral obscuration of underlying basaltic materials with coatings/layers > ~3 μm and < 100 μm thick, indicates that the spectral absorption properties of silica can shift the sensing depth to shallower depths. We argue that thinner coatings or more heterogeneous silica-enrichment does not provide enough silica to cause this shift. It is important from a TIR remote sensing point of view, that relatively thin silica layers can cause the abundance of silica in a sample to be grossly over estimated compared to the bulk mineral abundance of the entire sample.

Similarly, we argue that the presence or absence of the 1220 cm^{-1} feature is related to the overall percentage of silica making up the outer surface of the sample. The 1220 cm^{-1} spectral feature is found in many silica-rich glasses and silica-rich amorphous alteration phases, and represents one of two states of the SiO_2 asymmetric stretching mode [*Minitti et al.,* 2007]. It is absent in the TIR spectra of basalt with silica coatings < ~3 μm thick [*Kraft et al*., 2003] and basalt with heterogeneous alteration. Additionally, *Crisp et al*. [1990] found that all three spectral features associated with silica-rich coatings/layers (~1090 – 1100 cm^{-1}, 465 cm^{-1}, and 1220 cm^{-1} shoulder features) are very common in spectra from lava flows over 50 years old, which presumably have well developed silica-rich coatings, yet flows that are only weeks old are missing the 1220 cm^{-1} shoulder

feature.

EDS measurements detected small concentrations of Al and Ca in the silica-enriched regions and layers in ICE170 and BAS101 samples exposed to acid A. This is consistent with the location of the Si-O stretching emission feature of these samples at ~1090 – 1100 cm^{-1}, which is shifted to lower wavenumber than that of opal-A at 1115 cm^{-1}, indicating that the silica layers/regions are less polymerized than opal. The degree of polymerization of a silicate glass or amorphous substance is a function of the number of shared, or bridging oxygens per network forming tetrahedral [*Henderson*, 2005; *Calas et al.*, 2006], which is affected the abundance of network modifying cations (e.g., Na^{+}, K^{+}, Mg^{2+}, and Ca^{2+}) and H_2O [*Henderson*, 2005; *Michalski et al.*, 2005; *Calas et al.*, 2006]. Network modifying cations and H_2O molecules cause a structure to depolymerize by forcing openings within the structure and creating charge imbalance which are neutralized with non-bridging oxygens (NBOs) [*Farnan et al.*, 1987]. Al^{3+} and Fe^{3+} substitution in network forming tetrahedron can also decrease polymerization due to longer bond distances as a result of the increased ionic radius relative to Si^{4+}. The substitution also introduces a charge imbalance that is neutralized with network modifying cations, which further depolymerizes the structure [*Henderson*, 2005; *Michalski et al.*, 2005; *Calas et al.*, 2006]. Thus, TIR and EDS measurements are consistent with a silica-rich phase that is less polymerized, and therefore, less pure, than opal-A.

3.5.4 Effects of silica-rich alteration morphology on visible to near-infrared spectra

The more crystalline samples (BAS205 and ICE170) exposed to acid A solutions exhibit visible and near-infrared spectral absorption bands that indicate a change in

mineralogy, predominantly the appearance of hydrated silica. The spectra do not exhibit any features that indicate alteration morphology. This is consistent with thermal-infrared spectra of the same samples, where the only indications of alteration are the appearance of secondary minerals in the spectral mixture analyses.

In contrast, both of the basalt glass samples altered in pH 1 acid solutions develop a strong concave-up slope (greater blue slope at shorter wavelengths) in the near-infrared. This shape has been attributed to leached rinds formed on natural glass samples during acid leaching [*Minitti et al*., 2007; *Horgan and Bell*, 2012; *Horgan et al*., submitted]. While the SEM results from this study confirm the presence of silica-enriched layers on the basalt glass samples, it is not certain that the layers are leached rinds, as will be discussed in Section 3.5.6.

In the visible and near-infrared, the basalt (BAS205) and glassy basalt (ICE170) samples exposed to acid B show no change in spectral shape, while the basaltic glass samples (BAS101 and BSB101) develop spectral features that are most consistent with an oxide coating [*Horgan et al*., submitted]. Yet, none of the samples show evidence for oxide coatings in the mid-infrared. This discrepancy could be a result of the wavelength of measurement. Very thin (sub-micron to a few microns thick) oxide coating would be detected with the visible and near infrared wavelengths, which penetrate only the very surface of a sample, whereas a similar thickness of coating would be invisible to the longer mid-infrared wavelengths. However, it should be noted that the BSE images show no indication of oxide coatings on any of the samples.

3.5.5 Comparison to other studies

The fractured textures that we see on the basaltic glass (BAS101) surfaces after exposure to pH 1 acid solutions look similar to what were described in previous experiments as leached layers on basaltic glass [*Tosca et al.*, 2004], plagioclase [*Schott et al.*, 2009], and wollastonite [*Schott et al.*, 2012]. *Gislason and Oelkers* [2003] also noticed similar fractures on altered basalt glass and suggested that this texture was due to 1) preferential dissolution along weak areas incurred when the glass was initially cooling; 2) effects of drying the grains after the experiments and/or 3) spalling of an altered layer precipitated on the surface. In this study, the fractured textures appear on the angular sides of the grains. Therefore, it is likely that this texture represents preferential dissolution along weak areas incurred when the glass was being ground to sand sized particles.

The basalt glass (BAS101 and BSB101) and glassy basalt (ICE170) samples exposed to acid A solutions, look spectrally similar to some of the naturally altered Hawaiian basalt glass samples studied by *Minitti et al.* [2007]. The natural samples most spectrally similar to our laboratory samples in the thermal-infrared all have continuous, silica-rich layers, with marble-texture, capped with thin, discontinuous Ti- and Fe- oxides and S-rich phases. The silica-rich layers on the natural samples appear similar in porosity to the silica-enriched regions/layer our laboratory samples, but none have the conchoidal fracturing found in the layers on our basalt glass samples. Additionally, none of our samples have evidence for oxide or S-rich capping layers, which could have been washed away during sample processing. Regardless, the spectral similarity suggests that thin oxide and S-rich capping layers must have very little effect on the thermal-infrared spectrum.

Our altered basalt glass samples are most spectrally consistent with a sample acquired from a basalt flow at Kilauea (KW) and from the Mauna Iki flow field along the Kilauea SW rift zone (MIO). BSE imagery shows that these samples have thick (10 – 35 μm and 20 – 80 μm, respectively) silica-rich layers. Whereas, the glassy basalt (ICE170) samples exposed to acid A look most spectrally similar in the thermal-infrared to a naturally altered sample collected from a lava channel at Mauna Ulu (MUO), which has much thinner (~2 – 3 μm) silica-rich layers [*Minitti et al.*, 2007]. This observation supports our hypothesis that thin layers and heterogeneous alteration spectra combine more linearly with the substrate spectra than thicker alteration layers, so that both are visible in the resulting thermal-infrared spectral shape.

The naturally altered Hawaiian basalt glass samples most similar to our laboratory samples in the thermal-infrared are not necessarily the samples most similar in the VNIR. This is most certainly a result of differences in alteration morphology, sensing depth, and the variety of thin surficial oxide and S-rich coatings on the natural samples that are not seen in our laboratory samples. None of the naturally altered glass samples look similar in the VNIR to our more crystalline samples altered in acid A. This is predominantly because all of the natural basalt glass samples have coatings/layers that introduce a blue slope to the VNIR spectra, and our more crystalline samples do not have coatings/layers. Our glass samples (BAS101 and BSB101) altered in acid A do exhibit spectral characteristics of coatings (blue slope), and so they appear more similar spectrally to the naturally altered basalt glass samples. Additionally, a good number of the VNIR spectra of naturally altered basalt glass samples have a concave up slope that is similar to what we see in the laboratory altered basalt glass grain samples.

3.5.6 Possible formation mechanisms for silica-enriched layers and zones

Here we discuss possible formation mechanisms based on spectral, chemical and morphologic observations. None of the silica-enriched samples show layers that appear to have been accreted, and none contain detritus or other mineral fragments. This allows us to eliminate a silica coating formation mechanism, as defined in Section 3.2.1. Additionally, the silica-rich phases appear to be amorphous according to the thermal-infrared spectra, so we can also eliminate mineral replacement. Thus, the surface altered layers and zones must either be a result of leaching or dissolution-reprecipitation.

The Si-enriched regions in ICE170 samples maintain the space and morphologic characteristics of the plagioclase quench crystals, which indicates that the phase change is very similar to replacement, though with an amorphous phase, and is therefore a result of dissolution-reprecipitation mechanisms. The increased fractures and porosity results from both the molar volume differences between parent and product as well as the relative solubilities of the phases in the specific fluid at the interface [*Pollok et al.*, 2011]. The composition of the silica-enriched regions is also consistent with dissolution-reprecipitation.

The thickness of the silica-enriched layers found on the basalt glass samples (BAS101) altered in pH 1 acid solutions are much greater than the thicknesses of reported leached layers (50 – 200 nm, *Eick et al.* [1996]; 1 – 2 μm, *Berger et al.* [1987]; 2 - 4 μm, *Thorseth et al*. [1991]; 5 μm, *Guy and Schott* [1989]; 10 μm, *Tosca et al*. [2004]), and are much more consistent with thicknesses of precipitated layers [*Chemtob and Rossman*, 2014], indicating that they were more likely formed via precipitation. The layers are highly porous and fractured, which frequently forms as a result of volumetric changes

during phase changes [*Pollok et al.*, 2011; *Chemtob and Rossman*, 2014]. The plagioclase crystal in figure 3.9a is starting to be substituted with silica, and so we can assume that some dissolution-reprecipitation is occurring. Additionally, the honeycomb texture on the surface of BAS101 grains would indicate congruent dissolution if it formed as similar textures do when etch pits coalesce. Congruent dissolution would also point toward a dissolution-reprecipitation mechanism. Compositional EDS point scan data are also supportive of dissolution-reprecipitation since the composition of the Si-enriched layers is nearly pure silica, with minimal Al and Ca.

Therefore, we conclude that the silica-enrichment of basaltic materials exposed to low pH acid solutions results from dissolution-reprecipitation mechanisms, and that silica-rich precipitated layers form selectively on basalt glass. Our conclusions are consistent with those of *Chemtob and Rossman* [2014] who observed natural silica-rich layers on Hawaiian basalt materials and determined that silica-rich alteration layers formed selectively on surfaces with glassy surface layers. Additionally, they concluded that the layers formed through the acidic dissolution of near-surface basalt, followed by in situ precipitation of amorphous silica.

3.5.7 Implications for Mars

Any phase proposed to exist on the Martian surface in great abundance (> ~5 - 15%) [*Christensen et al.*, 2001b] must agree with both near- and mid-infrared datasets. Large regions of the northern lowland plains of Mars, including Siton Undae and much of Acidalia and Utopia Planitiae, have near-infrared spectral characteristics consistent with basalt glass altered in very strong acid (pH 1) [*Horgan and Bell*, 2012; *Horgan et al.*, submitted]. On the global scale, these same regions are found to contain high abundances

of high silica phases (15 – 20%) [*Bandfield*, 2002]. Basalt glass altered at pH 1 has a very strong silica spectral signature in the mid-infrared, which initially makes it consistent with spectral data from the Martian surface. Since only very low pH fluids (pH < 3) are capable of producing silica-enriched layers and/or zones that are significant enough to contribute to the mid-infrared spectrum, any alteration of primary basaltic rock in these regions must have been the result of interactions with strongly acidic fluids.

Our companion paper demonstrated that the thermal-infrared spectra of basalt glasses altered in acid A are modeled with ~65 – 70% high silica phases [*Horgan et al*., submitted], which are abundances far too high to be consistent with modeled abundances for the northern lowland plains. This suggests that the surface is actually a mixture of silica-rich alteration layers on basalt glass and primary phases, an interpretation that is consistent with previous mapping studies from the northern polar region [*Tanaka et al.*, 2008; *Horgan and Bell*, 2012].

We do not think that, given enough time, basalt glass exposure to more moderate acid fluids (~pH 3) would eventually attain the same level of alteration as that observed at lower pH, because there is little evidence for silica-rich phase precipitation on our samples even after 220 days of exposure to acid. This suggests that large regions on Mars, particularly in the northern polar sand seas, are consistent with alteration by very acidic fluids. We propose that fluids derived from ice or snowmelt at low water/rock ratios are capable of obtaining the acidity needed to form alteration layers on basalt glass.

In summary, we find that large regions of the Martian surface including Siton Undae and much of Acidalia and Utopia Planitiae are spectrally consistent with the alteration of basalt glass in a low pH environment in both the VNIR and thermal-infrared data, but are

not consistent with crystalline basalt altered in low pH fluids. Thus, it is highly likely that some amount of explosive volcanism has taken place on the Martian surface, and the deposits were later altered at low water/rock ratios with highly acidic fluids. Detailed thermal-infrared analysis of the northern polar region using the spectra of acid-altered basaltic materials from *Horgan et al*. (submitted) would help support this hypothesis.

3.6 Conclusions

- Alteration morphology is strongly controlled by pH of alteration solution and texture of starting material
- Only pH < 3 acid is strong enough to create silica-enriched layers/zones in basaltic materials that are detectable in the near-infrared or thermal-infrared
- Silica-enriched layers/zones appear to result from a dissolution-reprecipitation mechanism
- Crystal grain boundaries provide pathways for fluid to enter the interior of a grain, creating patchy alteration throughout the particle
- Less crystalline material has fewer pathways for the fluid to penetrate along, and so alteration is restricted to the exterior of the grain, creating a thick surface altered layer around the particle
- Grains with continuous surface altered layers enriched in silica have thermal-infrared spectra dominated by an amorphous silica spectral shape, while grains with patchy alteration have thermal-infrared spectra that show elevated silica content when compared to the starting material
- Only basalt glass samples exposed to low pH fluids (~1) have VNIR and thermal-infrared spectra that are consistent with the low-albedo northern lowland regions

on Mars

- Explosive volcanism likely took place, creating volcanic glass deposits that were later altered in low water:rock ratios by highly acidic fluids

CHAPTER 4

NEW INSIGHT INTO TES SURFACE TYPE 2 ORIGIN AND COMPOSITION

4.1. Introduction

A wide variety of element and mineral mapping techniques have been used to study the composition of low albedo regions of Mars. These surfaces are largely some combination of the primary volcanic minerals plagioclase, orthopyroxene, clinopyroxene and olivine, as well as one or more high-silica phases such as volcanic glass, zeolites, secondary silica, and/or poorly crystalline silicates [e.g., *Bell*, 2008, and references therein]. The majority of previous compositional mapping studies have focused on the regional distribution of minerals in comparison to geographic and geologic setting, surface age, and other surface properties [*Hamilton et al.*, 2001; *Bandfield*, 2002; *Rogers and Christensen*, 2007; *Koeppen and Hamilton*, 2008]. Recent work by *Rogers and Hamilton* [2015] has investigated the spatial distribution of lithologies or mineral assemblages, which is important for determining the processes controlling surface evolution. In this study, fundamental principles of vibrational spectroscopy are applied to data from the Mars Global Surveyor (MGS) Thermal Emission Spectrometer (TES) instrument to calculate spectral parameters that are mapped across the Martian surface at a spatial scale of 4 pixels per degree (ppd). These parameters yield constraints on the chemical composition and mineralogical complexity of the surface.

The compositions of low-albedo regions on Mars have been studied and debated for decades [e.g., *Singer*, 1982; *Soderblom*, 1992; *Bell et al.*, 1997; *Christensen*, 1998], especially with the introduction of data from the TES [*Christensen et al.*, 1992], Observatoire pour la Minéralogie, l'Eau, les Glaces et l'Activité (OMEGA) [*Bibring et*

al., 2004] and Compact Reconnaissance Imaging Spectrometer for Mars (CRISM) [*Murchie et al.*, 2007] instruments. *Bandfield* [2002] used TES data to define two surface spectral types: Surface Type 1 consistent with basalt, and Surface Type 2 initially interpreted as basaltic andesite to andesite. The idea that large regions of evolved magma could exist on the Martian surface without evidence for subduction zones or plate tectonics sparked debate over whether Surface Type 2 was indeed primary, or whether the higher silica content modeled in the spectra could be attributed to alteration products with similar spectral features [*Wyatt and McSween*, 2002].

Rogers et al. [2007] further subdivided Surface Type 1 and Surface Type 2 surfaces into eleven distinct and spatially contiguous regions based on more detailed spectral analyses. This mapping investigation revealed that most of Surface Type 2 was found in the northern lowlands of Mars, interpreted as a catchment for valley networks and outflow channels, where aqueous alteration could be possible. However, there were also high abundances of the Surface Type 2 spectral shape in parts of the southern highlands and in Solis Planum, where a primary surface could be equally likely. The spatial distribution and geologic context of each location led *Rogers et al.* [2007] and *Rogers and Christensen* [2007] to conclude that a single process alone could not explain Surface Type 2.

The source of the high-silica phases modeled in Surface Type 2 spectra has been the focus of numerous investigations. To date, most of these studies have used one of two methods: 1) they derive mineral abundance maps using thermal-infrared datasets and a spectral library [e.g., *Bandfield*, 2002; *Wyatt and McSween*, 2002; *Rogers and Christensen*, 2007; *Rogers et al.*, 2007], or 2) they study the properties of a specific

alteration phase and determine the likelihood of it existing on the surface of Mars by comparing it to data from the surface [e.g., *Kraft et al.*, 2003; *Michalski et al.,* 2003, 2005*; Poulet et al.*, 2005; *Minitti et al.*, 2007; *Milliken et al.*, 2008; *Horgan et al.*, 2009; *Ehlmann et al.*, 2012; *Rampe et al.*, 2012; *Horgan et al*., submitted]. Both these techniques are limited in that the modeling relies on a previously existing spectral library that may (or may not) contain the specific phases that are actually present on the surface. Furthermore, most mineralogical studies using TES data have ignored the northern polar region of Mars because of low surface temperatures, which decrease the signal to noise ratio of the TIR data and introduce high-frequency noise features that complicate spectral deconvolution techniques. Nonetheless, *Bandfield* [2002] was able to detect some of the highest abundances of high-silica phases on the planet within the northern polar region, and visible and near infrared (VNIR) investigations there have identified strong sulfate signatures as well as spectral features similar to leached rinds on iron-bearing glass. Taken together, these observations suggest this region is worthy of additional study [*Langevin*, 2005; *Fishbaugh et al.*, 2007; *Horgan et al.*, 2009; *Horgan and Bell*, 2012]. Thus, it is useful to develop an alternative spectral analysis technique that is independent of spectral libraries and is less sensitive to low radiance signals from cold surfaces.

A curve-fitting technique, commonly used in Raman [e.g., *Mysen et al.*, 1982] and gamma-ray spectral analyses [e.g., *Helmer et al.*, 1967], does not require the use of a spectral library, and has not yet been applied to thermal emission spectra of the Martian surface. This technique fits Lorentzian or Gaussian curves to absorption features, and then examines the following spectral parameters: peak center location, peak width, and peak amplitude. These parameters are functions of the composition, the structure, and the

physical state of the phases being measured. Peak center location varies with the major mineral groups present at the surface, and can also vary with SiO_2 content, and the degree of polymerization of silicates. Peak width is used as a proxy for the mineralogical complexity of the surface. Peak amplitude changes with the physical state of the surface (e.g., grain size, porosity). The combination of these parameters yields insight into the regional compositional variability of Surface Type 2 and allows inferences about geologic processes that altered large portions of the Martian crust in the past.

4.2. Background

4.2.1 Fundamentals of TIR spectroscopy

Solids are made up of atoms attached to each other by bonds so that the atoms within the solid cannot move independently. Instead, solids have lattice vibrations, or collective modes, that can be thought of as waves propagating through the material. Collective vibrational modes can accept energy only in discrete amounts, and these quanta of energy are known as phonons [e.g., *Cahill and Pohl*, 1988]. The phonon frequencies in geologic solids depend primarily on the atomic structure of the material [*Lyon*, 1965; *Farmer*, 1974; *Christensen et al.*, 1992]. In this sense, the atoms within a solid can be approximated as masses on springs and Hooke's Law can approximate the frequency at which these vibrations occur:

$$\nu = 1/2\pi * \sqrt{(k/m)}$$

Where ν is the frequency of vibration, k is the force constant of the spring, and m is the mass. As the force constant, or bond strength, increases the vibrational frequency also increases. Likewise, as the atomic mass increases, the vibrational frequency decreases. Thus, the frequency of vibration can be used to differentiate between not only different

mineral groups (e.g. silicates, carbonates, sulfates, oxides, and phosphates), but also between minerals within each group. Most geologic materials have fundamental vibrational frequencies that occur in the thermal-infrared (TIR) region of the electromagnetic spectrum, between ~5 – 100 μm (~100 – 2000 cm^{-1}) [e.g., *Launer*, 1952; *Lyon*, 1965; *Salisbury and Walter*, 1989].

The different fundamental vibration modes for solids include stretching, both asymmetric and symmetric, and bending. The magnitude of the frequency of the vibration associated with these modes occur as follows: asymmetric stretching > symmetric stretching > bending [*Salisbury and Walter*, 1987]. For example, the most intense spectral features associated with silicate minerals occur between 1176 – 833 cm^{-1} (8.5 – 12 μm), and are related to asymmetric Si-O stretching [*Salisbury and Walter*, 1987]. This study is primarily interested in identifying silicate minerals, and so we focus on this asymmetric Si-O stretching feature. All vibrational modes are designated by ν and a subscript that denotes the type of mode. For example, asymmetric stretching is noted as ν_3 [*Herzberg,* 1945]. Therefore, we will abbreviate the asymmetric Si-O stretching feature as SiO ν_3.

While TIR spectral analysis is a very powerful remote sensing tool, there are important caveats to keep in mind when interpreting TIR data. First, in order to be detected by the TES instrument, individual phases must be present in abundances greater than ~ 5-15% depending on the mineral group [*Feely and Christensen*, 1999; *Christensen et al.*, 2001b]. Second, it is assumed that the minerals present in a surface combine linearly so that the energy radiated from each component is proportional to its areal percentage [e.g., *Lyon*, 1965; *Ramsey and Christensen*, 1998]. This assumption has been

shown to not be true when dealing with fine particle sizes (with diameters smaller than the wavelength) and thin silica-rich layers/coatings on rock surfaces and particles [*Kraft et al.*, 2003; *Minitti et al.*, 2007]. Lastly, one must take into account the sampling depth of TIR measurements, usually 10s of micrometers, but which can change based on the optical properties of the material being measured. For example, silica-rich layers only a few micrometers thick are capable of obscuring the SiO ν_3 feature from the substrate below [*Kraft et al.*, 2003; *Minitti et al.*, 2007], because of the high absorption coefficients at these wavenumber [*Clark*, 1999].

One major assumption of this current study is that the SiO ν_3 vibration is the sole contributor to the spectrum between 825 – 1300 cm^{-1}. This is generally a safe assumption unless sulfates are present, because some sulfate minerals have fundamental absorption features at wavelengths that overlap with the Si-O stretching region (between ~1050 – 1250 cm^{-1}; for example, gypsum in Figure 4.1). A sulfate spectrum can effectively shift the broad surface emissivity feature toward higher wavenumber when present in abundances over the detection limit.

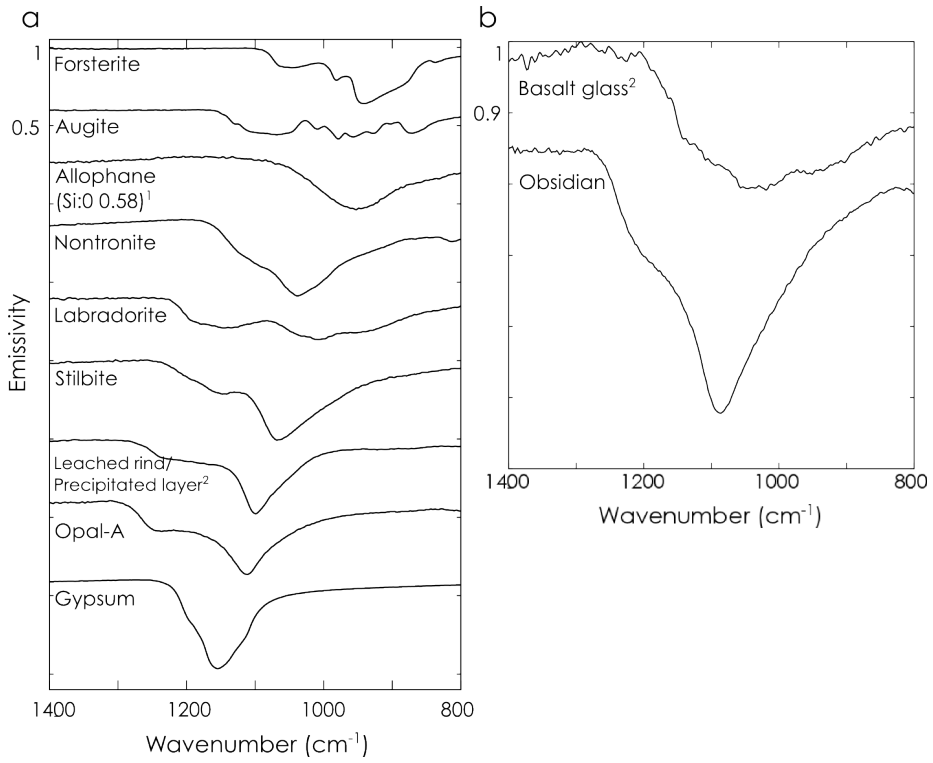

Figure 4.1. TIR spectral plot of many of the phases discussed in this study, showing absorption features in the main SiO ν_3 wavenumber range for (a) minerals and (b) volcanic glasses. Spectral contrast is normalized and spectra are offset for clarity.

[1] *Rampe et al.* [2012]
[2] *Horgan et al*. [submitted]

4.2.2 Degree and range of polymerization in minerals and rocks

The polymerization of a silicate refers to the degree of interconnectedness of the network-forming tetrahedra. A tetrahedron consists of a network-forming cation (e.g., Si^{4+}, Al^{3+}, Fe^{3+}) bonded to four oxygen atoms, which make up the corners of the tetrahedron. Each "corner" oxygen atom can then be bonded to either another network-forming cation, which increases the degree of polymerization of the structure, or to a network-modifying cation (e.g., Na^{+}, K^{+}, Ca^{2+},Al^{3+}), which decreases the degree of polymerization [*Farnan et al.*, 1987; *Henderson*, 2005; *Michalski et al.*, 2005; *Calas et al.*, 2006]. Therefore, the degree of polymerization (Q^n) can be classified according to the number of oxygen atoms that each tetrahedron shares in a silicate structure (n). Nesosilicates, such as olivine, have no shared oxygen atoms and so they have a Q^0 structure; chain silicates, like pyroxenes, have a Q^2 structure; phyllosilicates (e.g., clay and mica minerals) have a Q^3 structure; tectosilicates (e.g., quartz, feldspars and zeolites) have a Q^4 structure [*Mysen et al.*, 1982; *White and Minser*, 1984]. Numerous studies have determined how the SiO ν_3 wavenumber position shifts with the degree of polymerization of silicate minerals (Figure 4.2) [e.g., *Launer*, 1952; *Lyon*, 1965]. In general, Q^0 silicates have SiO ν_3 features between ~ 820 – 1040 cm^{-1}, Q^2 silicates have SiO ν_3 features between ~ 860 – 1090 cm^{-1}, Q^3 silicates have SiO ν_3 features between ~ 960 – 1075 cm^{-1}, and Q^4 silicates have SiO ν_3 features between ~ 990 – 1110 cm^{-1}. Thus, the wavenumber position of the SiO ν_3 feature increases with increasing polymerization. However, this explanation is somewhat oversimplified because the wavenumber position also depends on other lattice parameters such as bond length. When Al^{3+} substitutes for Si^{4+} in tetrahedral coordination, the bond distances are increased due to the larger ionic radius of

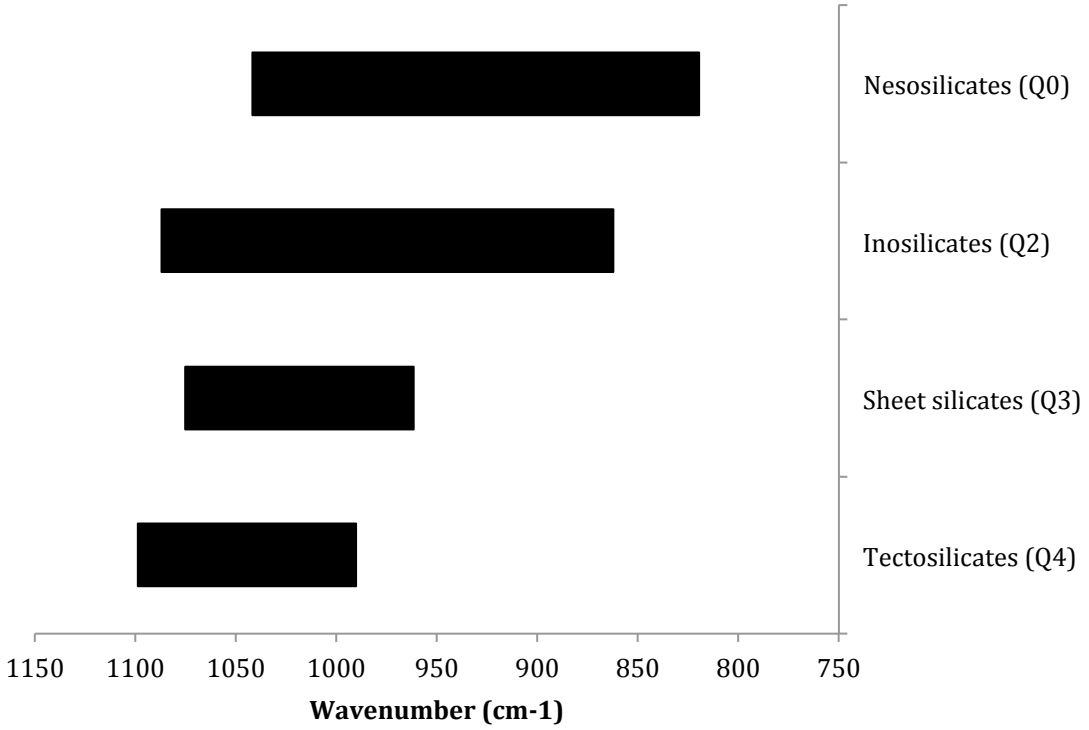

Figure 4.2. Wavenumber regions of SiO ν_3 features for the different silicate structures. Adapted from *Launer* [1952].

Al^{3+} [*Zotov*, 2003]. The longer bond distances cause the spectral features to shift to lower wavenumber. Thus, some framework silicates with high Al/Si ratios can have lower wavenumber spectral features than less polymerized silicates, as is the case for feldspars.

The range of polymerization in a rock is related to the number of different components in the rock. Most crystalline igneous rocks contain silicate minerals with a wide range of polymerizations, and so they tend to have broad spectral shapes within the Si-O stretching region. For example, basalt is generally made of some combination of orthopyroxene, clinopyroxene, plagioclase and sometimes olivine, and so the range of polymerization varies from Q^0 to Q^4. Igneous glasses lack minerals and so the "range" of polymerization is more directly linked to the chemistry of the glass, instead of a range of crystal structures. The greater the number of network modifying cations (e.g., Na^+, Mg^{2+}), the greater the range of potential polymerizations within a glass structure [*Henderson*, 2005; *Michalski et al.*, 2005; *Calas et al.*, 2006]. A glass made of nearly pure silica would have most of the tetrahedra linked and would therefore have fewer potential degrees of polymerization within the glass structure (~Q^4). Thus, within the Si-O stretching region, basalt glass has a broad spectral shape centered at lower wavenumber while the same feature for obsidian is narrower and is positioned at higher wavenumber (Figure 4.1b).

Secondary minerals and surfaces are more complex, but in general, the same principle holds true that the degree of polymerization increases with increasing silica linkage and Si content. For example, clay mineral structures are composed of octahedral (O) sheets bonded to tetrahedral (T) sheets, and can also contain interlayer cations that help maintain charge neutrality. Tetrahedral sheets have the composition T_2O_5 where T =

Si, Al, Fe^{3+}, and each tetrahedron is linked to three others by sharing their base corners. The remaining apical tetrahedron corners are then bonded to the O sheet where the O cation = e.g., Mg^{2+}, Al^{3+}, Fe^{2+}, Fe^{3+} [*Bailey*, 1966]. The TO sheet structure differs from that of pure opal (SiO_2), which is essentially comprised of randomly oriented clusters of silica framework structures and water molecules. Thus, despite the fact that opal-A does not have long-range order like the clay minerals, the opal-A structure still has a higher degree of polymerization (Q^4) than a clay mineral (Q^3), because all of the silica tetrahedra are linked to one another. Thus, the opal-A SiO ν_3 feature occurs at a higher wavenumber than for the clay minerals (Figure 4.1a).

Chemically altered rocks usually contain a mixture of primary and secondary minerals, and so most chemically altered surfaces should have a wider range of polymerization and exhibit broad emission features in the Si-O stretching region. An important exception occurs when silica-rich coatings/alteration layers are present. Even when these are very thin (a few micrometers), they tend to dominate the TIR spectral signature [*Kraft*, 2003; *Minitti et al.*, 2007; *Horgan et al.*, submitted; *Smith et al.*, submitted] masking the more diverse chemistry or mineralogy of the underlying substrate. Thus, silica-rich coatings/alteration layers can cause the SiO ν_3 feature to narrow, as illustrated in the "Leached rind/precipitated layer" spectrum in Figure 4.1a.

4.2.3 Aqueous alteration and Surface Type 2

A number of secondary, high-silica phases have been found to exhibit spectral features similar to the silica-rich volcanic glass used to model the Surface Type 2 spectrum. The proposed secondary phase(s) include: clay minerals [*Wyatt and McSween*, 2002], silica-rich rock coatings [*Kraft et al.*, 2003], zeolites [*Ruff*, 2003, 2004],

allophane/allophanic substances [*Rampe et al.*, 2012], acid-leached rinds/precipitated layers on iron-bearing glass [*Minitti et al.*, 2007; *Horgan and Bell*, 2012; *Horgan et al.*, submitted; *Smith et al.*, submitted], and anhydrous oxidative weathering rinds [*Salvatore et al.*, 2013].

On Earth, clay minerals are common alteration products formed through the interaction of water with Si-Al bearing primary minerals (such as feldspars). They can form in a wide range of pH and temperature conditions [e.g., *Colman*, 1982; *Eggleton et al.*, 1987; *Nesbitt and Wilson*, 1992; *Thorn et al.*, 2001]. Thus, clay minerals are a viable component of an aqueously altered basaltic Martian surface. The SiO ν_3 feature of the average Surface Type 2 spectrum is fit relatively well with clay minerals [*Wyatt and McSween*, 2002], which have SiO ν_3 emission features between ~960 – 1075 cm^{-1} (Figure 4.2). However, in-depth spectral analyses have shown that most Surface Type 2 regions lack the lower wavenumber feature (~530 cm^{-1}) present in smectite clay mineral spectra [*Ruff and Christensen*, 2007]. *Michalski et al.* [2005] argued that the SiO ν_3 feature for clays is actually at a lower wavenumber than that for most Surface Type 2 spectra. Additionally, hydration features found in all crystalline clay minerals are lacking in visible and near-infrared (VNIR) spectral measurements of Surface Type 2 regions [*Mustard et al.*, 2005]. Therefore, crystalline clay minerals are not likely components of Surface Type 2.

Silica rock coatings are sedimentary deposits of noncrystalline silica-rich material accreted as layers onto rock or grain surfaces [*Dorn*, 1998]. The silica-rich phase forms via precipitation from a bulk solution that is derived from an external source. The bulk solution can come from dissolved silicate dust particles, or from a source that is

millimeters to meters away [*Dorn*, 1998]. Si is highly mobile during near-surface alteration of basaltic rocks under a wide variety of temperature, pressure, and fluid conditions [*McLennan*, 2003]. The free silica can easily be precipitated as coatings [*Kraft et al.*, 2003]. Silica coatings are found on rocks in a wide variety of climate conditions on Earth, including: lava flows in the high deserts on Hawaiian volcanoes [e.g., *Curtiss et al.*, 1985; *Crisp et al.*, 1990; *Minitti et al.*, 2007; *Seelos et al.*, 2010; *Chemtob and Rossman*, 2014], glacial and subglacial settings [e.g., *Hallet*, 1975; *Peterson and Morseby*, 1979], in arctic climates [*Dixon and Thorn*, 2005], and in Antarctica [*Weed and Ackert*, 1986; *Weed and Norton*, 1991; *Matsuoka*, 1995]. Rocks at the Mars Pathfinder landing site are hypothesized to have silica coatings because they were noted to have ‘‘glass-like,’’ forward-scattering surfaces [*Johnson et al.*, 1999] and high silica and water contents [*Foley*, 2003]. Silica coatings are rarely pure opaline silica, and generally contain some small amount (~10 %) of Fe, Al, or mineral detritus [*Dorn*, 1998]. As is the case for feldspars, the substitution of Al^{3+} and Fe^{3+} for Si^{4+} in natural silica coatings increases bond lengths so that the SiO ν_3 emission features appear at lower wavenumber (~1010 – 1250 cm^{-1}; Figure 4.3) than for materials with similar structures (~Q^4), such as opal-A (~1015 – 1250 cm^{-1}; Figure 4.3) [*Minitti et al.*, 2007]. Even thin coatings (>10 μm thick) are known to obscure basalt substrates such that the effect on IR spectra is to make the rock appear more polymerized than it actually is [e.g., *Kraft et al.*, 2003; *Minitti et al.*, 2007].

Acid leaching is a form of silicate dissolution thought to occur at low pH through the ion exchange of lower valence, network-modifying cations for protons. The preferential release of cations leaves behind a relatively silica-rich tetrahedral network to

form noncrystalline "leached rinds" [*Crovisier et al.*, 1987; *Casey et al.*, 1989a, 1989b; *Guy and Schott*, 1989; *Petit et al.*, 1989, 1990; *Thorseth et al.*, 1991] that can later be restructured [*Paces*, 1973; *Casey and Bunker*, 1990; *Casey et al.*, 1993; *Banfield et al.*, 1995; *Schweda et al.*, 1997; *Tsomaia et al.*, 2003]. Recent investigations have found evidence contrary to this simplified view of the leaching hypothesis, and argue that noncrystalline silica-rich layers form through the complete dissolution of the rock at a thin interfacial boundary followed by the reprecipitation of noncrystalline silica [*Putnis and Putnis*, 2007; *Hellmann et al.*, 2012; *Ruiz-Agudo et al.*, 2014]. Regardless of formation mechanism, acid-leached rinds/precipitation layers normally contain small amounts of Fe^{3+} and Al^{3+}, and they are structurally and spectrally very similar to silica coatings [*Kraft et al.*, 2003; *Minitti et al.*, 2007; *Horgan et al*., submitted; *Smith et al*., submitted]. Theoretically, the main difference between acid-leached rinds/surface altered layers and silica coatings is that the silica in rinds comes from the rock or surface being altered, so that the silica source is internally derived, whereas the silica in silica coatings is externally derived. To date, there is no way of discerning between coatings, leached rinds, and precipitated layers using TIR spectral data. No TIR spectral studies of Mars have included either coatings or leached rinds/precipitated layers in the spectral endmember libraries.

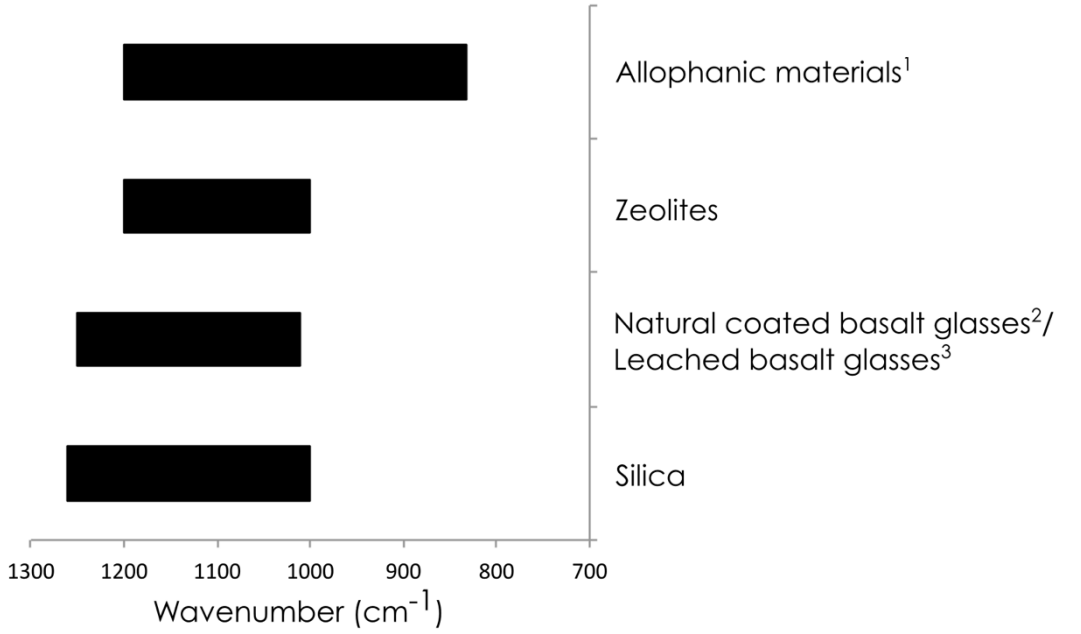

Figure 4.3. Wavenumber regions of SiO ν_3 features for the different alteration products discussed in section 4.2.3.

[1]*Rampe et al.* [2012]
[2]*Minitti et al.* [2007]
[3]*Horgan et al.* [submitted]

Zeolites are crystalline framework (Q^4) aluminosilicates commonly formed through the chemical weathering of volcanic glass under alkaline conditions at temperatures <200°C [e.g., *Zelazny and Calhoun*, 1977; *Ming and Boettinger*, 2001]. Zeolites are common components of volcanic soils indicating pedogenic origins, but can also be found in saline/alkaline lakes, deep-sea sediments, and hydrothermal systems [*Hay and Sheppard*, 2001]. The different zeolite compositions have relatively narrow SiO ν_3 features positioned between ~1000 – 1200 cm^{-1} (Figure 4.3) [*Zelazny and Calhoun*, 1977; *Ruff*, 2004], and some have TIR spectra that are similar to volcanic glass, the initial phase used to model the high-silica component of Surface Type 2 [*Ruff*, 2004]. However, there is no VNIR evidence for widespread crystalline zeolite minerals in Surface Type 2 surfaces, and so their presence is still debated.

Allophane is an important aluminosilicate component in mildly acidic to neutral (pH ~ 5 – 7) volcanic soils and forms through the interaction of water with volcanic ash and/or glass [*Wada*, 1977]. Allophane is a term used to describe a series of noncrystalline hydrous aluminosilicate clays that are characterized by short-range order and the predominance of Si-O-Al bonds [*Wada*, 1987]. Allophane, $1.0 - 2.0SiO_2 \cdot Al_2O_3 \cdot 2.5 - 3.0H_2O$, can range from being Si-rich (Al/Si ratio ~0.5) to Al-rich (Al/Si ratio ~1) [*Colman*, 1982; *Wada*, 1987] and the structure is thought to be hollow spherules with walls made of one (Al-O, OH) octahedral sheet and one (Si, Al-O, OH) tetrahedral sheet [*Wada*, 1987]. When allophane is Si-rich, the structure can have a polymerization similar to sheet silicates (Q^3) and has SiO ν_3 features between ~1000 – 1200 cm^{-1} [*Levard et al.*, 2012; *Rampe et al.*, 2012], whereas Al-rich allophane spectra are dominated by Al-O-Si features, which occur at lower wavenumber between ~830 – 1100 cm^{-1} (Figure 4.3)

[*Levard et al.*, 2012; *Rampe et al.*, 2012].

Weathering rinds formed through anhydrous oxidative alteration have also been shown to create spectral effects similar to those exhibited by silica-rich rinds/layers formed through aqueous alteration. *Salvatore et al.* [2013] studied the interiors and exteriors of dolerite rock samples from Beacon Valley, a hyperarid valley in Antarctica. They found that oxidation rinds on the exteriors of mafic rocks cause the TIR SiO ν_3 feature to narrow and shift to a higher wavenumber position around 1090 cm^{-1}. The oxidative rinds form in response to the high oxidation potential between the rock interior and the surrounding environment. Divalent cations migrate to the free surface, and the charge imbalance is compensated by the conversion of Fe^{2+} to Fe^{3+}, which creates an inward flux of positive charge, forming electron "vacancies" [*Salvatore et al.*, 2013]. However, despite powerful analysis techniques, *Salvatore et al.*, [2013] could find no direct chemical or mineralogical source of the spectral changes on the rock surfaces.

In summary, the polymerization and spectral properties of a surface can change through chemical weathering. Alteration products of basaltic materials generally have polymerizations ranging between Q^3 and Q^4, which is a smaller and more polymerized range than the range for basaltic materials (Q^0 to Q^4). The change in mineralogy affects TIR spectra by narrowing the SiO ν_3 feature and shifting the position toward higher wavenumber. A great number of secondary minerals/phases can produce these spectral changes, but the SiO ν_3 feature location can help determine which phases are present.

4.2.4 Vibrational spectral properties

Minerals exhibit multiple spectral bands that are essentially Lorentzian curves who's center locations, widths, and amplitudes are all dependent on the lattice parameters

and physical state of the material. For this reason, it is possible to identify individual minerals by examining the properties of curves that are fitted to combined spectral shapes. Most curve-fitting algorithms have been developed for use with Raman spectra, where the bands are exhibited as peaks. Emission bands, on the other hand, are represented as troughs in plots; thus, for the sake of continuity and ease in calculations, emission features will be inverted and referred to as peaks.

The peak center location is the same as the fundamental vibration mode frequency discussed in Section 4.2.1. The SiO ν_3 features of planetary surfaces represent combinations of multiple phases; when the feature is fit with a single curve, the peak center values correspond to the assemblage of phases present in the surface. Thus, the peak center values represent the dominant polymerization/composition. Similarly, when the SiO ν_3 feature of planetary surface is fit with a single curve, the peak width is related to the range of polymerizations present. Wide peaks indicate the individual phases in the assemblage represent a large range in polymerization, so that there is a large spread about the dominant peak center location. Narrow peaks indicate either that individual phases have similar degrees of polymerization or that there are fewer phases present so that the peak center location is more representative of the polymerization of the surface.

The peak amplitude, or spectral contrast, is a complicated function of surface properties such as particle size and porosity. In general, when particle sizes are on the order of the incident wavelength or smaller, the materials become optically thin so that photons easily pass through a number of particles before exiting the surface. This adds reflected and emitted energy so that more energy reaches the detector, effectively reducing the spectral contrast of the main absorption features [*Hunt and Logan*, 1972;

Salisbury and Eastes, 1985]. Additionally, porosity is enhanced with decreasing particle size so that particles are forced apart, creating volume scattering cavities that can further reduce the spectral band depth [*Salisbury and Wald*, 1992]. In contrast, compaction and cementation of fine particles can reduce void space, allowing the surface to scatter coherently as if they were large, optically thick, surface-scattering particles. Thus, compaction and cementation can increase spectral contrast [*Salisbury and Eastes*, 1985].

As a result of these particle size effects, spectral contrast can be compared to albedo and thermal inertia, which are also functions of particle size. Albedo is related to the amount of light reflected from a surface, and will increase as silicate particle size decreases [*Kieffer et al.*, 1977; *Christensen*, 1988; *Ruff*, 2002]. Thermal inertia represents the resistance to change in temperature of the upper few centimeters of a surface, and is most closely related to the thermal conductivity of the surface materials [*Christensen et al.*, 2001b; *Fergason et al.*, 2006; *Piqueux and Christensen*, 2009a]. Fine particles have a lower thermal inertia, whereas surfaces composed of sand, duricrust, rock fragments, or a combination of these materials have higher thermal inertia [*Fergason et al.*, 2006]. However, multiple physical states can complicate thermal inertia calculations including the presence of a duricrust, subsurface layering, and mixtures of different particle sizes [*Fergason et al.*, 2006; *Piqueux and Christensen*, 2009a, 2009b]. In general, high albedo/low thermal inertia measurements are consistent with dusty surfaces, and low albedo/high thermal inertia measurements are consistent with coarse-grained, relatively dust-free surfaces.

Albedo, thermal inertia, and spectral contrast are all calculated from different data and therefore result in differences in sampling depth for each of the quantities. Albedo is

sensitive to the top few micrometers of the surface, spectral contrast is sensitive to the top few 10s of micrometers of the surface, and thermal inertia senses the top few centimeters [*Mellon et al.*, 2000]. So very thin dust covers could easily increase surface albedo and potentially affect the spectral contrast without significantly affecting the thermal inertia.

The final property determined from the curve-fitting technique is the number of peaks in the spectrum. This property depends primarily on the parameters used in the model, such as minimum peak width and amplitude. As the crystal chemistry of a surface becomes more complex, more peaks must be added to the spectrum. A surface spectrum essentially becomes one wide peak when a continuous range of polymerizations is present in the surface materials so that there are a number of phases similar enough in composition and crystal chemistry. However, distinct spectral peaks can occur if there are gaps in the frequencies of spectral features. Gaps can occur if the materials in the surface are chemically and structurally heterogeneous. Thus, if there are a number of large, differentiated peaks, the surface most likely contains discrete phases that are significantly different from each other.

4.3 Methods

4.3.1 TES surface data selection and reduction

Atmospherically adjusted TES data [*Bandfield*, 2002] were selected for this study by restricting: lambertian albedo < 0.15, surface temperature > 255 K, dust opacity < 0.17, ice opacity < 0.1, emission angle < 30°, and high gain antenna and solar panel motion = 0 °/sec. TES data for latitudes between 70° N and 70° S were also constrained to orbital counts (OCK) 1563 – 7500, because a spacecraft vibration anomaly after this

orbital period caused a sporadic minor feature in the data at ~1000 cm^{-1} [*Bandfield*, 2002].

Many previous TIR global mapping studies chose to omit the polar regions (latitudes above 70° N and 70° S) because these surfaces tend to have lower temperatures. Cold surfaces emit less thermal radiation, or signal, for thermal-infrared sensors to detect. High-frequency noise exists as a background in all spectral measurements due to inherent inefficiencies in the instrument. Thus, a decrease in the signal leads to lower signal to noise ratios (SNR), producing spectra with high-frequency noise features that can be confused with compositional features in spectral unmixing analyses. However, the northern polar region was of great interest to this study, and so the orbit count for TES spectra from latitudes > 70° N and 70° S was not constrained in order to increase the number of viable spectra in this region. All data from OCKs > 7500 were visually inspected and none of the spectra with the sporadic1000 cm^{-1} feature were used in this study.

The TES spectra used for the global maps in this study were atmospherically adjusted by *Bandfield* [2002] with a linear least squares fitting algorithm to model the measured spectrum using surface and atmosphere components. This process removes the main CO_2 absorption region (508 – 825 cm^{-1}) from the selected TES spectra because it contains numerous sharp absorptions with opacities >> 1 [*Bandfield*, 2002]. The curve-fitting algorithm used in this study is designed to fit broad, low frequency shapes, and the atmospherically corrected data of *Bandfield* [2002] is sufficient for this purpose. However, when performing surface-atmosphere separations with the intent to derive mineral abundances from the surface spectra, it is advisable to use a more detailed

mineral library than that used by *Bandfield* [2002] as we do for spectra from the northern polar region in this study, as described below.

Lambertian albedo is used as a dust-cover proxy, and similar to other global compositional studies of the Martian surface, we restricted our analysis to low albedo regions. However, it should be noted that by restricting TES data to spectra with albedo < 0.15, we are automatically excluding certain areas that are known to have high albedo but low dust cover (e.g., northern Meridiani and part of Solis Planum) [*Ruff*, 2002].

The selected atmospherically corrected TES spectra were truncated to the main SiO ν_3 feature region (825 – 1301 cm^{-1}) since we are primarily interested in silicate phases (Figure 4.4). The shortened spectra were smoothed with a moving average (length = 3) in order to focus on low frequency features, and inverted in order to ease the MATLAB calculations (Figure 4.4).

JMARS data visualization software was used to select TES spectra from the northern polar region for a more detailed investigation. Raw spectra were selected using the constraints listed above, and were then atmospherically adjusted using the methods of *Bandfield et al.* [2000b]. Mineral abundances were derived using an endmember spectral library (Table 4.1) and a non-negative least squares fitting algorithm to model the TES data between 307 cm^{-1} and 1301 cm^{-1} [*Ramsey and Christensen*, 1998; *Rogers and Aharonson*, 2008]. The difference between the measured spectrum and modeled fit is recorded in the root-mean-square (RMS) error, and a low RMS error is generally taken to represent a more accurate model.

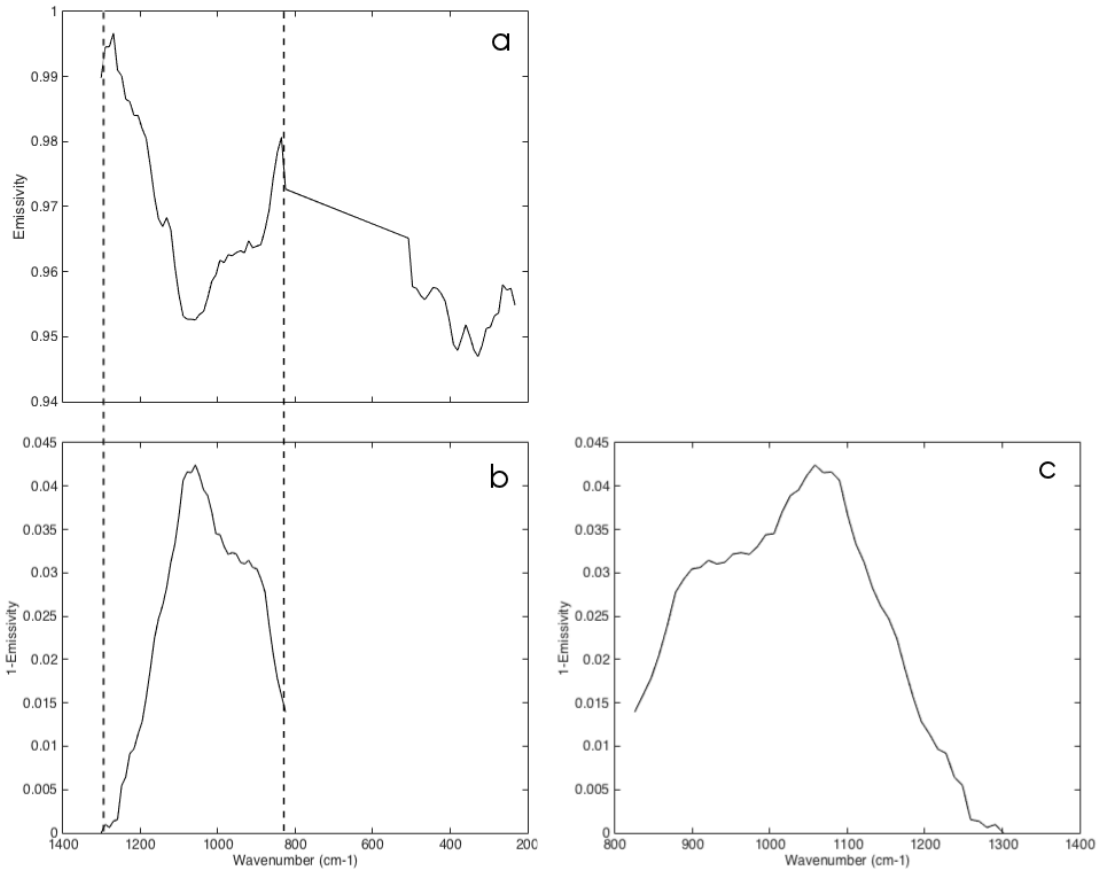

Figure 4.4. Sample TES spectrum (a) before and (b) after truncating and inversion. (c) Final spectral product for the MATLAB algorithm.

Table 4.1 Thermal-infrared spectral endmember library

Mineral Group	*Endmember*
Alkali feldspar	Microcline CUR-3460A
Plagioclase	Albite WAR-0235 Andesine WAR-0024 Anorthite BUR-340 Bytownite WAR-1384 Labradorite BUR-3080A Oligoclase BUR-060
Orthopyroxene	Bronzite NMNH-93527 Enstatite HS-9.4B Hypersthene NMNH-B18247
High-Ca clinopyroxene	Augite NMHN-93527 Augite NMHN-9780 Diopside WAR-6474 Hedenbergite manganoan DSM-HED01
Low-Ca clinopyroxene	Avg. Lindsley pigeonite
Olivine	Fayalite WAR-FAY01 Forsterite AZ-01 KI3008Fo10 KI3373Fo35 KI3362 Fo60
Phyllosilicates	Antigorite MINUN-30 Biotite BUR-840 Illite ECL:ILL102 Kaolinite ECL:KAO103 Montmorillonite (Ca) STx-1 Montmorillonite (Na) Swy-2 Muscovite WAR-5474 Nontronite ECL:NON104 Saponite < 0.2 mic Serpentine HS-8.4B Smectite Swa-1
Sulfate	Anhydrite S16 Blodite S33 Coquimbite/Para-coquimbite S46 Gypsum S6 Jarosite S51 Kieserite

Carbonate	Calcite C40
Zeolite	Crystalline heulandite Crystalline stilbite
Oxide	Hematite BUR-2600 Ilmenite WAR-4119 Magnetite WAR-0384
Noncrystalline aluminosilicate	Allophane Si:Al 5.6 ALLO560[1] Aluminous opal[1]
Quartz	Quartz BUR-4120
Noncrystalline silica	Opal-A Opal-CT
Felsic volcanic glass	Dacite glass MEM-4 K-rich glass (obsidian) SiO_2 glass
Mafic volcanic glass	TES Basalt proxy glass MEM-1 BAS 101[2] ICE 170[2]
Silica-enriched altered mafic volcanic glass	BAS 101A[2] ICE 170A[2]

[1]*Rampe et al.* [2012]
[2]*Horgan et al.* [submitted]

4.3.2 Spectral index calculations

Spectral indices were calculated in Matlab using 'peakfit', a signal processing software that uses a non-linear optimization algorithm to decompose complex signals. Peakfit allows users to define several fitting parameters such as number of peaks, peak shape, and the number of fitting trials, where the trial with the lowest fitting error is selected. The function returns the following properties: peak center, amplitude, width, area, and two "goodness of fit" parameters including the RMS error of the best trial fit and the R-squared value (coefficient of determination). The TES data analysis began with a simple model using one symmetric Lorentzian curve, allowing for 10 fitting trials to each spectrum. This curve shape was chosen because the line-profile in mid-infrared and Raman spectra has an intrinsically Lorentzian shape; although, the profile broadens and becomes asymmetric due to instrumental effects or based on sample characteristics [*Meier*, 2005]. The qualities of the fits are discussed in the following section.

Various endmembers from the spectral library were also processed using the Peakfit function in order to assist with the interpretation of peak properties from the Martian surface. TIR spectra of representatives from each silicate structure group discussed in Section 4.2.2 were averaged together and processed in the same manner as the TES data. Secondary silicate and sulfate phases were also evaluated separately because of the degree of overlap in the SiO ν_3 feature for primary and secondary framework silicates and for silicates and sulfates in general.

4.3.3 Quality analyses

The coefficient of determination, or R-squared value, is commonly used to represent the goodness of fit of a curve to data and is expressed by the following

equation:

$$r^2 = 1 - \frac{SS_{res}}{SS_{tot}}$$

Where SS_{res} represents the difference between the measured values and the fitted function values, and SS_{tot} represents the difference between the measured and the mean values. Therefore, when the fit is good, the residual will be small and the R-squared value will be close to 1. There are two major reasons why the fits in this study might produce low R-squared values: 1) the data are so noisy that they deviate greatly from a smooth Lorentzian curve and 2) the spectrum in the SiO_2 stretching region is not fit well with one peak.

The amount of noise in a spectrum can be investigated by calculating a quality factor 'q' using the following equation:

$$q(\nu) = \frac{A(\nu)}{S(\nu)}$$

Where A(ν) is the moving average as a function of wavenumber ν and S(ν) is given by:

$$S(\nu) = |D(\nu) - A(\nu)|$$

Where D(ν) are the original data. The average q is taken as a single value to represent the quality of each spectrum; larger q values represent higher quality data. The value q is used to flag spectra with high-frequency noise features so these spectra can be examined to ensure the broad, low-frequency features used to calculate the spectral properties are still discernable.

4.3.4 Mapping procedure

The spectral parameter, R-squared and quality index data are visualized by creating 4 pixel per degree (ppd) maps using ArcMAP 10.2. The data were interpolated using an

Inverse Distance Weighting (IDW) calculation with a power of 2 and a fixed radius of 2°. The interpolated layer was masked to only include TES pixels that had at least 10 surrounding TES pixels within a 1° radius. Doing so ensures that the interpolated trend is supported by significant data points, and is not being swayed by one isolated TES pixel. The stretched data were then colorized, and plotted over a Mars Orbiter Laser Altimeter (MOLA) shaded relief map. Areas with no data points are regions where there were no TES pixels that fit the selection constraints. The lack of data can usually be attributed to surfaces with high albedo or dust cover, or temperatures below the threshold.

4.4 Results

4.4.1 Quality factor maps

The global average R-squared value is 0.8242 when TES spectra are fit with a single Lorentzian curve, which is reasonable for such a broad approximation. However, when the R-squared data are mapped, it is apparent that the lowest values (~0.1 – 0.70) are concentrated in the northern polar region (Figure 4.5). This raises the question of whether the data from this colder region are too noisy to recognize broad spectral shapes, or if they are not modeled well with one curve.

The minimum q value for all TES spectra is 5 and the maximum is essentially infinite, though the majority of spectra have q values that range between ~25 – 350. The lowest q values, and therefore the noisiest data, are found in the northern polar region with an average q value ~60 (Figure 4.6). In order to visualize the meaning of the q factor, we compare a spectrum with the lowest q value (q = 5; Figure 4.7a) from the northern polar region to another spectrum from the northern polar region that has a q value of 25 (Figure 4.7c), and then compare both northern polar region spectra to a high

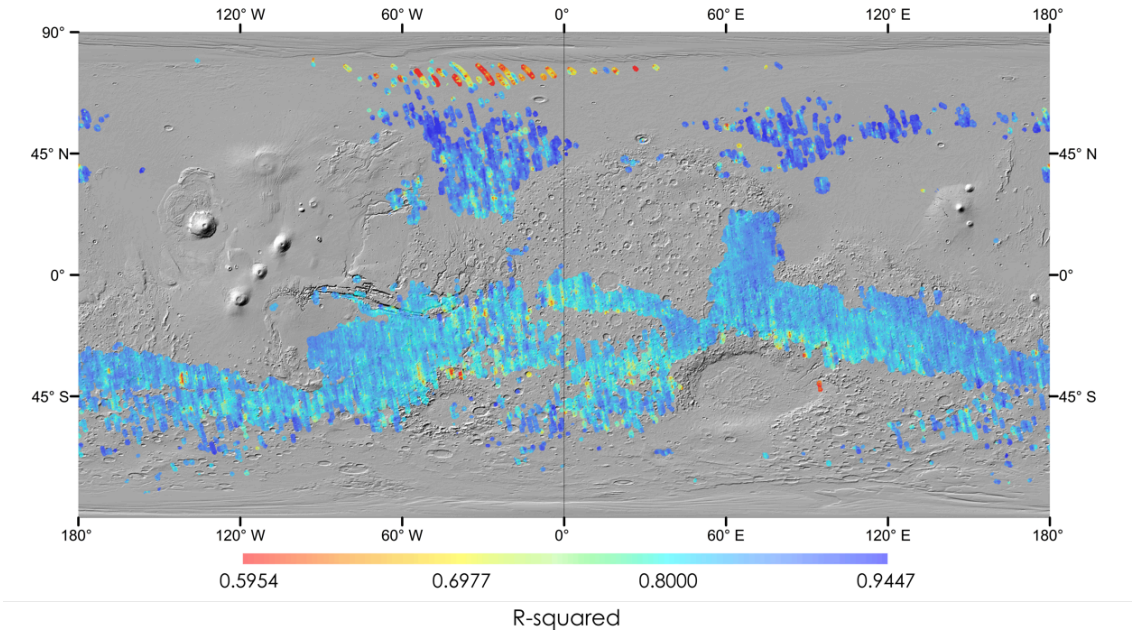

Figure 4.5. Map of R-squared value for one-peak fits to TES spectra data over MOLA topography. Values close to 1 indicate better fits to the measured spectrum. Regions without data are areas where data did not fall within the TES data selection constraints – most likely albedo > 0.15.

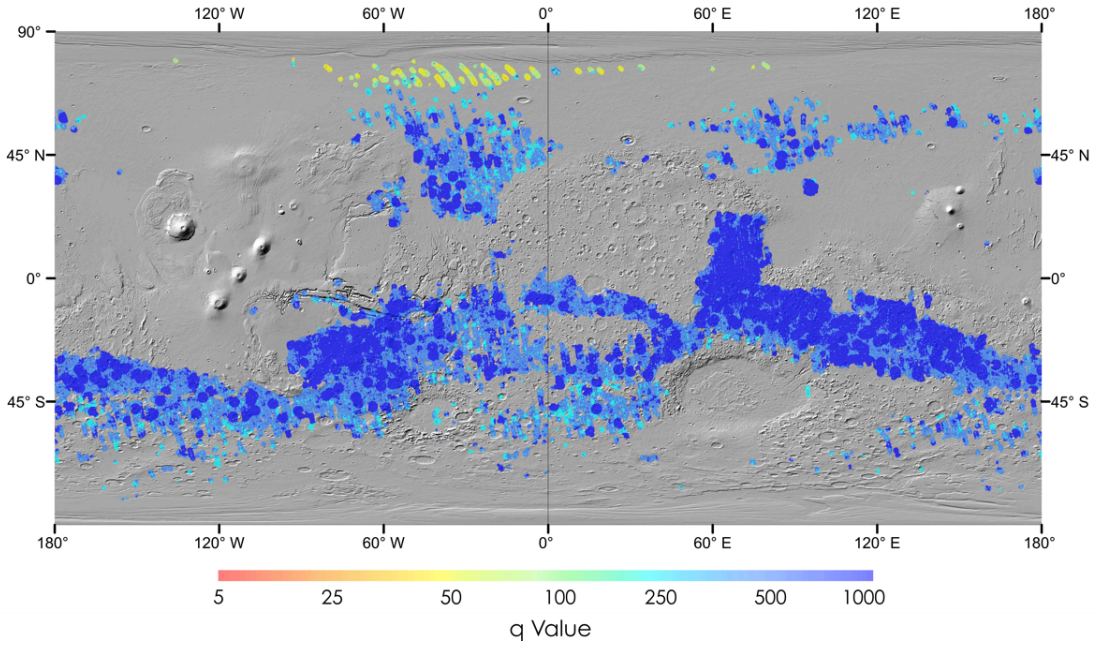

Figure 4.6. Map showing quality factor (q) over MOLA topography. Higher q values indicate smoother data and lower values indicate data with more high frequency noise. Regions without data are areas where data did not fall within the TES data selection constraints – most likely albedo > 0.15.

quality spectrum (q = 100; Figure 4.7e) from the equatorial regions. The unfiltered processed spectra are in blue and the smoothed spectra that are used in the peakfit function are in red. The spectra with the lowest q values (Figure 4.7a and c) have many high frequency features, yet the low frequency shapes are still visible, especially in the smoothed spectra. It appears the spectra generally consist of two or three broad peaks. The higher quality spectrum (Figure 4.7e) has fewer high frequency features, overall.

The plots in Figures 4.7b, d, and f show the results from the peakfit function for each sample spectrum, with the smoothed spectral data as blue dots, the modeled fits to the data as red lines, and the individual peaks that make up the modeled fits as green lines. When the smoothed spectra with low q values from the northern polar region are fit with a single Lorentzian curve (Figure 4.7b and d top), the R-squared values are very low (0.09 and 0.50, respectively). Both spectra have local minima around 1000 cm^{-1} and local maxima around 900 and 1100 cm^{-1} that are not modeled well with a single curve. However, when the model is adjusted to use two Lorentzian curves, the fit is much improved and the R-squared values increase to 0.50 and 0.75, respectively (a 455% and 50% increase; Figure 4.7b and d bottom). In contrast, the high quality sample spectrum from the equatorial plains is fit relatively well with a single Lorentzian curve (R-squared = 0.86; Figure 4.7f top). However, the fit does not model local minima at around 1000 and 1225 cm^{-1} or local maxima around 900, 1075 and 1160 cm^{-1}. When two curves are used in the model, the fit is improved, but the R-squared value only increases by 10% (0.95; Figure 4.7f bottom).

In summary, low R-squared and q values flagged potentially problematic spectra, but further investigation determined that noise in the data does not mask the broad

emission features used in their spectral parameter calculations. These results indicate that the northern polar region is unlike the rest of the Martian surface in that it cannot be sufficiently modeled using a single curve. Spectra from this region contain at least two distinct emission bands that signify chemically and structurally different phases present in those surfaces.

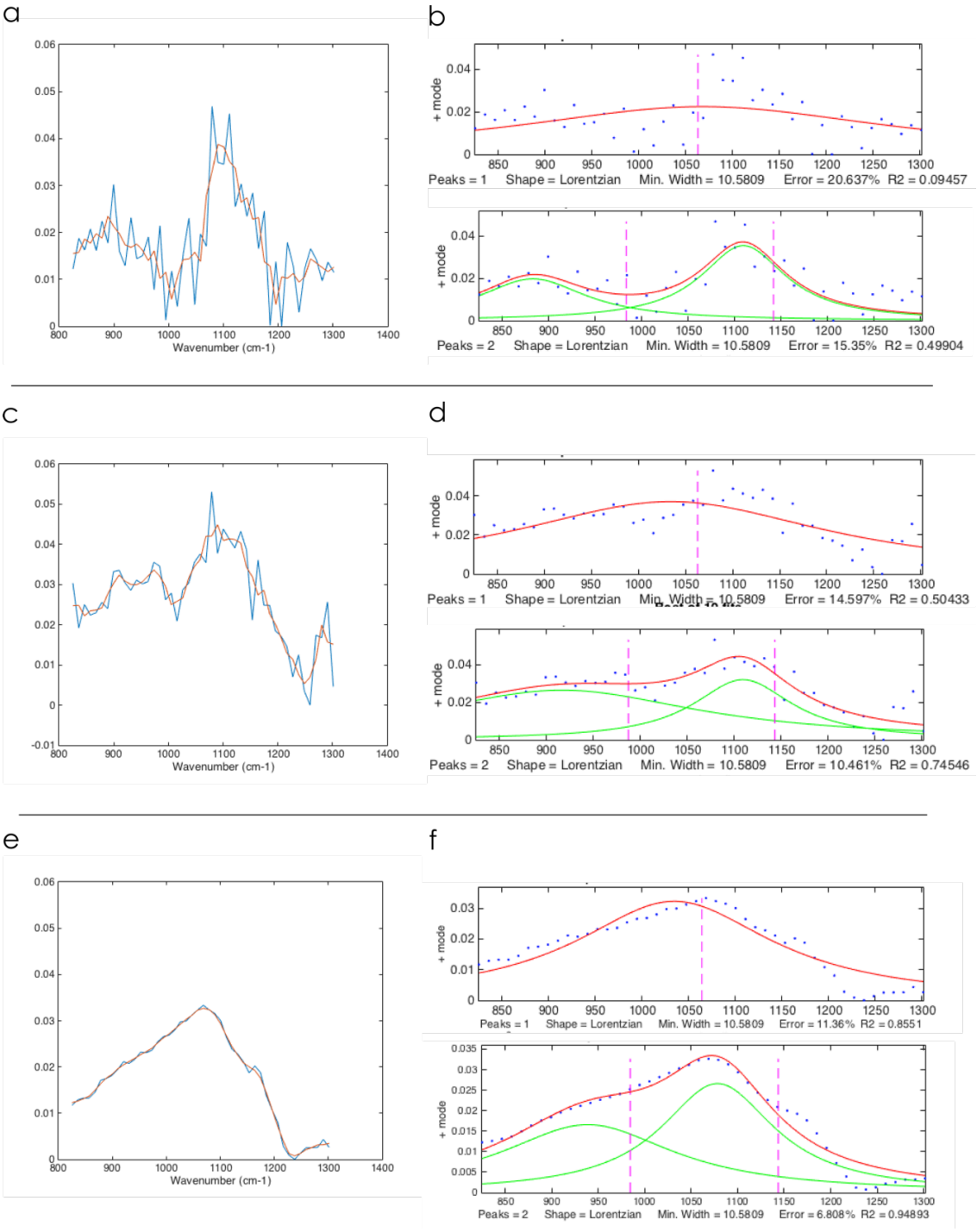
a
b
c
d
e
f
Wavenumber (cm-1)
+ mode
Peaks = 1 Shape = Lorentzian Min. Width = 10.5809 Error = 20.637% R2 = 0.09457
Peaks = 2 Shape = Lorentzian Min. Width = 10.5809 Error = 15.35% R2 = 0.49904
Peaks = 1 Shape = Lorentzian Min. Width = 10.5809 Error = 14.597% R2 = 0.50433
Peaks = 2 Shape = Lorentzian Min. Width = 10.5809 Error = 10.461% R2 = 0.74546
Peaks = 1 Shape = Lorentzian Min. Width = 10.5809 Error = 11.36% R2 = 0.8551
Peaks = 2 Shape = Lorentzian Min. Width = 10.5809 Error = 6.808% R2 = 0.94893

Figure 4.7. (a, c, e) Examples of original (blue) and smoothed (red) spectra. (a) and (c) are spectra from the northern polar region with q factors of 5 and 25, respectively. (e) is a spectrum from the equatorial regions of Mars with a q factor of 100. (b, d, f) Show the peakfit results for each spectrum using a single curve (top) and two curves (bottom). Original spectra (blue dots) are modeled with curves (red lines). When two curves are used (green lines) their shapes are combined to form the spectrum model (red line).

4.4.2 Spectral properties

4.4.2.1 Peak center location

The peak center location changes for each mineral type increases in the following order: nesosilicates (Q^0) = 902 cm^{-1}, allophane (Q^3) = 959 cm^{-1}, inosilicates (Q^2) = 975 cm^{-1}, feldspars (Q^4) = 1024 cm^{-1}, sheet silicates (Q^3) = 1042 cm^{-1}, zeolites (Q^4) = 1052 cm^{-1}, silica-rich coatings/leached rinds/precipitated layers (Q^4) = 1090 cm^{-1}, silica (Q^4) = 1130 cm^{-1}, and sulfates = 1149 cm^{-1}. Overall, the older, heavily cratered equatorial and southern highland regions exhibit lower peak center location values, ranging between ~1000 – 1040 cm^{-1}, indicating surfaces with high abundances of Q^2 – Q^4 silicate structures (Figure 4.8). The younger northern lowland surfaces, have generally higher peak center location values, which range from ~1030 to 1165 cm^{-1} and indicate higher abundances of silicates with Q^4 structures. Peak center location values vary significantly within these regions and will be discussed in Section 4.4.3.

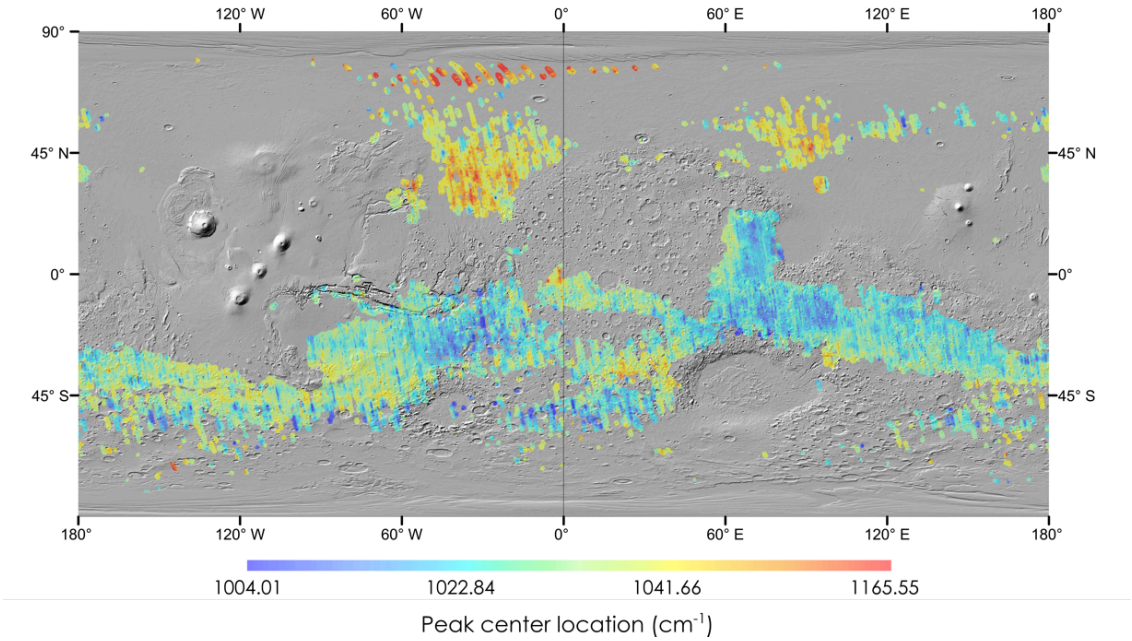

Figure 4.8. Map of peak center location wavenumbers over MOLA. Regions without data are areas where data did not fall within the TES data selection constraints – most likely albedo > 0.15.

4.4.2.2 Peak width

Individual phases with more symmetric SiO ν_3 features, such as feldspars, are fit with relatively wide peaks (~272 cm^{-1}; Figure 4.9a), while phases with very asymmetric SiO ν_3 features, such as silica-rich alteration layers, are fit with narrower peaks that have properties dependent on the dominant spectral band (~1090 cm^{-1}; Figure 4.9b). The same should hold true for spectra that represent complex mixtures of phases, such as planetary surfaces.

Spectrally distinct regions in the peak width map (Figure 4.10) correspond with distinct regions in the peak center location map; for the most part the values are inversely

related. Spectra from the equatorial regions and southern highlands of Mars are generally fit with wider peaks (280 – 475 cm^{-1}) than spectra from the northern lowlands (250 – 325 cm^{-1}), though regional variations exist, as will be discussed in Section 4.4.3. The lower peak width values in the northern lowlands indicate that a significant portion of the surface components have Q^4 structures, and the wider peaks in the southern highlands indicate that the surfaces contain detectable amounts of silicates with Q^0 and Q^4 structures. There are a few spectra with peak widths greater than the SiO ν_3 spectral range being measured (> 475 cm^{-1}). However, these spectra are scattered across the surface, and tend to have very low R-squared values despite reasonably good q values, indicating poor fits to the data. These high peak-width spectra are ignored in our results.

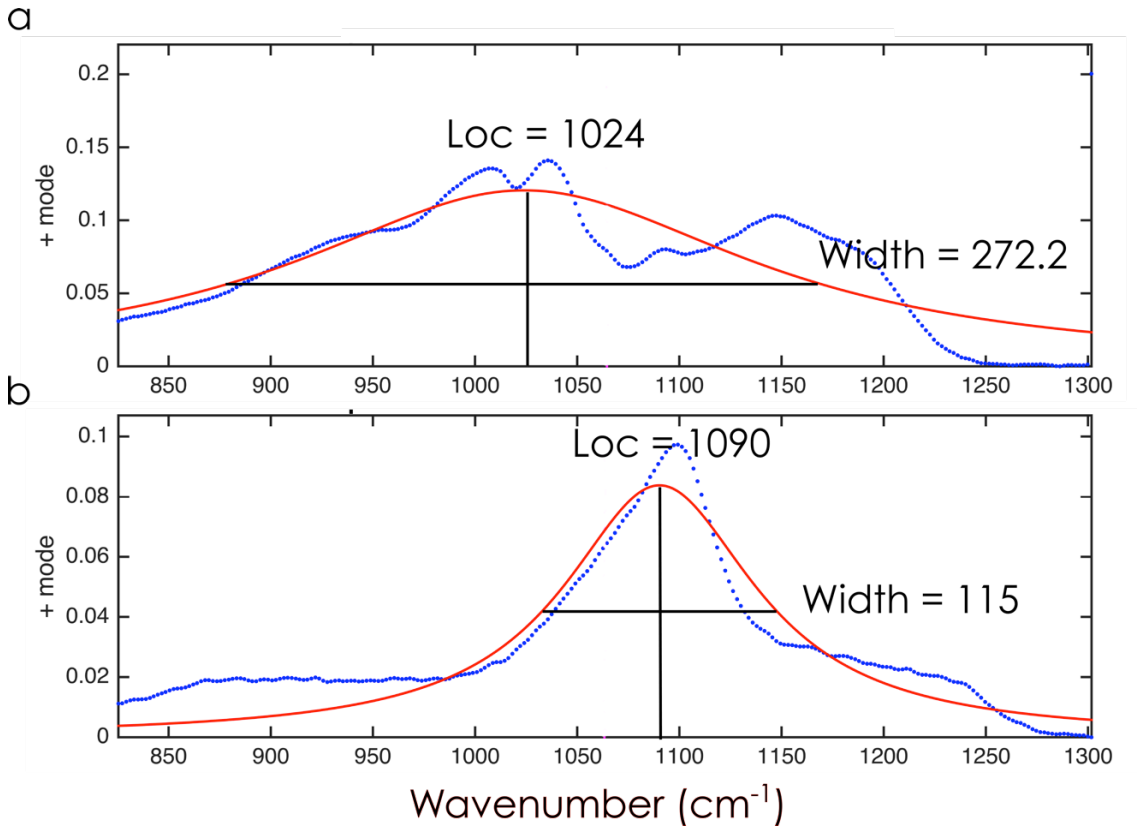

Figure 4.9. Example of peakfit result for (a) average feldspar and (b) silica-rich alteration layers. Feldspars have a wider SiO ν_3 feature than the silica-rich alteration layers as discussed in Section 4.4.3.

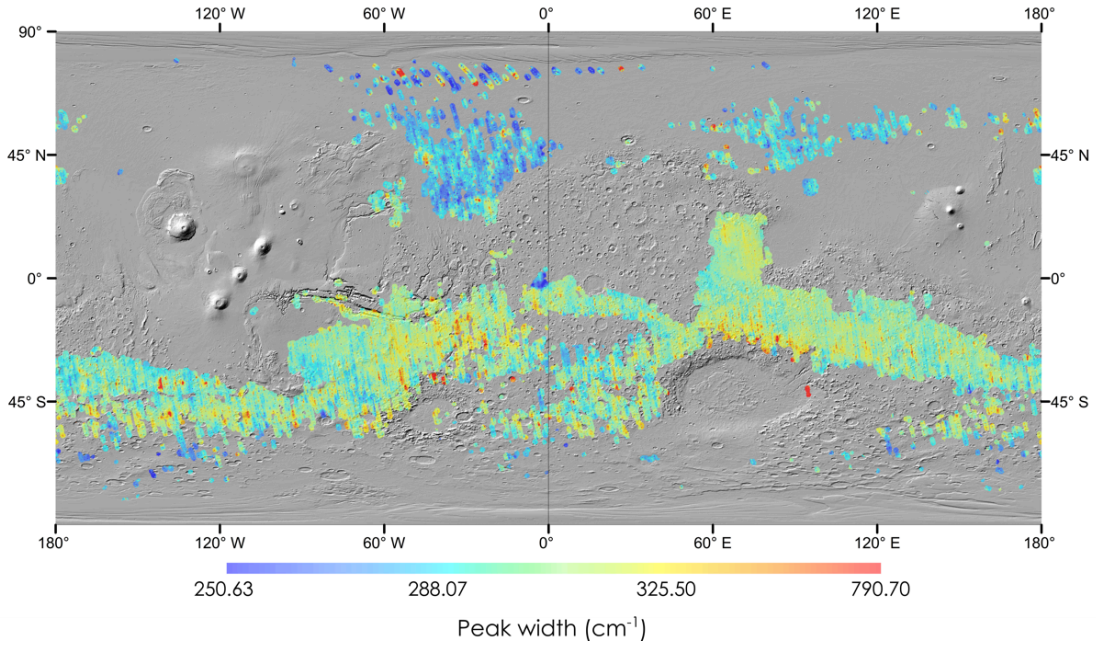

Figure 4.10. Map of peak width superimposed over MOLA shaded relief. Regions without data are areas where data did not fall within the TES data selection constraints – most likely albedo > 0.15.

4.4.2.3 Peak amplitude/spectral contrast

Peak amplitude, or spectral contrast, is associated with the physical properties (e.g., grain size, rock abundance, compaction, cementation, etc.) of the surface being measured. The spectral contrast varies greatly between regions across the Martian surface (Figure 4.11), but there is no general trend separating the southern highlands and the northern lowlands. Some regions with distinct spectral contrast are also distinct in the peak center location and peak width maps, such as eastern Syrtis Major Planum, but this is not always the case. When compared to the other surface properties related to the physical state of the surface, the spectral contrast and thermal inertia (Figure 4.12) correspond well in a generally positive relationship, whereas spectral contrast and albedo (Figure 4.13) are inversely related. Most regions with high spectral contrast have relatively low albedo, indicating that they are dust free, while almost all regions with lower spectral contrast have higher albedo indicating smaller grain size particulates.

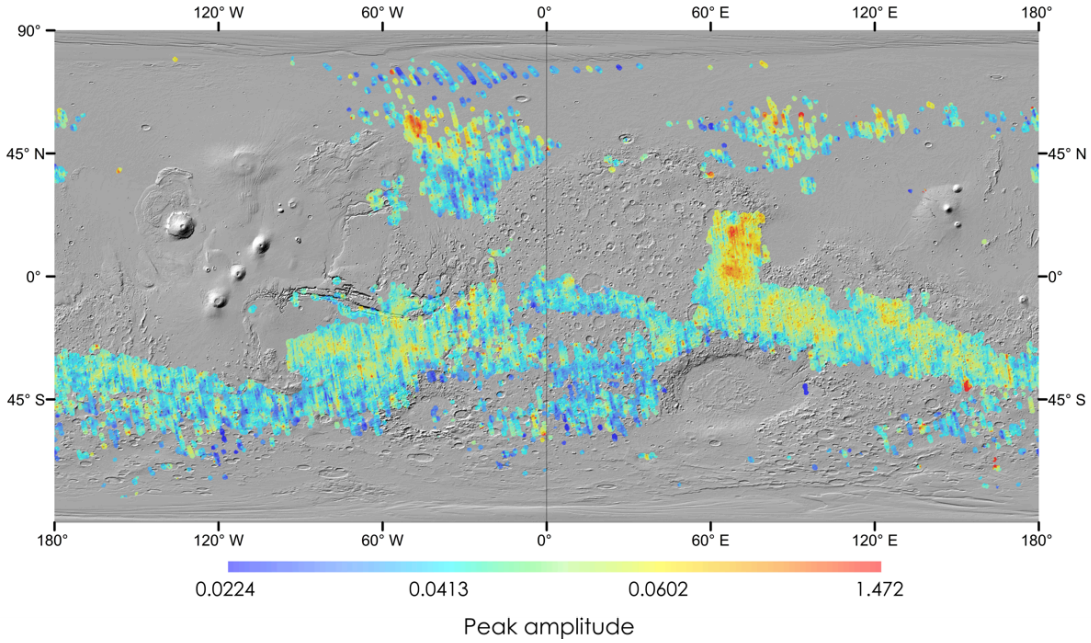

Figure 4.11. Map of spectral contrast (peak amplitude) superimposed over MOLA shaded relief. Regions without data are areas where data did not fall within the TES data selection constraints – most likely albedo > 0.15.

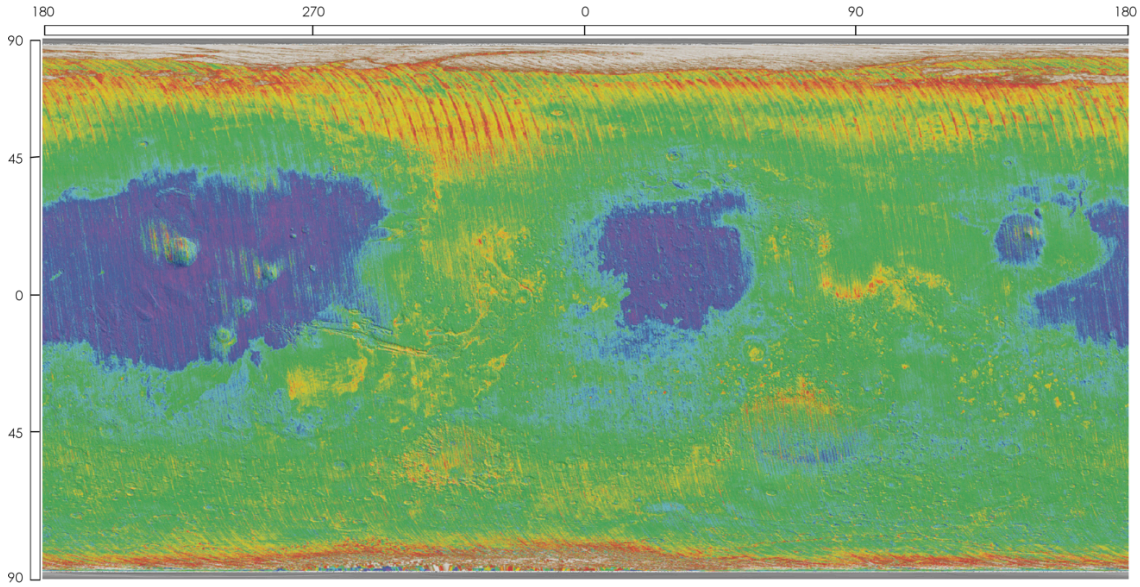

Figure 4.12. TES-derived apparent thermal inertia [*Putzig and Mellon*, 2007]. Thermal inertia values range from 5 thermal inertia units (tiu; purple) to 1000 tiu (brown).

4.4.3 Regional variations

Specific regions discussed throughout the following section are labeled on the albedo map in Figure 4.13. The results from the curve-fitting technique are compared to previous studies in regions where linear deconvolution techniques are thought to work well (i.e., Syrtis Major Planum, Meridiani Planum). Once the validity of this new technique is confirmed, it is then used to interpret results from regions where either the data is thought to be too noisy for linear deconvolution methods (i.e., northern polar region) and/or where linear deconvolution analyses have given ambiguous results (i.e., Acidalia Planitia). Other interesting regional variations are observed and described.

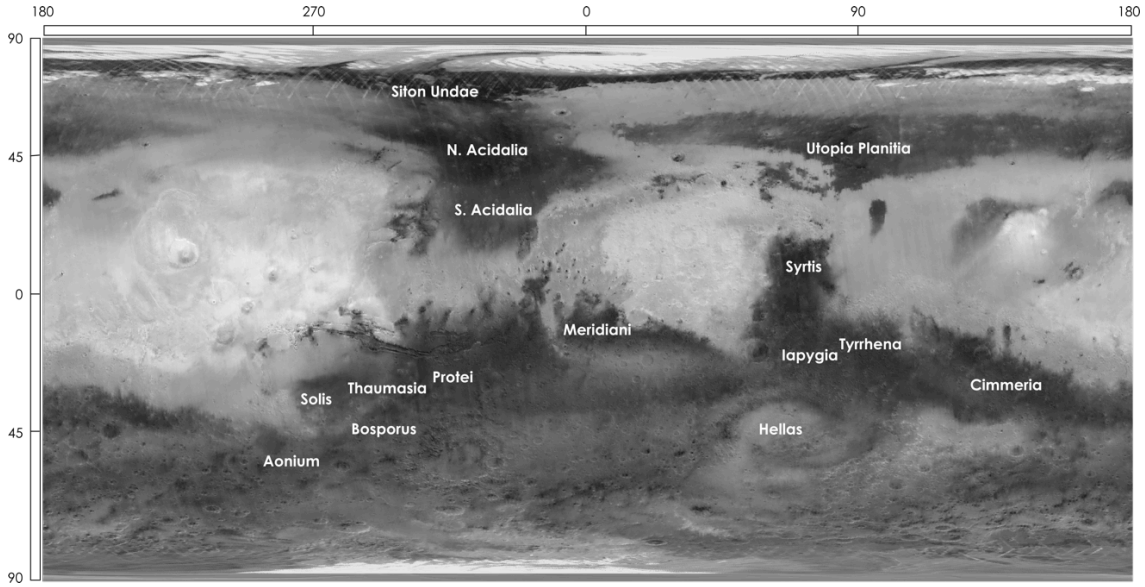

Figure 4.13. TES lambert albedo [*Christensen et al.*, 2001b] over MOLA topography with names of locations discussed in this study. Albedo ranges from 0.07 (darkest tones) to 0.35 (lightest tones).

4.4.3.1 Syrtis Major Planum

Syrtis Major Planum can be divided into two regions based on the spectral properties maps in Figures 4.8 and 4.10. Eastern Syrtis Major Planum is characterized by low peak center location values (1000 – 1025 cm^{-1}) and wide peaks (~300 – 330 cm^{-1}), which is consistent with Q^0 – Q^4 structures (e.g., olivine, pyroxene, feldspars) and indicates a primary basaltic surface. Western Syrtis Major, has higher peak center location values (1022 – 1040 cm^{-1}) and slightly narrower peaks (~280 – 300 cm^{-1}), indicating a surface with a higher percentage of more polymerized phases; most likely, feldspar. Eastern Syrtis is also distinguished from the western portion by greater spectral contrast, suggesting the eastern portion of Syrtis might experience more wind activity, which removes fine dust.

Syrtis Major Planum has relatively warm surface temperatures, and the composition of the surface is fairly well constrained through TIR linear deconvolution and VNIR spectral analyses. A number of spectral studies have also noted spectral differences between western and eastern Syrtis Major. *Bandfield et al*. [2000] found the highest concentrations of Surface Type 1 (basalt) in eastern Syrtis Major, and *Koeppen and Hamilton* [2008] modeled up to 10% greater olivine abundance in eastern Syrtis Major than in the western reaches. VNIR mapping efforts by *Clenet et al.* [2013] also distinguish a spectral boundary between the eastern and western portions of Syrtis Major Planum. They found that the eastern portion exhibits elevated high-Ca pyroxene and olivine when compared to the western portion. Additionally, *Rogers and Hamilton* [2015] found that the western portion exhibits slightly higher abundances of low-Ca pyroxene, high-silica phases, and sulfates when compared to the eastern portion. Thus, TIR curve-fitting, linear deconvolution and VNIR analyses all agree that Syrtis Major Planum is divided into a mafic eastern portion, and a western portion with higher abundances of more polymerized phases; giving confidence to this new curve-fitting technique.

4.4.3.2 Meridiani Planum

The R-squared and q values from the curve-fitting technique are relatively high in Meridiani Planum, indicating quality data and good fits. The Meridiani Planum region has some of the highest peak center location values and smallest peak widths in the southern highlands, suggesting the surface is dominated by phases with relatively similar degrees of polymerization. Most peak center location values at Meridiani range from ~ 1040 to 1070 cm^{-1}, consistent with Q^3 and Q^4 polymerized silicate phases such as sheet silicates, feldspars, and zeolites. In support of this observation, orbital VNIR spectral

investigations have detected phyllosilicate minerals using the OMEGA and CRISM instruments [*Gendrin et al.*, 2005; *Flahaut et al.*, 2015].

There are three large locations within Meridiani Planum where the peak center location values are very high, ranging between ~1100 and 1160 cm^{-1}. The lower values in this range are consistent with high-silica phases such as silica-rich coatings/leached rinds/precipitated layers. TES linear deconvolution investigations of Meridiani indicate relatively high abundances of high-silica phases (18 - 28%) [e.g., *Arvidson*, 2003; *Rogers and Aharonson*, 2008; *Rogers and Hamilton*, 2015]. Additionally, the Miniature Thermal Emission Spectrometer (Mini-TES) instrument on the Mars Exploration Rover (MER) Opportunity detected a noncrystalline high-silica phase component that was best modeled with high-silica glass (10 – 25%) in most of the rock outcrops in the rims of Eagle and Endurance craters, located within Meridiani Planum [*Christensen et al.*, 2004]. Subsequent TIR spectral work has shown that silica-rich coatings/leached rinds/precipitated layers can have spectral features similar to high-silica glass [*Minitti et al*., 2007; Chapter 2]. Therefore, these silica-rich coatings/leached rinds/precipitated layers are potential components of the Meridiani Planum surface.

The highest peak center location values (~1120 – 1165 cm^{-1}) are beyond the spectral range for silicates, and can only be obtained if mineral groups with higher wavenumber spectral features are present; sulfates have S-O stretching features in this range (Figure 4.1a). The OMEGA, CRISM and TES instruments have all detected sulfates in Meridiani Planum from orbit [*Arvidson*, 2003; *Gendrin et al.*, 2005; *Rogers and Aharonson*, 2008; *Flahaut et al.*, 2015; *Rogers and Hamilton*, 2015]. Additionally, the Opportunity instrument suite detected hydrated sulfate minerals (jarosite, Ca- and

Mg-sulfates) in rock outcrops in the rims of Eagle and Endurance craters [*Christensen et al.*, 2004; *Klingelhöfer et al.*, 2004]. Where TES and OMEGA datasets overlap, locations with the highest peak center location values correspond well with strong VNIR sulfate signatures [*Flahaut et al.,* 2015]. Thus, curve-fitting methods can be used to identify sulfate deposits in other locations on Mars that have similar peak center location values.

The Meridiani region does not stand out as being distinct in the spectral contrast map. It is generally associated with moderate to low spectral contrast, which suggests the surface material exists as smaller particle sizes.

4.4.3.3 Northern Polar Region (~70 – 90°N)

The northern polar region requires two Lorentzian curves to fit data reasonably well. The spectra from this region are best fit with two narrow peaks, one at a lower wavenumber centered between ~850 and 1020 cm^{-1}, and one at a higher wavenumber centered between ~1050 and 1150 cm^{-1} (see Figure 4.14). The first peak center range is consistent with $Q^0 – Q^4$ silicate structures similar to olivine, pyroxene, allophane and, to a lesser degree, feldspars. The majority of spectra in the northern polar region have this peak positioned at ~910 cm^{-1}, indicating that this surface contains a high abundance of nesosilicates (olivine). In support of these observations, *Poulet et al*. [2008] detected olivine- and pyroxene-rich units in the circumpolar terrains using VNIR spectral data from the OMEGA instrument.

The lower bounds of the higher wavenumber peak center range (from ~1050 to 1100 cm^{-1}) is consistent with Q^4 silicate structures such as zeolites, silica-rich coatings/leached rinds/precipitated layers, and silica; though the majority of spectra from this region have this second peak positioned at 1100 cm^{-1}, which is consistent with silica-

rich coatings/leached rinds/precipitated layers. The upper bounds of the higher peak center range (> ~1150 cm^{-1}) indicate that sulfates are also contributing to the spectral signal. The presence of both gypsum and silica-rich alteration layers on volcanic glass is supported by satellite VNIR observations from this region using the OMEGA and CRISM instruments [*Langevin*, 2005; *Fishbaugh et al.*, 2007; *Horgan et al.*, 2009; *Horgan and Bell*, 2012; Chapter 2].

The two peaks in the northern polar region spectra create a local minimum, or "gap" in the spectra between ~990 and 1040 cm^{-1} (Figure 4.7b and d). The gap indicates that there is little spectral contribution from minerals with SiO ν_3 features in this spectral range; namely, minerals with intermediate SiO_2, such as plagioclase. The spectral gap must not be present in other Martian surface spectra because the fits with a single curve model are relatively good. For example, the spectrum from the equatorial regions shown in Figure 4.7e does not have a gap in the ~990 – 1040 cm^{-1} spectral range; there is only a subdued local minimum that is more visible in Figure 4.7f. Thus, curve-fitting results indicate that the northern polar region surface has lesser abundances of intermediate silicate minerals (i.e. plagioclase) than the rest of the Martian surface, suggesting a significantly different geologic history.

The northern polar region has low spectral contrast, which would normally indicate small particle size, but the surface also has high thermal inertia and low albedo, which indicates larger particle size, compaction or cementation [*Tsoar et al.*, 1979; *Thomas and Weitz*, 1989; *Lancaster and Greeley*, 1990]. Thus, the low spectral contrast is most likely due to low surface temperatures, which decreases the signal as explained in 4.3.1.

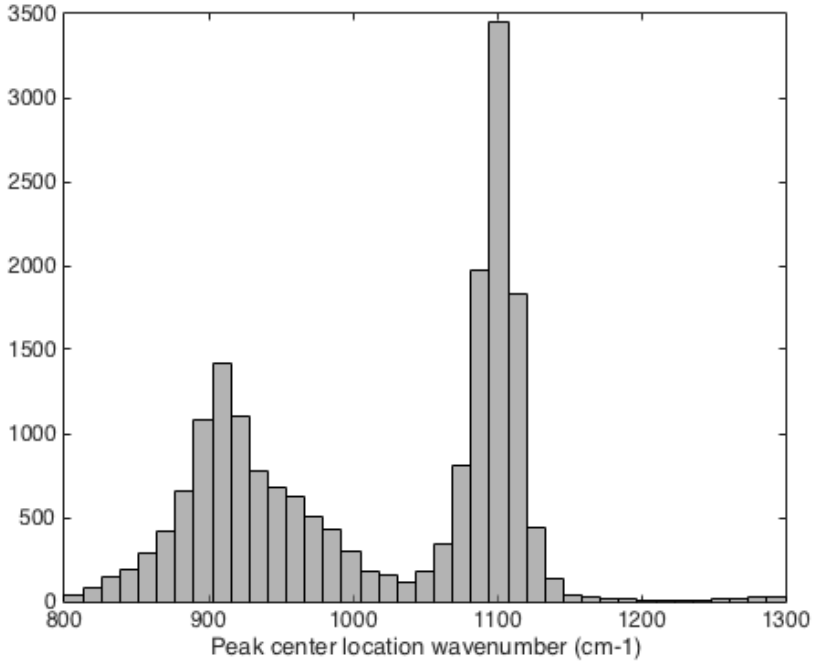

Figure 4.14. Histogram showing the peak center location results for spectra from the northern polar region when two curves are used in the spectral modeling.

4.4.3.4 Acidalia and Utopia Planitiae

Acidalia and Utopia Planitiae have similar spectral properties, both having generally higher peak center location values and smaller peak width values than the southern highlands. Additionally, both surfaces show distinct spectral boundaries in the peak center location map corresponding with latitude (~45°N).

Northern Acidalia and Utopia Planitiae (~45 - 70°N) surfaces have lower wavenumber peak center locations (~1030 – 1070 cm^{-1}) compared to the southern reaches. The peak center location values are consistent with high abundances of Q^3 and Q^4 structures similar to feldspars, sheet silicates, and zeolites. This observation is consistent with these regions being classified as Surface Type 2, which was modeled with

high abundances of high-silica phases [*Bandfield et al.*, 2000a]. There is little evidence for sulfates as major components of the northern Acidalia and Utopia Planitiae, except for a number of small, isolated locations within northern Utopia Planitiae (Figure 4.8). However, sulfates may be present elsewhere in low abundances or in locations smaller than the spatial resolution of TES. This observation is consistent with results from linear deconvolution analyses by *Rogers and Hamilton* [2015], which modeled these surfaces with low abundances of sulfates (near the detection limit ~10%).

Southern Acidalia and Utopia Planitiae (~20 – 45°N) have higher peak center location values (~1050 to 1100 cm^{-1}) than the northern reaches. The peak center location values are indicative of highly polymerized (Q^4) phases such as zeolites and silica-rich coatings/leached rinds/precipitated layers. The southern portions also have a number of locations with very high peak center locations (~1160 cm^{-1}), indicative of sulfates. Like the northern portions, the southern reaches of Acidalia and Utopia Planitiae were classified as Surface Type 2, indicating high abundances of high-silica phases [*Bandfield et al.*, 2000a]. However, subsequent linear deconvolution modeling suggested that these surfaces have lower abundances of high-silica phases and higher abundances of sulfates than the northern reaches [*Rogers and Hamilton*, 2015]; which is relatively consistent with spectral property results from these locations.

The southern Acidalia/Utopia surfaces have lower spectral contrast, when compared to spectra from the northern reaches. The decrease in spectral contrast from northern to southern Acidalia is suggested to be an indication of dust cover [*Rogers and Christensen*, 2007] which is perhaps thin enough to affect albedo and spectral contrast,

but not thick enough to have a significant effect on the thermal inertia (~millimeters thick).

4.4.3.5 Tyrrhena, Terra Cimmeria, and Protei Regio

Tyrrhena, Terra Cimmeria, and Protei Regio have some of the lowest peak center locations on the planet (ranging between ~1000 – 1020 cm^{-1}) and the largest peak widths (ranging between ~ 300 – 330 cm^{-1}). The peak center location values indicate high abundances of phases with polymerization ranging between ~ Q^0 and Q^2, consistent with neso- and inosilicates, such as olivines and pyroxenes, that tend to have wide SiO ν_3 spectral features (Figures 4.1a and 4.2). Tyrrhena, Terra Cimmeria, and Protei Regio all exhibit high spectral contrast, indicating that they are relatively dust-free regions. In support of these observations, *Rogers and Hamilton* [2015] found that Tyrrhena, Terra Cimmeria, and the region classified here as Protei Regio consist of basaltic mineral assemblages and exhibit slightly elevated olivine abundances when compared to the surrounding regions.

4.4.3.6 Hesperia and Thaumasia

Peak center location values are slightly higher in Hesperia and Thaumasia than in their surrounding regions (Tyrrhena and Protei Regio, respectively) indicating elevated abundances of more polymerized phases. Most of the spectra from Hesperia and Thaumasia have peak center locations ~1020 – 1040 cm^{-1}, which are consistent with Q^3 – Q^4 phases, specifically structures similar to feldspars, sheet silicates, and zeolites. The spectra are also fit with relatively narrow peak widths, indicating a lesser abundance of neso- and inosilicate minerals. Similarly, *Rogers and Hamilton* [2015] differentiated the Hesperia and Thaumasia regions from their surroundings, by slightly decreased olivine

and elevated high-silica phase content. Hesperia and Thaumasia have strong spectral contrast similar to the surrounding regions, suggesting that there is little change in the physical state of the surface between these regions.

4.4.3.7 Solis Planum

Solis Planum is just south of Thaumasia, and the spectra from this region exhibit higher average peak center location values (~1040 – 1050 cm^{-1}) that are consistent with higher abundances of Q^3 and Q^4 structures such as feldspars, sheet silicates, and zeolites. Solis Planum was initially grouped in the same spectral class with northern Acidalia, the location of the original Surface Type 2 spectrum [*Rogers and Christensen*, 2007]. However, when compared to northern Acidalia, the spectral properties of Solis Planum are more indicative of increased feldspar abundances than secondary phase abundances (wider peaks and lower peak center location values than those of high-silica phases). *Rogers and Hamilton* [2015] also noted spectral distinctions between the two regions, and modeled Solis Planum spectra with higher abundances of feldspar minerals. Nevertheless, peak widths in Solis Planum are decreased when compared to the surrounding basaltic regions, indicating some elevated abundance of high-silica phases such as sheet silicates and zeolites, which have narrower features. Solis Planum has slightly lower spectral contrast than surrounding regions, indicating that particle size is slightly lower.

4.4.3.8 Western Hellas Basin

The region just west of Hellas basin in the southern highlands has relatively high peak center location values that range between ~1030 and 1100 cm^{-1}, and moderate peak widths ranging between ~270 and 325 cm^{-1}. These properties are consistent with Q^3 and

Q^4 silicate phases, primarily feldspars, sheet silicates, zeolites, and silica-rich coatings/leached rinds/precipitated layers. The moderate peak widths suggest there are also spectral contributions from other, less polymerized phases, and some potential contribution from sulfate minerals. These observations are supported by previous studies that have detected relatively high abundances of TES Surface Type 2 [*Bandfield et al.*, 2000a] and high-silica phases and sulfates [*Rogers and Hamilton,* 2015] within western Hellas. In addition, the western Hellas region exhibits lower spectral contrast than it's surroundings, suggesting the surface has smaller particle sizes.

4.4.4 Selected spectra deconvolution results

A number of linear deconvolution analyses have been performed on thermal infrared spectral data from the northern polar region [*Bandfield*, 2002; *Wyatt and McSween*, 2002; *Koeppen and Hamilton*, 2008]. However, these studies focused either on individual mineral abundances [*Bandfield*, 2002; *Koeppen and Hamilton*, 2008] or TES Surface Type abundances [*Wyatt and McSween*, 2002]. The northern polar region has been excluded from most TIR mineral assemblage/lithology analyses because the cold surfaces result in low SNR [e.g., *Rogers and Christensen*, 2007; *Rogers et al.*, 2007; *Rogers and Hamilton*, 2015]. Nevertheless, results from the curve-fitting technique have shown that the lithology of the northern polar region is spectrally distinct from the rest of the Martian surface, and so a detailed mineral assemblage analysis is warranted.

Linear deconvolution spectral analysis is performed on high-quality TES data from Siton Undae, a sand sea within the northern polar region. Twenty spectra (centered at 293.80°E, 74.80°N; Figure 4.15) were selected, atmospherically corrected and averaged for use in the linear least squares fitting algorithm. The spectrum is best

modeled with sulfate (20%), plagioclase (20%), silica-rich acid alteration layers (20%), olivine (15%), phyllosilicates (10%), and other minor phases that are modeled in abundances less than the detection limit (~5%) (Figure 4.16). The RMS error of the modeled fit increases when sulfates are excluded from the mineral library, indicating that they are an important component of the surface.

The spectral properties for the TES data from Siton Undae are representative of the spectral properties of the majority of the northern polar region (similar peak center locations, small peak widths, low spectral contrast); thereby allowing the spectral mixture analysis results from Siton Undae to be extrapolated to the other TES spectra in the northern polar region with some confidence. The spectral mixture analysis results are supportive of a surface composition comprised of ~35% primary mafic minerals, ~55% secondary phases (sulfates and silica-rich acid alteration layers), and ~10% primary felsic glass. It should be noted that pyroxene is absent in linear deconvolution models, an observation that is supported by weak or absent absorptions in VNIR spectral data [*Poulet et al*., 2008; *Horgan and Bell*, 2012]. Additionally, plagioclase is modeled in very low abundances.

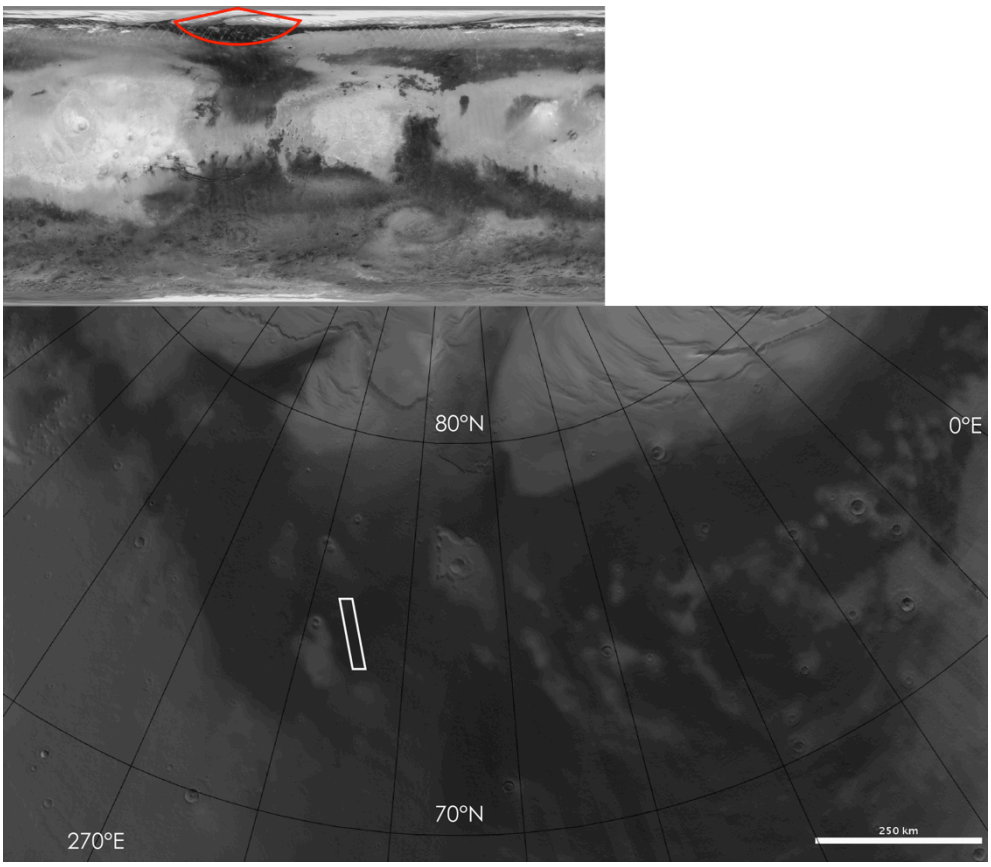

Figure 4.15. Top image is a TES albedo map [*Christensen et al.*, 2001b], and the shape outlined in red shows the location of Siton Undae. Bottom image is a detailed OMEGA albedo mosaic from the red outlined region [*Ody et al.*, 2012] with the location of TES spectra used in spectral deconvolution outlined by the white rectangular box.

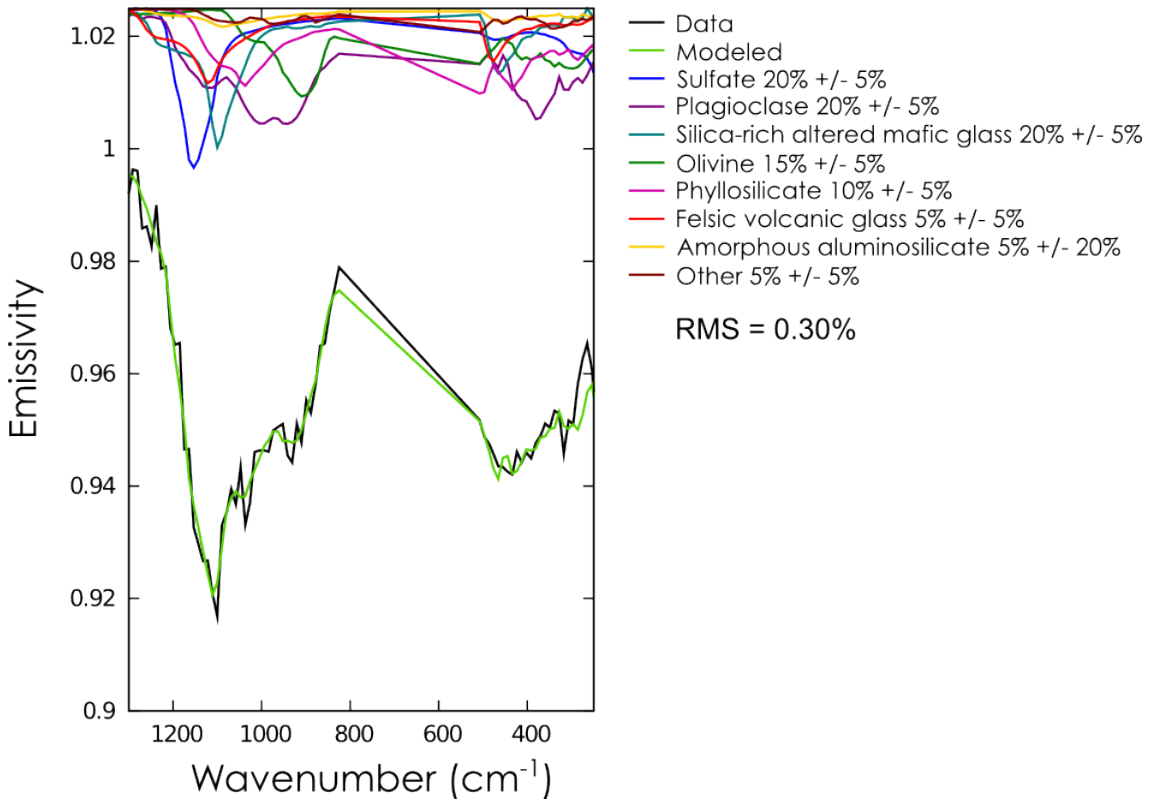

Figure 4.16. Spectral linear deconvolution mineral abundance results showing the surface TES spectrum from the Siton Undae dune field (black line), the individual mineral spectra (above) scaled to the abundances listed on the right, and the modeled fit (green line) that is a linear combination of the individual spectra. RMS error increased to 0.35% when sulfates were excluded from the analysis.

4.5 Discussion

4.5.1 Assessment of Lorentzian curve-fitting technique

The simplest curve-fitting model, using a single symmetric curve, is able to provide the general lithology of much of the Martian surface. The fit improves when spectra are modeled with two curves, as is observed in the increasing R-squared values in Figure 4.7. It is conceivable that R-squared values would continue to increase as more curves are allowed in each model until all of the mineral and instrument-related features in a spectrum are accounted for. Linear deconvolution performs a similar task, but the "curves" used in the fitting contain implicit structural and compositional information that add constraints to the model.

Interpretations of thermal-infrared spectral data can be complicated by the physical state of a surface because a number of physical properties greatly affect thermal-infrared spectra, as will be discussed in 4.5.2. The linear deconvolution analysis technique is further constrained by the surface temperature and the mineralogy of the surface. Linear deconvolution results are thought to be robust for relatively warm primary surfaces where all of the components of the surface are most likely represented in spectral libraries (i.e. Syrtis Major Planum). However, much of the Martian surface does not fall within these constraints, and so the Lorentzian curve-fitting technique can be useful for determining the composition of colder surfaces and/or surfaces with diverse mineralogy, as was shown for the northern polar region.

Another method similar to Lorentzian curve-fitting is the "center of gravity" technique [*Smith et al*., 2013], recently renamed the "weighted absorption center" (WAC) technique [*Amador and Bandfield*, 2016]. This method determines the center of the SiO

ν_3 feature by calculating the wavelength at which half of the integrated area under a spectrum is located on each side of the center wavelength [*Amador and Bandfield*, 2016]. The WAC is similar to the peak center location derived using a single curve; both methods are capable of representing the dominant lithology of the surface. Yet these values are not equal. The integration used in the WAC method accounts for any asymmetry in the SiO ν_3 feature while the simple symmetric curve used in this study does not. However, it is possible to adjust the peakfit function to use asymmetric curves, and it is also possible to increase the number of curves used in the curve-fitting model, which would account for any asymmetry in the spectrum. The addition of more curves to the model can also help identify individual components of the surface, as is discussed in 4.5.3, but this is not possible for the WAC technique. Additionally, the WAC technique is limited in that it delivers a single value related to the composition of the surface, but does not give information about the width and depth of the spectral band, which provide important information about the range of compositions and physical state of the surface.

4.5.2. Physical properties of weathered surfaces and their spectral effects

The physical state of a surface (e.g., particle size, porosity, coatings) can have significant effects on infrared spectra. Thermal-infrared spectral analysis methods work well when surfaces have particle sizes >~ 60 μm, or finer particle sizes that are compacted or cemented to reduce porosity [*Ramsey and Christensen*, 1998]. Additionally, linear deconvolution breaks down when coatings with strong absorption coefficients (i.e., silica) are present. Fresh igneous surfaces (i.e., lava flows, tephra deposits) generally have large particle sizes without coatings, and so thermal-infrared spectral analyses of such surfaces are relatively uncomplicated. However, most surfaces

on Earth and presumably on Mars have undergone some degree of weathering since the time of emplacement, altering the physical state.

Chemical and physical weathering processes work in concert to reduce particle size. Chemical weathering can promote physical weathering when fluids penetrate rocks through preexisting zones of weakness, such as fractures and crystal grain boundaries, dissolving the primary minerals and precipitating secondary phases. With time, the physical strength of the rock is compromised, and the mass eventually breaks apart along the planes of weakness [*Taylor and Eggleton*, 2001]. Additionally, Mars surfaces have been subjected to high degrees of physical weathering in the form of impact, aeolian, and potentially freeze-thaw processes [*Gooding et al*., 1992]. Images from the Viking Pathfinder lander and MER rovers show that weathering processes on Mars have produced a wide range of particle sizes including: rocks, sand, and dust found in close proximity in low albedo regions [*Mutch et al*., 1976a, 1976b; *Golombek et al*., 1997; *Squyres et al*., 2004a, 2004b].

Particle size mixtures are most certainly represented in low spatial resolution TES pixels (each pixel measures an area ~3 km x ~8 km), and this can cause potential problems for thermal-infrared spectral analyses. The minimum amount of a material that can be detected depends in part on the spectral contrast, which decreases with particle size as discussed in 4.2.4 [*Kirkland et al*., 2001]. Thus, in a mixture, smaller particles contribute less to the TIR spectrum than larger particles. Composition tends to vary with grain size, and secondary minerals, such as clays, are generally found in the smaller grain size fraction (< 2 μm) [e.g., *Colman*, 1982]. Therefore, loose secondary products would most likely be underestimated in linear deconvolution abundance analyses.

If Surface Type 2 spectra represent altered surfaces, the secondary phases must be in a physical state that reduces porosity (e.g., compacted, cemented, or as coatings) in order to increase the effective radiating diameter [*Ramsey and Christensen*, 1998]. In most arid locations on Earth, fine-grained soil particles are cemented together via precipitation from circulating chemical fluids to form duricrusts. The cement usually consists of silica, carbonate, iron oxide, and sulfate [*Dury*, 1969]. Thermophysical properties of the Martian surface suggest that duricrusts are globally important [e.g., *Jakosky and Christensen*, 1986; *Piqueux and Christensen*, 2009]. Additionally, physical properties of the soil at the Viking 1 landing site in Acidalia Planitia [*Moore et al*., 1977] are in support of the presence of duricrusts in Surface Type 2 regions. Thus, the high-silica phases measured in TES spectra might be present in the form of cemented material or the cement itself.

Secondary phases can also form as coatings on rocks or particles [e.g., *Colman*, 1982; *Curtiss et al*., 1985; *Dorn*, 1998; *Dixon and Thorn*, 2005]. Rock coatings can have a significant effect on the TIR spectrum, but the effect varies with coating thickness and composition. Silica has very high absorption coefficients in the TIR spectral range, so coatings <10 μm thick are able to obscure any spectral contribution from the underlying substrate [e.g., *Kraft et al*., 2003]. Therefore, silica-rich rock coatings can spectrally dominate a surface, elevating the apparent abundance of SiO_2, without significant chemical Si-enrichment. Silica-rich coatings are a proposed component of Surface Type 2 surfaces [*Kraft et al*., 2003], and a number of regions (i.e., northern polar region, southern Acidalia, Meridiani, western Hellas) have been shown to have peak center locations that are consistent with silica-rich alteration layers as will be discussed in 4.5.3.

4.5.3 New constraints on Surface Type 2 compositions

Surface Type 2 regions are found in a number of locations across the Martian surface. The most notable Surface Type 2 locations are the northern polar region, Acidalia and Utopia Planitiae, western Syrtis Major Planum, and Solis Planum. The spectral property variance between these locations indicates that the dominant minerals and phases also vary, suggesting that there is no single underlying mechanism forming Surface Type 2. These are each distinct regions that most likely formed through independent processes. New insight into potential formation mechanisms for the northern polar region and Acidalia/Utopia Planitiae surfaces are discussed below.

Much of the low albedo surfaces in the northern polar region correspond with the Olympia Undae unit; a unit that primarily consists of sand dune deposits thought to be sourced from within the polar ice cap [*Byrne and Murray*, 2002; *Fishbaugh and Head*, 2005; *Tanaka et al.*, 2008]. The northern polar region has been shown to consist of a mixture of primary, mafic minerals, and aqueous alteration phases (silica-rich alteration layers and sulfates). The primary mineralogy in Siton Undae is consistent with an ultramafic parent rock, having no pyroxene and low abundances of plagioclase (20%) when compared to other broad regions of the Martian surface (between ~24 – 33%), with the exception of some locations within Meridiani Planum (19% plagioclase) [*Rogers and Hamilton*, 2015]. There are three potential explanations for the apparent ultramafic mineralogy in the Siton Undae sand sea deposits: (1) the primary magma source for the dune material was ultramafic, (2) the deposits represent a mechanical mixture of sediments where olivine was preferentially sourced from a basaltic rock, or (3) basaltic

composition materials were transported to the dunes and subsequent alteration preferentially dissolved plagioclase and pyroxene crystals.

An ultramafic peridotite composition source rock could explain the lower abundances of pyroxene and plagioclase in the Siton Undae dune material, and peridotites are known to be present on Mars. For example, the Chassigny and NWA2737 meteorites, sourced from unknown locations on Mars, are ultramafic cumulate rocks (dunnites) [*Bridges and Warren*, 2006]. Therefore, a primary ultramafic composition for the dune material in the northern polar region is possible.

A basaltic source rock composition that underwent subsequent mineral segregation through aeolian transport is also possible [*Mangold et al*., 2011]. Olivine is a harder mineral than plagioclase and pyroxene, and can potentially survive being transported farther distances. Additionally, minerals can be segregated by aeolian activity based on density, and olivine is denser than both plagioclase and pyroxene [*Mangold et al.*, 2011]. Thus, the deposits could become relatively enriched in olivine with distance from the source material solely through mechanical transport processes.

The high abundances of alteration phases associated with the dune deposits would favor the third explanation. However, the detected alteration phases indicate acidic alteration, and at pH < 8, olivine and pyroxene dissolve at much faster rates than plagioclase [*Hausrath et al*., 2008]. Therefore, the first two explanations for the observed ultramafic compositions are favored.

The dunes in the northern polar region are geologically young, based on crater age dating, and the hydrated minerals deposits have most likely developed as a consequence of warm climatic excursions throughout the late Amazonian [*Langevin*, 2005; *Madeleine*

et al., 2014]. However, it is still uncertain at what point the alteration phases in the dune materials developed. They could represent the in situ alteration of primary minerals in the dunes, or they could have been transported to the current location after forming elsewhere [*Fishbaugh et al*., 2007; *Horgan et al*., 2009]. The co-location of gypsum and silica-rich alteration layers strongly suggests the interaction of basaltic materials with acidic water/snow, most likely at low water/rock ratios, followed by the evaporation of salt-rich water [*Horgan et al*., submitted (Chapter 2); *Smith et al*., submitted (Chapter 3)].

The exact position and nature of the compositional boundary between the northern polar region and northern Acidalia is impossible to determine from this study (because of the gap in TES spectral data), but it must occur between ~65 - 70°N. Collectively, Acidalia Planitia is older and has lower wavenumber peak center locations than the northern polar region, which suggests different formation mechanisms between the two regions.

The northern reaches of Acidalia and Utopia Planitiae are distinguished from the southern portions by having lower wavenumber peak center locations (1030 and 1070 cm^{-1}) that are most consistent with feldspars, clays, and zeolites. However, there is no evidence for widespread crystalline clays in global VNIR datasets [*Mustard et al*., 2005], and zeolites are generally modeled in abundances at or near the detection limit of TES in TIR spectral datasets [*Minitti and Hamilton*, 2010]. Therefore, crystalline clays and zeolites are most likely not major surface components in Acidalia Planitia, and the SiO ν_3 feature between ~1030 and 1070 cm^{-1} must be attributed to some other phase(s).

Rampe et al. [2012] measured the TIR spectra of various synthesized allophane compositions as well as an amorphous Si-Al gel. The allophane spectra are used in this

study and have SiO ν_3 features at low wavenumber as discussed in 4.4.2.1. The spectrum of the Si-Al gel was not included in our average allophane spectrum because it has a much higher Si:Al ratio (5.6) than is normally considered for allophane [*Wada*, 1987]. *Rampe et al*. [2012] found that the Si-Al gel has spectral features similar to stilbite (a zeolite), silica-rich volcanic glass, and aluminous opal, but with a SiO ν_3 feature around 1070 cm^{-1}. Therefore, Si-Al gels are potential components of the northern Acidalia and Utopia Planitiae surfaces. In fact, when incorporated in the linear deconvolution of spectra from northern Acidalia, *Rampe et al*. [2012] found that Si-Al gel spectra reduced the modeled phyllosilicate abundances; abundances of zeolites were not significantly affected indicating that they are required for good fits to the data, and are most likely present in the surface. The Si-Al gel was formed in mildly acidic to neutral pH conditions, and zeolites form in neutral to alkaline conditions, so the combination of the phases in northern Acidalia/Utopia Planitiae would be suggestive of aqueous alteration in a relatively neutral pH environment. However, further analysis of the surface spectra could be useful in determining the compositions of other high-silica phases present, as will be discussed in Section 4.5.4.

Most of southern Acidalia/Utopia Planitiae has peak center values similar to highly polymerized alteration phases such as zeolites and silica-rich alteration layers. Gamma Ray Spectrometer (GRS) data from southern Acidalia show only slightly elevated Si content when compared to the global mean, indicating that the weathering environment was not conducive to mobilizing and depositing large concentrations of silica [*Rogers and Hamilton*, 2015]. Silica-rich alteration layers/coatings generally form in environments with low water/rock ratios, and they can be thick enough to obscure the

substrate in TIR spectra, but thin enough that the surface does not become significantly enriched with Si [*Kraft et al.*, 2003; *Horgan et al.*, submitted (Chapter 2); *Smith et al.*, submitted (Chapter 3)]. Thus, silica-rich alteration layers are a likely component of southern Acidalia. Additionally, some locations in southern Acidalia are indicative of sulfate minerals. The collocation of sulfates with these silica-rich phases suggests acidic low water/rock ratio conditions [*Tosca et al.*, 2004; *Hurowitz et al.*, 2006]. The acidic alteration at low water/rock ratios most likely takes place through interactions with seasonal/episodic thin films of liquid water derived from ice or snow melt.

Sulfate detections in Acidalia Planitia have always been uncertain. *Rogers and Hamilton* [2015] modeled relatively high abundances of sulfate (16%) in southern Acidalia, but were reluctant to confirm their presence due to the fact that S data is lacking from GRS measurements, and other mineral datasets (e.g., OMEGA and CRISM) lack parameters that can confidently map sulfates globally. Our results strongly argue for the presence of sulfate minerals in parts of southern Acidalia/Utopia Planitia because the peak center location values in some locations are higher than what's allowable with silicate structures. Additionally, the spectral properties of these locations within southern Acidalia are similar to regions with more definitive detections of sulfates, such as Meridiani Planum and the northern polar region. Future work could target these locations for a more detailed study with VNIR datasets.

Acidalia and Utopia Planitiae surfaces are mantled by what are thought to be deposits of episodic airfall and concurrent cementation by water ice during periods of high obliquity [*Mustard et al.*, 2001; *Tanaka et al.*, 2005; *Tanaka and Fortezzo*, 2012]. The mantling creates a generally smoother surface than that of the southern highlands

that displays hummocky textures at sub-kilometer scales [*Kreslavsky and Head*, 2000]. The presence of hummocky terrain throughout Acidalia and Utopia Planitiae suggests the northern and southern areas could share a common depositional origin [*Kraft et al.*, 2010], but the diffuse spectral boundary at ~45°N indicates a subsequent divergence of dominant surface processes [*Rogers and Christensen*, 2007; *Rogers and Hamilton*, 2015; this study].

A clear morphological transition ~45 – 50°N and coinciding with the spectral boundary is overprinted on the hummocky terrain. South of this transition, Utopia and Acidalia Planitiae display increased small-scale surface roughness (< 1 km) [*Kreslavsky and Head*, 2000] and dissected terrain that is thought to form through the devolitalization of ground ice [*Mustard et al.*, 2001]. Areas north of the boundary grade into subdued hummocky terrain with overprinted periglacial features [*Kraft et al.*, 2010] such as small-scale polygonal cracks that may form through ice-wedge growth or mud desiccation [*Seibert and Kargel*, 2001]. Thus, the Acidalia Planitia surface represents deposits that have been modified by the subsequent removal of or interaction with interstitial water ice. The ice was removed at rates and times that varied depending on latitude and orbital configurations, but most likely remained in the northern reaches for longer durations due to greater stability at higher latitudes [*Head et al.*, 2003].

The Acidalia and Utopia Planitiae surfaces most likely represent basaltic materials chemically weathered through episodic or seasonal wetting [*Seibert and Kargel*, 2001; *Kraft et al.*, 2007, 2010]. The presence of zeolites and Si-Al gel in the northern reaches are suggestive of higher water/rock ratios because they form in relatively neutral pH environments. Additionally, GRS measurements indicate elevated Si abundances to

depths of the upper ~one meter of material in the northern reaches, suggesting significant Si mobility [*Rogers and Hamilton*, 2015]. This could be indicating a greater weathering intensity in the northern reaches, and the higher water/rock ratios could be attributed to the greater stability of water ice at higher latitudes, allowing for long-lasting post-emplacement periglacial alteration.

There are certainly even more localized variations within these broad regions, but this study allows us to compare potential processes happening globally in different geographic locations and in different geologic times. Higher spatial resolution mapping of morphology and spectral properties within these regions can help further distinguish paleo-environments.

4.5.4 Next steps with the curve-fitting technique

Linear deconvolution has failed to provide unambiguous mineral models for Surface Type 2 spectra. Reasons for the non-unique solutions include that: (1) the surfaces contain one or more phase(s) that have non-unique spectral signatures so that they can easily substitute for each other, (2) one or more phase(s) present in the surfaces are not available in the spectral library, or (3) some combination of both explanations. As discussed in 4.2.3 a number of high-silica phases have been shown to have similar TIR spectral features [e.g. *Hamilton et al.*, 2008; *Minitti and Hamilton*, 2010]. For example, high-silica volcanic glass can be reasonably replaced by Fe-smectite and Ca-montmorillonite clay minerals in Surface Type 2 spectral models [*Wyatt and McSween*, 2002]. However, linear deconvolution models generally require a combination of high-silica phases to provide a good fit to the Surface Type 2 spectra, and many phases are modeled in abundances at or near the detection limit. Therefore, it is possible that the

combined high-silica phase spectrum represents a spectrally similar phase that is not available in the spectral library [*Minitti and Hamilton*, 2010].

Minitti and Hamilton [2010] attempted to derive spectral shapes for the high-silica component(s) of Surface Type 2 spectra by taking the modeled abundances of each member of the high-silica phase group, normalizing them to 100%, and adding together the spectra of each component in proportion to their abundances. However, this method is biased in that the resulting high-silica component spectral shape is derived from the minerals in the spectral library. Thus, linear deconvolution is not able to independently identify the high-silica phase spectrum.

The Lorentzian curve-fitting technique could potentially be used to derive the spectral shape of the high-silica phases in Surface Type 2 regions by increasing the number of allowed curves in the model until all of the features in the surface spectrum are accounted for in the model. The fitted curves could then be compared to features of measured phases in order to locate fitted curves with properties that have no measured mineral counterpart in the spectral library. Doing so would allow the structure/composition of the missing phase(s) to be further constrained.

4.6 Conclusions

- The Lorentzian curve fitting technique produced spectral property maps that correlate well with traditional TIR spectral mapping techniques, and even allows for the use of spectral data from regions that were previously disregarded due to low surface temperatures.
- TIR spectra from most of the Martian surface can be modeled well with one symmetric Lorentzian peak in the strong Si-O stretching vibration wavenumber

region. However, this simple model does not work for the northern polar region, which requires at least two peaks for a model of comparable quality. Thus, the northern polar region is mineralogically distinct from the rest of the Martian surface, implying a significantly different geologic history.

- Future modeling should increase the number of peaks allowed in order to improve the quality of the fits, and potentially determine the structures and compositions of phases not available in spectral libraries.
- High abundances of sulfate (~20%) and silica-rich alteration rinds on basalt glass (~19%) were detected in the northern polar region, specifically in the polar sand sea Siton Undae. Thus, the ultramafic or mafic northern polar deposits have most likely been altered with acidic ice melt from the polar cap at low water/rock ratios to form sulfates and silica-rich alteration layers. These findings support the conclusions of previous studies.
- Acidalia and Utopia Planitiae are separated into northern and southern parts with a boundary ~45°N based on morphological and compositional differences. The older southern portions have compositions that indicate acidic water interactions at low water/rock ratios, most likely though periodic interstitial ice melt, forming sulfates and silica-rich alteration layers. The younger northern parts have compositions (Si-Al gel and zeolites) more indicative of circum-neutral pedogenic alteration in a periglacial environment under potentially higher water/rock ratios than in the southern parts.
- All Surface Type 2 regions are spectrally distinct, and have undergone diverse geologic processing and alteration events that vary with geographic location.

CHAPTER 5

AMORPHOUS MATERIAL FROM RAPID EVAPORATION OF BASALT WEATHERING SOLUTIONS: IMPLICATIONS FOR AMAZONIAN ALTERATION ON MARS

5.1 Introduction

The characterization of amorphous and poorly crystalline silicates has increasingly become of interest due to their prevalence on the Martian surface as detected through ground-based spectroscopic observations [*Mccord et al.*, 1982; *Singer*, 1985], orbital thermal-infrared spectroscopic measurements [*Bandfield*, 2002; *Wyatt and McSween*, 2002], and *in-situ* measurements by rovers and landers [*Ming et al.*, 2006; *Ruff et al.*, 2006; *Bish et al.*, 2013; *Morris et al.*, 2013]. On Earth, soils are known to frequently contain amorphous and poorly crystalline silicate weathering products, yet these phases are poorly constrained and understood because they lack the long-range order that makes their crystalline counterparts so distinctive. Exploring potential silicate weathering product formation pathways can help constrain past and present aqueous environments on Mars.

The current Martian surface environment is cold and relatively dry, with regionally, seasonally, and diurnally variable atmospheric water vapor pressure [e.g., *Farmer*, 1976; *Haberle et al.*, 2001; *Smith et al.*, 2001]. Similar conditions have likely persisted through most of the Amazonian (roughly the last 3 billion years) [*Bibring et al.*, 2006; *Ehlmann et al.*, 2011]. It has been suggested that weathering under these conditions might be driven by small amounts of transient, circum-neutral pH liquid water (e.g., melt from ice, snow, or frost) interacting with the Martian surface (Figure 5.1) [e.g., *Haskin et*

al., 2005; *Richardson and Mischna*, 2005; *Yen et al.*, 2005; *Chevrier and Mathé*, 2007; *Kraft et al.*, 2007]. Aqueous solutions resulting from weathering would rapidly evaporate or freeze under these conditions, potentially precipitating amorphous materials since little time is allowed to develop well-crystalized precipitates. Currently, there is a deficiency in our understanding of what amorphous silicate materials form under these conditions, and how the phases change with varying parameters such as duration of water-rock interaction, starting material, and water composition.

In order to address this deficiency, we constructed a laboratory in which we performed weathering experiments to better understand the types of secondary products that form through the rapid evaporation of weathering solutions. The laboratory was designed to produce weathering solutions of varying composition under two different atmospheres: an oxidizing Earth atmosphere and a Martian atmosphere. The resulting weathering solutions were rapidly evaporated onto sample cup substrates in order to collect the precipitates for further analysis. Physical and chemical properties of the precipitates were studied using infrared (IR) spectroscopy and x-ray diffraction (XRD). Doing so, we gained insight into the types of secondary phases that might have formed under Amazonian conditions, and determined the potential of this pathway as a formation mechanism for the amorphous phases detected on the Martian surface.

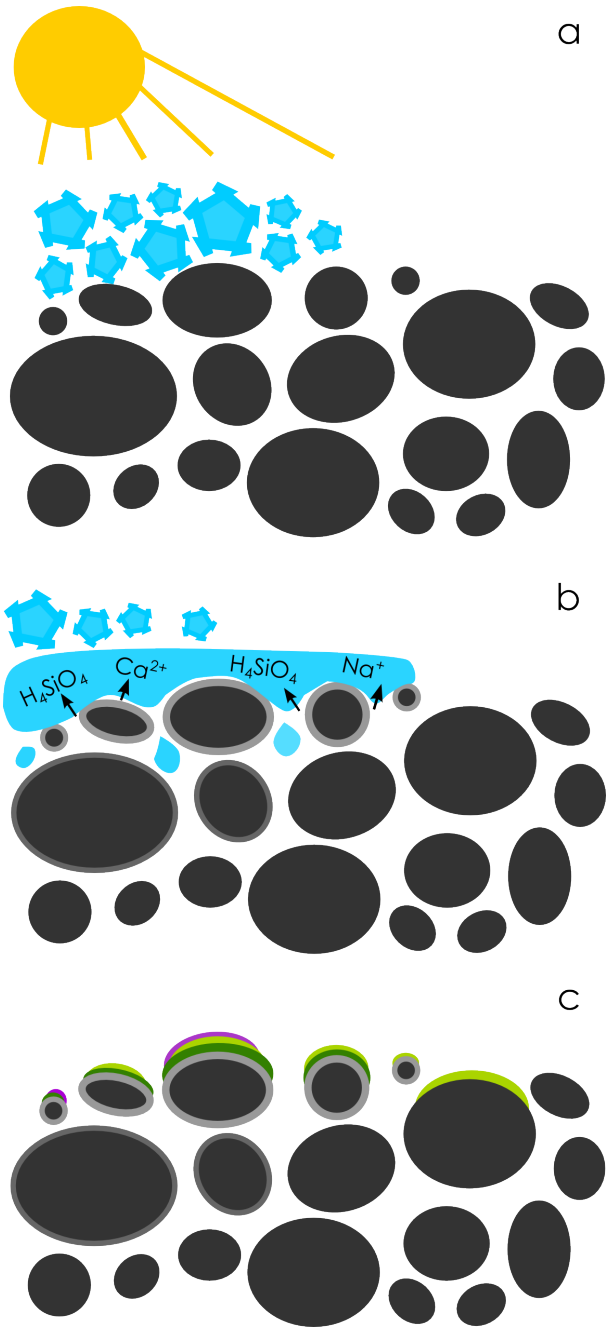

Figure 5.1. Model of Amazonian weathering process. (a) water ice, snow, or frost in contact with primary igneous materials is heated to form (b) thin films of transient liquid water that dissolve ions from the rock forming a weathering solution, which is evaporated (c) leaving behind amorphous silicate precipitates potentially in the form of rock coatings.

5.2 Background

5.2.1 Amazonian weathering model

Mars has significant amounts of water ice [*Boynton et al.*, 2002], water frost [e.g., *Carrozzo et al.*, 2009], and putative snow deposits from previous climatic conditions [*Christensen*, 2003]. However, liquid water is not currently stable on the Martian surface due primarily to the low vapor pressure of water in the atmosphere. The vapor pressure depends on the temperature of the principal reservoir of water on the surface (currently the northern polar ice cap) [*Richardson and Mischna*, 2005]. At current average surface temperatures, the water vapor pressure is ~1 Pa, which is well below the triple point pressure [*Richardson and Mischna*, 2005]. However, radiative heating conditions on Mars change diurnally, seasonally, and with shifting orbital parameters such that liquid water could exist briefly during the conversion of ice to vapor (and vice versa) [e.g., *Farmer*, 1976; *Haberle et al*., 2001; *Möhlmann*, 2004, 2010; *Richardson and Mischna*, 2005; *Kereszturi and Rivera-Valentin*, 2012].

The weathering model presented in Figure 5.1 describes what could happen to rock that comes into contact with transient liquid water. Water ice, snow, or frost at or near the surface is heated until it melts (Figure 5.1a). The liquid water briefly interacts with the surrounding rock, dissolving ions into solution (Figure 5.1b) through mechanisms depending on a number of factors including: the aqueous composition, the environmental temperature, and the degree of crystallinity of the rock. It is thought that under acidic conditions, some silicate minerals and glasses undergo leaching, where mono- and divalent cations are preferentially removed from the materials and are exchanged for protons, leaving behind a silica-rich rind (represented as the grey layers

surrounding the parent rock in Figure 5.1b) [e.g. *Schott et al.*, 2009]. Dissolution under more neutral pH conditions might be congruent, where all of the atoms of the solid are dissolved stoichiometrically, leaving no residual rind [e.g. *Petit et al.*, 1990]. There are theoretical uncertainties in the evaporation rates of liquid water on the current Martian surface [*Haberle et al*., 2001] so it is uncertain how long the liquid water could remain in contact with the rock. However, it is certain that the weathering solution would eventually evaporate or freeze (if the liquid condenses out of the atmosphere in the evening as temperatures drop), forcing ions to precipitate out of solution (Figure 5.1c). Precipitates could form as small particles or rock coatings. At low water/rock ratios, each interaction would likely precipitate small volumes of secondary phases. Yet, a substantial volume of material could accumulate over 3 billion years, forming coatings or deposits that are thick enough to be spectrally significant (the products of each interaction represented as a different color coating in Figure 5.1c).

Natural weathering systems can be open or closed. Open weathering systems allow for the composition of the system to change as some ions are transported away from the system. Closed systems do not allow ions to be lost, so that the system composition depends on the composition of the parent rock, the starting solution composition, and the dissolution mechanism (leaching vs. congruent). The weathering scenario in Figure 5.1 is a closed system, where none of the solution is transported away from the weathering system. This is a safe assumption for weathering systems with low water/rock ratios. At higher water/rock ratios, the solution may become more mobilized such that the more soluble ions are transported away from the system, leaving behind the less soluble ions to form precipitates.

Serious limitations arise when simulating transient water-rock interactions over billions of years. The primary purpose of this study is to isolate amorphous phases formed through the rapid evaporation of basalt weathering solutions. Higher water/rock ratios substitute for long periods of geologic time in order to obtain reasonable experiment durations and precipitate volumes large enough to analyze using various methods. Additionally, while no ions were "lost" to the system, solutions were transported away from the parent rock surfaces in order to isolate and characterize the mineralogy of the precipitates; thus, avoiding the complex spectral effects of coatings on substrates [e.g. *Christensen and Thliveris Harrison*, 1993; *Kraft et al*., 2003; *Minitti et al*., 2007].

5.2.2 Amorphous/poorly crystalline phases on Mars

Amorphous or noncrystalline phases lack long-range structural order, or translational periodicity. The long-range order is what makes crystalline phases so unique in common mineral identification measurement techniques [*Handke and Mozgawa*, 1993]. Amorphous phases can be primary (i.e., volcanic glass) or secondary in origin. Secondary amorphous phases, or weathering products, are common components of soils as clay-sized particles or as coatings or rinds on rocks within the soil [e.g., *Ashley*, 1909; *Colman*, 1982; *Eggleton et al.*, 1987; *Dorn*, 1998; *Essington*, 2004]. Most crystalline substances that contain a sufficient amount of network forming components (e.g., Si, Al, Fe) can form as noncrystalline phases under the right conditions [*Yamane and Asahara*, 2000]. Thus, there are myriad possible compositions of the amorphous phases. Fortunately, even "amorphous" phases usually have some degree of short-range order, so that distinction can be made between compositions [*Handke and Mozgawa*, 1993].

Noncrystalline phases have been recognized for decades as being potentially important components of the Martian surface. Chemical X-ray fluorescence data and surface reflectance spectra from the Viking Lander and Orbiter instruments were used to detect poorly crystalline Fe^{3+}-bearing phases in parts of the low-albedo Martian surface [e.g., *Toulmin III et al.*, 1977; *Evans and Adams*, 1980; *Allen et al.*, 1981; *Singer*, 1982; *Golden et al.*, 1993; *Morris et al.*, 1993, 2001, 2003]. Suggestions for the poorly crystalline phases found at the Viking 1 Lander site in Chryse Planitia (in the northern lowlands) include hydrous ferric-oxide gels [*Evans and Adams*, 1980] and palagonite, a heterogeneous basalt glass alteration product with highly variable optical and structural properties [*Soderblom and Wenner*, 1978; *Allen et al.*, 1981]. Both of these materials were found to have strong spectral similarities to the Viking 1 Lander site, but neither match is perfect.

Thermal-infrared (TIR) spectra from the Thermal Emission Spectrometer (TES) instrument suggest the presence of high abundances (~15 - 25%) of amorphous silicate phases in large swaths of low-albedo regions on Mars [*Bandfield*, 2002; *Wyatt and McSween*, 2002; *Rogers and Christensen*, 2007; *Rampe et al.*, 2012]. The amorphous silicate spectral signature was initially identified as silica-rich volcanic glass [*Bandfield*, 2002], but subsequent studies have shown that the phases might be amorphous weathering products [*Wyatt and McSween*, 2002; *Kraft et al.*, 2003; *Michalski et al.*, 2005; *Minitti et al.*, 2007; *Rampe et al.*, 2012]. Recent TES mapping has shown that the composition of the amorphous silicate phases most likely varies from region to region [*Rampe et al.*, 2012; *Rogers and Hamilton*, 2015; *Smith and Christensen*, 2016]. Visible and near-infrared (VNIR) and TIR spectra from parts of the northern lowlands,

specifically the polar sand sea Siton Undae and parts of Acidalia Planitia, are consistent with amorphous silica-rich alteration layers on basalt glass [*Horgan and Bell*, 2012; *Horgan et al*., submitted (Chapter 2)], while TES spectra from other parts of the northern lowlands, such as Northern Acidalia and Utopia Planitia, are used to detect Si-Al gels and allophane. Allophanes are poorly-crystalline hydrated aluminosilicates with a variable chemical formula ($1.0 - 2.0SiO_2 \cdot Al_2O_3 \cdot 2.5 - 3.0H_2O$) that are alteration products of basaltic materials under weakly acidic to neutral pH aqueous environments [*Wada*, 1987; *Rampe et al.*, 2012; *Bishop et al.*, 2013].

Localized deposits of amorphous phases have been identified *in situ* by the Spirit rover in Gusev Crater. The Mini-TES instrument on the Spirit rover detected amorphous silicate phases in the TIR spectra of the Clovis and Watchtower sites within the Columbia Hills in Gusev Crater [*Ruff et al.*, 2006]. The spectra were best modeled using high abundances (35 – 40%) of basalt glass, but the authors were careful to note that no secondary amorphous silicate phases were available in the spectral library at the time of the study, and so they could not conclude whether the amorphous silicate phase was primary or secondary in origin [*Ruff et al.*, 2006]. *Morris et al.* [2006] used elemental compositions from the Alpha Particle X-ray Spectrometer (APXS) and mineralogical compositions from the Mössbauer Spectrometer (MB) on board the Spirit rover to show that the Clovis and Watchtower rocks in the Columbia Hills had undergone significant aqueous alteration. They found that the rocks are enriched in S, Cl, and Br, are highly oxidized, and contain the mineral goethite. Thus, the amorphous silicate phase detected by Mini-TES is most likely secondary in origin.

The Chemistry and Mineralogy (CheMin) instrument, which utilizes XRD, onboard the Mars Science Laboratory (MSL) rover in Gale Crater has also detected high abundances (~27%) of amorphous phases [*Bish et al.*, 2013]. *Bish et al.* [2013] identified basalt glass and allophane using XRD pattern analysis at the Rocknest sample site. CheMin, Alpha Particle X-Ray Spectrometer (APXS), and Sample Analysis at Mars (SAM) instruments were used to determine that, with the exception of S abundance, the amorphous component(s) at the Rocknest site have chemistry and volatile content similar to amorphous components in terrestrial palagonitic volcanic soils [*Bish et al.*, 2013].

5.2.3 Chemical weathering of basaltic glass

The majority of the Martian surface is thought to be basaltic in composition [e.g., *Singer et al.*, 1979; *Bandfield et al.*, 2000a; *Hamilton et al.*, 2001; *Rogers and Christensen*, 2007; *Rogers et al.*, 2007]. Some of the low-albedo regions are consistent with crystalline basalt even though environmental conditions on Mars are more conducive to explosive volcanism [*Wilson and Head*, 1994]. In fact, basaltic glass is not detected in the TIR spectral analyses of Martian surface spectra, even when a range of igneous glass compositions are included in the modeling [*Minitti and Hamilton*, 2010]. Thus, if any glassy material formed, it must have been altered after emplacement [*Minitti and Hamilton*, 2010].

One common type of alteration is chemical weathering, a process that involves the coupling and feedback of dissolution, precipitation, and mineral replacement reactions [*Gislason and Oelkers*, 2003]. In this study, we are specifically interested in the chemical weathering of basaltic glass in the following two types of water-rock environments: (1) fresh ice/snow/frost melt or pore space water that is essentially pure

water with pH ~7 and (2) ice/snow/frost melt or pore space water that has interacted with a current day Martian atmosphere that would have a pH ~5. Here we explore the various aspects of basaltic glass chemical weathering in mildly acidic to neutral aqueous environments in low to ambient temperatures (< ~25°C).

Dissolution is the first step in chemical weathering, and many studies have focused on the dissolution mechanisms and dissolution rates for basaltic glass [e.g., *Crovisier et al*., 1987; *Guy and Schott*, 1989; *Oelkers*, 2001; *Gislason and Oelkers*, 2001; *Oelkers and Gislason*, 2001; *Stefánsson and Gíslason*, 2001]. Basaltic glass is essentially a multioxide silicate with Si and Al in tetrahedral coordination forming a random network structure that is linked by sharing corner oxygen atoms (bridging oxygens) [*Henderson*, 2005]. The network structure is modified by the addition of other cations, such as Mg^{2+}, Ca^{2+}, Fe^{2+}, K^{+}, and Na^{+} that fit into larger coordination sites [*Henderson*, 2005]. There is general disagreement about whether basalt glass dissolves congruently (stoichiometrically) or whether ions are selectively leached from the glass (incongruently/nonstoichiometrically) [see *Ruiz-Agudo et al.*, 2012]. Incongruent dissolution has been the favored mechanism for decades and is a multi-step process involving: 1) the substitution of H^{+} for monovalent and divalent cations (K^{+}, Na^{+}, Mg^{2+}, Ca^{2+}) that are subsequently leached from the silicate structure; 2) exchange of trivalent cations (Al^{3+}, Fe^{3+}) for H^{+}, which partially liberates Si; and 3) breaking of Si-O bonds, most likely through the absorption of H_2O [*Oelkers*, 2001]. Results from new measurement techniques are in support of congruent dissolution mechanisms, specifically interfacial dissolution-reprecipitation, for all silicates, potentially including glass [*Hellmann et al.*, 2004, 2012; *Putnis and Putnis*, 2007; *Geisler et al.*, 2010; *Ruiz-Agudo*

et al., 2012]. In this mechanism, all ions are dissolved in proportion to their stoichiometric abundance, but Si and Al become supersaturated in the interfacial fluid, and precipitate as silica-rich layers. This mechanism attributes the apparent selective dissolution of monovalent and divalent cations that is commonly observed in solution chemistry to the precipitation of secondary phases [e.g., *Hellmann et al.*, 2004, 2012]. In general, at 25°C and circum-neutral pH (~5 – 9), cation release rates from basalt glass follow the order $Na^+ > K^+ > Ca^{2+} \approx Mg^{2+} > Al^{3+} \approx Fe^{2+}$ [*Guy and Schott*, 1989; *Hurowitz et al.*, 2006].

Bulk glass dissolution rates change as a function of pH and temperature. Most studies agree that at temperatures < ~200°C the dissolution rate exhibits a parabolic relationship with pH so that rates increase at the extremes, and reach a minimum at circum-neutral pH conditions. Although the exact pH at which the minimum occurs is known to shift as a function of temperature [*Oelkers and Gislason*, 2001]. *Gislason and Oelkers* [2003] calculated experimental steady-state bulk glass dissolution rates and found that at temperatures between ~ 11°C and 50°C the dissolution rate reached a minimum at a pH between ~4.5 and 6. *Bandstra and Brantley* [2008] and *Hausrath et al.* [2008] calculated a minimum bulk basalt glass dissolution rate around pH 5. *Guy and Schott* [1989] calculated a minimum basalt glass dissolution rate at pH ~5.6 for experiments at 50°C, using Si release rates as a proxy for bulk glass dissolution. Similary, *White* [1983] reported an Si release rate minimum at pH 5.2 for experiments performed at 25°C. Therefore, at temperatures < ~50°C, bulk glass dissolution rates should be lower at pH 5 (environment 2) than at pH 7 (environment 1).

As environmental conditions change, elements in solution may precipitate as secondary phases. The natural weathering of basaltic glass usually forms some mixture of allophane, iron oxide-hydroxide, clay minerals [*Eggleton et al.*, 1987], imogolite [*Wada*, 1987; *Bishop et al.*, 2013], zeolite [*Hay and Sheppard*, 2001], palagonite [*Hay and Iijima*, 1968], and salts [*Doner and Lynn*, 1977]. Hydrous aluminosilicate gels can also form as intermediate steps between the parent material and a more crystalline phase [*Ashley*, 1909; Strawn, 2015]. The exact phases and quantities precipitated depend on a number of factors including: the composition of the starting material, the composition of the solution, the time allowed for formation, and the temperature of the system.

5.2.4 Previous basalt weathering models and experiments under current Martian conditions

Gooding [1978] used thermodynamic equilibrium models to predict the types of alteration products that form from basalt minerals assuming current partial pressures (p) of O_2, H_2O, and CO_2 in the Martian atmosphere and H_2O as vapor and liquid phases. He found the products were largely dependent on the primary minerals and their relative abundances, the weathering environment, and the reaction pathways. At the p_{CO2} and p_{O2} for the current Martian atmosphere, *Gooding's* [1978] thermodynamic modeling indicated that the chemical weathering of olivine yields: magnesite + hematite + quartz; pyroxene weathering yields: calcite + magnesite + hematite + quartz + Al_2O_3; plagioclase weathering yields: Ca-beidellite + calcite + quartz + Al_2O_3; basaltic glass weathering yields: palagonite, oxides, carbonates, and sulfates (± chlorides); and magnetite readily oxidizes to hematite. *Gooding* [1978] also noted that the premature arrest of chemical reactions could yield different metastable mineral assemblages, such as clays, than those

predicted. On Earth, with significant water, most basaltic materials are altered to clays, goethite [*Gooding*, 1978], allophane, imogolite [*Colman*, 1982; *Wada*, 1987], and noncrystalline silica [*McLennan*, 2003]. The exact compositions of the phases are determined by the particular environmental conditions.

A number of studies have experimentally weathered basaltic materials under conditions that mimic the Martian atmospheric. *Bullock et al.* [2004] and *Bullock and Moore* [2004] dissolved mineral mixtures meant to simulate the composition of Martian meteorites in water. The experiments were performed under Earth and Martian atmospheres. The resulting solutions were analyzed in order to determine the composition of salts that would have precipitated if the solutions evaporated (though the solutions were not evaporated). They found the dominant cations dissolved in the Mars atmosphere solutions were Ca^{2+}, Mg^{2+}, Al^{3+}, and Na^{+}, and the major anions dissolved were C^{-}, F^{-}, SO_4^{2-}, and Cl^{-}. Based on these results, *Bullock et al.* [2004] concluded that the salts measured at the two Viking Lander sites and at the Mars Pathfinder landing site were most likely formed through the interaction of surface or subsurface liquid water with basalt under conditions similar to those found on Mars today. *Bullock et al.* [2004] and *Bullock and Moore* [2004] did not study Si or the types of silicates that could form through similar interactions.

The experimental apparatus designed by *Bullock et al.* [2004] informed the design of the experimental chamber used in this study. Their apparatus consisted of a sealed glove box in which they isolated a set of sample flasks that each had their own separate gas circuit. The temperature and pressure were controlled inside the glove box and within each of the flask subsystems. The pressure inside the glove box was kept at slightly

higher than ambient pressure to ensure that lab air did not contaminate the experiment. *Bullock et al.* [2004] choose to run their experiments at a total pressure of ~ 1 bar with an atmosphere gas blend that matched the present-day composition of the Martian atmosphere. They reasoned that a lithostatic pressure of one bar is encountered in the Mars subsurface at a depth of about 10m, where brines might be present.

5.3 Methods

5.3.1 Laboratory design

The weathering laboratory utilizes a four-port isolation acrylic glovebox (60" W x 24" D x 25" H) outfitted with gas inlet and outlet ports and an electrical outlet strip (Figure 5.2). An automatic Relief-Bleed (RB) valve from Terra Universal was added to the chamber in order to keep it at a safe overpressure, and a hole was drilled in the back panel in order to accommodate the vacuum pump hose used for filtration. The hole was fitted with a rubber grommet to achieve a tight seal (Figure 5.2).

The layout of the glove box is roughly divided into thirds where the main steps of the experiments are performed: dissolution, filtration, and evaporation/precipitation (Figure 5.2). Dissolution occurs in 1000 mL Nalgene beakers that are covered with aluminum foil in order to reduce evaporation. After dissolution, the solution is separated from the tephra solids via vacuum filtration using a Buchner funnel and filter paper with a nominal 2.5 μm pore size. The weathering solution is then dripped at a rate of 0.02 mL/minute, using a peristaltic pump, into stainless steel sample cups coated with Aeroglaze Z306 high emissivity paint. The sample cups are heated to a temperature of ~ 40 °C on a hot plate, in order to achieve rapid evaporation of each drop before the next drop falls. The entire 1000 mL of solution is deposited in ~ 60 days.

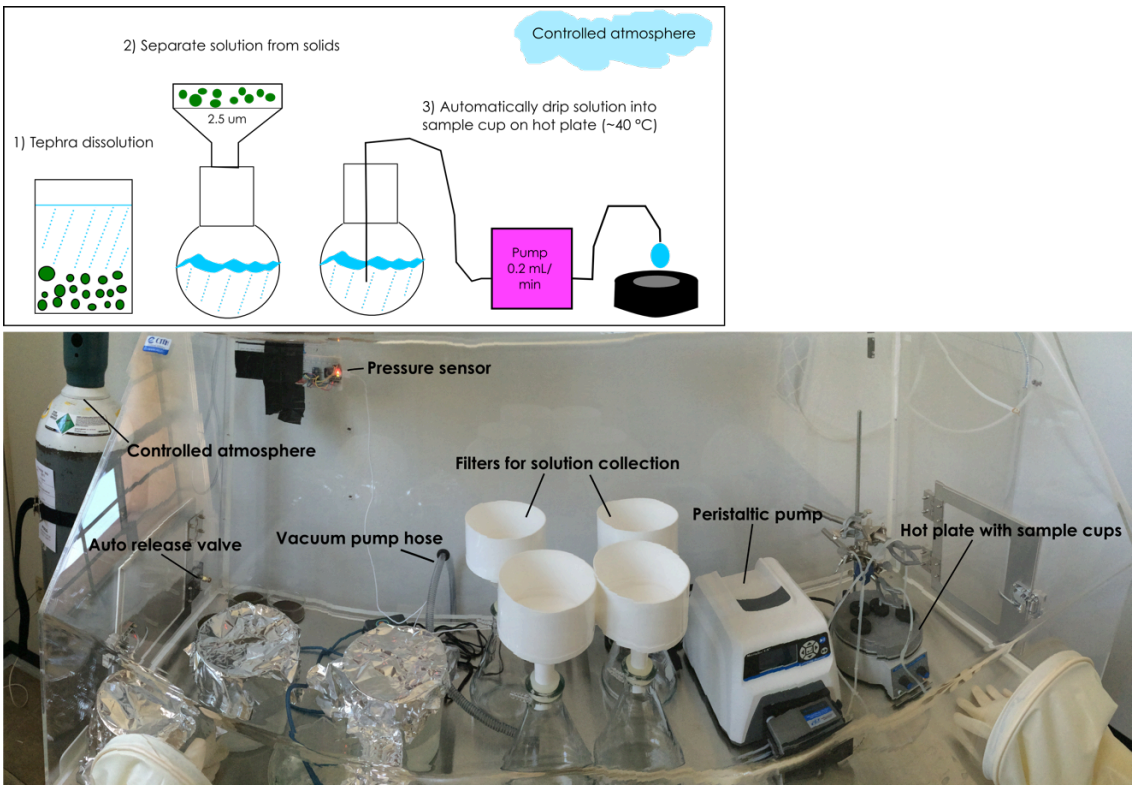

Figure 5.2. (Top) Schematic configuration of the experimental chamber including: (1) Tephra dissolution, (2) solution filtration, (3) solution dripping and evaporation. (Bottom) photograph of the chamber in use with notes describing some of the modifications to the glove box.

A constant overpressure (~1.05 atm) inside the chamber ensures that the composition of the atmosphere is controlled throughout the duration of the experiments. Pressure is recorded using a custom-made differential pressure sensor consisting of an Arduino board outfitted with a temperature and pressure sensor and wireless capabilities. The pressures inside and outside the glove box are recorded in a single file. During the experiments, the desired gas composition is introduced to the glove box through a flow meter and the inlet valve on the chamber; excess gas exits the chamber via the automatic RB valve. Large volumes of water are evaporated during the experiments, and so a desiccant (Clariant – Container Dri II) is used to control the humidity in the chamber.

5.3.2 Starting material collection and processing

Two different basaltic tephra samples were collected from the San Francisco Volcanic Field in northern Arizona (Figure 5.3). Two compositions were selected in order to determine how the mineralogy of the precipitates varies with starting material composition. The samples were wet and dry sieved to collect sand-sized particles (106 μm – 1 mm). After sieving, multiple density separations in DI water were used to remove organics and clinging fines. The samples were then dried in a furnace at 80 °C for 24 hours, and sterilized at 300 °C for 5 hours.

The processed starting material was sent to Actlabs for major and minor oxide and elemental analysis. Weight percent (wt.%) oxides were measured using X-ray fluorescence, except FeO, which was measured using a titration method. S was measured through Combustion Infrared Detection, and Cl was measured through Instrumental Neutron Activation Analysis (INAA).

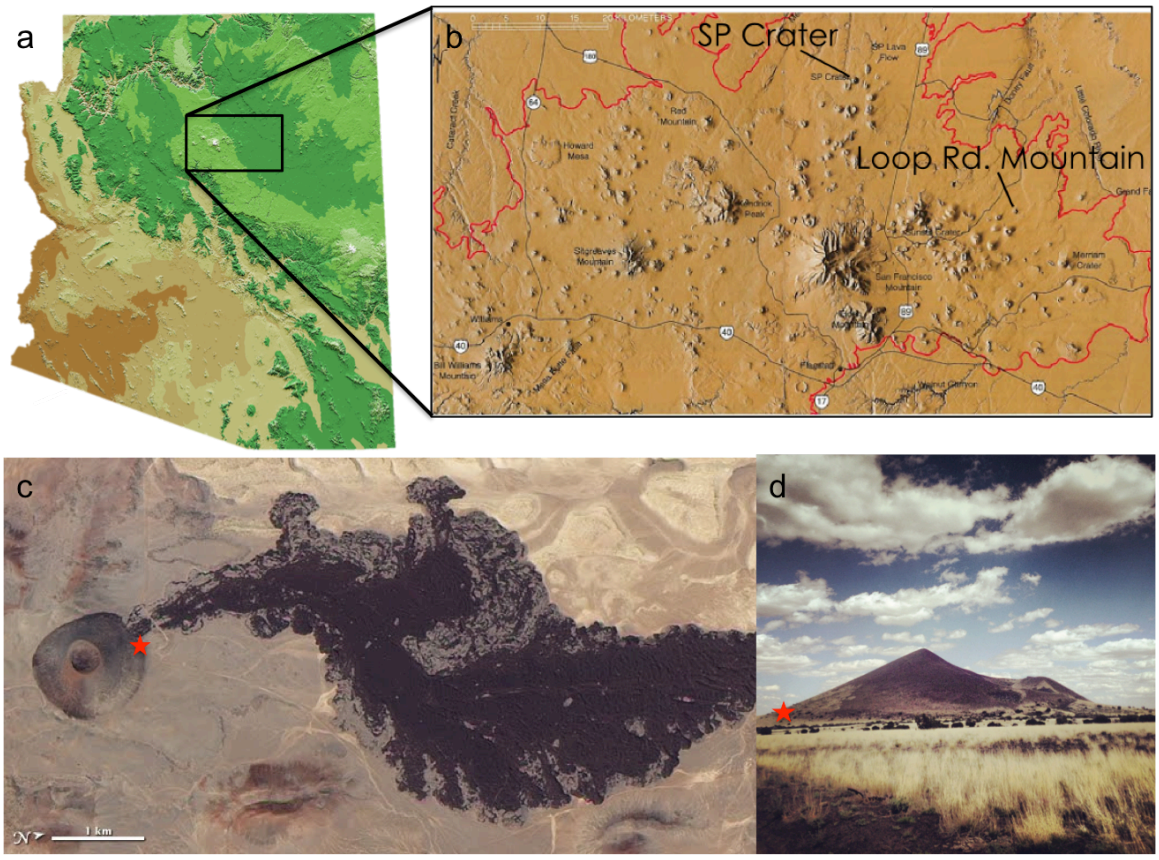

Figure 5.3. (a) Context map of the San Francisco Volcanic Fields in northern Arizona. The black box highlights the enlarged region in (b). (b) Digital Elevation Model of the San Francisco Volcanic Fields [*Hanson*, 2003] modified to show the locations where the starting material was collected. (c) Red star indicates the sampling site at SP Crater. (d) Red star indicates the sampling site at Loop Rd. Mountain.

5.3.3 Experiment design

Two successful sets of experiments have been run in the laboratory (Figure 5.4): one under an "Earth" atmosphere, and one under a Martian atmosphere. Each set consists of four experiments that are divided such that each starting material composition is included in two experiments that differ in the length of time of dissolution (4 and 10 days). The experimental dissolution time periods were selected based on ion release rates determined from previous basalt glass dissolution experiments [e.g., *Gislason et al.*, 1993]. The duration of dissolution needed to be long enough that the solution precipitated enough material to be detected using the various measurement techniques. It was also important to determine how the solution changed with dissolution time to understand how well the experiments approximate the solution chemistry of very brief water-rock interactions. The experimental design described here sets the foundation for a variety of future experiments by providing a framework that can be modified to test specific parameters not considered in these initial experiments.

The chamber was loaded with all of the necessary equipment, labware, and consumables for an entire run. The starting solution chemistry was obtained for each experiment by bubbling the desired atmosphere through 1000 mL of DI water. A 5 mL sample was taken for chemical analysis. 50 g of processed tephra was then added to the starting solution and the rock was dissolved for the desired length of time. The tephra and solution mixture was stirred once a day to expose new surface areas, and 5 mL of solution was sampled from the mixture on days 4, 6, and 10 to track changes in the solution composition.

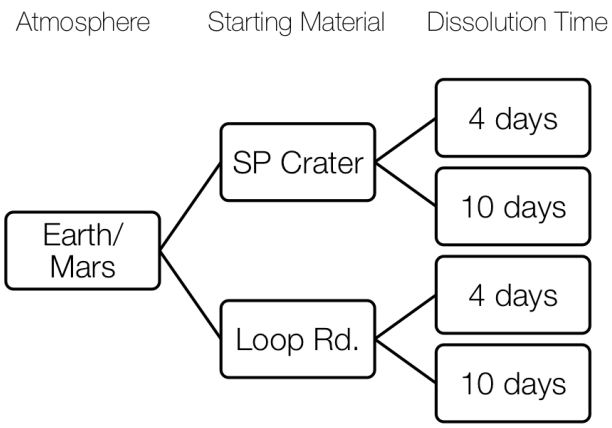

Figure 5.4. Experimental matrix

The Earth analog atmosphere was delivered to the chamber from an air scrubber, which removes carbon dioxide and water, so that the starting composition of the solution was relatively neutral (pH ~7) and oxidizing. The Martian atmosphere was more complicated to produce since current Martian atmospheric pressure is ~ 6.0 mbar on average, which is ~1/100 of the atmospheric pressure on Earth (Figure 5.5). Obstacles increase significantly when a laboratory is run at less than Earth pressure, including a greater potential for contamination by the laboratory atmosphere. In order to avoid complications, we simulated the Martian atmosphere by using a gas blend that achieved the correct solution chemistry while maintaining a slightly positive over-pressure within the chamber. The Mars analog gas blend has the correct number of moles of chemically significant gas species in the Martian atmosphere, while maintaining Earth's atmospheric pressure with inert N_2 (Figure 5.5). This atmospheric chemistry produced a relatively low-oxygen, carbonic acid with pH ~5, and a dissolved oxygen (DO) content of ~$1.3*10^{-5}$ mM, calculated using pO_2.

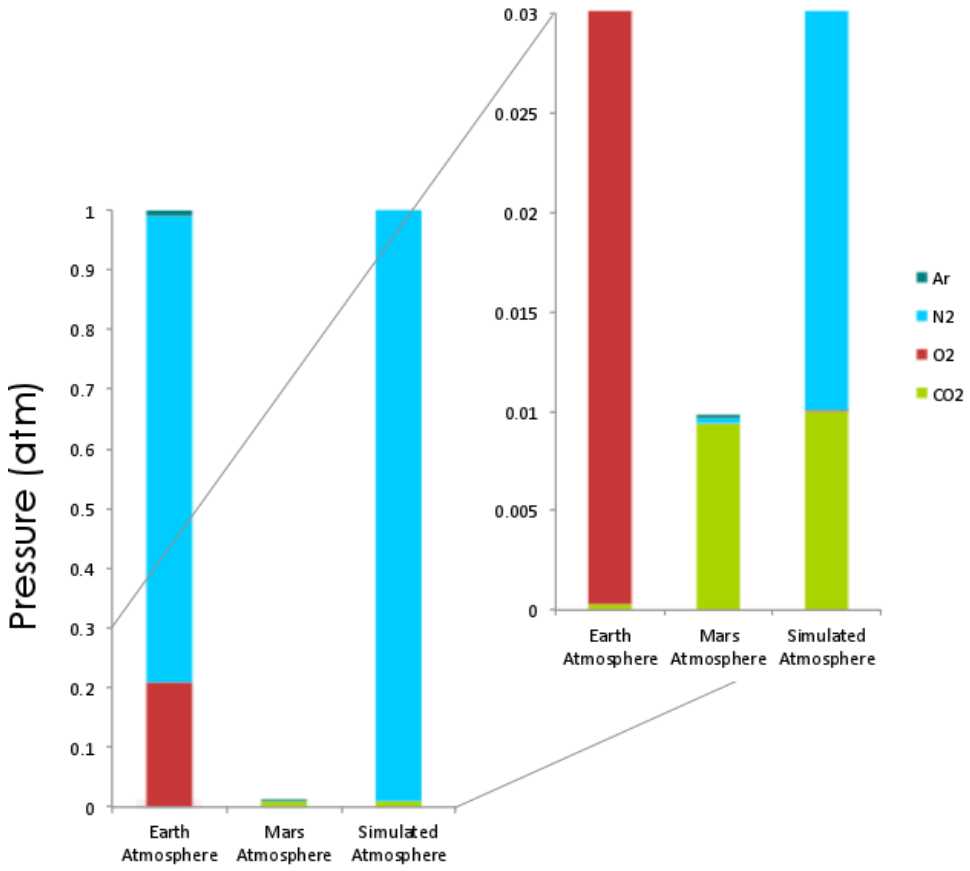

Figure 5.5. Plot of Earth's atmospheric pressure and composition with Mars's atmosphere and the simulated Martian atmosphere (left). The right panel expands the pressure scale so the Mars atmosphere can be seen. The Mars analog gas mixture is 99.458% N_2, 0.541% CO_2, and 0.001% O_2.

5.3.4 Solution analysis

Solution samples were analyzed using Ion-Chromatography (IC) in the Group Exploring Organic Processes in Geochemistry (GEOPIG) laboratory at ASU. Cation and anion concentrations were determined to ppb levels using a Dionex DX 600 IC System instrument to measure Na^+, K^+, Mg^{2+}, Ca^{2+}, SO_4^{2-}, F^-, Cl^- and PO_3^{4-}. Additionally, samples were analyzed for Si, Al, Ti and Fe in the KECK Laboratory at ASU using a Thermo X Series Quadrupole Inductively Coupled Plasma Mass Spectrometer (ICP-MS).

5.3.5 Precipitate analysis

The precipitates were analyzed with instruments similar to those that have detected amorphous/poorly crystalline phases on the Martian surface so that we can directly compare data. The precipitates were measured using VNIR spectroscopy, TIR spectroscopy, and XRD.

The TIR spectra of the precipitates were measured at the Arizona State University Mars Space Flight Facility using a Nicolet Nexus 670 spectrometer and at the Vibrational Spectroscopy Laboratory Facilities at Stony Brook University using a Nicolet 6700 Fourier Transform Infrared (FTIR) spectrometer; both instruments are configured to measure emissivity [*Ruff et al.*, 1997]. Spectra were collected at a spectral resolution of 2 cm^{-1} over the range of 200 – 2000 cm^{-1}. Samples were precipitated into stainless steel cups coated with high emissivity black paint to achieve near unit emissivity. The cups and samples were heated to 80 °C for at least an hour prior to being measured, and this temperature was maintained during spectral acquisition by actively heating the sample with a hotplate.

Mineral abundances were estimated by modeling the TIR spectra using a spectral library of potential phases (Table 5.1) including common basalt weathering products and a blackbody spectrum to obtain a non-negative linear least squares fit to each measured spectrum [*Ramsey and Christensen*, 1998; *Rogers and Christensen*, 2007]. End-members were chosen based on multiple parameters including spectrum quality, sample quality, and sample size - selecting coarse particulate or hand samples when possible. The detection limit for the linear deconvolution method ranges between 5 – 10% [*Feely and Christensen*, 1999], and the quality of the model is quantified by the root-mean-square (RMS) error, a parameter that compares the modeled emissivity spectrum to the measured spectrum [*Ramsey and Christensen*, 1998; *Rogers and Aharonson*, 2008]. In general, a lower RMS value indicates a better fit, though the model should also be visually inspected for quality. Additionally, it is possible for the algorithm to select phases not present in the sample in order to substitute for end-members that are not available in the spectral library [e.g., *Ruff et al.*, 2006].

VNIR spectra of the precipitates were collected using the SCORPIUN laboratory at ASU with an ASD Fieldspec 3 Portable Spectroradiometer, attached to a fiber-optic light source and goniometer at a phase angle of 30°. Data were acquired between 350 – 2500 nm with a spectral resolution of 3 nm at 700 nm and 10nm at 1400/2100 nm. The spectrometer is calibrated using a Labsphere Spectralon white reference (SRS-99-10), which is 99% reflective and optically flat (+/- 4%) over the entire spectral range. Sample reflectance was obtained by co-adding 100 individual measurements, and is reported relative to the white reference.

Table 5.1. Spectral endmember library

Mineral Group	*Endmember*
Phyllosilicates	Beidellite SBId-1
	Illite ECL:ILL102
	Kaolinte KGa-1b
	Kaolinite (poorly ordered) ECL:KAO104
	Montmorillonite (Ca) STx-1
	Montmorillonite (Na) SWy-2
	Nontronite WAR-5108
	Saponite
	Serpentine ECL:SRP109
	Smectite SWa-1
	Talc BUR-4640C
Zeolites	Analcime WAR49-0672
	Heulandite agu_heu1[1]
	Stilbite agu_stil[1]
Sulfates	Anhydrite S9
	Bassanite S11
	Burkeite S71
	Gypsum S11
	Jarosite S51
	Kieserite
	Natroalunite MINUN-22
	Szomolnokite 104276
	Thenardite S22
Carbonates	Calcite C27
	Dolomite C20
	Magnesite C55
	Siderite C50
Oxides	Brucite RAN-45
	Hematite BUR-2600
Amorphous aluminosilicates	Allophane Si:Al 0.44 ALLO044[2]
	Allophane Si:Al 0.58 ALL0058[2]
	Allophane Si:Al 0.92 ALLO092[2]
	Aluminosilicate gel Si:Al 5.6 ALL0560[2]
	Aluminous opal
Silica	Opal-A
	Opal-CT
	Quartz BUR-4120
Felsic volcanic glass	K-rich glass (obsidian)
Mafic volcanic glass	BAS101 baseline[3]
	ICE170 baseline[3]
Altered mafic volcanic glass	BAS101A (213 days)[3]
	ICE170A (213 days)[3]

[1]*Ruff* [2004]
[2]*Rampe et al*. [2012]
[3]*Horgan et al*. [submitted]

XRD patterns were measured at the LeRoy Eyring Center For Solid State Science using a PANalytical X'Pert PRO MRD diffractometer. Patterns were obtained using fixed divergent slit incident beam optics and X'celerator diffracted beam optics. Patterns were measured between 10° – 70° (2θ), with a step size of 0.0501°, a rate of 189.865 seconds per step, and a scan speed of 0.033534 °/s. The patterns were analyzed using X'Pert High Score Plus software. It must be noted that the samples were measured without removing the precipitates from the substrate, which could introduce sampling bias due to the fact that any crystals in the particulate would not be randomly orientated. The reason for not removing the samples is to maintain the precipitation structure for future analysis using other methods such as transmission electron microscopy (TEM) and electron microprobe.

5.4 Results

5.4.1 Starting material composition

The compositions of the starting materials are given in Table 5.2. The tephra from Loop Rd. Mountain is basaltic (based on silica content, 47.76%), whereas the tephra from SP crater has higher silica content (54.05%) and is more of a basaltic andesite. The Loop Rd. Mountain tephra also has significantly greater Al_2O_3, FeO, Fe_2O_3, and Mg content than the SP Crater tephra. It is clear that the SP Crater tephra must contain some small fraction of weathering products that were not removed during sample processing because it has a higher concentration of volatiles lost on ignition (LOI; 3.19%) than the tephra from Loop Rd. Mountain (0.81%). Both samples contain small amounts of sulfur, but Loop Rd. Mountain tephra has a greater concentration (0.1%) than SP Crater tephra (<0.1%).

Table 5.2. **Starting material composition (wt%)**

	Loop Rd. Mountain	***SP Crater***
SiO_2	47.76	54.05
TiO_2	1.63	1.06
Al_2O_3	16.34	14.99
FeO	6.9	4.0
Fe_2O_3	4.57	3.72
MnO	0.186	0.172
MgO	9.62	6.3
CaO	8.27	7.68
Na_2O	2.64	2.76
K_2O	0.88	1.85
MgO	9.62	6.3
CaO	8.27	7.68
Na_2O	2.64	2.76
K_2O	0.88	1.85
P_2O_5	0.41	0.43
S	0.01	< 0.01
C	0.05	0.11
Other	0.507	0.502
LOI	0.81	3.19
Total	100.00	100.09

5.4.2 Laboratory and experimental setup

All experiments were successfully completed within the glove box. The chamber maintained a relatively constant atmospheric over-pressure throughout the duration of the experiments, only dropping briefly with the use of the vacuum pump as the solution was filtered. Additionally, there was no condensation/humidity build up during the experiments, so the desiccant was able to help maintain a more realistic current-day Martian environment.

The volume of solution extracted at each step was sufficient for most elemental abundance measurements. However, the uncertainty in the Si measurements using ICP-MS was too great to definitively detect abundance differences between the Earth and Martian atmosphere solutions. Future experiments should extract a greater volume of solution at each step in order to measure Si using the silicomolybdate method, which has greater precision (± 4% under ideal test conditions). Additionally, it would be helpful to have a separate volume of solution available for pH measurements to reduce the risk of contaminating solutions with the KCl pH probe calibration standards.

5.4.3 Solution composition

The concentrations of all cations increase with increased dissolution time (Figure 5.6), with no major differences in the ratios of ion concentrations between the different dissolution time periods. Cation concentrations in solution follow the trend Na > Si > K ≈ Ca > Mg > Al > Ti > Fe ≈ Mn in almost all cases for solutions formed under both atmospheres (see Figure 5.6 for graphical representation and Table 5.3 for exact values). Our results are consistent with cation concentrations from basalt glass dissolution experiments reported by *Guy and Schott* [1989], but are quite different from solution

cation concentrations in the order Mg ≈ Ca > Si > Na ≈ Al > K > Fe ≈ Mn reported by *Bullock et al.* [2004] who dissolved basaltic crystalline minerals in water under Earth and Mars atmospheres. This difference suggests different mechanisms for crystalline basalt and basalt glass dissolution. In general, the cation concentration differences between SP Crater and Loop Rd. Mountain tephra solutions can be attributed to differences in the starting chemistry. SP Crater starting material has lower Al and higher K and Si than Loop Rd. Mountain starting material, and these differences are reflected in the measured cation abundances in solution.

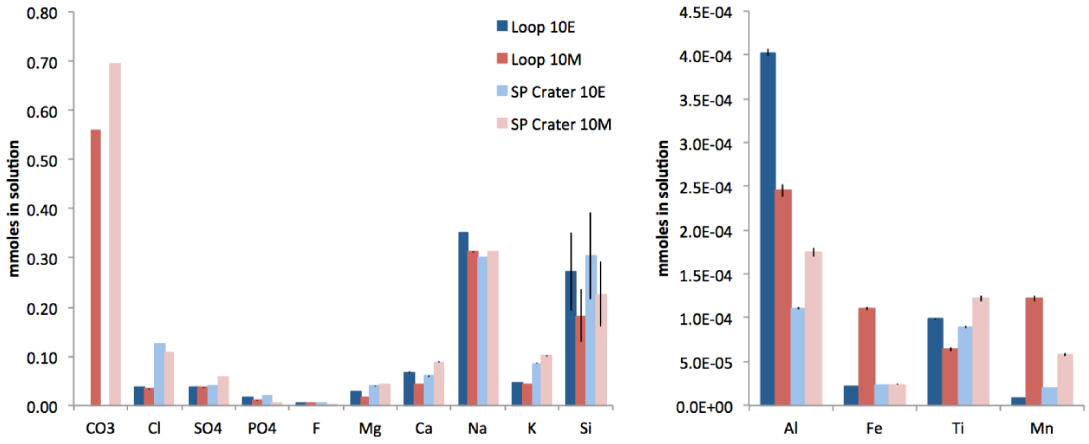

Figure 5.6. Solution chemistry for major cations and anions in solution after 10 days dissolution time. Colors represent the same experiments in both graphs. Note the change in scale for the plot on the right. Error bars represent the standard deviation in measurements based on two injections for IC data, and standard tests for ICP-MS data. All data points except CO_3 have error bars (representing one standard deviation), but for some elements, the error is so low that the bar is not visible.

Table 5.3. Abundances of ions in solution (mmoles/L)

		Earth Atmosphere				Mars Atmosphere			
Starting Material		**4 days**	**SD[1]**	**10 days**	**SD[1]**	**4 days**	**SD[1]**	**10 days**	**SD[1]**
Loop Rd. Mountain	**Si**	1.98E-01	29	2.71E-01	29	1.05E-01	29	1.82E-01	29
	Al	1.13E-03	1	4.02E-04	1	5.56E-04	3	2.45E-04	3
	Fe	1.67E-04	1	2.17E-05	1	2.87E-05	2	1.11E-04	2
	Mg	8.41E-03	4.08	2.91E-02	0.27	2.51E-02	1.66	1.73E-02	1.54
	Ca	2.27E-02	5.37	6.73E-02	1.87	2.52E-01	1.70	4.30E-02	2.35
	Na	2.96E-01	0.02	3.51E-01	0.16	2.58E-01	0.25	3.12E-01	0.52
	K	2.75E-02	0.03	4.58E-02	0.41	2.88E-01	0.67	4.33E-02	1.09
	Ti	6.51E-05	1	9.89E-05	1	4.31E-05	3	6.40E-05	3
	Mn	5.64E-05	2	7.95E-06	2	8.91E-05	3	1.22E-04	3
	Cl	3.37E-02	0.57	3.77E-02	0.12	2.47E-02	0.30	3.29E-02	0.35
	SO_4	3.64E-02	0.20	3.85E-02	0.32	3.15E-02	1.71	3.57E-02	1.08
	PO_4	2.79E-02	0.95	1.68E-02	0.23	5.63E-03	0.98	9.36E-03	0.61
	F	6.11E-03	1.04	5.60E-03	3.33	8.91E-03	4.63	4.44E-03	4.80
	CO_3	N/A	N/A	N/A	N/A	3.34E-01	N/A	5.60E-01	N/A

		4 days	**SD[1]**	**10 days**	**SD[1]**	**4 days**	**SD[1]**	**10 days**	**SD[1]**
SP Crater	**Si**	2.00E-01	29	3.03E-01	29	1.47E-01	29	2.26E-01	29
	Al	1.14E-04	1	1.11E-04	1	3.02E-04	3	1.75E-04	3
	Fe	3.16E-05	1	2.37E-05	1	4.19E-05	2	2.42E-05	2
	Mg	3.27E-02	1.09	3.91E-02	1.41	3.33E-02	0.70	4.25E-02	0.89
	Ca	5.20E-02	2.30	5.95E-02	2.43	6.94E-02	0.46	8.81E-02	1.12
	Na	3.03E-01	0.26	3.01E-01	0.38	2.88E-01	0.14	3.13E-01	0.05
	K	6.74E-02	0.18	8.56E-02	0.28	6.44E-02	0.16	1.01E-01	1.69
	Ti	7.83E-05	1	8.93E-05	1	1.06E-04	3	1.22E-04	3
	Mn	2.00E-04	2	2.03E-05	2	8.86E-04	3	5.81E-05	3
	Cl	1.45E-01	0.14	1.25E-01	0.07	7.63E-02	0.08	1.08E-01	0.11
	SO_4	4.03E-02	0.04	3.92E-02	0.03	5.41E-02	1.06	5.89E-02	0.31
	PO_4	1.70E-02	0.00	2.01E-02	1.70	4.28E-03	2.70	4.72E-03	2.46
	F	6.13E-03	1.76	5.20E-03	1.07	2.91E-03	0.38	3.45E-03	0.32
	CO_3	N/A	N/A	N/A	N/A	4.98E-01	N/A	6.94E-01	N/A

[1]Standard deviation (%) for each measurement

Anion concentrations in Loop Rd. Mountain weathering solutions under both atmospheres follow the trend $SO_4 \approx Cl > PO_4$. In contrast, Cl is significantly higher than SO_4 and PO_4 in the SP Crater weathering solutions (Figure 5.6), and since the Loop Rd. Mountain and SP Crater starting material have comparable Cl concentrations, Cl must be in a more soluble phase in the SP Crater tephra. Aqueous carbonate concentration was calculated via charge balance using pH measurements with the assumption that OH^- and carbonate are the only anions making up the remaining negative charge. Unfortunately, no pH measurements were available for the Earth atmosphere solutions; however, we can assume the carbonate concentration was minimal due to the lack of CO_2 in the scrubbed atmosphere. *Guy and Schott* [1989] did not report anion concentrations, and so we must compare our basalt glass dissolution anion concentrations to results from crystalline basalt dissolution experiments. *Bullock et al.* [2004] measured much higher sulfate abundances than Cl or HPO_4, but generally found that Cl concentrations were greater than HPO_4. They attributed the large abundance of SO_4 to the dissolution of pyrite.

For the most part, ion concentration differences between the Earth and Martian atmosphere solutions are very small (~1/100 mmole). Si exhibits the most significant difference in the measured ion concentrations, but the Si measurements have a large standard deviation that prevents a definitive conclusion (Figure 5.6). Yet, the observation of decreased Si concentrations in Martian atmosphere solutions would be consistent with previous studies of bulk basalt glass dissolution rates that found a minimum rate at pH ~5.5, as discussed in Section 5.2.2.

5.4.4 Precipitate physical properties

All of the samples are generally similar in color and physical nature (Figures 5.7 and 5.8). They are heterogeneous mixtures of light colored material and some darker red and sometimes black material. The darker/redder material looks glassy while the lighter material tends to be fractured at 10^2 μm scales (Figure 5.7b, d and 5.8b, d) and can sometimes contain crystals around 10^2 μm in length (Figure 5.7f, h and Figure 5.8d). The darker/redder material generally forms along the perimeter of the precipitates, but can sometimes be found intruding into the center of the precipitates such as in L10E and SP4E (Figure 5.7c and Figure 5.8a). Both of the Martian 10-day solution precipitates are overall lighter-toned than those of the other samples.

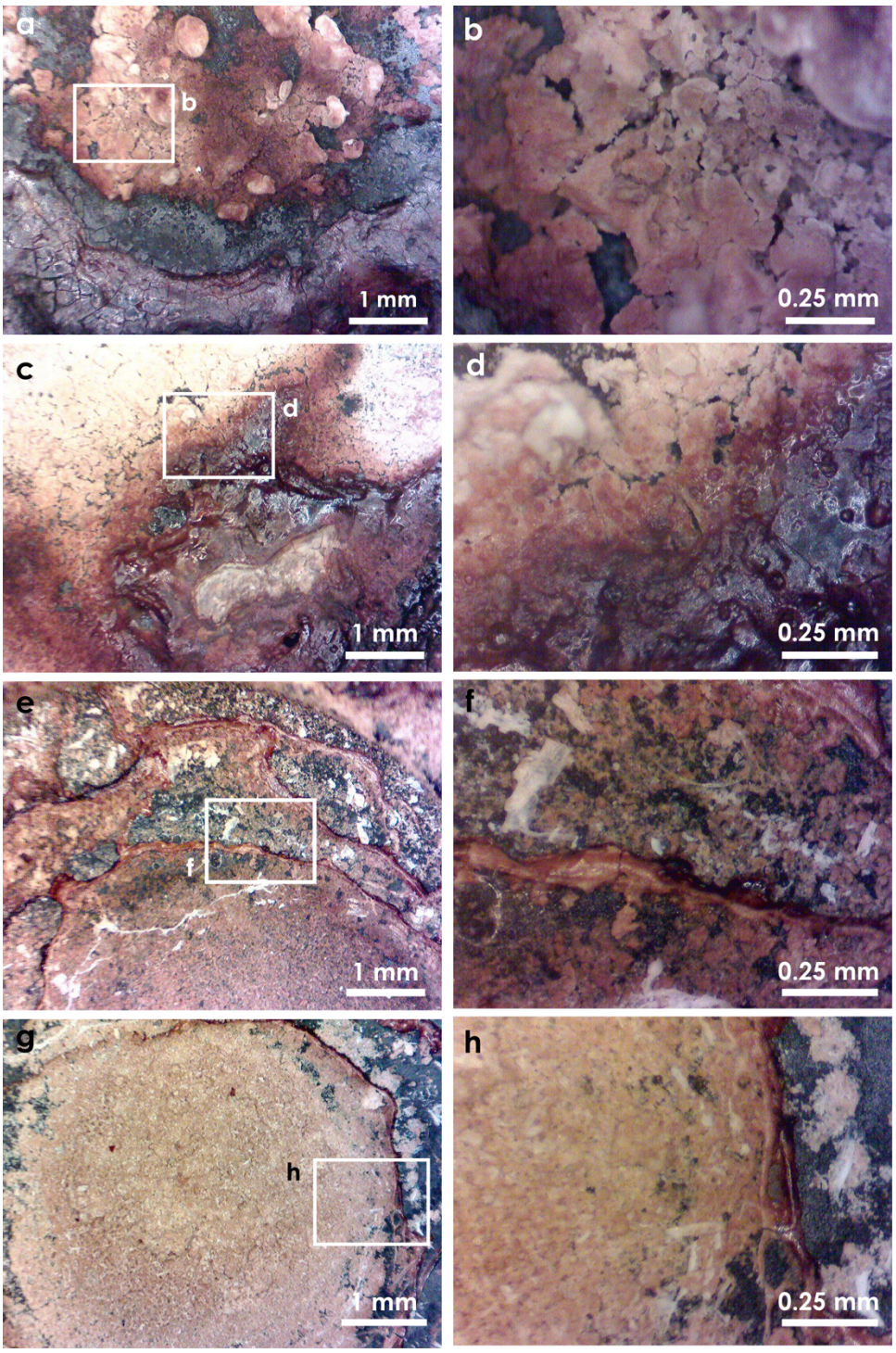

Figure 5.7. Loop Rd. precipitates from 4-day Earth atmosphere solution (a and b), 10-day Earth atmosphere solution (c and d), 4-day Martian atmosphere solution (e and f), and 10-day Martian atmosphere solution (g and h).

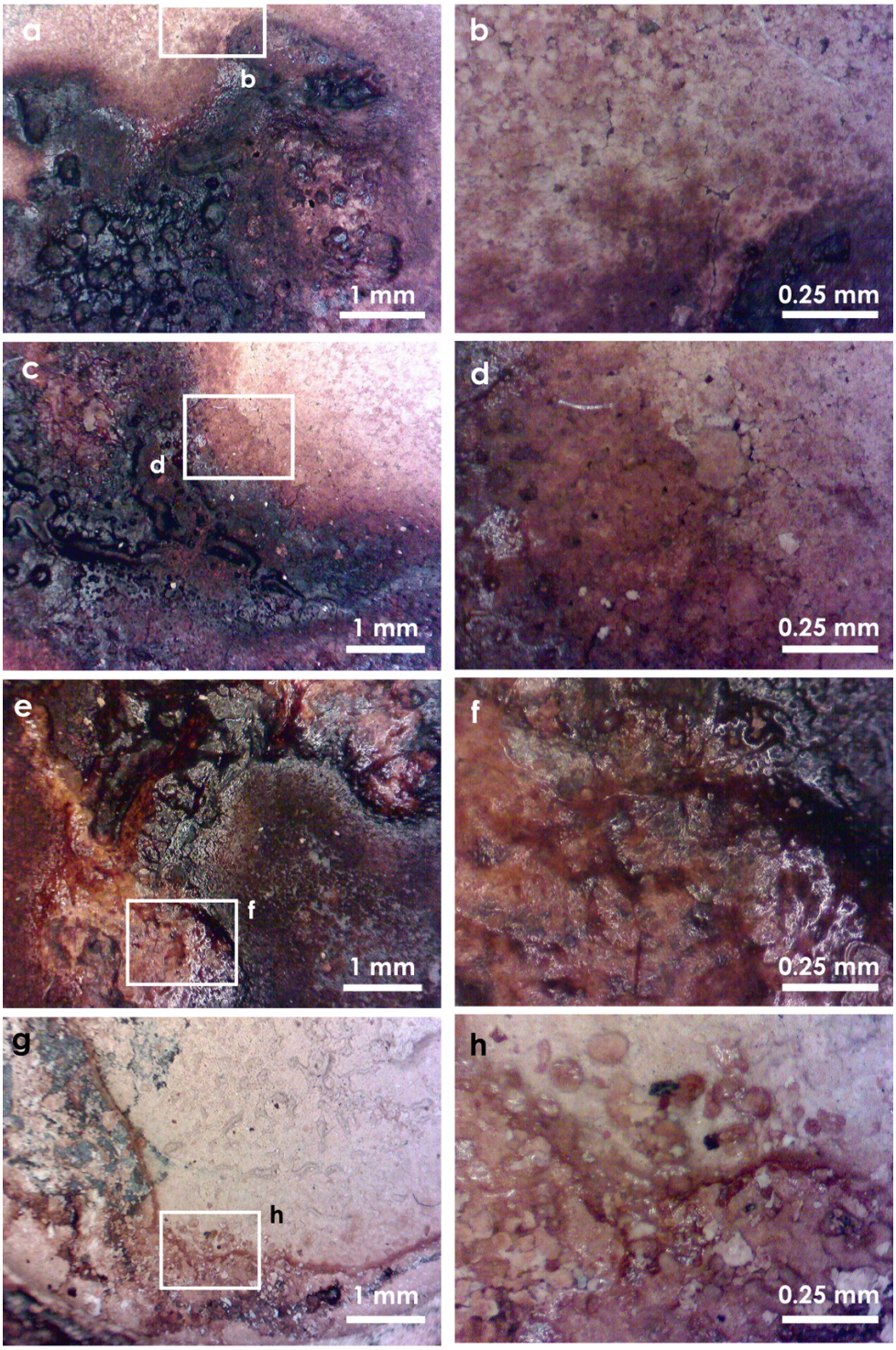

Figure 5.8. SP Crater precipitates from 4-day Earth atmosphere solution (a and b), 10-day Earth atmosphere solution (c and d), 4-day Martian atmosphere solution (e and f), and 10-day Martian atmosphere solution (g and h).

5.4.5 Precipitate analyses

Each measurement type has its strengths and weaknesses. For example, TIR is capable of determining mineral abundances and identifying crystalline and noncrystalline silicates, but has a sampling depth of the upper 10s of micrometers of the surface with a spot size ~1 cm and spectral analysis is impossible when too little material or fine particles (<~60 μm) are formed; VNIR can easily identify transition metal minerals and hydrous phases, but only detects the upper few micrometers of the surface and cannot give quantitative mineral abundances; XRD can identify crystalline phases, but is difficult to interpret if little or no crystalline material forms. The results from these analyses are summarized in Table 5.4.

Table 5.4. Summary of precipitate mineralogy

Mineralogy of precipitates formed in Earth atmosphere			
	Thermal-infrared	***Near-infrared***	***XRD***
Loop Rd. 4-days	N/A	Nanophase Fe-oxides, saponite, opal	N/A
Loop Rd. 10-days	Basalt glass, aluminiosilicate gel, aluminous opal	Nanophase Fe-oxides, magnesite, opal	Magnesite, ilmenite
SP Crater 4-days	Basalt glass	Nanophase Fe-oxides, saponite, brucite, opal, eugsterite	N/A
SP Crater 10-days	Basalt glass, serpentine	Nanophase Fe-oxides, magnesite, opal	N/A
Mineralogy of precipitates formed in Martian atmosphere			
Loop Rd. 4-days	Serpentine, altered basalt glass, aluminosilicate gel, jarosite	Nanophase Fe-oxides, brucite, saponite	Thermonatrite, nontronite, silica
Loop Rd. 10-days	Altered basalt glass, aluminosilicate gel, serpentine, montmorillonite, jarosite, magnesite	Nanophase Fe-oxides, brucite, saponite	Thermonatrite, nontronite, silica, sodium carbonate sulfate
SP Crater 4-days	Burkeite, natroalunite, altered basalt glass	Nanophase Fe-oxides, magnesite, saponite, brucite, eugsterite	Thenardite, hydrated sodium bicarbonate
SP Crater 10-days	Allophane, magnesite, dolomite, serpentine	Nanophase Fe-oxides, magnesite, brucite	Thenardite, silica, artinite, brucite, magnesite, aluminum sulfate hydrate

5.4.5.1 TIR spectra of precipitates: Major component mineralogy

For the most part, TIR spectra of precipitates formed from 4-day solutions look similar to those from 10-day solutions for the same starting material and atmosphere, indicating that, at least for the time periods tested here, the duration of dissolution has little bearing on the resulting precipitate mineralogy (Figures 5.9 and 5.10). The Loop Rd. 4-day Earth atmosphere precipitates spectrum resembles that of the sample cup, indicating that the sample is too thin (< ~10 μm) for TIR spectral analysis, and so we do not include it in the results. The spectra of Earth atmosphere precipitates could be sufficiently modeled with a mineral endmember library, but the Martian atmosphere precipitate spectra were much more complex as will be discussed below.

All Earth atmosphere solution samples exhibit relatively broad and smooth spectral emission features in the asymmetric Si-O stretching region (SiO ν_3; 833 – 1176 cm^{-1}) and in the Si-O bending region (350 – 480 cm^{-1}) (Figures 5.9 and 5.10) [*Salisbury and Walter*, 1987; *Michalski et al.*, 2005], signifying the precipitation of silicate phases. The location of the SiO ν_3 feature is a function of the polymerization of the silicate structure, where higher wavenumber positions indicate a higher degree of silica tetrahedra connectedness. The Loop Rd. 10-day Earth sample has one single SiO ν_3 feature with a position centered at ~1040 cm^{-1}, which is consistent with basalt glass, while the SP Crater 10-day Earth atmosphere sample has its SiO ν_3 feature centered at ~1015 cm^{-1}, indicating that the silicate structure is less polymerized than the Loop Rd. sample. The SP Crater 4-day Earth atmosphere precipitate sample also has a SiO ν_3 band at ~1015 cm^{-1}, but exhibits additional spectral features at 610 cm^{-1} and 1100 cm^{-1}, which

are indicative of sulfates (Figure 5.10). The combination of the 1015 cm^{-1} and 1100 cm^{-1} bands create a doublet feature that is centered at ~1050 cm^{-1}, similar to basalt glass. The Si-O bending feature for all Earth atmosphere samples occurs at ~460 cm^{-1}, and has a smooth positive slope toward lower wavenumber.

All precipitates from solutions formed in an Earth atmosphere are modeled with high abundances of basalt glass, and small abundances of other aluminosilicate phases (Figure 5.11). When basalt glass is excluded from the end member library, the Si-O bending features at 460 cm^{-1} are modeled relatively well with amorphous aluminosilicates (Si-Al gel and aluminous opal), serpentine, and obsidian, but the RMS errors increase significantly and visually the spectral fits worsen for the main SiO ν_3 features, especially for the SP Crater 4-day Earth atmosphere solution precipitates (Figure 5.11d). When basalt glass is included, the Loop Rd. Mountain 10-day sample is modeled with detectable abundances of "amorphous aluminosilicates", while serpentine and obsidian are included in most sample models at abundances below the detection limit. Basalt glass is not a potential phase for the precipitates, since it forms under significantly different environmental conditions, but it is included in the spectral unmixing analysis because basalt glass is modeled in TIR spectra from what are thought to be altered rocks on the Martian surface [*Ruff et al.*, 2006]. Thus, the basalt glass shape must be substituting for a secondary amorphous or poorly ordered aluminosilicate(s) of which there is no current spectrum in the library.

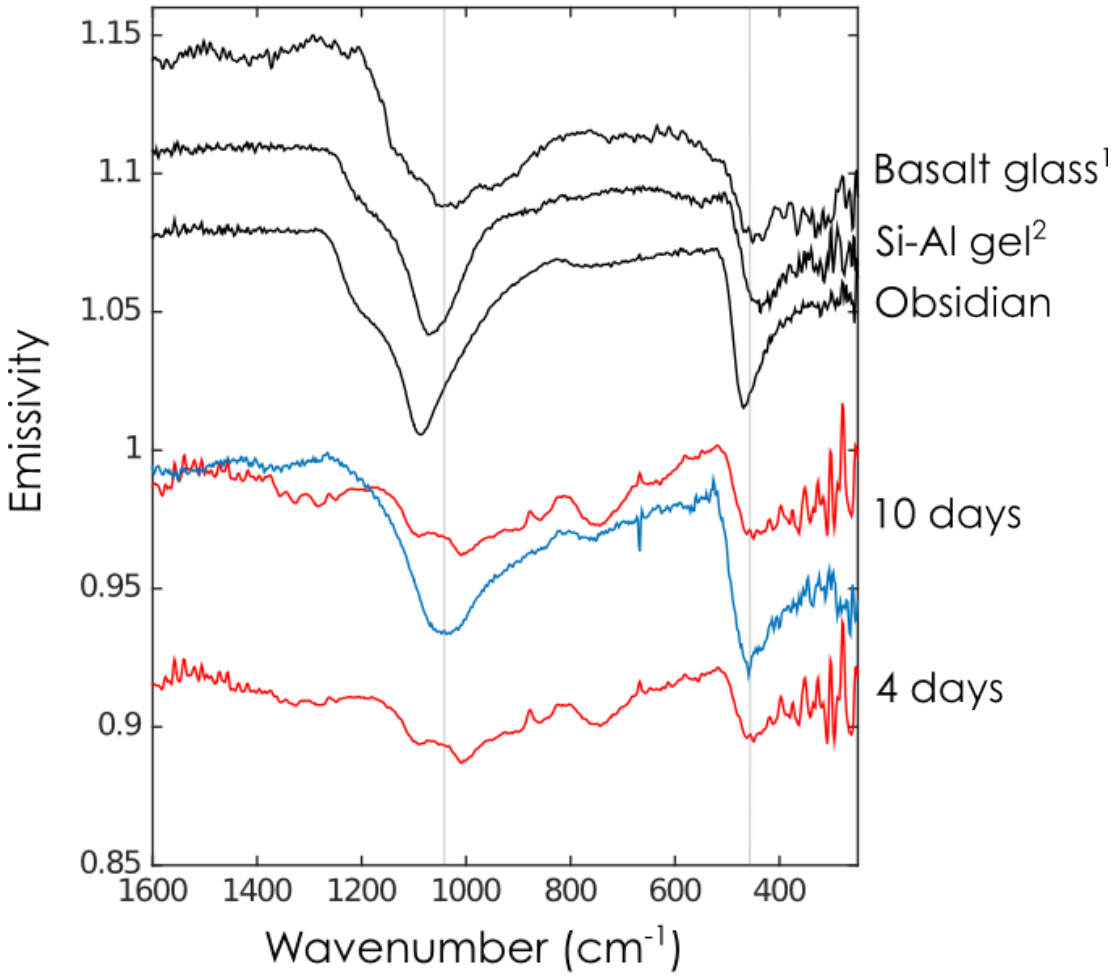

Figure 5.9. TIR spectra of Loop Rd. Mountain Earth atmosphere (blue) and Martian atmosphere (red) precipitates compared to spectra of phases in the endmember spectral library. Grey lines indicate position of major emission features in precipitate spectra. Spectra are offset for clarity (from top to bottom, offset = +0.15, +0.11, +0.08, 0, 0, -0.08). The 4-day solution Earth atmosphere precipitates were not thick enough to obscure the sample cup substrate, and so the spectrum is not included.

[1]*Horgan et al.* [submitted]
[2]*Rampe et al.* [2012]

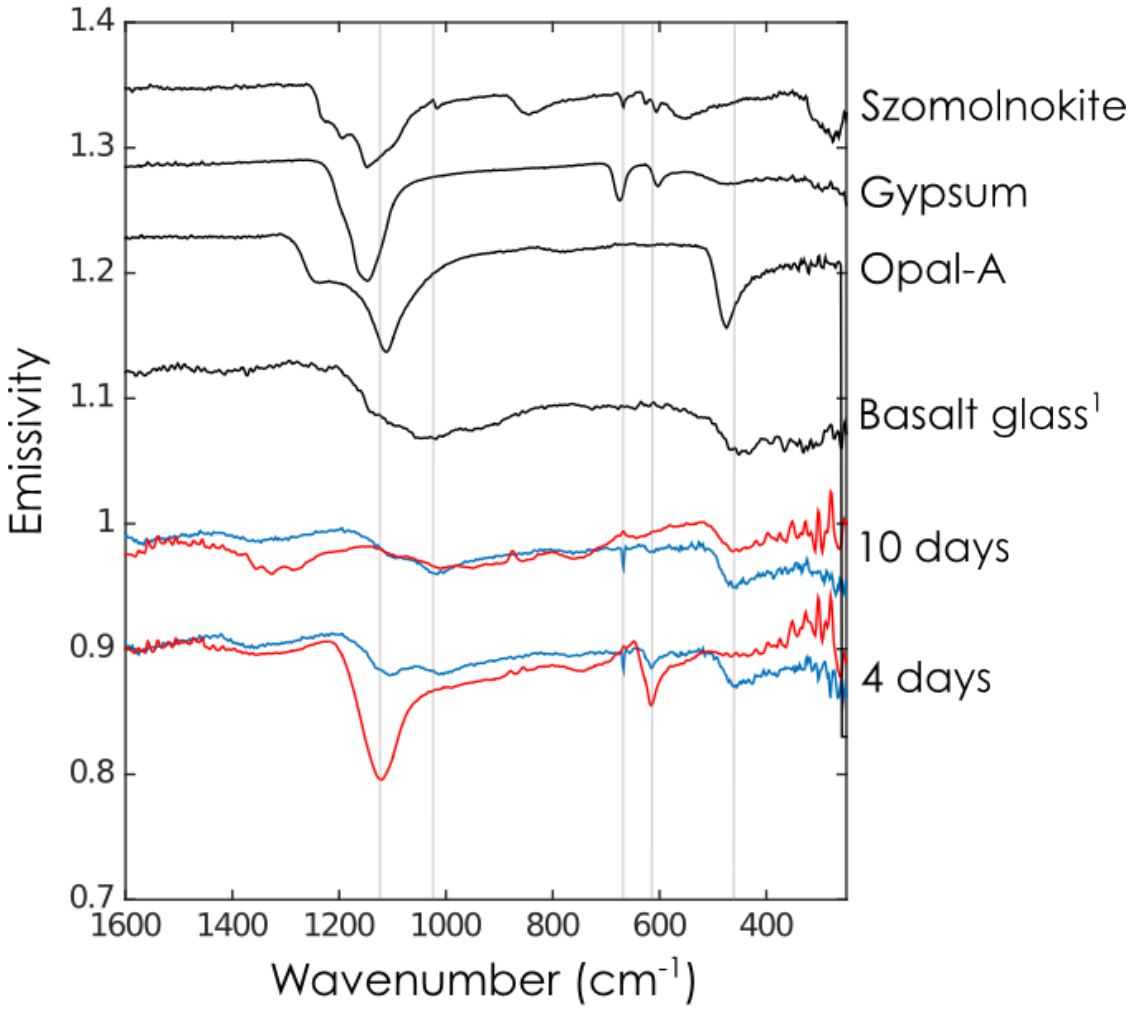

Figure 5.10. TIR spectra of SP Crater Earth atmosphere (blue) and Martian atmosphere (red) precipitates compared to spectra of phases in the endmember spectral library. Grey lines indicate position of major emission features in precipitate spectra. Spectra are offset for clarity (from top to bottom, offset = +0.35, +0.29, +0.23, +0.13, 0, 0, -0.08, -0.08).

[1]*Horgan et al.* [submitted]

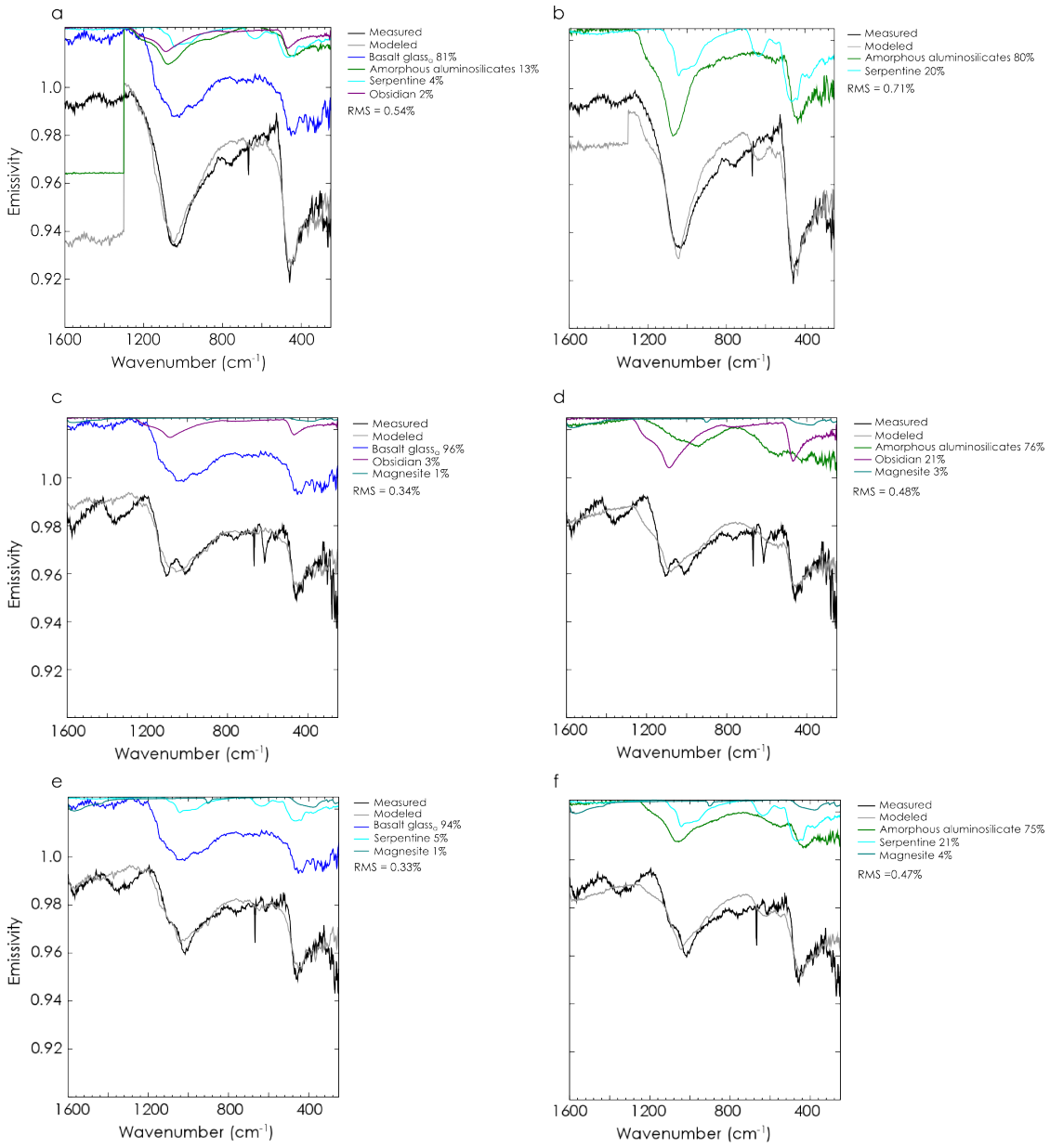

Figure 5.11. TIR spectral mixture analysis results for (a) Loop Rd. Mountain 10 day Earth atmosphere solution precipitates modeled with basalt glass and (b) without basalt glass; (c) SP Crater 4 day Earth atmosphere solution precipitates modeled with basalt glass and (d) without basalt glass; (e) SP Crater 10 day Earth atmosphere solution precipitates modeled with basalt glass and (f) without basalt glass.

All Mars atmosphere solution samples exhibit relatively broad Si-O bending spectral emission features, and all except for the SP Crater 4-day Martian atmosphere precipitates exhibit SiO ν_3 features, indicating that silicates were precipitated in all experiments (Figures 5.9 and 5.10). For the three samples with significant SiO ν_3 bands, the region between ~ 600 – 900 cm^{-1} cannot be modeled well with any endmembers in the spectral library. The features within this region are reminiscent of transparency features, which are particle size effects that occur where the absorption coefficient is low enough so that grains become optically thin and volume scattering occurs as the particle size range is reduced [*Salisbury and Walter*, 1987; *Moersch and Christensen*, 1995; *Ruff*, 2002]. In order to avoid particle size effects, but still gain some information about the potential silicate mineralogy, spectral mixture analyses were performed between 800 – 1300 cm^{-1} (Figure 5.12). The spectra are fit relatively well within this spectral range with high abundances of altered basalt glass (essentially silica-rich alteration rinds), hematite, amorphous aluminosilicates (allophane and Si-Al gel), clay minerals, and sulfates, but the fits to the broad Si-O bending feature at 460 cm^{-1} are very poor, especially with the inclusion of hematite in the models (Figure 5.12a, b, and d). This suggests that the abundances of amorphous silicates are being under-estimated, while the crystalline phases are being over-estimated. Additionally, some of the phases used in the fits are unlikely given the alteration environment. For example, jarosite is most certainly not present in these samples because it forms in a much more acidic environment (pH ~1 – 3) than was obtained in these experiments [*Elwood Madden et al.*, 2004].

The SP Crater 4-day Martian atmosphere solution sample has strong emission features at wavelengths (615 cm^{-1} and 1120 cm^{-1}) that are indicative of sulfates, and

weaker emission features in the Si-O bending region between ~400 – 500 cm^{-1} that suggest some silicate phases also formed. The entire spectral range is modeled with high abundances of Na-sulfates/carbonates (burkeite: $Na_6(CO_3)(SO_4)_2$; natroalunite: $NaAl_3(SO_4)_2(OH)_6$) and altered basalt glass. However, the RMS error is high, and the misfit between the model and the data is large, indicating that the particular sulfates present in the sample are not available in the spectral library.

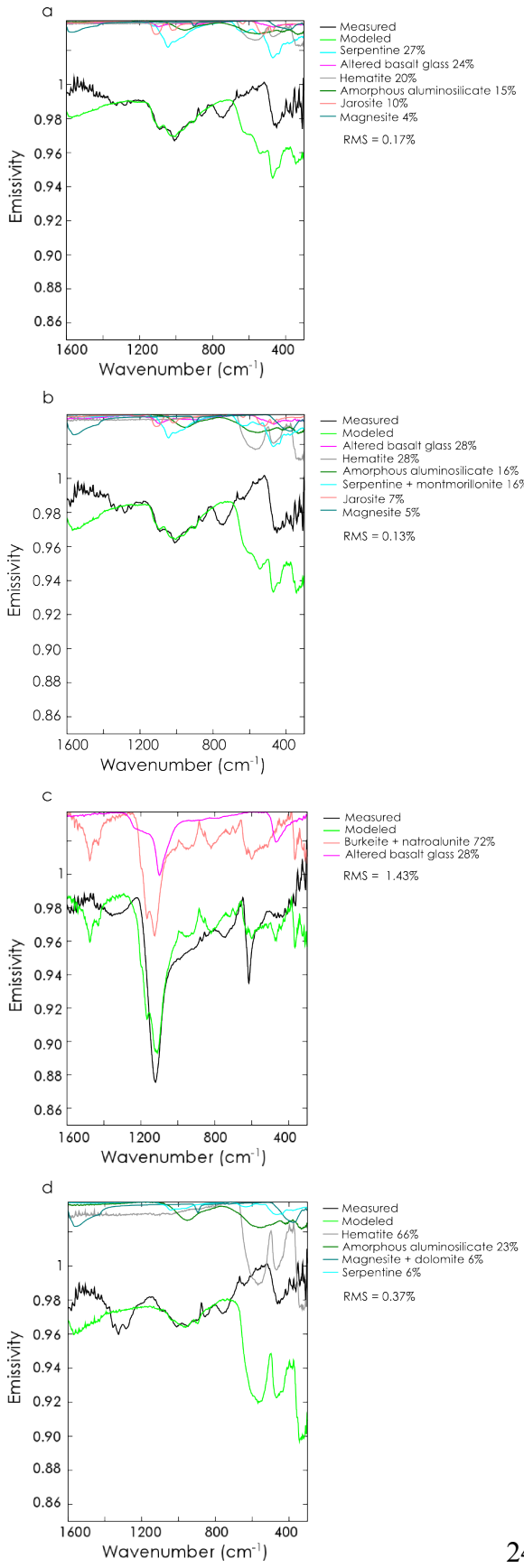
a
Measured
Modeled
Serpentine 27%
Altered basalt glass 24%
Hematite 20%
Amorphous aluminosilicate 15%
Jarosite 10%
Magnesite 4%
RMS = 0.17%
b
Measured
Modeled
Altered basalt glass 28%
Hematite 28%
Amorphous aluminosilicate 16%
Serpentine + montmorillonite 16%
Jarosite 7%
Magnesite 5%
RMS = 0.13%
c
Measured
Modeled
Burkeite + natroalunite 72%
Altered basalt glass 28%
RMS = 1.43%
d
Measured
Modeled
Hematite 66%
Amorphous aluminosilicate 23%
Magnesite + dolomite 6%
Serpentine 6%
RMS = 0.37%
Emissivity
Wavenumber (cm-1)
1600
1200
800
400
0.86
0.88
0.90
0.92
0.94
0.96
0.98
1

Figure 5.12. TIR spectral mixture analysis results modeled from for Loop Rd. Mountain (a) 4 and (b) 10 day Martian atmosphere solution precipitates, and SP Crater (c) 4 and (d) 10 day Martian atmosphere solution precipitates. All spectra were modeled from 800 – 1301 cm^{-1}.

5.4.5.2 VNIR spectra of Precipitates: Hydrated and Fe-bearing mineralogy

Similarly to the TIR spectra, the dissolution duration has little effect on the VNIR spectra compared to the effect of the atmosphere. The precipitates from solutions formed in an Earth atmosphere have higher reflectivity and greater spectral contrast than precipitates from solutions formed in a Martian atmosphere, and some of the spectral features are shifted as will be discussed below (Figures 5.13 and 5.14).

Hydrated minerals are identified in all samples by overtones and combinations of fundamental OH and H_2O vibrational absorption features at ~1.4 μm and 1.9 μm, with additional structural OH combination stretching plus bending vibrations that are found between 2.1 and 2.5 μm (Figures 5.13 and 5.14) [*Clark et al.*, 1990; *Ehlmann et al.*, 2009]. The exact position of the ~1.4 μm and 2.1 – 2.5 μm features depends on the type of octahedral cations (Mg, Al, Fe) present and the mineral structure. The position of the ~1.4 μm feature changes between Earth and Mars atmosphere precipitates, but the position of the 2.1 – 2.5 μm feature is around 2.31 μm for all of the samples, which is consistent with 3Mg-OH bending and stretching vibrations [*Ehlmann et al.*, 2012]. Additionally, all of the samples have a shallow ~2.2 μm feature that is frequently associated with Si- or Al-OH stretching and bending vibrations [*Clark et al.*, 1990]. The greater spectral contrast of the Earth atmosphere precipitates indicates that those samples

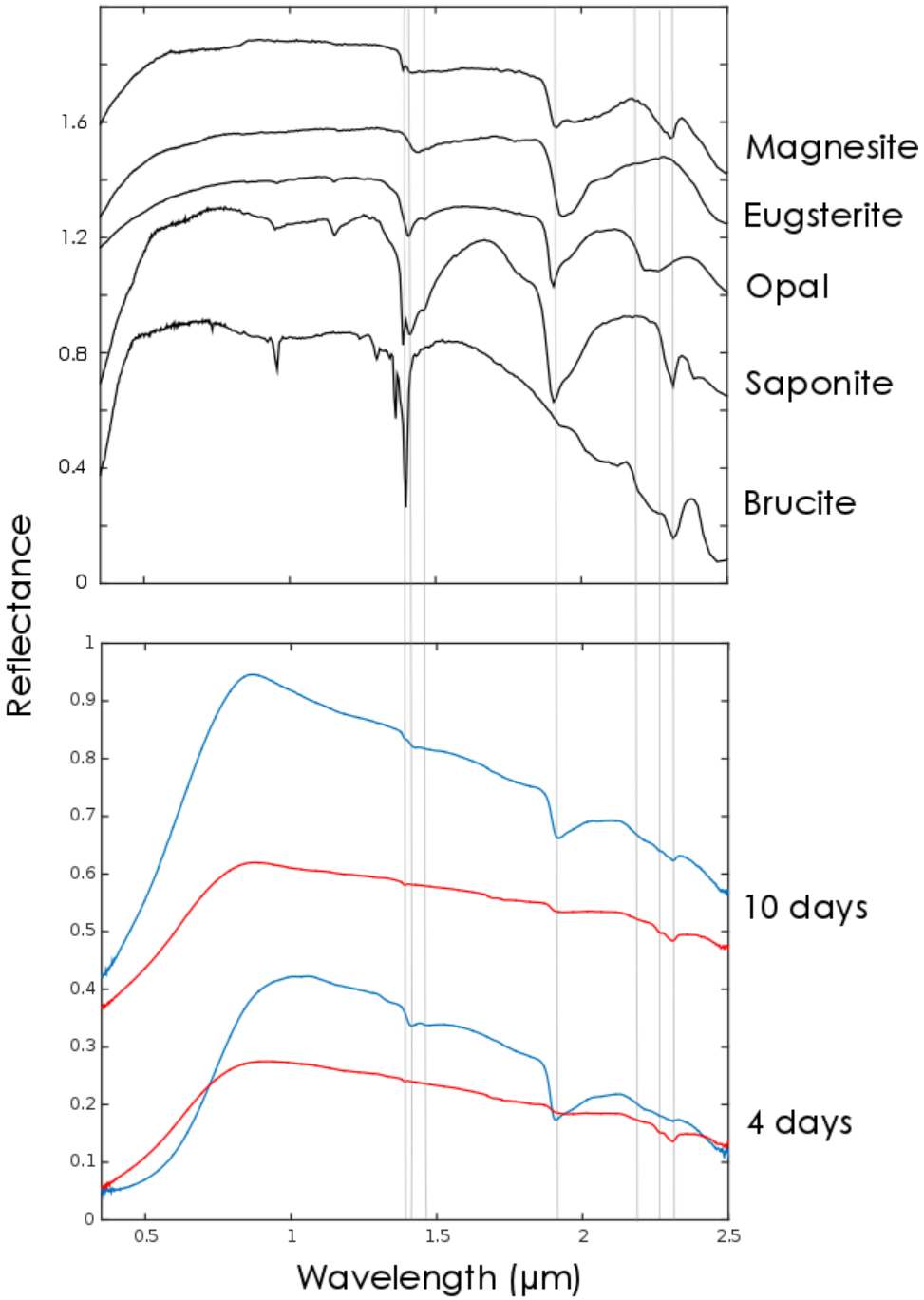

Figure 5.13. VNIR spectra of Loop Rd. Mountain Earth atmosphere (blue) and Martian atmosphere (red) precipitates compared to spectra of detected phases. Grey lines indicate position of major absorption features in precipitate spectra. Spectra are offset for clarity.

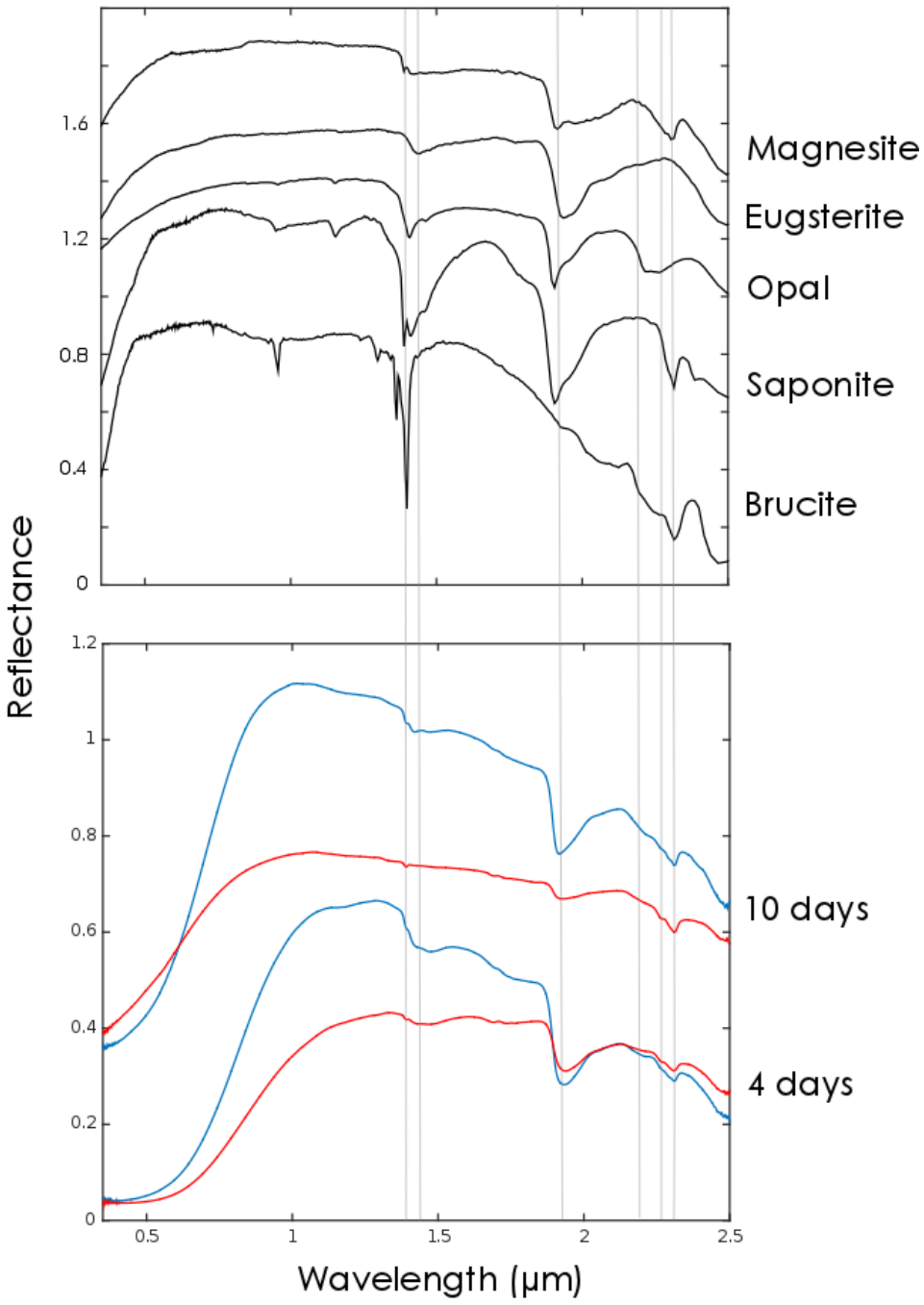

Figure 5.14. VNIR spectra of SP Crater Earth atmosphere (blue) and Martian atmosphere (red) precipitates compared to spectra of detected phases. Grey lines indicate position of major absorption features in precipitate spectra. Spectra are offset for clarity.

are most likely more hydrated [*Ehlmann et al.*, 2012; *Rice et al.*, 2013] and/or the crystals that formed were larger than those in the Martian atmosphere because increasing contrast is also related to increasing grain size [*Horgan et al.*, 2009].

In addition to the hydration features, all samples have an increasing slope between ~ 0.5 to 0.8 μm, which is a ferric absorption edge, indicating the presence of Fe^{3+}-bearing phases. The smoothness of the slope indicates that the Fe^{3+}-bearing substances are nanophase or amorphous, and are consistent with phases such as Fe-Si or Fe-Al-Si gels [*Evans and Adams*, 1980], palagonite [*Singer*, 1982], allophane or imogolite [*Bishop et al.*, 2013], or nanophase hematite [*Morris et al.*, 1985; *Morris*, 1988]. No crystalline hematite is detected in the VNIR, which is further evidence against it being included in the TIR model of the Martian atmosphere precipitate spectra.

The 1.41, 1.46, 1.91, and broad 2.21 μm features of the Loop Rd. 4-day solution precipitates in Earth's atmosphere are consistent with opal, while the 1.41, 1.91, and 2.30 μm features are consistent with saponite (Figure 5.13) [*Bishop et al.*, 2008]. For the Loop Rd. 10-day solution precipitates in Earth's atmosphere, the 1.9 feature shifts to ~1.92 μm and the 2.30 μm feature shifts to 2.31 μm so that the spectrum becomes more consistent with magnesite. The 1.42, 1.46, and 2.21 μm features indicate that opal is most likely present, which is consistent with the detection of aluminous opal in the TIR.

In general, the SP Crater Earth atmosphere samples exhibit deeper hydration features than the Loop Rd. samples. The SP Crater 4-day Earth atmosphere precipitates exhibit a broad 1.4 μm feature centered around 1.45 μm that is a combination of 1.39, 1.42, and 1.47 μm absorptions, and this sample also has features at 1.7, 1.93, 2.2 and 2.31 μm. The combination of the 1.39, ~2.1, 2.2, and 2.3 μm features are consistent with

brucite and the 1.7 μm feature also suggests saponite. The combination of 1.42, 1.47, and 2.2 μm features are consistent with opal, and the broad ~1.45 and 1.93 μm features are also possibly suggesting the presence of eugsterite ($Na_4Ca(SO_4)_3 \cdot 2H_2O$). Opal and sulfate VNIR detections are consistent with the TIR spectral shape, though these phases were not identified in the TIR spectral modeling. The SP Crater 10-day Earth atmosphere precipitates show a slight change in mineralogy; the 1.9 feature shifts to ~1.91 μm, which suggests the absence of eugsterite, and the spectrum looses some of it's definition around 2.2 μm, though the feature is still visible, possibly indicating a decrease in opal abundance or particle size. The decrease in sulfate and opal is also indicated in the TIR spectrum, which shows the loss of a sulfate and/or highly polymerized silicate phase in the 10-day solution precipitates. The 1.4 μm feature in this sample develops more structure, which, along with the 1.91 μm and 2.31 μm features, indicates the presence of magnesite, which was not detected in the TIR.

The precipitates formed under a Martian atmosphere have a lower reflectance than the terrestrial experiments, indicating a difference in precipitate mineralogy or a smaller grain size. The Mars atmosphere spectra are also more red than the Earth spectra, indicating that the Fe^{3+} is in greater abundance and/or more spectrally dominant than in the precipitates formed under Earth conditions. The Loop Rd. 4-day and Loop Rd.10-day Martian atmosphere precipitate spectra are essentially identical (Figure 5.13); they have very shallow 1.39, 1.7, 1.91, and 2.21μm features, and an asymmetric 2.31 μm feature, which are all consistent with saponite and brucite, neither of which was detected in the TIR spectra.

The SP Crater 4- and 10-day Martian atmosphere precipitates both share 1.39, 1.92, 2.21, 2.27, and 2.31 μm features, indicating magnestie and brucite, yet the spectra also have some striking differences (Figure 5.14). The 4-day solution precipitates have deeper 1.4 and 1.9 μm hydration features, and also have broad features centered ~1.45 and 1.7 μm, indicating eugsterite and saponite might also be components. The resulting spectrum of the 4-day solution precipitates is essentially that of the SP Crater 4-day Earth atmosphere precipitates, but with lower reflectance at shorter wavelength. These results are mostly consistent with TIR spectral analyses that detected carbonate minerals in the 10-day solution sample, and sulfates in the 4-day solution precipitates.

5.4.5.3 XRD analysis of precipitates: Crystalline phase mineralogy

Measurements of the sample at $2\theta < \sim 20°$ were most likely obstructed by the sample cup because of the geometry between the detector and the samples at these angles, so we do not try to match peaks at locations $< 2\theta \sim 20°$. Amorphous materials are not easily identifiable in XRD; they occasionally have diffuse peaks but are most often detected as broad "humps" in the background due to the scattering of x-rays in many directions [*Cullity and Stock*, 2001]. At the time of analysis, neither allophane nor basalt glass XRD patterns were available in our database to directly compare to our sample patterns, but previous work has shown that allophane generally has broad XRD peaks at 3.4 and 2.3 Å [*Levard et al.*, 2012]. Additionally, the substrate in our experiments was contributing to the signal, and so the background was necessarily removed from our patterns in order to perform a pattern matching analysis.

XRD patterns for precipitates formed in Earth atmosphere are very noisy, with few well-defined peaks, so that no phases can be definitively identified. Reasons for such

low quality patterns include a lack of crystalline substances formed, and/or crystals were precipitated in a preferred orientation so that their complete XRD pattern is not recognizable. TIR spectra indicate that the samples are predominantly amorphous silicate material, and so the first explanation is favored. We were able to identify two phases with some certainty in the Loop Rd. 10-day Earth atmosphere precipitates, which are magnesite and ilmenite (Figure 5.15). The detection of magnesite is supported by VNIR detections, but not TIR. Iron-bearing phosphates were also selected as partial matches to the XRD pattern, but some of the important peaks are missing from the sample pattern. Unidentified peaks at 3.4 and 2.21 Å are reminiscent of allophane, but are not exact matches (Figure 5.15). Additionally, there is little to no spectral evidence for allophane having formed in this sample.

The patterns for precipitates formed in a Martian atmosphere have sharp, well-defined peaks, and so we were able to confidently identify a number of crystalline phases. Loop Rd. 4- and 10-day Martian atmosphere precipitates had very similar crystalline mineralogy, and were mixtures of thermonatrite $Na_2CO_3 \cdot H_2O$, nontronite, and silica SiO_2 (Figure 5.16). The only difference between the precipitates was the addition of sodium carbonate sulfate with 10 days of dissolution. None of these phases were identified in the TIR or VNIR spectra of these samples, with the possible exception of altered basalt glass in the TIR measurement, which is essentially a proxy for a silica-rich amorphous phase.

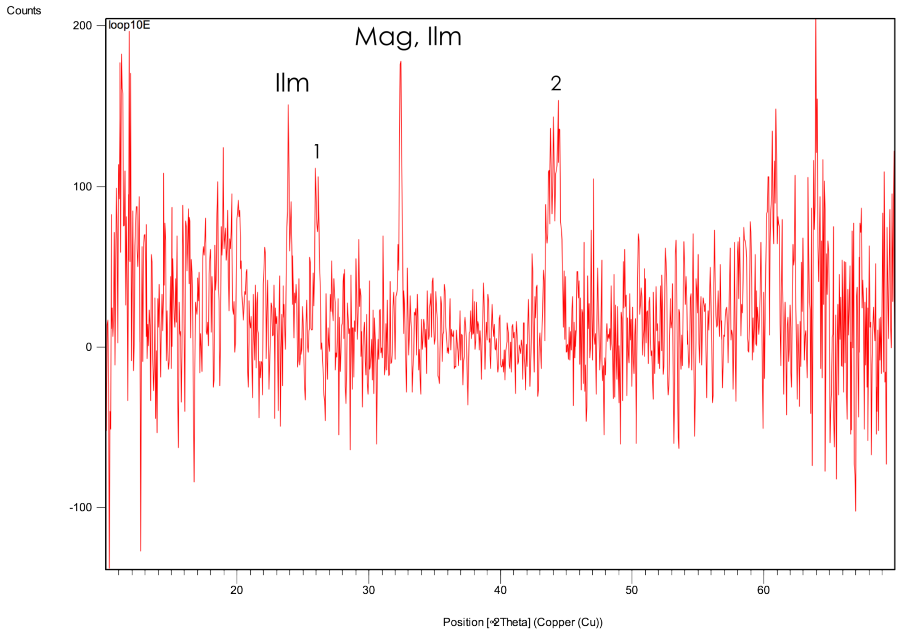

Figure 5.15. XRD pattern of Loop Rd. Earth atmosphere 10-day solution precipitates. Ilm = ilmenite and Mag = magnesite. The numbered peaks were not identified, and their d-spacings are as follows: 1 = 3.4 Å and 2 = 2.21 Å.

The SP Crater 4-day Martian atmosphere precipitates included thenardite (Na_2SO_4) and hydrated sodium bicarbonate (Figure 5.17a). Neither of these specific minerals was identified in the TIR and VNIR spectra, but both wavelength ranges detected chemically similar phases (burkeite, natroalunite, and eugsterite). The SP Crater 10-day Martian atmosphere precipitates included thenardite, silica, artinite ($Mg_2(CO_3)(OH)_2 \cdot 3H_2O$), brucite, magnesite, and aluminum sulfate hydrate (Figure 5.17b). TIR and VNIR detected magnesite, and VNIR also detected brucite. None of the other phases were detected in TIR.

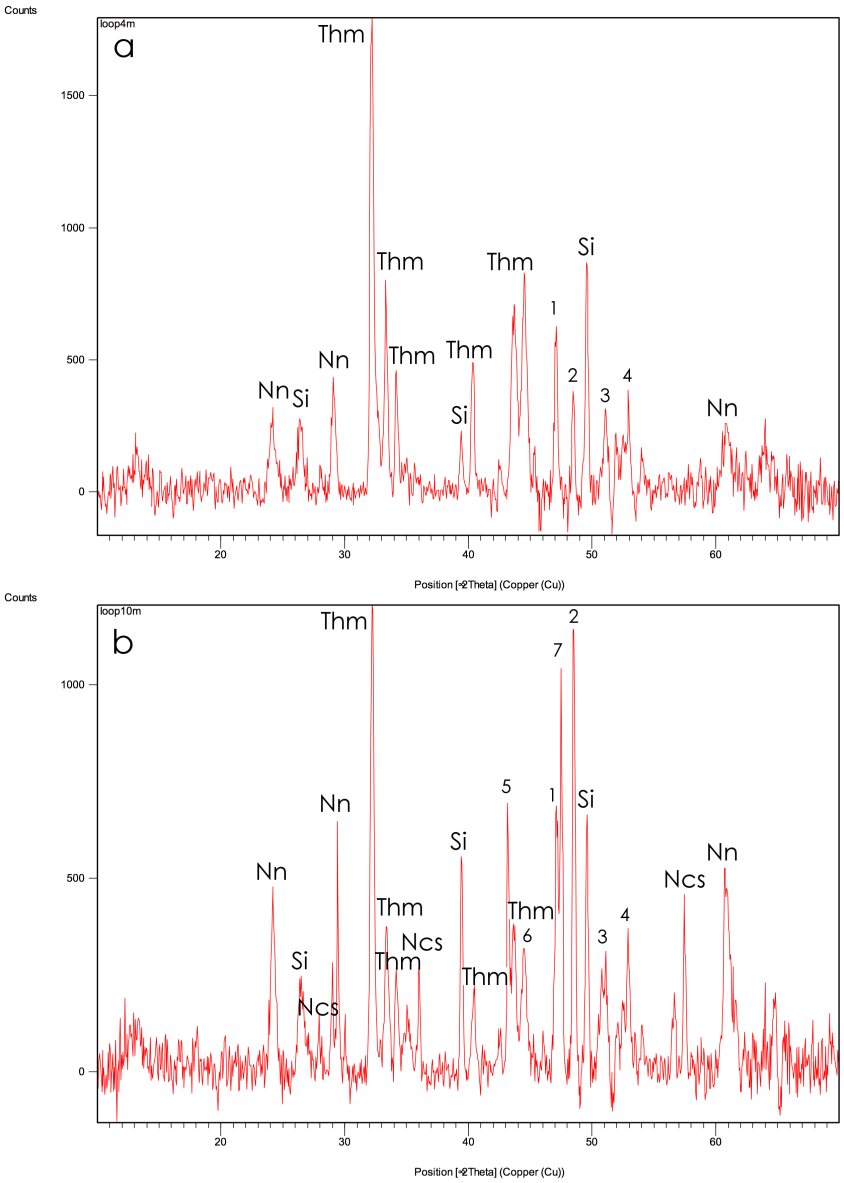

Figure 5.16. XRD patterns of Loop Rd. Martian atmosphere (a) 4-day and (b) 10-day solution precipitates. Nn = nontronite, Si = silica, Thm = thermonatrite, and Ncs = sodium carbonate sulfate. The numbered peaks were not identified, and their d-spacings are as follows: 1 = 1.93 Å, 2 = 1.88 Å, 3 = 1.79 Å, 4 = 1.73 Å, 5 = 2.10 Å, 6 = 2.04 Å, and 7 = 1.91 Å.

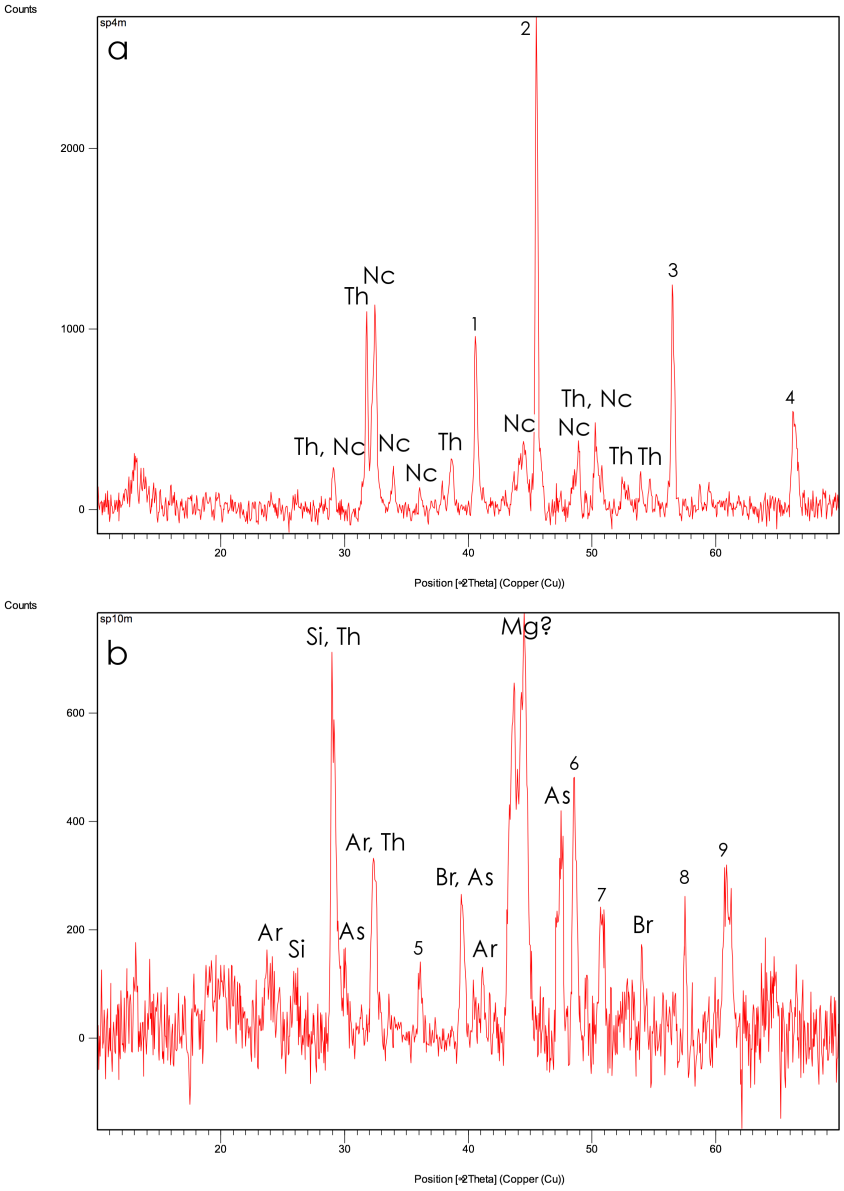

Figure 5.17. XRD patterns of SP Crater Martian atmosphere (a) 4-day and (b) 10-day solution precipitates. Th = thenardite, Nc = hydrated sodium bicarbonate, Ar = artnite, Si = silica, As = hydrated aluminum sulfate, Br = brucite, and Mg = magnesite. The numbered peaks were not identified, and their d-spacings are as follows: 1 = 2.22 Å, 2 = 2.0 Å, 3 = 1.63 Å, 4 = 1.49 Å, 5 = 2.49 Å, 6 = 1.88 Å, 7 = 1.79 Å, 8 =1.60 Å, and 9 = 1.52 Å.

5.4.5.4 Precipitate mineralogy: Summary

The combination of results from VNIR, TIR, and XRD analyses help determine the mineral assemblages precipitated from Earth and Martian atmosphere. The weak and/or broad XRD lines, the Si-O stretching and broad 460 cm^{-1} Si-O bending features in the TIR spectra, and the detection of Si-OH and Al-OH vibrations in the VNIR spectra indicate that the Earth atmosphere solution precipitates are dominated by noncrystalline hydrated aluminosilicate phases. VNIR analyses suggest the precipitation of crystalline silicates (saponite) and sulfates (eugsterite), but neither phase was detected in TIR or XRD analyses, so this detection remains ambiguous. Small abundances (< ~5%) of crystalline magnesite, ilmenite, and boehmite are potentially present in the Earth atmosphere precipitates because they were detected in XRD, but not in TIR analyses. All precipitates formed under an Earth atmosphere contain nanophase Fe-oxides.

Martian atmosphere solutions also precipitated noncrystalline silicates, based on the Si-O stretching and broad 460 cm^{-1} Si-O bending features in the TIR spectra, but the XRD patterns indicate that a greater abundance of crystalline phases formed including sodium and magnesium carbonates, sodium sulfates, sodium-ferric phyllosilicates, and magnesium hydrates. TIR and VNIR results are in general agreement with XRD detections, though there are some discrepancies with the exact phases including the lack of nontronite detected in the TIR and VNIR spectra of the Martian precipitates. VNIR spectra indicate that the Martian atmosphere precipitates are less hydrated than the Earth atmosphere precipitate samples, and all precipitates formed under a Martian atmosphere contain nanophase Fe-oxides.

5.5 Discussion

5.5.1 Basalt glass dissolution

From the cation concentration time series measurements, we can determine whether the basalt tephra was dissolving congruently or incongruently. *Guy and Schott* [1989] quantified reaction stoichiometry by defining a quantity R_x, which reflects the relative release of other cations (x) to Si and is defined by:

$$R_X = \left(\frac{n_x}{n_{Si}}\right)_{aq} \Big/ \left(\frac{n_x}{n_{Si}}\right)_{solid}$$

Where $(n_x)_{aq}$ is the number of moles of the desired cation in solution, $(n_{si})_{aq}$ is the number of moles of Si in solution, $(n_x)_{solid}$ is the number of moles of the desired cation in the starting material, are $(n_{Si})_{solid}$ is the number of moles of Si in the starting material. Thus, an R_x value ~ 1 means that the cation (x) is being released at a stoichiometric rate, and values > 1 indicate apparent preferential leaching of the cation. Plots of R_x for some of the important cations measured in solution in this study are shown in Figure 5.18. These plots distribute the cations into two groups: (1) glass network formers (Al, Fe), which do not readily dissolve, and (2) network modifying cations (Na, K, Ca) that show apparent incongruent release, and these results are similar to the findings of *Guy and Schott* [1989]. Mg is also considered a network modifying cation, yet it is not as readily dissolved as the other network modifying cations, and some of it remains in the solid. Ca is the only cation to be released relatively congruently. We can approximate a chemical reaction for the dissolution of basalt glass with the following equation:

$$(Si_{2.43}Al_{0.54}Fe_{0.54}Mg_{1.08}Ca_{0.63}Na_{0.27}K_{0.09}O_{10})_{solid} + 1.62\ H^{+}$$
$$\leftrightarrow\ (Si_{2.43}Al_{0.54}Fe_{0.54}Mg_{1.08}O_{10}H_{1.62})_{solid} + (0.63\ Ca^{2+})_{aq}$$
$$+\ (0.27\ Na^{+})_{aq} +\ (0.09\ K^{+})_{aq}$$

Where protons (H^+) are exchanged in the solid for the more readily dissolved cations, leaving behind a cation depleted solid.

5.5.2 Crystalline precipitates

The atmosphere is the most important factor determining the precipitate mineral assemblages in these experiments. Both atmospheres produced solutions that precipitated nanophase iron oxides and noncrystalline silicates, but the Martian atmosphere solutions also formed a variety of (Na, Ca, Al) sulfate and (Ca, Mg, Na) carbonate crystalline phases that correspond well with the alteration product assemblages predicted through thermodynamic models of the current-day Martian weathering regime [*Gooding*, 1978]. Sulfates and carbonates are also common evaporite minerals on Earth, and so their absence in the Earth atmosphere samples is very interesting.

The solution chemistries for the experiments in different atmospheres were similar except for a potential increase in Si in the Earth atmosphere solutions, and the introduction of HCO_3^- into solution through CO_2 in the Martian atmosphere. The lower Si and higher HCO_3^- abundances in the Martian atmosphere solutions increase the SO_4/Si and HCO_3/Si ratios, so that a greater fraction of the precipitates formed have sulfate and carbonate as base anions. Thus, the mineral assemblage differences might be attributed to differences in ion concentration ratios. Unfortunately, the large uncertainty in the Si measurements precludes definitive conclusions.

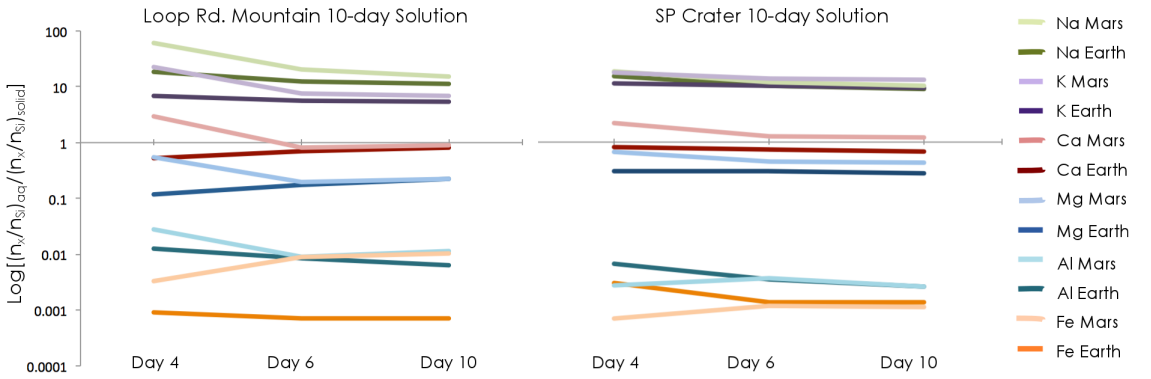

Figure 5.18. Shows stoichiometry of basalt glass dissolution with time. Values ~1 mean that the ion is dissolving congruently, > 1 imply the ion is preferentially dissolved, < 1 imply that the ion is remaining in the solid.

The SO_4 in all solutions most likely resulted from the oxidation of primary sulfide minerals, which react with oxygen and water to form sulfuric acid and metal oxides. SO_4 abundances were comparable in both Earth and Martian atmosphere solutions, and so it is uncertain why sulfate minerals are not more prevalent in the Earth atmosphere solution precipitates. Possible explanations include: (1) only nano- or noncrystalline sulfates formed in the Earth atmosphere precipitates, (2) the higher abundance of silicates overwhelmed the TIR signatures, masking any sulfates, (3) sulfates formed but were not included in the spot size for each of the measurements because they formed in the initial stages of evaporation around the perimeter of the inside of the sample cup. Further analyses using TEM should be able to discern between these explanations.

Despite having a relatively CO_2-free atmosphere, carbonate (magnesite) is detected in the Loop Rd. and SP Crater 10-day solution Earth atmosphere precipitates. However, the abundance of magnesite must be small (< ~5%) because it is not detected in

the TIR spectra for either sample, and is not detected in XRD for the SP Crater samples. The source of carbon is most likely from the very low abundances measured in the starting material (Table 5.2).

Chlorides are common weathering components of soils [*Doner and Lynn*, 1977], and solution chemistry mass balance predicts the precipitation of up to several milligrams of (K,Na)Cl, yet the phases are not detected in any of the samples. Cl abundance in solution is comparable to SO_4, and the detection of sulfates in the Martian samples further confounds the absence of chloride phases. The spectral methods used here are incapable of detecting chlorides, but KCl and NaCl should be easily identified in XRD patterns. Based on the physical properties of the samples, few crystals larger than 10^2 μm formed, so it is unlikely that chloride crystals are so large that their patterns are not recognizable (> ~1 mm). The most likely explanation is that chlorides are represented in the unidentified XRD peaks, and that they were not recognized during the peak matching for some reason despite chlorides being available in the XRD pattern database. Further mineralogical and chemical analyses using TEM and electron microprobe can confirm this hypothesis.

Clay minerals are some of the most frequently cited alteration products of basalt rock on Earth [*Borchardt*, 1977; *Nesbitt and Wilson*, 1992; *Stefánsson and Gíslason*, 2001; *Dixon et al.*, 2002], and thermodynamic modeling by *Gooding* [1978] concludes that clay minerals should be major weathering products when liquid water is present. Yet, based on TIR and XRD data, few clay minerals are formed though the rapid evaporation of weathering solutions. Saponite is detected in the VNIR spectra of most of the Earth and Martian atmosphere solution precipitates, but only the two Loop Rd. Martian

atmosphere solution precipitates exhibit XRD properties of clay minerals (nontronite). The potentially small abundance of clays formed in these experiments indicates that these minerals need more time to crystalize than the time allowed during evaporation, and most of the Si and Al in solution went into forming an intermediate amorphous silicate phase.

5.5.3 Noncrystalline precipitates

All samples exhibit TIR spectral features that indicate the precipitation of silicate phases, and TIR spectral analyses can inform about the noncrystalline silicate phase structure and composition where the other analysis methods cannot. All samples, except SP Crater 4-day solution precipitates, exhibit a well developed 460 cm^{-1} feature that is most consistent with basaltic glass, though similarly shaped Si-O bending features are present in Si-Al gel (positioned at ~450 cm^{-1}) [*Rampe et al.*, 2012] and highly polymerized high-silica phases such as opal-A (positioned at ~475 cm^{-1}), zeolites (positioned at ~450 and 470 cm^{-1} depending on composition) [*Ruff*, 2004], obsidian (positioned at ~465 cm^{-1}), and dicotahedral clays (positioned at ~465 cm^{-1}, but can shift depending on composition) [*Ruff and Christensen*, 2007]. The absence of another Si-O deformation feature at ~530 cm^{-1} and an Al-OH deformation vibration feature at ~300 cm^{-1} indicates that the samples did not precipitate detectable abundances of either smectite clays or allophane [*Ruff and Christensen*, 2007; *Rampe et al.*, 2012].

Since few other phases formed in the Earth atmosphere solution precipitates, it is likely that most of the cations in solution were incorporated into the noncrystalline silicate structure, leaving some iron to form the nanophase iron oxides detected in the VNIR spectra. The position of the SiO ν_3 feature for the Loop Rd. 10-day Earth atmosphere sample suggests that the noncrystalline silicate has a composition and

structure that is similar to basalt glass, whereas the SP Crater 4- and 10-day Earth atmosphere sample's silicate structures are less polymerized and are not indicative of any individual phase in the current spectral library. The reason for the difference in silicate structure is uncertain since the SP Crater solution composition was not significantly different from the Loop Rd. solution. However, the SP Crater precipitates exhibit deeper hydration bands in the VNIR spectra, possibly indicating an increased abundance of H_2O molecules, which can cause a structure to depolymerize by forcing openings within the structure and creating charge imbalance which are neutralized with non-bridging oxygens (NBOs) [*Farnan et al.*, 1987]. Thus, different starting materials are capable of producing different secondary noncrystalline silicate materials, and the silicates formed in these experiments are unique phases not currently represented in the TIR spectral library.

The SiO ν_3 feature for the Martian atmosphere samples is most likely affected by particle-size effects, and so little more information about the composition of the noncrystalline silicates can be gained from the TIR spectra. However, the formation of a variety of carbonate and sulfate crystalline phases most certainly deducted from the pool of cations in solution, leaving fewer cations available to be included in the silicate structures. Therefore, we might expect silicates with fewer network-modifying cations.

Nanophase, or amorphous iron oxides were detected in the VNIR spectra of all of samples. Nanophase iron oxides is a generic name for poorly crystalline and nanometer-sized particles of ferric iron that are associated with variable amounts of H_2O and OH [*Morris et al.*, 2000]. Phases that could be contributing to the nanophase iron oxide signature include schwertmannite, ferrihydrate, palagonite, akaganéite, and poorly

crystalline hematite, goethite, and maghemite [*Morris et al.*, 2000]. These phases could not be differentiated using the methods in this study.

Our results are essentially consistent with the mineralogy and formation mechanisms of palagonite, a hydrated heterogeneous material that may be amorphous, or consist of poorly crystalline clay minerals [*Thorseth et al.*, 1991]. The palagonitization of basalt glass generally results in the oxidation of Fe, the uptake of H_2O, and loss of CaO and Na_2O. No oxides were "lost" in our experiments, but we do notice the oxidation of Fe and addition of H_2O for all samples in the VNIR spectra. Additionally, in the Martian atmosphere solution samples, there is evidence that CaO and Na_2O were "lost" to form sulfates, which are more soluble phases that could get washed away in an open system.

5.5.4 Applicability to natural systems

The laboratory experiments in this study deviate from a natural system. Therefore, it is important to discuss differences that potentially impact the outcomes. In a natural isochemical (constant elemental composition) closed system, each new volume of liquid water is able to interact with the primary basalt, any potential weathering rinds/leached layers, and any previously precipitated secondary products. The experiments in this study become isochemical post-filtration; however, they are not modeling a closed system because the solution is transported away from the parent rock in order to isolate the precipitates. In doing so, the solution is not allowed to continuously interact with the primary and weathered surfaces; it is only allowed to interact with previously deposited precipitates.

In a strictly open system, it is likely that ions would segregate throughout the transport process based on solubility. Less soluble ions (e.g., Al^{3+}, Fe^{3+}) would form

precipitates early on in the transport process, whereas more soluble ions (e.g., Na^+, K^+, Cl^-) could be transported farther distances before precipitating [*Nesbitt and Young*, 1982; *Nesbitt and Wilson*, 1992]. Thus, Al- and Fe-oxides, as well as some clay minerals, would be found near the parent rock, while chlorides could form away from the parent rock location. No segregation of ions occurred during the experiments in this study, and so the precipitation of all secondary phases was relatively synchronous. Thus, the experiments in this study represent a weathering scenario with water/rock ratios high enough to mobilize the solution, but low enough so that the most soluble ions were not lost to the system. It is possible that in some locations on Mars (such as in the subsurface of ice-rich soils) enough water could form so that the solution becomes mobilized, transporting ions isochemically to another location nearby before deposition. Subsequent wind erosion could help expose the secondary products.

5.5.5 Comparison to phases on Mars

Amorphous silicate alteration phases have been detected in TES data as major components of broad regions on the Martian surface, as discussed above in Section 5.2.1, and their presence is highly correlated with a low wavenumber Si-O bending spectral feature positioned at ~465 cm^{-1} [*Ruff and Christensen*, 2007]. This feature is reminiscent of, but no match for, the 460 cm^{-1} Si-O bending feature exhibited by the amorphous silicate phases formed in our experiments. Additionally, all of our samples exhibit 1.4 and 1.9 μm hydration features that are not found in global VNIR spectra from most areas associated with amorphous silicate phases in the low-albedo regions on Mars [*Bibring et al.*, 2005]. The hydration features are quite weak in the Martian atmosphere samples, and could potentially become absent if the coatings were reduced in particle size, but the lack

of a spectral match in the TIR reduces the likelihood that the exact compositions formed in our experiments are found in broad regions of the Martian surface.

Based on currently available data, the noncrystalline silicates formed in our experiments correlate relatively well with phases found in Gusev and Gale Craters by the Spirit and Curiosity rovers. The Mini-TES is the only instrument on the Spirit rover that allows for direct comparison to the analyses performed on our samples. The Curiosity rover has no TIR spectrometer instrument, but does have an x-ray diffractometer, with which we can compare results. Future work should include chemical analyses that can be compared to information from the APXS instrument onboard both the Spirit and Curiosity rovers; however, in the meantime, we can compare chemistry results from APXS to solution chemistry results.

Chemical evidence (high S, Cl, and Fe^{3+}/Fe_{total}) strongly suggests that the Clovis and Watchtower class rocks within Gusev Crater have been aqueously altered [*Ming et al.*, 2006; *Squyres et al.*, 2006]. *Ming et al.* [2006] synthesized findings from the APXS, Mössbauer, and Mini-TES instruments on the Spirit rover, and found that the Clovis class rocks had secondary mineral assemblages consisting of Fe-oxides/oxyhydroxides (nanophase iron oxides, hematite, goethite), Ca-phosphates, Ca-sulfates, and secondary aluminosilicates (e.g., allophane-like material, amorphous silica), and Watchtower class rock assemblages consisted of Fe-oxides/oxyhydroxides (nanophase iron oxides, hematite, goethite), ilmenite, Ca-phosphates (e.g., brushite), Mg-sulfates, and secondary aluminosilicates. These assemblages are very similar to the results from the Martian atmosphere experiments in this study except our solutions precipitated Na- and Fe-sulfates instead of Ca- and Mg-sulfates, though *Squyres et al.* [2006] did note that Na and

K also correlate well with S in the Clovis class rocks, indicating that some Na- and K-sulfates might be present. Additionally, our experiments also precipitated carbonates, which were not present in the Watchtower or Clovis class rocks [*Ruff et al.*, 2006; *Morris et al.*, 2013].

Similarly to the precipitates from this study, the Clovis and Watchtower class rocks exhibit a spectral feature at ~460 cm^{-1} that was previously only known to be present in the spectra of basalt glass and some terrestrial palagonitized basalt samples, and so the Mini-TES spectra from these rocks were modeled with high abundances of basalt glass, despite the vast chemical evidence for aqueous alteration [*Ruff et al.*, 2006]. Our results indicate that solutions formed through relatively short-lived interactions of basalt glass with circum-neutral pH water at low temperatures are capable of forming noncrystalline silicates that are spectrally and chemically similar to those found in the Clovis and Watchtower class rocks in Gusev Crater on Mars.

The amorphous phases detected in the Rocknest soil sample from Gale Crater are H_2O, CO_2, SO_3, and Cl-bearing, indicating that they are aqueous alteration products [*Morris et al.*, 2013], and the chemistry is similar to the assemblage of phases formed in our Martian atmosphere samples. However, the CheMin instrument also detected positive XRD pattern matches for basalt glass and allophane in the soil [*Levard et al.*, 2012], yet there is no evidence for allophane having formed in any of our Martian atmosphere samples. Interestingly, *Morris et al.* [2013] observed that the SiO_2/Al_2O_3 ratios for Rocknest soils were too high to be consistent with allophane, and *Bish et al.* [2013] noted that the CheMin XRD analyses do not unambiguously identify allophane and basalt glass because the patterns may be XRD surrogates for another amorphous phase. Additionally,

Morris et al. [2013] found that the bulk TiO_2 and Fe_2O_3 concentrations of the amorphous component in Rocknest were suggestive of near-neutral aqueous weathering conditions, which is similar to the conditions simulated in our experiments. Therefore, we conclude that the amorphous silicates formed in our experiments are consistent with the noncrystalline silicate components in Rocknest soil.

The rapid evaporation of basalt weathering solutions formed similar mineral assemblages to the secondary phases found in the Clovis and Watchtower rocks in Gusev Crater, and possibly in the soils on the floor of Gale Crater. Such a process would be likely to form rock coatings, similar to silica glazes found in most desert landscapes on Earth [*Dorn*, 1998]. Elevated S, Cl, and Br concentrations were detected the Clovis rock outcrop even at the maximum depth obtained using the Rock Abrasion Tool (RAT) (~9 mm), and so a rock coating would have to be at least this thick [*Ming et al.*, 2006; *Squyres et al.*, 2006]. Therefore, we can use the results from our experiments to estimate how much water would be needed to create such a coating thickness. Our experiments yielded roughly ~0.4 cm^3 of material per 1 L of weathering solution. For a rock ~100 cm^2 in surface area, similar to some of the Clovis class outcrops [*Arvidson et al.*, 2006], a total volume of ~250 L would be needed to precipitate enough material to form a 9 mm thick continuous coating. For an outcrop with a surface area ~1 m^2, representing some of the largest outcrops in Gusev Crater [*Golombek et al.*, 2006], a volume of 2.47 x 10^6 L of weathering solution would be required to precipitate a coating of the same thickness. This upper limit of required weathering solution equates to ~1.6 mL/year of water over the duration of the Amazonian period. In order to compare this volume of water to terrestrial examples, we calculate an equivalent annual precipitation over the outcrop surface area

of only ~1.6 x 10^{-3} mm. In comparison, the driest parts of the Atacama desert have annual rainfalls of ~0.5 mm [*Clarke*, 2006]. Our results show that short-lived interactions with circum-neutral pH fluids (potentially snow or ice melt water) at low volumes over geologically significant periods of time (~3 billion years) could form the noncrystalline silicates and associated phase assemblages that are observed in parts of Gusev and Gale Crater on Mars.

5.5.6 Future work

These initial experiments have opened up a number of questions that can be addressed in future work. A more detailed analysis of the precipitates formed in these experiments should include chemical measurements from techniques such as electron microprobe in order to better constrain the composition of the amorphous silicate phases, and TEM analysis to help determine if salts had formed and to examine the heterogeneity of the precipitates. It would also be useful to perform micro-TIR analyses of the precipitates, which has a spot size ~100 μm [*Edwards and Christensen*, 2013], in order to determine the TIR spectra of select phases in the heterogeneous samples.

Future experiments could examine the repeatability of these results, and should sample greater volumes of solution (~10 mL) in order to obtain more precise Si and pH measurements. Additionally, future experiments could explore how the composition or crystallinity of the precipitates might change with different evaporation rates, and could examine the spectral effects that these phases have as coatings on rocks.

5.6 Conclusions

- Two basalt glass compositions were weathered in closed systems under Earth and Martian atmosphere conditions, and the resulting weathering solutions were

rapidly evaporated to simulate a current day Mars alteration scenario. Amorphous aluminosilicates were precipitated in all experiments, while crystalline sulfates and carbonates were only precipitated in the Martian atmosphere experiments.

- The weathering solution and precipitate composition is primarily affected by atmosphere composition, and to lesser degrees, the starting material composition and duration of dissolution.
- There were no unambiguous detections of clay minerals in any of the samples, indicating that these phases need more time to form than what was allowed, and that they are not necessarily produced in all chemical weathering scenarios.
- The amorphous silicates that precipitated from these experiments are most spectrally similar to basalt glass and Si-Al gel, but represent phases that are new to spectral libraries.
- Weathering products produced through the rapid evaporation of basalt weathering solutions are spectrally and chemically similar to amorphous phases on Mars, and transient water-rock interactions over billions of years are sufficient to reach the volumes of materials observed on the Martian surface.
- Thus, large volumes of persistent water are not necessary to produce the alteration profiles exhibited in various locations on Mars that were previously thought to experience intense aqueous alteration.

REFERENCES

Abrams, M., E. Abbott, and A. Kahle (1991), Combined use of visible, reflected infrared, and thermal infrared images for mapping Hawaiian lava flows, *J. Geophys. Res.*, *96*(B1), 475, doi:10.1029/90JB01392.

Adams, J. B. (1968), Lunar and Martian Surfaces: Petrologic Significance of Absorption Bands in the Near-Infrared, *Science*, *159*(3), 1453–1455, doi:10.1126/science.159.3822.1453.

Adams, J. B., C. Pieters, and T. B. McCord (1974), Orange glass - Evidence for regional deposits of pyroclastic origin on the moon, *In: Lunar Science Conference*, *5*, 171–186.

Allen, C. C., M. Jercinovic, K. Keil, and J. L. Gooding (1981), Altered basaltic glass - A terrestrial analog to the soil of Mars, *Icarus*, *45*, 347–369, doi:10.1016/0019-1035(81)90040-3.

Almeida, R. M. (1992), Detection of LO modes in glass by infrared reflection spectroscopy at oblique incidence, *Phys. Rev. B*, *45*(1), 161, doi:10.1103/PhysRevB.45.161.

Amador, E. S., and J. L. Bandfield (2016), Elevated bulk-silica exposures and evidence for multiple aqueous alteration episodes in Nili Fossae, Mars, *Icarus*, 276, 39-51, doi:10.1016/j.icarus.2016.04.015.

Arvidson, R. E., F. P. Seelos IV, K. S. Deal, W. C. Koeppen, N. O. Snider, J. M. Kieniewicz, B. M. Hynek, M. T. Mellon, and J. B. Garvin (2003), Mantled and exhumed terrains in Terra Meridiani, Mars, *J. Geophys. Res.*, *108*(E12), doi:10.1029/2002JE001982.

Arvidson, R. E., S.W. Squyres, R. C. Anderson, J. F. Bell III, D. Blaney, J. Brückner, N. A. Cabrol, W. M. Calvin, M. H. Carr, P. R. Christensen, B. C. Clark, L. Crumpler, D. J. Des Marais, P. A. de Souza Jr., C. d'Uston, T. Economou, J. Farmer, W. H. Farrand, W. Folkner, M. Golombek, S. Gorevan, J. A. Grant, R. Greeley, J. Grotzinger, E. Guinness, B. C. Hahn, L. Haskin, K. E. Herkenhoff, J. A. Hurowitz, S. Hviid, J. R. Johnson, G. Klingelhöfer, A. H. Knoll, G. Landis, C. Leff, M. Lemmon, R. Li, M. B. Madsen, M. C. Malin, S. M. McLennan, H. Y. McSween, D. W. Ming, J. Moersch, R. V. Morris, T. Parker, J. W. Rice Jr., L. Richter, R. Rieder, D. S. Rodionov, C. Schröder, M. Sims, M. Smith, P. Smith, L. A. Soderblom, R. Sullivan, S. D. Thompson, N. J. Tosca, A. Wang, H. Wänke, J. Ward, T. Wdowiak, M. Wolff, and A. Yen (2006), Overview of the Spirit Mars Exploration Rover Mission to Gusev Crater: Landing site to Backstay Rock in the Columbia Hills, *J. Geophys. Res. E Planets*, *111*(2), 1–22, doi:10.1029/2005JE002499.

Ashley, H. E. (1909), The colloid matter of clay and its measurement, *United States Geol. Surv.*, *Bulletin 3*, 1–65.

Atkinson, S.S. (1990) *Geochemical and Isotopic Study of the Roza Member Feeder System, Columbia River Basalt Group;* M.Sc. thesis, University of Alberta, Edmonton, AB, 112 pp.

Bailey, S. W. (1966), The Status of Clay Mineral Structures, in *National Conference on Clays and Clay Minerals*, vol. 14, pp. 1–23.

Banfield, J. F., G. G. Ferruzzi, W. H. Casey, and H. R. Westrich (1995), HRTEM study comparing naturally and experimentally weathered pyroxenoids, *Geochim. Cosmochim. Acta*, *59*(1), 19–31, doi:10.1016/0016-7037(94)00372-S.

Bandfield, J. L., V. E. Hamilton, and P. R. Christensen (2000a), A Global View of Martian Surface Compositions from MGS-TES, *Science*, *287*, 1626, doi:10.1126/science.287.5458.1626.

Bandfield, J. L., P. R. Christensen, and M. D. Smith (2000b), Spectral data set factor analysis and end-member recovery: Application to analysis of Martian atmospheric particulates, *J. Geophys. Res.*, *105*(E4), 9573, doi:10.1029/1999JE001094.

Bandfield, J. L. (2002), Global Mineral Distributions on Mars, *J. Geophys. Res.*, *107*(January), doi:10.1029/2001JE001510.

Banin, A., F. X. Han, I. Kan, and A. Cicelsky (1997), Acidic volatiles and the Mars soil, *Journal of Geophysical Research*, *102*(E6), 13341, doi:10.1029/97JE01160.

Belkorissat, R., A. E. D. Kadoun, M. Dupeyrat, B. Khelifa, and C. Mathieu (2004), Direct Measurement of Electron Beam Scattering in the Low Vacuum SEM, *Microchim. Acta*, *147*(3), 135–139, doi:10.1007/s00604-004-0182-x.

Bell, J. F., III (2008), The Martian Surface: Composition, Mineralogy, and Physical

Properties, Cambridge Univ. Press, New York.

Berger, G., C. Claparols, C. Guy, and V. Daux (1994), Dissolution rate of a basalt glass in silica-rich solutions: implications for long-term alteration, *Geochimica et Cosmochimica Acta*.

Berner, R. A. (1978), Rate control of mineral dissolution under earth surface conditions, *Am. J. Sci.*, *278*, 1235–1252.

Berner, R. A., and G. R. Holdren (1977), Mechanism of feldspar weathering. 2 Observation of feldspars from soils., *Geology*, *5*, 369–372.

Bibring, J. -P., A. Soufflot, M. Berthé, Y. Langevin, B. Gondet, P. Drossart, M. Bouyé, M. Combes, P. Puget, A. Semery, G. Bellucci, V. Formisano, V. Moroz, V. Kottsov and the OMEGA Co-I team: G. Bonello, S. Erard, O. Forni, A. Gendrin, N. Manaud, F. Poulet, G. Poulleau, T. Encrenaz, T. Fouchet, R. Melchiori, F. Altieri, N. Ignatiev, D. Titov, L. Zasova, A. Coradini, F. Capacionni, P. Cerroni, S. Fonti, N. Mangold, P. Pinet, B. Schmitt, C. Sotin, E. Hauber, H. Hoffmann, R. Jaumann, U. Keller, R. Arvidson, J. Mustard & F. Forget (2004), OMEGA: Observatoire pour la Mineralogie, l'Eau, les Glaces et l'Activite, *Eur. Sp. Agency, (Special Publ. ESA SP*, *SP*(1291), 75–95.

Bibring, J.-P., Y. Langevin, A. Gendrin, B. Gondet, F. Poulet, M. Berthé, A. Soufflot, R. Arvidson, N. Mangold, J. Mustard, P. Drossart, and the OMEGA team (2005), Mars surface diversity as revealed by the OMEGA/Mars Express observations., *Science*, *307*(5715), 1576–1581, doi:10.1126/science.1108806.

Bibring, J.-P., Y. Langevin, J. Mustard, F. Poulet, R. Arvidson, A. Gendrin, B. Gondet, N. Mangold, P. Pinet, F. Forget, and the OMEGA team (2006), Global Mineralogical and Aqueous Mars History Derived from OMEGA/Mars Express Data, *Science*, *312*, 400–404, doi:10.1126/science.1122659.

Bish, D. L., D. F. Blake, D. T. Vaniman, S. J. Chipera, R. V. Morris, D. W. Ming, A. H. Treiman, P. Sarrazin, S. M. Morrison, R. T. Downs, C. N. Achilles, A. S. Yen, T. F. Bristow, J. A. Crisp, J. M. Morookian, J. D. Farmer, E. B. Rampe, E. M. Stolper, N. Spanovich, and the MSL Science Team (2013), X-ray Diffraction Results from Mars Science Laboratory: Mineralogy of Rocknest at Gale Crater, *Science*, *341*(6153), doi:10.1126/science.1238932.

Bishop, J. L., M. D. Lane, M. D. Dyar, and A. J. Brown (2008), Reflectance and emission spectroscopy study of four groups of phyllosilicates: smectites, kaolinite-serpentines, chlorites and micas, *Clay Miner.*, *43*(1), 35–54, doi:10.1180/claymin.2008.043.1.03.

Bishop, J. L., E. B. Rampe, D. L. Bish, Z. Abidin, L. L. Baker, N. Matsue, and T. Henmi (2013), Spectral and hydration properties of allophane and imogolite, *Clays Clay Miner.*, *61*(1), 57–74, doi:10.1346/CCMN.2013.0610105.

Blake, D., R. V. Morris, G. Kocurek, S. M. Morrison, R. T. Downs, D. Bish, D. W. Ming, K. S. Edgett, D. Rubin, W. Goetz, M. B. Madsen, R. Sullivan, R. Gellert, I. Campbell, A. H. Treiman, S. M. McLennan, A. S. Yen, J. Grotzinger, D. T. Vaniman, S. J. Chipera, C. N. Achilles, E. B. Rampe, D. Sumner, P-Y. Meslin, S. Maurice, O. Forni, O. Gasnault, M. Fisk, M. Schmidt, P. Mahaffy, L. A. Leshin, D. Glavin, A. Steele, C. Freissinet, R. Navarro-Gonzalez, R. A. Yingst, L. C. Kah, N. Bridges, K. W. Lewis, T. F. Bristow, J. D. Farmer, J. A. Crisp, E. M. Stolper, D. J. Des Marais, P. Sarrazin, and the MSL Science Team (2013), Curiosity at Gale Crater, Mars: Characterization and Analysis of the Rocknest Sand Shadow, *Science*, 341, doi:10.1126/science.1239505

Boynton, W. V, W. C. Feldman, S. W. Squyres, T. H. Prettyman, J. Brückner, L. G. Evans, R. C. Reedy, R. Starr, J. R. Arnold, D. M. Drake, P. A. J. Englert, A. E. Metzger, Igor Mitrofanov, J. I. Trombka, C. d'Uston, H. Wänke, O. Gasnault, D. K. Hamara, D. M. Janes, R. L. Marcialis, S. Maurice, I. Mikheeva, G. J. Taylor, R. Tokar, C. Shinohara (2002), Distribution of hydrogen in the near surface of Mars: evidence for subsurface ice deposits, *Science*, *297*(5578), 81–5, doi:10.1126/science.1073722.

Bridges, J. C., and P. H. Warren (2006), The SNC meteorites: basaltic igneous processes on Mars, *Journal of the Geological Society, London*, 163, 229-251, doi:10.1144/0016-764904-501.

Brown, A. J. (2014), Spectral bluing induced by small particles under the Mie and Rayleigh regimes, *Icarus*, *239*(C), 85–95, doi:10.1016/j.icarus.2014.05.042.

Bullock, M. A., and J. M. Moore (2004), Aqueous alteration of Mars-analog rocks under an acidic atmosphere, *Geophys. Res. Lett.*, *31*(14), 2–5, doi:10.1029/2004GL019980.

Bullock, M. A., J. M. Moore, and M. T. Mellon (2004), Laboratory simulations of Mars aqueous geochemistry, *Icarus*, *170*(2), 404–423, doi:10.1016/j.icarus.2004.03.016.

Byrne, S., and B. C. Murray (2002), North polar stratigraphy and the paleo-erg of Mars, *J. Geophys. Res.*, *107*(E6), 1–13, doi:10.1029/2001JE001615.

Cahill, D. and R. Pohl (1988), Lattice vibration and heat transport in crystals and glasses, *Annual Review of Physical Chemistry*, 39(2), 93-121, doi:10.1146/annurev.physchem.39.1.93.

Calas, G., G. S. Henderson, and J. F. Stebbins (2006), Glasses and melts: Linking geochemistry and materials science, *Elements*, *2*, 265–268, doi:10.2113/gselements.2.5.265.

Carrozzo, F. G., G. Bellucci, F. Altieri, E. D'Aversa, and J. P. Bibring (2009), Mapping of water frost and ice at low latitudes on Mars, *Icarus*, *203*(2), 406–420, doi:10.1016/j.icarus.2009.05.020.

Casey, W. H., H. R. Westrich, G. W. Arnold, and J. F. Banfield (1989a), The surface chemistry of dissolving labradorite feldspar, *Geochim. Cosmochim. Acta*, *53*(4), 821–832, doi:10.1016/0016-7037(89)90028-8.

Casey, W. H., H. R. Westrich, T. Massis, J. F. Banfield, and G. W. Arnold (1989b), The surface of labradorite feldspar after acid hydrolysis, *Chem. Geol.*, *78*(3-4), 205–218, doi:10.1016/0009-2541(89)90058-2.

Casey, W.H., Bunker, B. (1990) Leaching of mineral and glass surfaces during dissolution, in: Mineral–Water Interface Geochemistry, edited by M. F. Hochella Jr., A. F. White, Reviews in Mineralogy, Mineralogical Society of America, Washington, D.C., pp. 397–426.

Casey, W. H., H. R. Westrich, J. F. Banfield, G. Ferruzzi, and G. W. Arnold (1993), Leaching and reconstruction at the surfaces of dissolving chain-silicate minerals, *Nature*, *366*(6452), 253–256, doi:10.1038/366253a0.

Cheek, L. C., and C. M. Pieters (2014), Reflectance spectroscopy of plagioclase-dominated mineral mixtures: Implications for characterizing lunar anorthosites remotely, *American Mineralogist*, *99*(10), 1871–1892, doi:10.2138/am-2014-4785.

Chemtob, S. M., B. L. Jolliff, G. R. Rossman, J. M. Eiler, and R. E. Arvidson (2010), Silica coatings in the Ka'u Desert, Hawaii, a Mars analog terrain: A micromorphological, spectral, chemical, and isotopic study, *Journal of Geophysical Research*, *115*(E4), E04001, doi:10.1029/2009JE003473.

Chemtob, S. M., and G. R. Rossman (2014), Timescales and mechanisms of formation of amorphous silica coatings on fresh basalts at Kīlauea Volcano, Hawai'i, *Journal of Volcanology and Geothermal Research*, *286*, 41–54, doi:10.1016/j.jvolgeores.2014.08.029.

Chevrier, V., and P. E. Mathé (2007), Mineralogy and evolution of the surface of Mars: A review, *Planet. Space Sci.*, *55*(3), 289–314, doi:10.1016/j.pss.2006.05.039.

Christensen, P. R. (1988), Global albedo variations on Mars - Implications for active aeolian transport, deposition, and erosion, *J. Geophys. Res.*, *93*(B7), 7611–7624, doi:10.1029/JB093iB07p07611.

Christensen, P. R., D. L. Anderson, L. Stillman, C. Chase, R. N. Clark, H. H. Kieffer, M. C. Malin, J. C. Pearl, J. Carpenter, N. Bandiera, F. G. Brown, and S. Silverman (1992), Thermal emission spectrometer experiment: Mars Observer mission, *J. Geophys. Res.*, *97*(E5), 7719, doi:10.1029/92JE00453.

Christensen, P. R., and S. Harrison Thliveris (1993), Thermal infrared emission spectroscopy of natural surfaces: Application to desert varnish coatings on rocks, *J. Geophys. Res.*, *98*, doi:10.1029/93JB00135.

Christensen, P. R. (1998), Variations in Martian surface composition and cloud occurrence determined from thermal infrared spectroscopy: Analysis of Viking and Mariner 9 data, *J. Geophys. Res.*, *103*(E1), 1733–1746, doi:10.1029/97JE02114.

Christensen, P. R., J. L. Bandfield, R. N. Clark, K. S. Edgett, V. E. Hamilton, T. Hoefen, H. H. Kieffer, R. O. Kuzmin, M. D. Lane, and M. C. Malin (2000), Detection of Crystalline Hematite Mineralization on Mars by the Thermal Emission Spectrometer: Evidence for Near-surface Water, *Jouranl Geophys. Res.*, *105*(E4), 9623–9642, doi:10.1029/1999JE001093.

Christensen, P. R., R. V. Morris, M. D. Lane, J. L. Bandfield, and M. C. Malin (2001a), Global mapping of Martian hematite mineral deposits: Remnants of water-driven processes on early Mars, *J. Geophys. Res.*, *106*(E10), 23873, doi:10.1029/2000JE001415.

Christensen, P. R., J. L. Bandfield, V. E. Hamilton, S. W. Ruff, H. H. Kieffer, T. N. Titus, M. C. Malin, R. V. Morris, M. D. Lane, R. L. Clark, B. M. Jakosky, M. T. Mellon, J. C. Pearl, B. J. Conrath, M. D. Smith, R. T. Clancy, R. O. Kuzmin, T. Roush, G. L. Mehall, N. Gorelick, K. Bender, K. Murray, S. Dason, E. Greene, S. Silverman, and M. Greenfield (2001b), Mars Global Surveyor Thermal Emission Spectrometer experiment: Investigation description and surface science results, *Journal of Geophysical Research*, *106*, 23823–23872, doi:10.1029/2000JE001370.

Christensen, P. R. (2003), Formation of recent martian gullies through melting of extensive water-rich snow deposits., *Nature*, *422*(6927), 45–48, doi:10.1038/nature01436.

Christensen, P. R., M. B. Wyatt, T. D. Glotch, A. D. Rogers, S. Anwar, R. E. Arvidson, J. L. Bandfield, D. L. Blaney, C. Budney, W. M. Calvin, A. Fallacaro, R. L. Fergason, N. Gorelick, T. G. Graff, V. E. Hamilton, A. G. Hayes, J. R. Johnson, A. T. Knudson, H. Y. McSween Jr., G. L. Mehall, L. K. Mehall, J. E. Moersch, R. V. Morris, M. D. Smith, S. W. Squyres, S. W. Ruff, and M. J. Wolff (2004), Mineralogy at Meridiani Planum from the Mini-TES Experiment on the Opportunity Rover., *Science*, *306*(5702), 1733–9, doi:10.1126/science.1104909.

Clark, R. N. (1999), Spectroscopy of Rocks and Minerals, and Principles of Spectroscopy, in: Manual of Remote Sensing, Volume 3, Remote Sensing for the Earth Sciences, (A.N. Rencz, ed.) John Wiley and Sons, New York, p 3- 58.

Clark, R. N., T. V. V. King, M. Klejwa, G. A. Swayze, and N. Vergo (1990), High spectral resolution reflectance spectroscopy of minerals, *J. Geophys. Res.*, *95*(B8), 12653, doi:10.1029/JB095iB08p12653.

Clarke, J. D. A. (2006), Antiquity of aridity in the Chilean Atacama Desert, *Geomorphology*, *73*(1-2), 101–114, doi:10.1016/j.entcs.2005.12.035.

Clenet, H., P. Pinet, G. Ceuleneer, Y. Daydou, F. Heuripeau, C. Rosemberg, J. P. Bibring, G. Bellucci, F. Altieri, and B. Gondet (2013), A systematic mapping procedure based on the Modified Gaussian Model to characterize magmatic units from olivine/pyroxenes mixtures: Application to the Syrtis Major volcanic shield on Mars, *J. Geophys. Res. E Planets*, *118*(8), 1632–1655, doi:10.1002/jgre.20112.

Cloutis, E. A., and M. J. Gaffey (1991), Spectral-compositional variations in the constituent minerals of mafic and ultramafic assemblages and remote sensing implications, *Earth Moon Planets*, *53*, 11–53, doi:10.1007/BF00116217.

Cloutis, E., F. Hawthorne, S. Mertzman, K. Krenn, M. Craig, D. Marcino, M. Methot, J. Strong, J. Mustard, and D. Blaney (2006), Detection and discrimination of sulfate minerals using reflectance spectroscopy, *Icarus*, *184*(1), 121–157, doi:10.1016/j.icarus.2006.04.003.

Colman, S. M. (1982), Chemical Weathering of Basalts and Andesites: Evidence from Weathering Rinds, in *Geological Survey Professional Paper 1246*, p. 51.

Crisp, J., A. B. Kahle, and E. A. Abbott (1990), Thermal infrared spectral character of Hawaiian basaltic glasses, *Journal of Geophysical Research (ISSN 0148-0227)*, *95*(B13), 21657–21669, doi:10.1029/JB095iB13p21657.

Crovisier, J. L., J. Honnorez, and J. P. Eberhart (1987), Dissolution of basaltic glass in seawater: Mechanism and rate, *Geochimica et Cosmochimica Acta*, *51*(1), 2977–2990, doi:10.1016/0016-7037(87)90371-1.

Curtiss, B., J. B. Adams, and M. S. Ghiorso (1985), Origin, development and chemistry of silica-alumina rock coatings from the semi-arid regions of the island of Hawaii, *Geochim. Cosmochim. Acta*, *49*(1), 49–56, doi:10.1016/0016-7037(85)90190-5.

Daval, D., O. Sissmann, N. Menguy, G. D. Saldi, F. Guyot, I. Martinez, J. Corvisier, B. Garcia, I. Machouk, K. G. Knauss, R. Hellmann (2011), Influence of amorphous silica layer formation on the dissolution rate of olivine at 90°C and elevated pCO2, *Chem. Geol.*, *284*(1-2), 193–209, doi:10.1016/j.chemgeo.2011.02.021.

Dixon, J. C., C. E. Thorn, R. G. Darmody, and S. W. Campbell (2002), Weathering rinds and rock coatings from an Arctic alpine environment, northern Scandinavia, *Bull. Geol. Soc. Am.*, *114*(2), 226–238, doi:10.1130/0016-7606(2002)114<0226:WRARCF>2.0.CO;2.

Doremus, R. H. (1975), Interdiffusion of hydrogen and alkali ions in a glass surface, *J. Non. Cryst. Solids*, *19*(C), 137–144, doi:10.1016/0022-3093(75)90079-4.

Dorn, R. I. (1998), *Rock coatings*, Elsevier, New York, 429 pp.

Dury, G.H. (1969). Rational descriptive classification of duricrusts. Earth Science Journal, 3(2), 77-86.

Edwards, C. S., and P. R. Christensen (2013), Microscopic emission and reflectance thermal infrared spectroscopy: instrumentation for quantitative in situ mineralogy of complex planetary surfaces., *Appl. Opt.*, *52*(11), 2200–17, doi:10.1364/AO.52.002200.

Eggleton, R. A., C. Foudoulis, and D. Varkevisser (1987), Weathering of Basalt: Changes in Rock Chemistry and Mineralogy, *Clays Clay Miner.*, *35*(3), 161–169, doi:10.1346/CCMN.1987.0350301.

Ehlmann, B. L., J. F. Mustard, G. A. Swayze, R. N. Clark, J. L. Bishop, F. Poulet, D. J. Des Marais, L. H. Roach, R. E. Milliken, J. J. Wray, O. Barnouin-Jha, and S. L. Murchie (2009), Identification of hydrated silicate minerals on Mars using MRO-CRISM: Geologic context near Nili Fossae and implications for aqueous alteration, *J. Geophys. Res. E Planets*, *114*(10), 1–33, doi:10.1029/2009JE003339.

Ehlmann, B. L., J. F. Mustard, S. L. Murchie, J.-P. Bibring, A. Meunier, A. A. Fraeman, and Y. Langevin (2011), Subsurface water and clay mineral formation during the early history of Mars, *Nature*, *479*(7371), 53–60, doi:10.1038/nature10582.

Ehlmann, B. L., D. L. Bish, S. W. Ruff, and J. F. Mustard (2012), Mineralogy and chemistry of altered Icelandic basalts: Application to clay mineral detection and understanding aqueous environments on Mars, *J. Geophys. Res. E Planets*, *117*(10), doi:10.1029/2012JE004156.

Eick, M. J., P. R. Grossl, D. C. Golden, D. L. Sparks, and D. W. Ming (1996), Dissolution kinetics of a lunar glass simulant at 25C: The effect of pH and organic acids, *Geochim. Cosmochim. Acta*, *60*(1), 157–170, doi:10.1016/0016-7037(95)00377-0.

Elwood Madden, M. E., R. J. Bodnar, and J. D. Rimstidt (2004), Jarosite as an indicator of water- limited chemical weathering on Mars, *Nature*, *431*(August), 821–823, doi:10.1038/nature02934.1.

Essington, M. E. (2004), *Soil and Water Chemistry: An integrative approach*, CRC Press, Boca Raton, FL.

Evans, D. L., and J. B. Adams (1980), Amorphous gels as possible analogs to martian weathering products, *Proc. Lunar Planet. Sci. Conf. 11th*, 757–763.

Farmer, V. C. (1974), Infrared Spectra of Minerals, Mineralogical Society, London, 539 pp.

Farmer, C. B. (1976), Liquid water on Mars, *Icarus*, *28*(2), 279–289, doi:10.1016/0019-1035(76)90038-5.

Farnan, I., S. C. Kohn, and R. Dupree (1987), A study of the structural role of water in hydrous silica glass using cross-polarisation magic angle spinning NMR, *Geochim. Cosmochim. Acta*, *51*(10), 2869–2873, doi:10.1016/0016-7037(87)90165-7.

Farr, T. G., and J. B. Adams (1984), Rock coatings in Hawaii., *Geol. Soc. Am. Bull.*, *95*(9), 1077–1083, doi:10.1130/0016-7606(1984)95<1077:RCIH>2.0.CO;2.

Farrand, W. H., T. D. Glotch, J. W. Rice Jr, J. A. Hurowitz, and G. A. Swayze (2009), Discovery of jarosite within the mawrth vallis region of mars: Implications for the geologic history of the region, *Icarus*, 52, doi:10.1016/j.icarus.2009.07.014.

Feely, K. C., and P. R. Christensen (1999), Quantitative compositional analysis using thermal emission spectroscopy: Application to igneous and metamorphic rocks, *Journal of Geophysical Research*, *104*(E), 24195–24210, doi:10.1029/1999JE001034.

Fergason, R. L., P. R. Christensen, and H. H. Kieffer (2006), High-resolution thermal inertia derived from the Thermal Emission Imaging System (THEMIS): Thermal model and applications, *J. Geophys. Res. E Planets*, *111*(12), 1–22, doi:10.1029/2006JE002735.

Fischer, E. M., and C. M. Pieters (1993), The continuum slope of Mars - Bidirectional reflectance investigations and applications to Olympus Mons, *Icarus*, *102*, 185–202, doi:10.1006/icar.1993.1043.

Fishbaugh, K. E., and J. W. Head (2005), Origin and characteristics of the Mars north polar basal unit and implications for polar geologic history, *Icarus*, *174*(2 SPEC. ISS.), 444–474, doi:10.1016/j.icarus.2004.06.021.

Fishbaugh, K. E., F. Poulet, V. Chevrier, Y. Langevin, and J. P. Bibring (2007), On the origin of gypsum in the Mars north polar region, *J. Geophys. Res. E Planets*, *112*(7), 1–17, doi:10.1029/2006JE002862.

Flahaut, J., J. Carter, F. Poulet, J. P. Bibring, W. van Westrenen, G. R. Davies, and S. L. Murchie (2015), Embedded clays and sulfates in Meridiani Planum, Mars, *Icarus*, *248*, 269–288, doi:10.1016/j.icarus.2014.10.046.

Foley, C. N. (2003), Final chemical results from the Mars Pathfinder alpha proton X-ray spectrometer, *J. Geophys. Res.*, *108*(E12), 8096, doi:10.1029/2002JE002019.

Fulignati, P., A. Sbrana, R. Clocchiatti, and W. Luperini (2006), Environmental impact of the acid fumarolic plume of a passively degassing volcano (Vulcano Island, Italy), *Environ. Geol.*, *49*(8), 1139–1155, doi:10.1007/s00254-005-0158-0.

Ganguly, J., R. N. Bhattacharya, and S. Chakraborty (1988), Convolution Effect in the Determination of Compositional Profiles and Diffusion-Coefficients By Microprobe Step Scans, *Am. Mineral.*, *73*(7-8), 901–909.

Geisler, T., A. Janssen, D. Scheiter, T. Stephan, J. Berndt, and A. Putnis (2010), Aqueous corrosion of borosilicate glass under acidic conditions: A new corrosion mechanism, *Journal of Non-Crystalline Solids*, *356*(28-30), 1458–1465, doi:10.1016/j.jnoncrysol.2010.04.033.

Geisler, T., T. Nagel, M. R. Kilburn, A. Janssen, J. P. Icenhower, R. O. C. Fonseca, M. Grange, and A. A. Nemchin (2015), The mechanism of borosilicate glass corrosion revisited, *Geochimica et Cosmochimica Acta*, *158*, 112–129, doi:10.1016/j.gca.2015.02.039.

Gendrin, A., N. Mangold, J.-P. Bibring, Y. Langevin, B. Gondet, F. Poulet, G. Bonello, C. Quantin, J. Mustard, R. E. Arvidson, and S. Le Mouélic (2005), Sulfates in martian layered terrains: the OMEGA/Mars express view, *Science*, *307*(5715), 1587–1591, doi:10.1002/9780470114735.hawley00624.

Gin, S., J. V. Ryan, D. K. Schreiber, J. Neeway, and M. Cabié (2013), Contribution of atom-probe tomography to a better understanding of glass alteration mechanisms: Application to a nuclear glass specimen altered 25 years in a granitic environment, *Chem. Geol.*, *349-350*, 99–109, doi:10.1016/j.chemgeo.2013.04.001.

Gislason, S. R., D. R. Veblen, and K. J. T. Livi (1993), Experimental meteoric water-basalt interactions: Characterization and interpretation of alteration products, *Geochim. Cosmochim. Acta*, *57*(7), 1459–1471, doi:10.1016/0016-7037(93)90006-I.

Gislason, S., and E. Oelkers (2003), Mechanism, rates, and consequences of basaltic glass dissolution: II. An experimental study of the dissolution rates of basaltic glass as a function of pH and temperature, *Geochimica et Cosmochimica Acta*, *67*(20), 3817–3832, doi:10.1016/S0016-7037(00)00176-5.

Glass, B. (1984), Tektites, *Journal of Non-Crystalline Solids*, *67*, 333–344, doi:10.1016/0022-3093(84)90158-3.

Golden, D. C., R. V. Morris, D. W. Ming, H. V. Lauer, and S. R. Yang (1993), Mineralogy of three slightly palagonitized basaltic tephra samples from the summit of Mauna Kea, Hawaii, , *98*, 3401–3411, doi:10.1029/92JE02590.

Golden, D. C., D. W. Ming, R. V. Morris, and S. A. Mertzman (2005), Laboratory-simulated acid-sulfate weathering of basaltic materials: Implications for formation of sulfates at Meridiani Planum and Gusev crater, Mars, *Journal of Geophysical Research*, *110*, doi:10.1029/2005JE002451.

Golombek, M. P., L. S. Crumpler, J. A. Grant, R. Greeley, N. A. Cabrol, T. J. Parker, J. W. Rice Jr., J. G. Ward, R. E. Arvidson, J. E. Moersch, R. L. Fergason, P. R. Christensen, A. Castaño, R. Castaño, A. F. C. Haldemann, R. Li, J. F. Bell III, and S. W. Squyres (2006), Geology of the Gusev cratered plains from the Spirit rover transverse, *J. Geophys. Res. E Planets*, *111*(2), 1–27, doi:10.1029/2005JE002503.

Gooding, J. L. (1978), Chemical Weathering on Mars: Thermodynamic Stabilities of Primary Minerals (and Their Alteration Products) from Mafic Igneous Rocks, *Icarus*, *33*, 483–513.

Gooding, J. L., R. E. Arvidson, and M. Y. Zolotov (1992), Physical and chemical weathering, in: Mars, H. H. Kieffer, B. M. Jakosky, C. W. Snyder, M. S. Matthews (eds.), University of Arizona Press, Tucson & London, 626-651.

Grambow, B. (2006), Nuclear Waste Glasses-How Durable? *Elements*, *2*(6), 357.

Guy, C., and J. Schott (1989), Multisite surface reaction versus transport control during the hydrolysis of a complex oxide, *Chem. Geol.*, *78*(3-4), 181–204, doi:10.1016/0009-2541(89)90057-0.

Haberle, R. M., C. P. Mckay, J. Schaeffer, N. A. Cabrol, E. A. Grin, A. P. Zent, and R. Quinn (2001), On the possibility of liquid water on present-day Mars, *J. Geophys. Res.*, *106*, 23317–23326.

Hallet, B. (1975), Subglacial silica deposits, *Nature*, *254*(5502), 682–683, doi:10.1038/254682a0.

Hamilton, V. E., M. B. Wyatt, H. Y. McSween, and P. R. Christensen (2001), Analysis of terrestrial and Martian volcanic compositions using thermal emission spectroscopy: 2. Application to Martian surface spectra from the Mars Global Surveyor Thermal Emission Spectrometer, *J. Geophys. Res.*, *106*(E7), 14733–14746, doi:10.1029/2000JE001356.

Hamilton, V. E., R. V. Morris, J. E. Gruener, and S. A. Mertzman (2008), Visible, near-infrared, and middle infrared spectroscopy of altered basaltic tephras: Spectral signatures of phyllosilicates, sulfates, and other aqueous alteration products with application to the mineralogy of the Columbia Hills of Gusev Crater, Mars, *J. Geophys. Res. E Planets*, *113*(12), 1–30, doi:10.1029/2007JE003049.

Handke, M., and W. Mozgawa (1993), Vibrational spectroscopy of the amorphous silicates, *Vib. Spectrosc.*, *5*, 75–84, doi:10.1016/0924-2031(93)87057-Z.

Haskin, L. A., A. Wang, B. L. Jolliff, H. Y. McSween, B. C. Clark, D. J. Des Marais, S. M. McLennan, N. J. Tosca, J. A. Hurowitz, J. D. Farmer, A.Yen, S. W. Squyres, R. E. Arvidson,G. Klingelhöfer, C. Schröder, P. A. de Souza Jr, D. W. Ming, R.Gellert, J. Zipfel, J. Brückner, J. F. Bell III, K. Herkenhoff, P. R. Christensen, S. Ruff, D. Blaney, S. Gorevan, N. A. Cabrol1, L. Crumpler, J. Grant, and L. E. Soderblom (2005), Water alteration of rocks and soils on Mars at the Spirit rover site in Gusev crater., *Nature*, *436*(7047), 66–69, doi:10.1038/nature03640.

Hausrath, E. M., A. K. Navarre-Sitchler, P. B. Sak, C. I. Steefel, and S. L. Brantley (2008), Basalt weathering rates on Earth and the duration of liquid water on the plains of Gusev Crater, Mars, *Geology*, *36*(1), 67–70, doi:10.1130/G24238A.1.

Hausrath, E. M., and S. L. Brantley (2010), Basalt and olivine dissolution under cold, salty, and acidic conditions: What can we learn about recent aqueous weathering on Mars? *Journal of Geophysical Research*, doi:10.1029/2010JE003610.

Hay, R.L., Sheppard, R.A., 2001. Occurrence of zeolites in sedimentary rocks: an overview. In: Bish, D.L.,Ming, D.W. (Eds.), Natural Zeolites: Occurrence, Properties, Applications. Mineralogical Society of Amer- ica,Washington, DC, pp. 217‑234.

He, G. S., H.-Y. Qin, and Q. Zheng (2009), Rayleigh, Mie, and Tyndall scatterings of polystyrene microspheres in water: Wavelength, size, and angle dependences, *J. Appl. Phys.*, *105*(2), 023110, doi:10.1063/1.3068473.

Head, J. W., J. F. Mustard, M. a Kreslavsky, R. E. Milliken, and D. R. Marchant (2003), Recent ice ages on Mars., *Nature*, *426*(6968), 797–802, doi:10.1038/nature02114.

Hellmann, R., J. M. Penisson, R. L. Hervig, J. H. Thomassin, and M. F. Abrioux (2003), An EFTEM/HRTEM high-resolution study of the near surface of labradorite feldspar altered at acid pH: Evidence for interfacial dissolution-reprecipitation, *Phys. Chem. Miner.*, *30*(4), 192–197, doi:10.1007/s00269-003-0308-4.

Hellmann, R., J.-M. Penisson, R. L. Hervig, J.-H. Thomassin, and M. F. Abrioux (2004), Chemical alteration of feldspar: a comparative study using SIMS and HRTEM/EFTEM. , *Water Rock Interact.* , *II*, 753–756.

Hellmann, R., R. Wirth, D. Daval, J.-P. Barnes, J.-M. Penisson, D. Tisserand, T. Epicier, B. Florin, and R. L. Hervig (2012), Unifying natural and laboratory chemical weathering with interfacial dissolution–reprecipitation: A study based on the nanometer-scale chemistry of fluid–silicate interfaces, *Chemical Geology*, *294-295*, 203–216, doi:10.1016/j.chemgeo.2011.12.002.

Helmer, R. G., R. L. Heath, N. Reactor, T. Stathm, M. Putnam, D. H. Gipson, P. P. Company, and T. Station (1967), Photopeak analysis program for photon energy and intensity determinations: Ge(Li) and NaI(Tl) spectrometers, *Nucl. Instruments Methods*, *57*(0), 46–57, doi:http://dx.doi.org/10.1016/0029-554X(67)90496-X.

Henderson, G. S. (2005), The structure of silicate melts: A glass perspective, *Can. Mineral.*, *43*(6), 1921–1958, doi:10.2113/gscanmin.43.6.1921.

Herzberg, G. (1945), Molecular spectra and molecular structure, II. Infrared and Raman spectra of polyatomic molecules, Van Nostrand Reinhold, New York, 632 pp.

Horgan, B. H., J. F. Bell III, E. Z. Noe Dobrea, E. A. Cloutis, D. T. Bailey, M. A. Craig, L. H. Roach, and J. F. Mustard (2009), Distribution of hydrated minerals in the north polar region of Mars, *J. Geophys. Res.*, *114*(November 2008), E01005, doi:10.1029/2008JE003187.

Horgan, B., and J. F. Bell (2012), Widespread Weathered Glass on the Surface of Mars, *Geology*, *40*, 391–394, doi:10.1130/G32755.1.

Horgan, B., E. A. Cloutis, P. Mann, and J. F. Bell (2014), Near-infrared spectra of ferrous mineral mixtures and methods for their identification in planetary surface spectra, *Icarus*, *234*, 132–154, doi:10.1016/j.icarus.2014.02.031.

Horgan, B., R. J. Smith, P. Mann, E. A. Cloutis, P. R. Christensen, Acid weathering of basalt and basaltic glass: I. Near-infrared spectra, thermal-infrared spectra, and implications for Mars, submitted to *Journal of Geophysical Research*

Hu, X., D. A. Grossie, and S. R. Higgins (2005), Growth and dissolution kinetics at the dolomite-water interface: An in-situ scanning probe microscopy study, *Am. Mineral.*, *90*(5-6), 963–968, doi:10.2138/am.2005.1798.

Hunt, G. R., and L. M. Logan (1972), Variation of Single Particle Mid-Infrared Emission Spectrum with Particle Size, *Appl. Opt.*, *11*(1), 142–147, doi:10.1364/AO.11.000142.

Hurowitz, J. A., S. M. Mclennan, D. H. Lindsley, and M. A. A. Schoonen (2005), Experimental epithermal alteration of synthetic Los Angeles meteorite: Implications for the origin of Martian soils and identification of hydrothermal sites on Mars, *Journal of Geophysical Research*, *110*(E), 7002, doi:10.1029/2004JE002391.

Hurowitz, J. A., S. M. McLennan, N. J. Tosca, R. E. Arvidson, J. R. Michalski, D. W. Ming, C. Schröder, and S. W. Squyres (2006), In situ and experimental evidence for acidic weathering of rocks and soils on Mars, *J. Geophys. Res. E Planets*, *111*(2), 1–16, doi:10.1029/2005JE002515.

Jakosky, B. and P. R. Christensen (1986), Global duricrust on Mars: Analysis of remote-sensing data, *Journal of Geophysical Research*, 91(B3), 3547-3559, doi:10.1029/JB091iB03p03547.

Jantzen, C., and M. Plodinec (1984), Thermodynamic model of natural, medieval and nuclear waste glass durability, *J. Non. Cryst. Solids*, *67*, 207–223.

Johnson, J. R., R. Kirk, L. A. Soderblom, L. Gaddis, R. J. Reid, D. T. Britt, P. Smith, M. Lemmon, N. Thomas, J. F. Bell III, N. T. Bridges, R. Anderson, K. E. Herkenhoff, J. Maki, S. Murchie, A. Dummel, R. Jaumann, F. Trauthan, and G. Arnold (1999), Preliminary results on photometric properties of materials at the Sagan Memorial Station, Mars, *J. Geophys. Res.*, *104*(E4), 8809–8830.

Jonas, L., T. John, H. E. King, T. Geisler, and A. Putnis (2014), The role of grain boundaries and transient porosity in rocks as fluid pathways for reaction front propagation, *Earth Planet. Sci. Lett.*, *386*, 64–74, doi:10.1016/j.epsl.2013.10.050.

Kahle, A. B., A. R. Gillespie, E. A. Abbott, M. J. Abrams, and R. E. Walker (1988), Relative dating of Hawaiian lava flows using multispectral thermal infrared images - A new tool for geologic mapping of young volcanic terranes, *J. Geophys. Res.*, *93*(B12), 15239–15251, doi:10.1029/JB093iB12p15239.

Kereszturi, A., and E. G. Rivera-Valentin (2012), Locations of thin liquid water layers on present-day Mars, *Icarus*, *221*(1), 289–295, doi:10.1016/j.icarus.2012.08.004.

Kieffer, H. H., T. Z. Martin, A. R. Peterfreund, B. M. Jakosky, E. D. Miner, and F. D. Palluconi (1977), Thermal and albedo mapping of Mars during the Viking primary mission, *J. Geophys. Res.*, *82*(28), 4249–4291, doi:10.1029/JS082i028p04249.

King, H. E., O. Plumper, T. Geisler, and A. Putnis (2011), Experimental investigations into the silicification of olivine: Implications for the reaction mechanism and acid neutralization, *American Mineralogist*, *96*(10), 1503–1511, doi:10.2138/am.2011.3779.

Klingelhöfer, G., R. V. Morris, B. Bernhardt, C. Schröder, D. S. Rodionov, P. A. de Souza Jr., A. Yen, R. Gellert, E. N. Evlanov, B. Zubkov, J. Foh, U. Bonnes, E. Kankeleit, P. Gütlich, D. W. Ming, F. Renz, T. Wdowiak, S. W. Squyres and R. E. Arvidson (2004), Jarosite and hematite at Meridiani Planum from Opportunity's Mossbauer spectrometer, *Science*, *306*(5702), 1740–1745.

Koeppen, W. C., and V. E. Hamilton (2008), Global distribution, composition, and abundance of olivine on the surface of Mars from thermal infrared data, *J. Geophys. Res.*, *113*(E5), 1–23, doi:10.1029/2007JE002984.

Kraft, M. D., J. R. Michalski, and T. G. Sharp (2003), Effects of pure silica coatings on thermal emission spectra of basaltic rocks: Considerations for Martian surface mineralogy, *Geophys. Res. Lett.*, *30*(24), 4, doi:10.1029/2003GL018848.

Kraft, M. D., T. G. Sharp, J. R. Michalski, and E. B. Rampe (2007), Combined Thermal and Near Infrared Spectra of Hydrous Silica Coatings: Implications for Surface Type 2 Mineralogy and Recent Liquid Water on Mars, *38th Lunar and Planetary Science Conference*, *38*, #2241.

Kraft, M. D., A. D. Rogers, R. L. Fergason, J. R. Michalski, and T. G. Sharp (2010), Spectral and geomorphic evidence for chemical weathering in the icy plains, in *41st Lunar and Planetary Science Conference*, p. Abstract 2600.

Kreslavsky, M.A., Head, J. W. (2000), Kilometer-scale roughness of Mars: Results from MOLA data analysis, *J. Geophys. Res.*, *105*(E11), 26695–26711, doi:10.1029/2000JE001259.

Kreslavsky, M. A., and J. W. Head (2002), Fate of outflow channel effluents in the northern lowlands of Mars: The Vastitas Borealis Formation as a sublimation residue from frozen ponded bodies of water, *J. Geophys. Res.*, *107*(E12), 1–25, doi:10.1029/2001JE001831.

Lancaster, N., and R. Greeley (1990), Sediment volume in the north polar sand seas of Mars, *J. Geophys. Res.*, *95*(B7), 10921–10927, doi:10.1029/JB095iB07p10921.

Langer, K., and O. Florke (1974), Near infrared absorption spectra of opals and the role of water in these SiO2-nH20 minerals, *Fortschritte der Mineralogie*, *52*(1), 17–51.

Langevin, Y., F. Poulet, J.-P. Bibring, and B. Gondet (2005), Sulfates in the North Polar Region of Mars Detected by OMEGA/Mars Express, *Science*, *307*(5715), 1584–1586, doi:10.1126/science.1109091.

Launer, P. J. (1952), Regularities in the infrared absorption spectra of silicate minerals, *Am. Mineral.*, *37*, 764.

Levard, C., E. Doelsch, I. Basile-Doelsch, Z. Abidin, H. Miche, A. Masion, J. Rose, D. Borschneck, and J. Y. Bottero (2012), Structure and distribution of allophanes, imogolite and proto-imogolite in volcanic soils, *Geoderma*, *183-184*, 100–108, doi:10.1016/j.geoderma.2012.03.015.

Lippincott, E. R., A. Van Valkenburg, and C. E. Weir (1958), Infrared studies on polymorphs of silicon dioxide and germanium dioxide, *Journal of Research of the National Bureau of Standards*, *61*(1), 61–70.

Luce, R. W., R. W. Bartlett, and G. A. Parks (1972), Dissolution kinetics of magnesium silicates, *Geochim. Cosmochim. Acta*, *36*, 35–50.

Lyon, R. J. P. (1965), Analysis of rocks by spectral infrared emission (8 to 25 microns), *Econ. Geol.*, *60*(4), 715–736, doi:10.2113/gsecongeo.60.4.715.

Madeleine, J. B., J. W. Head, F. Forget, T. Navarro, E. Millour, A. Spiga, A. Colaïtis, A. Määttänen, F. Montmessin, and J. L. Dickson (2014), Recent Ice Ages on Mars: The role of radiatively active clouds and cloud microphysics, *Geophys. Res. Lett.*, *41*(14), 4873–4879, doi:10.1002/2014GL059861.

Mangold, N., D. Baratoux, O. Arnalds, J.-M. Bardintzeff, B. Platevoet, M. Grégoire, and P. Pinet (2011), Segregation of olivine grains in volcanic sands in Iceland and implications for Mars, *Earth and Planetary Science Letters*, 310(2011), 233-243, doi:10.1016/j.epsl.2011.07.025.

Marcucci, E. C., and B. M. Hynek (2014), Laboratory simulations of acid-sulfate weathering under volcanic hydrothermal conditions: Implications for early Mars, *J. Geophys. Res. Planets*, *119*(3), 679–703, doi:10.1002/2013JE004439.

Matsuoka, N. (1995), Rock weathering processes and landform development in the Sor Rondane Mountains, Antarctica: Geomorphology, v. 12, p. 323–339.

McAdam, A. C., M. Y. Zolotov, T. G. Sharp, and L. A. Leshin (2008), Preferential low-pH dissolution of pyroxene in plagioclase pyroxene mixtures: Implications for martian surface materials, *Icarus*, *196*, 90–96, doi:10.1016/j.icarus.2008.01.008.

Mccord, T. B., R. N. Clark, and R. B. Singer (1982), Mars - Near-infrared spectral reflectance of surface regions and compositional implications, *J. Geophys. Res.*, *87*, 3021–3032, doi:10.1029/JB087iB04p03021.

McLennan, S. M. (2003), Sedimentary silica on Mars, *Geology*, *31*(4), 315–318, doi:10.1130/0091-7613(2003)031<0315:SSOM>2.0.CO;2.

Meier, R. J. (2005), On art and science in curve-fitting vibrational spectra, *Vib. Spectrosc.*, *39*(2), 266–269, doi:10.1016/j.vibspec.2005.03.003.

Mellon, M., B. M. Jackosky, H. H. Kieffer, and P. R. Christensen (2000), High-Resolution Thermal Inertia Mapping from the Mars Global Surveyor Thermal Emission Spectrometer, *Icarus*, *148*(2), 437–455, doi:10.1006/icar.2000.6503.

Michalski, J. R., M. D. Kraft, T. Diedrich, T. G. Sharp, P. R. Christensen (2003) Thermal emission spectroscopy of the silica polymorphs and considerations for remote sensing of Mars, *Geophysical Research Letters*, 30(19), doi:10.1029/2003GL018354.

Michalski, J. R., S. J. Reynolds, T. G. Sharp, and P. R. Christensen (2004), Thermal infrared analysis of weathered granitic rock compositions in the Sacaton Mountains, Arizona: Implications for petrologic classifications from thermal infrared remote-sensing data, *J. Geophys. Res.*, *109*(E3), E03007, doi:10.1029/2003JE002197.

Michalski, J. R., M. D. Kraft, T. G. Sharp, L. B. Williams, and P. R. Christensen (2005), Mineralogical constraints on the high-silica martian surface component observed by TES, *Icarus*, *174*(1), 161–177, doi:10.1016/j.icarus.2004.10.022.

Michalski, J. R., M. D. Kraft, T. G. Sharp, and P. R. Christensen (2006), Effects of chemical weathering on infrared spectra of Columbia River Basalt and spectral interpretations of martian alteration,, *248*, 822, doi:10.1016/j.epsl.2006.06.034.

Milliken, R. E., G.A. Swayze, R.E. Arvidson, J.L. Bishop, R.N. Clark, B.L. Ehlmann, R.O. Green, J.P. Grotzinger, R.V. Morris, S.L. Murchie, J.F. Mustard, and C. Weitz (2008), Opaline silica in young deposits on Mars, *Geology*, *36*(1), 847–850, doi:10.1130/G24967A.1.

Ming, D. W., and J. L. Boettinger (2001), Zeolites in Soil Environments, *Rev. Mineral. Geochemistry*, *45*(1), 323–345, doi:10.2138/rmg.2001.45.11.

Ming, D. W., D. W. Mittlefehldt, R. V. Morris, D. C. Golden, R. Gellert, A. Yen, B. C. Clark, S. W. Squyres, W. H. Farrand, S. W. Ruff, R. E. Arvidson, G. Klingelhöfer, H. Y. McSween, D. S. Rodionov, C. Schröder, P. A. de Souza Jr., and A. Wang (2006), Geochemical and mineralogical indicators for aqueous processes in the Columbia Hills of Gusev crater, Mars, *J. Geophys. Res. E Planets*, *111*(2), doi:10.1029/2005JE002560.

Minitti, M. E., J. F. Mustard, and M. J. Rutherford (2002), Effects of glass content and oxidation on the spectra of SNC-like basalts: Applications to Mars remote sensing, *Journal of Geophysical Research*, *107*(E5), 5030, doi:10.1029/2001JE001518.

Minitti, M., C. Weitz, M. Lane, and J. Bishop (2007), Morphology, chemistry, and spectral properties of Hawaiian rock coatings and implications for Mars, *Journal of Geophysical Research*, *112*, 24, doi:10.1029/2006JE002839.

Minitti, M. E., and V. E. Hamilton (2010), A search for basaltic-to-intermediate glasses on Mars: Assessing martian crustal mineralogy, *Icarus*, *210*(1), 135–149, doi:10.1016/j.icarus.2010.06.028.

Moersch, J. E., and P. R. Christensen (1995), Thermal emission from particulate surfaces: a comparison of scattering models with measured spectra, *J. Geophys. Res.*, *100*(E4), 7465–7477, doi:10.1029/94JE03330.

Möhlmann, D. (2010), The three types of liquid water in the surface of present Mars, *Int. J. Astrobiol.*, *9*(01), 45, doi:10.1017/S147355040999036X.

Möhlmann, D. T. F. (2004), Water in the upper martian surface at mid- and low-latitudes: Presence, state, and consequences, *Icarus*, *168*(2), 318–323, doi:10.1016/j.icarus.2003.11.008.

Moore, H. J., R. E. Hutton, R. F. Scott, C. R. Spitzer, and R. W. Shorthill (1977), Surface materials of the Viking landing sites, J. Geophys. Res., 82, 4497‐4523, doi:10.1029/JS082i028p04497.

Morris, R. V, H. V Lauer, C. A. Lawson, E. K. Gibson, G. A. Nace, and C. Stewart (1985), Spectral and other physicochemical properties of submicron powders of hematite (α-Fe2O3), maghemite (γ-Fe2O3), magnetite (Fe3O4), goethite (α-FeOOH), and lepidocrocite (γ-FeOOH), *J. Geophys. Res. Solid Earth*, *90*(B4), 3126–3144, doi:10.1029/JB090iB04p03126.

Morris, R. V. (1988), What ferric oxide/oxyhydroxide phases are present on Mars?, in *LPI Tech. Rep.*, pp. 126–127.

Morris, R. V., D. C. Golden, J. F. Bell, H. V. Lauer, and J. B. Adams (1993), Pigmenting agents in martian soils: Inferences from spectral, Mössbauer, and magnetic properties of nanophase and other iron oxides in Hawaiian palagonitic soil PN-9, *Geochim. Cosmochim. Acta*, *57*(19), 4597–4609, doi:10.1016/0016-7037(93)90185-Y.

Morris, R. V., D.C. Golden, J. F. Bell III, T. D. Shelfer, A. C. Scheinost, N. W. Hinman, G. Furniss, S. A. Mertzman, J. L. Bishop, D. W. Ming, C. C. Allen, and D. T. Britt (2000), Mineralogy, composition, and alteration of Mars Pathfinder rocks and soils: Evidence from multispectral, elemental, and magnetic data on terrestrial analogue, SNC meteorite, and Pathfinder samples, *J. Geophys. Res.*, *105*(E1), 1757, doi:10.1029/1999JE001059.

Morris, R. V., D. C. Golden, D. W. Ming, T. D. Shelfer, L. C. Jørgensen, J. F. Bell, T. G. Graff, and S. a. Mertzman (2001), Phyllosilicate-poor palagonitic dust from Mauna Kea Volcano (Hawaii): A mineralogical analogue for magnetic Martian dust?, *J. Geophys. Res.*, *106*(E3), 5057, doi:10.1029/2000JE001328.

Morris, R. V., T. G. Graff, S. A. Mertzman, M. D. Lane, and P. R. Christensen (2003), Palagonitic (not andesitic) Mars: Evidence from thermal emission and VNIR spectra of palagonitic alteration rinds on basaltic rock, in *Sixth International Conference on Mars (2003)*, vol. 77058, pp. 6–9.

Morris, R. V., G. Klingelhöfer, C. Schröder, D. S. Rodionov, A. Yen, D. W. Ming, P. A. de Souza Jr., I. Fleischer, T. Wdowiak, R. Gellert, B. Bernhardt, E. N. Evlanov, B. Zubkov, J. Foh, U. Bonnes, E. Kankeleit, P. Gütlich, F. Renz, S. W. Squyres, and R. E. Arvidson (2006), Mössbauer mineralogy of rock, soil, and dust at Gusev crater, Mars: Spirit's journey through weakly altered olivine basalt on the plains and pervasively altered basalt in the Columbia Hills, *J. Geophys. Res. E Planets*, *111*(2), doi:10.1029/2005JE002584.

Morris, R. V., D. W. Ming, D. F. Blake, D. T. Vaniman, D. L. Bish, S. J. Chipera, R. T. Downs, R. Gellert, A. H. Treiman, A. S. Yen, C. N. Achilles, R. C. Anderson, T. F. Bristow, J. A. Crisp, D. J. Des Marais, J. D. Farmer, J. P. Grotzinger, L. A. Leshin, A. C. McAdam, J. M. Morookian, S. M. Morrison, E. B. Rampe, P. C. Sarrazin, N. Spanovich, E. M. Stolper, and the MSL Science Team (2013), The amorphous component in martian basaltic soil in global perspective from MSL and MER missions, in *44th LPSC*, p. 1653.

Murchie, S., R. Arvidson, P. Bedini, K. Beisser, J.-P. Bibring, J. Bishop, J. Boldt, P. Cavender, T. Choo, R. T. Clancy, E. H. Darlington, D. Des Marais, R. Espiritu, D. Fort, R. Green, E. Guinness, J. Hayes, C. Hash, K. Heffernan, J. Hemmler, G. Heyler, D. Humm, J. Hutcheson, N. Izenberg, R. Lee, J. Lees, D. Lohr, E. Malaret, T. Martin, J. A. McGovern, P. McGuire, R. Morris, J. Mustard, S. Pelkey, E. Rhodes, M. Robinson, T. Roush, E. Schaefer, G. Seagrave, F. Seelos, P. Silverglate, S. Slavney, M. Smith, W.-J. Shyong, K. Strohbehn, H. Taylor, P. Thompson, B. Tossman, M. Wirzburger, and M. Wolff (2007), Compact Connaissance Imaging Spectrometer for Mars (CRISM) on Mars Reconnaissance Orbiter (MRO), *J. Geophys. Res. E Planets*, *112*(5), 1–57, doi:10.1029/2006JE002682.

Mustard, J. F., C. D. Cooper, and M. K. Rifkin (2001), Evidence for recent climate change on Mars from the identification of youthful near-surface ground ice., *Nature*, *412*(6845), 411–414, doi:10.1038/35086515.

Mustard, J. F., F. Poulet, A. Gendrin, J.-P. Bibring, Y. Langevin, B. Gondet, N. Mangold, G. Bellucci, and F. Altieri (2005), Olivine and pyroxene diversity in the crust of Mars, *Science (80-.).*, *307*(5715), 1594–1597.

Mutch, T. A., A. B. Binder, F. O. Huck, E. C. Levinthal, S. Liebes Jr., E. C. Morris,W. R. Patterson, B. Pollack, C. Sagan, and G. R. Taylor (1976a), The surface of Mars−The view from the Viking 1 lander, Science, 193, 791‑801.

Mysen, B. O., L. W. Finger, D. Virgo, and F. A. Seifert (1982), Curve-fitting of Raman spectra of silicate glasses., *Am. Mineral.*, *67*(7-8), 686–695.

Nesbitt, H. W., and I. J. Muir (1988), SIMS depth profiles of weathered plagioclase and processes affecting dissolved Al and Si in some acidic soil solutions, *Nature*, *334*, 336–338.

Nesbitt, H. W., and R. E. Wilson (1992), Recent chemical weathering of basalts, *Am. J. Sci.*, *292*(10), 740–777, doi:10.2475/ajs.292.10.740.

O'Neil, J., and H. Taylor (1967), The oxygen isotope and cation exchange chemistry of feldspars, *Am. Mineral.*, *52*(1431), 1414–1437.

Ody, A., F. Poulet, Y. Langevin, J. P. Bibring, G. Bellucci, F. Altieri, B. Gondet, M. Vincendon, J. Carter, and N. Manaud (2012), Global maps of anhydrous minerals at the surface of Mars from OMEGA/MEx, *J. Geophys. Res. E Planets*, *117*(9), 1–14, doi:10.1029/2012JE004117.

Oelkers, E. H. (2001), General kinetic description of multioxide silicate mineral and glass dissolution, *Geochim. Cosmochim. Acta*, *65*(21), 3703–3719, doi:10.1016/S0016-7037(01)00710-4.

Oelkers, E. H., and S. R. Gislason (2001), The mechanism, rates and consequences of basaltic glass dissolution: I. An experimental study of the dissolution rates of basaltic glass as a function of aqueous Al, Si and oxalic acid concentration at 25°C and pH = 3 and 11, *Geochimica et Cosmochimica Acta*, *65*(21), 3671–3681, doi:10.1016/S0016-7037(01)00664-0.

Oguchi, C. (2004), A porosity-related diffusion model of weathering-rind development, *Catena*, *58*(1), 65–75, doi:10.1016/j.catena.2003.12.002.

Paces, T. (1973), Steady-state kinetics and equilibrium between ground water and granitic rock, *Geochim. Cosmochim. Acta*, *37*(12), 2641–2663, doi:10.1016/0016-7037(73)90270-6.

Peacock, M.A. and R. E. Fuller (1928), Chlorophaeite, sideromelane and palogonite from the Columbia River Plateau of Washington of Washington, *Am. Mineral.*, 360 – 383.

Peterson, J., and Morseby, J., 1979, Subglacial travertine and associated deposits in the Carstensz area Irian Jaya, Republic of Indonesia: Zeitschrift für Gletscherkunde und Glaziologie, v. 15, p. 23–26.

Petit, J.-C., G. Delia Mea, J.-C. Dran, J. Schott, and R. A. Berner (1987), Mechanism of diopside dissolution from hydrogen depth profiling, *Nature*, *325*(6106), 705–707, doi:10.1038/325705a0.

Petit, J. C., J. C. Dran, A. Paccagnella, and G. Della Mea (1989), Structural dependence of crystalline silicate hydration during aqueous dissolution, *Earth Planet. Sci. Lett.*, *93*(2), 292–298, doi:10.1016/0012-821X(89)90077-0.

Petit, J., G. Mea, J. Dran, M. Magonthier, P. Mando, and A. Paccagnella (1990), Hydrated-layer formation during dissolution of complex silicate glasses and minerals, *Geochimica et Cosmochimica Acta*, *54*(7), 1941–1955.

Piqueux, S., and P. R. Christensen (2009a), A model of thermal conductivity for planetary soils: 1. Theory for unconsolidated soils, *J. Geophys. Res. E Planets*, *114*(9), 1–20, doi:10.1029/2008JE003309.

Piqueux, S., and P. R. Christensen (2009b), A model of thermal conductivity for planetary soils: 2. Theory for cemented soils, *J. Geophys. Res. E Planets*, *114*(9), 1–12, doi:10.1029/2008JE003309.

Pollok, K., C. V. Putnis, and A. Putnis (2011), Mineral replacement reactions in solid solution-aqueous solution systems: Volume changes, reactions paths and end-points using the example of model salt systems, *Am. J. Sci.*, *311*(3), 211–236, doi:10.2475/03.2011.02.

Poulet, F, J. –P. Bibring, J. F. Mustard, A. Gendrin, N. Mangold, Y. Langevin, R. E. Arvidson, B. Gondet, C. Gomez and the OMEGA Team (2005), Phyllosilicates on Mars and implications for early martian climate, *Nature*, *438*(7068), 623–627, doi:10.1038/nature04274.

Poulet, F., Y. Langevin, G. Boubin, D. Jouglet, J. –P. Bibring, B. Gondet (2008), Spectral variability of the Martian high latitude surfaces, *Geophysical Research Letters*, 35(20), 6-11, doi:10.1029/2008GL035450.

Putnis, A., and C. V. Putnis (2007), The mechanism of reequilibration of solids in the presence of a fluid phase, *J. Solid State Chem.*, *180*(5), 1783–1786, doi:10.1016/j.jssc.2007.03.023.

Putnis, C. V., and E. Ruiz-Agudo (2013), The mineral-water interface: Where minerals react with the environment, *Elements*, *9*(3), 177–182, doi:10.2113/gselements.9.3.177.

Putzig, N. E., and M. T. Mellon (2007), Apparent thermal inertia and the surface heterogeneity of Mars, *Icarus*, *191*(1), 68–94, doi:10.1016/j.icarus.2007.05.013.

Rampe, E. B., M. D. Kraft, T. G. Sharp, D. C. Golden, D. W. Ming, and P. R. Christensen (2012), Allophane detection on Mars with Thermal Emission Spectrometer data and implications for regional-scale chemical weathering processes, *Geology*, *40*(11), 995–998, doi:10.1130/G33215.1.

Ramsey, M. S., and P. R. Christensen (1998), Mineral abundance determination: Quantitative deconvolution of thermal emission spectra, *J. Geophys. Res.*, *103*, 577, doi:10.1029/97JB02784.

Rice, M. S., E. A. Cloutis, J. F. Bell, D. L. Bish, B. H. Horgan, S. A. Mertzman, M. A. Craig, R. W. Renaut, B. Gautason, and B. Mountain (2013), Reflectance spectra diversity of silica-rich materials: Sensitivity to environment and implications for detections on Mars, *Icarus*, *223*(1), 499–533, doi:10.1016/j.icarus.2012.09.021.

Richardson, M. I., and M. A. Mischna (2005), Long-term evolution of transient liquid water on Mars, *J. Geophys. Res.*, *110*(E3), 1–21, doi:10.1029/2004JE002367.

Rogers, A. D., and P. R. Christensen (2007), Surface mineralogy of Martian low-albedo regions from MGS-TES data: Implications for upper crustal evolution and surface alteration, *J. Geophys. Res. E Planets*, *112*(1), 1–18, doi:10.1029/2006JE002727.

Rogers, A. D., J. L. Bandfield, and P. R. Christensen (2007), Global spectral classification of Martian low-albedo regions with Mars Global Surveyor Thermal Emission Spectrometer (MGS-TES) data, *J. Geophys. Res.*, *112*(E2), 29, doi:10.1029/2006JE002726.

Rogers, A. D., and O. Aharonson (2008), Mineralogical composition of sands in Meridiani Planum determined from Mars Exploration Rover data and comparison to orbital measurements, *J. Geophys. Res. E Planets*, *113*(6), doi:10.1029/2007JE002995.

Rogers, A. D., and V. E. Hamilton (2015), Compositional provinces of Mars from statistical analyses of TES, GRS, OMEGA and CRISM data, *J. Geophys. Res. Planets*, *120*, 62–91, doi:10.1002/2014JE004690.

Ruff, S. W., P. R. Christensen, P. W. Barbera, and D. L. Anderson (1997), Quantitative thermal emission spectroscopy of minerals: A laboratory technique for measurement and calibration, *J. Geophys. Res.*, *102*(B7), 14899–14913, doi:10.1029/97JB00593.

Ruff, S.W. (1999), Development of Thermal Infrared Emission Spectroscopy for Geological Investigations of Earth and Mars, *Workshop on Thermal Emission Spectroscopy and Analysis of Dust, Disks, and Regoliths*, abstract #927.

Ruff, S. W. (2002), Bright and dark regions on Mars: Particle size and mineralogical characteristics based on Thermal Emission Spectrometer data, *J. Geophys. Res.*, *107*(E12), 1–22, doi:10.1029/2001JE001580.

Ruff, S. (2003), Basaltic andesite or weathered basalt: A new assessment, *Sixth Int. Conf. Mars*, *Abstract #*, 1–3.

Ruff, S. W. (2004), Spectral evidence for zeolite in the dust on Mars, *Icarus*, *168*(1), 131–143, doi:10.1016/j.icarus.2003.11.003.

Ruff, S. W., P. R. Christensen, D. L. Blaney, W. H. Farrand, J. R. Johnson, J. R. Michalski, J. E. Moersch, S. P. Wright, and S. W. Squyres (2006), The rocks of Gusev Crater as viewed by the Mini-TES instrument, *J. Geophys. Res.*, *111*(E), doi:10.1029/2006JE002747.

Ruff, S. W., and P. R. Christensen (2007), Basaltic andesite, altered basalt, and a TES-based search for smectite clay minerals on Mars, *Geophys. Res. Lett.*, *34*(10), 6, doi:10.1029/2007GL029602.

Ruff, S. W., J. D. Farmer, W. M. Calvin, K. E. Herkenhoff, J. R. Johnson, R. V. Morris, M. S. Rice, R. E. Arvidson, J. F. Bell III, P. R. Christensen, and S.W. Squyres (2011), Characteristics, distribution, origin, and significance of opaline silica observed by the Spirit rover in Gusev crater, Mars, *J. Geophys. Res. Planets*, *116*(E7), doi:10.1029/2010JE003767.

Ruiz-Agudo, E., C. V. Putnis, C. Rodriguez-Navarro, and A. Putnis (2012), Mechanism of leached layer formation during chemical weathering of silicate minerals, *Geology*, *40*(10), 947–950, doi:10.1130/G33339.1.

Ruiz-Agudo, E., C. V. Putnis, and A. Putnis (2014), Coupled dissolution and precipitation at mineral-fluid interfaces, *Chem. Geol.*, *383*, 132–146, doi:10.1016/j.chemgeo.2014.06.007.

Salisbury, J. W., and J. W. Eastes (1985), The effect of particle size and porosity on spectral contrast in the mid-infrared, *Icarus*, *64*(3), 586–588, doi:10.1016/0019-1035(85)90078-8.

Salisbury, J. W., and L. S. Walter (1987), Mid-infrared (2.1-25 μm) spectra of minerals: First edition, *USGS Open-File Rep.*, 390.

Salisbury, J. W., and L. S. Walter (1989), Thermal infrared (2.5-13.5 μm) spectroscopic remote sensing of igneous rock types on particulate planetary surfaces, *J. Geophys. Res.*, *94*(B7), 9192–9202, doi:10.1029/JB094iB07p09192.

Salisbury, J. W., and A. Wald (1992), The role of volume scattering in reducing spectral contrast of reststrahlen bands in spectra of powdered minerals, *Icarus*, *128*, 121–128, doi:10.1016/0019-1035(92)90009-V.

Salvatore, M. R., J. F. Mustard, J. W. Head, R. F. Cooper, D. R. Marchant, and M. B. Wyatt (2013), Development of alteration rinds by oxidative weathering processes in Beacon Valley, Antarctica, and implications for Mars, *Geochim. Cosmochim. Acta*, *115*, 137–161, doi:10.1016/j.gca.2013.04.002.

Schott, J., R. A. Berner, and E. L. Sjöberg (1981), Mechanism of pyroxene and amphibole weathering—I. Experimental studies of iron-free minerals, *Geochim. Cosmochim. Acta*, *45*(11), 2123–2135, doi:10.1016/0016-7037(81)90065-X.

Schott, J., O. S. Pokrovsky, and E. H. Oelkers (2009), The Link Between Mineral Dissolution/Precipitation Kinetics and Solution Chemistry, *Rev. Mineral. Geochemistry*, *70*(1), 207–258, doi:10.2138/rmg.2009.70.6.

Schott, J., O. S. Pokrovsky, O. Spalla, F. Devreux, A. Gloter, and J. A. Mielczarski (2012), Formation, growth and transformation of leached layers during silicate minerals dissolution: The example of wollastonite, *Geochim. Cosmochim. Acta*, *98*, 259–281, doi:10.1016/j.gca.2012.09.030.

Schweda, P., L. Sjöberg, and U. Södervall (1997), Near-surface composition of acid-leached labradorite investigated by SIMS, *Geochim. Cosmochim. Acta*, *61*(10), 1985–1994, doi:10.1016/S0016-7037(97)00074-4.

Seelos, K. D., R. E. Arvidson, B. L. Jolliff, S. M. Chemtob, R. V. Morris, D. W. Ming, and G. A. Swayze (2010), Silica in a Mars analog environment: Ka'u Desert, Kilauea Volcano, Hawaii, *J. Geophys. Res.*, *115*(E), doi:10.1029/2009JE003347.

Seibert, N. M., and J. S. Kargel (2001), Small Scale Martain Polygonal Terrain : Implications for Liquid Surface Water, *Geophys. Res. Lett.*, *28*(5), 899–902.

Singer, R. B., R. N. Clark, T. B. Mccord, J. B. Adams, and R. L. Huguenin (1979), Mars surface composition from reflectance spectroscopy - A summary, *J. Geophys. Res.*, *84*(B14), 8415–8426, doi:10.1029/JB084iB14p08415.

Singer, R. B. (1982), Spectral Evidence for the Mineralogy of High-Albedo Soils and Dust on Mars, *J. Geophys. Res.*, *87*(B12), 10159–10168, doi:10.1029/JB087iB12p10159.

Singer, R. B. (1985), Spectroscopic observation of Mars, *Adv. Sp. Res.*, *5*(8), 59–68, doi:10.1016/0273-1177(85)90242-X.

Smith, M. D., J. C. Pearl, B. J. Conrath, and P. R. Christensen (2001), One Martian year of atmospheric observations by the Thermal Emission Spectrometer, *Geophys. Res. Lett.*, *28*(22), 4263–4266, doi:10.1029/2001GL013608.

Smith, M. R., J. L. Bandfield, E. A. Cloutis, M. S. Rice (2013), Hydrated silica on Mars: Combined analysis with near-infrared and thermal-infrared spectroscopy, *Icarus*, 223(2), 633-648, doi:10.1016/j.icarus.2013.01.024.

Smith, R. J., B. Horgan, P. Mann, E. A. Cloutis, P. R. Christensen, Acid weathering of basalt and basaltic glass: II. Microscopic analyses and alteration mechanisms, submitted to *J. Geophys. Res*.

Soderblom, L. A., and D. B. Wenner (1978), Possible fossil H2O liquid-ice interfaces in the Martian crust, *Icarus*, *34*(3), 622–637, doi:10.1016/0019-1035(78)90050-7.

Soderblom, L. A. (1992), The composition and mineralogy of the Martian surface from spectroscopic observations: 0.3 μm to 50 μm, in Mars, edited by H. H. Kieffer et al., pp. 557-593, Univ. Ariz. Press, Tucson.

Squyres, S., J. P. Grotzinger, R. E. Arvidson, J. F. Bell III, W. Calvin, P. R. Christensen, B. C. Clark, J. A. Crisp, W. H. Farrand, K. E. Herkenhoff, J. R. Johnson, G. Klingelhöfer, A. H. Knoll, S. M. McLennan, H. Y. McSween Jr., R. V. Morris, J. W. Rice Jr., R. Rieder, and L. A. Soderblom (2004), In situ evidence for an ancient aqueous environment at Meridiani Planum, Mars, *Science*, *306*(5702), 1709–1714.

Squyres, S.W., R. E. Arvidson, J. F. Bell III, J. Brückner, N. A. Cabrol, W. Calvin, M. H. Carr, P. R. Christensen, B. C. Clark, L. Crumpler, D. J. Des Marais, C. d'Uston, T. Economou, J. Farmer, W. Farrand, W. Folkner, M. Golombek, S. Gorevan, J. A. Grant, R. Greeley, J. Grotzinger, L. Haskin, K. E. Herkenhoff, S. Hviid, J. Johnson, G. Klingelhöfer, A. Knoll, G. Landis, M. Lemmon, R. Li, M. B. Madsen, M. C. Malin, S. M. McLennan (2004a), The Spirit rover's Athena Science Investigation at Gusev Crater, Mars, Science, 305, 794‐799.

Squyres, S. W., R. E. Arvidson, J. F. Bell III, J. Brückner, N. A. Cabrol, W. Calvin, M. H. Carr, P. R. Christensen, B. C. Clark, L. Crumpler, D. J. Des Marais, C. d'Uston, T. Economou, J. Farmer, W. Farrand, W. Folkner, M. Golombek, S. Gorevan, J. A. Grant, R. Greeley, J. Grotzinger, L. Haskin, K. E. Herkenhoff, S. Hviid, J. Johnson, G. Klingelhöfer, A. H. Knoll, G. Landis, M. Lemmon, R. Li, M. B. Madsen, M. C. Malin, S. M. McLennan, H. Y. McSween, D. W. Ming, J. Moersch, R. V. Morris, T. Parker, J. W. Rice Jr., L. Richter, R. Rieder, M. Sims, M. Smith, P. Smith, L. A. Soderblom, R. Sullivan, H. Wänke, T. Wdowiak, M. Wolff, and A. Yen (2004b), The Opportunity Rover's Athena Science Investigation at Meridiani Planum, Mars, *Science*, *306*(5702), 1698–1703, doi:10.1126/science.1106171.

Squyres, S. W., R. E. Arvidson, D. L. Blaney, B. C. Clark, L. Crumpler, W. Farrand, S. Gorevan, K. E. Herkenhoff, J. Hurowitz, A. Kusack, H. Y. McSween, D. W. Ming, R. V. Morris, S. W. Ruff, A. Wang, and A. Yen (2006), Rocks of the Columbia Hills, *J. Geophys. Res. E Planets*, *111*(2), doi:10.1029/2005JE002562.

Staudigel, H., and S. R. Hart (1983), Alteration of basaltic glass: Mechanisms and significance for the oceanic crust-seawater budget, *Geochim. Cosmochim. Acta*, *47*, 337–350, doi:0016-7037/83/030337-14503.00/0.

Stefánsson, A., and S. R. Gíslason (2001), Chemical weathering of basalts, southwest Iceland: Effect of rock crystallinity and secondary minerals on chemical fluxes to the ocean, *Am. J. Sci.*, *301*(6), 513–556, doi:10.2475/ajs.301.6.513.

Stroncik, N. A., and H. U. Schmincke (2002), Palagonite - A review, *Int. J. Earth Sci.*, *91*(4), 680–697, doi:10.1007/s00531-001-0238-7.

Tanaka, B. K. L., J. A. Skinner, and T. M. Hare (2005), Geologic Map of the Northern Plains of Mars Pamphlet to accompany Scientific Investigations Map 2888.

Tanaka, K. L., J. A. P. Rodriguez, J. A. Skinner, M. C. Bourke, C. M. Fortezzo, K. E. Herkenhoff, E. J. Kolb, and C. H. Okubo (2008), North polar region of Mars: Advances in stratigraphy, structure, and erosional modification, *Icarus*, *196*(2), 318–358, doi:10.1016/j.icarus.2008.01.021.

Tanaka, K.L., and C.M. Fortezzo (2012), Geologic map of the north polar region of Mars: U.S. Geological Survey Science Investigations Map 3177, scale 1:2,000,000.

Taylor, R. and R. A. Eggleton (2001), Regolith Geology and Geomorphology, Wiley, Chichester, UK.

Techer, I., T. Advocat, J. Lancelot, and J. M. Liotard (2001), Dissolution kinetics of basaltic glasses: control by solution chemistry and protective effect of the alteration film, *Chemical Geology*, *176*(1-4), 235–263, doi:10.1016/S0009-2541(00)00400-9.

Thomas, P., and C. Weitz (1989), Sand dune materials and polar layered deposits on Mars, *Icarus*, *81*(1), 185–215, doi:10.1016/0019-1035(89)90133-4.

Thorn, C. E., R. G. Darmody, J. C. Dixon, and P. Schlyterd (2001), The chemical weathering regime of Kärkevagge, arctic-alpine Sweden, *Geomorphology*, *41*(1), 37–52, doi:10.1016/S0169-555X(01)00102-7.

Thorseth, I. H., H. Furnes, and O. Tumyr (1991), A textural and chemical study of Icelandic palagonite of varied composition and its bearing on the mechanism of the glass-palagonite transformation, *Geochim. Cosmochim. Acta*, *55*(3), 731–749, doi:10.1016/0016-7037(91)90337-5.

Tosca, N. J., S. M. Mclennan, D. H. Lindsley, and M. A. A. Schoonen (2004), Acid-sulfate weathering of synthetic Martian basalt: The acid fog model revisited, *J. Geophys. Res.*, *109*(E), 05003, doi:10.1029/2003JE002218.

Tosca, N. J., S. M. McLennan, B. C. Clark, J. P. Grotzinger, J. A. Hurowitz, A. H. Knoll, C. Schröder, and S. W. Squyres (2005), Geochemical modeling of evaporation processes on Mars: Insight from the sedimentary record at Meridiani Planum, *Earth Planet. Sci. Lett.*, *240*(1), 122–148, doi:10.1016/j.epsl.2005.09.042.

Toulmin III, P., A. K. Baird, B. C. Clark, K. Keil, H. J. Rose, Jr., R. P. Christian, P. H. Evans, and W. C. Kelliher (1977), Geochemical and Mineralogical Interpretation of the Viking Inorganic Chemical Results, *J. Geophys. Res.*, *82*(28), 4625–4634, doi:10.1029/JS082i028p04625.

Tsoar, H., R. Greeley, and A. R. Peterfreund (1979), Mars: The north polar sand sea and related wind patterns, *J. Geophys. Res.*, *84*(B14), 8167–8180, doi:10.1029/JB084iB14p08167.

Tsomaia, N., S. L. Brantley, J. P. Hamilton, C. G. Pantano, and K. T. Mueller (2003), NMR evidence for formation of octahedral and tetrahedral Al and repolymerization of the Si network during dissolution of aluminosilicate glass and crystal, *Am. Mineral.*, *88*(1), 54–67.

Wada, K. (1987), Minerals formed and mineral formation from volcanic ash by weathering, *Chem. Geol.*, *60*(1-4), 17–28, doi:10.1016/0009-2541(87)90106-9.

Weed, R., and Ackert, R.J., 1986, Chemical weathering of Beacon Supergroup sandstones and implications for Antarctic glacial chronology: South African Journal of Science, v. 82, p. 513–516.

Weed, R., and Norton, S.A., 1991, Siliceous crusts, quartz rinds, and biotic weathering of sandstones in the cold desert of Antarctica, in Berteline, *J., ed., Diversity of environmental geochemistry*: Amsterdam, Elsevier, p. 225–248.

White, A. F. (1983), Surface chemistry and dissolution kinetics of glassy rocks at 25°C, *Geochimica et Cosmochimica Acta*, *47*, 805–815, doi:10.1016/0016-7037(83)90114-X.

White, W. B., and D. G. Minser (1984), Raman spectra and structure of natural glasses, *Journal of Non-Crystalline Solids*, *67*(1-3), 45–59, doi:10.1016/0022-3093(84)90140-6.

Wilson, L., Head III, J. W. (1994), Mars: Review and analysis of volcanic eruption theory and relationships to observed landforms, *Rev. Geophys.*, *32*(3), 221–263, doi:10.1029/94RG01113.

Wolff-Boenisch, D., S. R. Gislason, and E. H. Oelkers (2004), The dissolution rates of natural glasses as a function of their composition at pH 4 and 10.6, and temperatures from 25 to 74 C, *Geochim. Cosmochim. Acta*, *68*(23), 4843–4858, doi:10.1016/j.gca.2004.05.027.

Wyatt, M. B., and H. Y. Mcsween (2002), Spectral evidence for weathered basalt as an alternative to andesite in the northern lowlands of Mars, *Nature*, *417*, 263.

Yamane, M., and Y. Asahara (2000), *Glasses for Photonics*, Cambridge University Press.

Yen, A. S. et al. (2005), An integrated view of the chemistry and mineralogy of Martian soils, *Nature*, *436*(July), 49–54, doi:10.1038/nature03637.

Zelazny LW, Calhoun FG (1977) Palygorskite, (attapulgite), sepiolite, talc, pyrophyllite, and zeolites, in: *Minerals in Soil Environments*, edited by J. B. Dixon, S. B. Weed, Soil Science Society of America, Madison, Wisconsin, p 435-470.

Zent, A. P., and C. P. Mckay (1994), The Chemical Reactivity of the Martian Soil and Implications for Future Missions, *Icarus*, *108*(1), 146–157, doi:10.1006/icar.1994.10